

Study of Inclusive b-Jet Production in ALICE Experiment at LHC

By

ASHIK IKBAL SHEIKH

Enrolment No.: PHYS04201404006

Variable Energy Cyclotron Centre, Kolkata

A thesis submitted to

The Board of Studies in Physical Sciences

In partial fulfillment of requirements

For the Degree of

DOCTOR OF PHILOSOPHY

of

HOMI BHABHA NATIONAL INSTITUTE




October, 2019

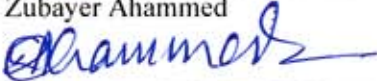


Homi Bhabha National Institute¹


Recommendations of the Viva Voce Committee

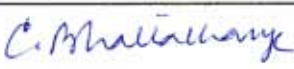
As members of the Viva Voce Committee, we certify that we have read the dissertation prepared by **Ashik Ikbal Sheikh** entitled "**Study of Inclusive b-Jet Production in ALICE Experiment at LHC**" and recommend that it may be accepted as fulfilling the thesis requirement for the award of Degree of Doctor of Philosophy.


Chairman - Prof. Subhasis Chattopadhyay  Date: 15/10/19

Guide / Convener - Prof. Zubayer Ahammed  Date: 15/10/19

Co-guide - - (if any) ----- Date: -----

Examiner - Prof. Santosh Kumar Das  Date: 15/10/19

Member 1 - Prof. Chandana Bhattacharya  Date:

Member 2 - Prof. Munshi Golam Mustafa  Date: 15/10/19

Final approval and acceptance of this thesis is contingent upon the candidate's submission of the final copies of the thesis to HBNI.

I/We hereby certify that I/we have read this thesis prepared under my/our direction and recommend that it may be accepted as fulfilling the thesis requirement.

Date: 15/10/19

Place: VECC, KOLKATA

Signature

Co-guide (if any)



Signature

Guide

¹ This page is to be included only for final submission after successful completion of viva voce.

STATEMENT BY AUTHOR

This dissertation has been submitted in partial fulfillment of requirements for an advanced degree at Homi Bhabha National Institute (HBNI) and is deposited in the Library to be made available to borrowers under rules of the HBNI.

Brief quotations from this dissertation are allowable without special permission, provided that accurate acknowledgement of source is made. Requests for permission for extended quotation from or reproduction of this manuscript in whole or in part may be granted by the Competent Authority of HBNI when in his or her judgment the proposed use of the material is in the interests of scholarship. In all other instances, however, permission must be obtained from the author.



Ashik Ikbal Sheikh

DECLARATION

I, hereby declare that the investigation presented in the thesis has been carried out by me. The work is original and has not been submitted earlier as a whole or in part for a degree / diploma at this or any other Institution / University.

Ashik Iqbal Sheikh
Ashik Iqbal Sheikh

List of Publications arising from the thesis

Journal

1. **“Effect of the chromo-electromagnetic field fluctuations on heavy quark propagation in a deconfined hadronic medium at energies available at the CERN Large Hadron Collider”**
Ashik Ikbāl Sheikh, Zubayer Ahammed, Prashant Shukla and Munshi G. Mustafa
 Phys. Rev. C **98**, (2018) 034915
 arXiv:1711.06245 [hep-ph].
2. **“Impact of the chromo-electromagnetic field fluctuations on transport coefficients of heavy quarks and shear viscosity to entropy density ratio of quark-gluon plasma”**
Ashik Ikbāl Sheikh and Zubayer Ahammed
 Nucl. Phys. A **986**, (2019) 48
 arXiv:1903.10690 [hep-ph].

Conferences

1. **“Optimization of secondary vertex based b-jet tagging algorithm with ALICE at the LHC”**
Ashik Ikbāl Sheikh, Zubayer Ahammed and Elena Bruna
 Proceedings of the DAE-BRNS Symp. on Nucl. Phys. **61**, (2016) 792.
2. **“Effect of initial state beam parton energy loss in Drell-Yan production for proton-nucleus collisions”**
Ashik Ikbāl Sheikh and Partha Pratim Bhaduri
 Proceedings of the DAE-BRNS Symp. on Nucl. Phys. **62**, (2017) 878.
3. **“The nuclear modification factor of D and B mesons in a field fluctuating quark-gluon plasma at LHC energies”**
Ashik Ikbāl Sheikh, Zubayer Ahammed and Munshi G. Mustafa
 PoS(BEAUTY2018) **062**, (2018).
4. **“Heavy quarks and chromo- electromagnetic field fluctuations: The Drag, Diffusion coefficient and Nuclear modification factor”**
Ashik Ikbāl Sheikh, Zubayer Ahammed and Munshi G. Mustafa
 Journal of Physics: Conf. Series **1137**, (2019) 012049.

Other publication

ALICE Analysis Note

1. “Inclusive b -jet tagging using the displaced secondary vertex method in p–Pb collisions at $\sqrt{s_{NN}} = 5.02$ TeV”
Ashik Ikbāl Sheikh, Artem Isakov, Róbert Vértési, Filip Krizek, Elena Bruna and Zubayer Ahammed,
 ANA **913** (<https://alice-notes.web.cern.ch/node/913>)

Communicated

1. “Heavy flavour Langevin diffusion with the chromo-electromagnetic field fluctuations in the quark-gluon plasma”,
Ashik Ikbāl Sheikh and Zubayer Ahammed
 arXiv:1902.02477 [hep-ph].
2. “The role of the stochastic color field fluctuations on J/ψ suppression in ultra-relativistic heavy-ion collisions”,
Ashik Ikbāl Sheikh, Zubayer Ahammed and Munshi G. Mustafa
 arXiv:1902.06989 [hep-ph].

Ashik Ikbāl Sheikh

Ashik Ikbāl Sheikh

DEDICATIONS

*Dedicated to my beloved Parents
who value education above all.*

ACKNOWLEDGEMENTS

First and foremost, I express my deepest gratitude and respect to my supervisor Prof. Zubayer Ahammed whose encouragement, guidance, invaluable academic and mental support enabled me to pursue my research work at VECC as well as in the international collaboration like ALICE at CERN, Geneva, Switzerland. Initially it was very hard for me to work with the scientists from abroad. He taught me how to work in the international environment. He always gave me the freedom in research and encouraged my idea even if it was silly. I am fortunate to have been able to work under his guidance.

I would like to convey special thanks to my international collaborators Dr. Elena Bruna (INFN-Torino, Italy) and Dr. Robert Vertesi (Wigner Institute, Budapest, Hungary) from whom I learnt the ALICE data analysis techniques. The beginning of my journey was very hard. Without their help and support, it was almost impossible for me to learn the complicated experimental framework in those days. I enjoyed to work with them at CERN. Specially, Elena and Robert cared and guided me during my academic visit at INFN-Torino, Turin, Italy and Wigner Institute, Budapest, Hungary. Beside the tight schedule of works, they also helped me to explore the beautiful cities of Italy and Hungary. That was really full of fun. I am thankful to Prof. Ralf Auerbeck (GSI, Darmstadt, Germany), Dr. Andrea Rossi (INFN-Padova, Italy), Prof. Guiseppe Bruno (INFN-Bari, Italy), Dr. Filip Krizek (Nuclear Physics Institute, Prague, Czech Republic) and Dr. Yuriy Karpenko (IMT Atlantique, France) for their help.

I sincerely thank to the members of my Doctoral Committee: Prof. Subhasis Chattopadhyay, Prof. Chandana Bhattacharya and Prof. Munshi Golam Mustafa for their insightful comments, encouragement and advices in each year of my PhD tenure. I have immensely been benefited from the discussions with Prof. Munshi Golam Mustafa, Prof. Jan-e Alam and Dr. Shantosh Kumar Das on heavy-flavor physics during my journey to this unknown path. I also acknowledge the discussions with Dr. Prithwish Tribedy (BNL, USA) and Dr. Partha Pratim Bhaduri. I am thankful to Mr. Prasun Singha Roy and the VECC grid computing team for constantly maintaining the grid facility active when my phenomenological works were done.

I am very much grateful to my teacher and mentor Dr. Jyotirmoy Guha (Santipur College, University of Kalyani), who taught me Physics during my college days. He first made me under-

stood what is the beauty of Physics, the funs in this subject. He always gave the energy tonic, the inspiration and encouragement. I am lucky to have this great man as my teacher.

I was gifted with a bunch of positive minded and helpful friends, seniors and juniors at VECC. It was a great pleasure to work in such environment. Specially, I would like to thank Sarwar da, Rana da, Atta da, Rajendra da, Noor da, Debojit da, Nachiketa, Shreyasi, Shabnam, Sumit, Sanchari and Mahfizur for their good companions and all beautiful moments we shared.

Finally, I owe everything to my beloved parents and brother who always gave me mental supports specially when the situation was not so good.

Indeed all praises be for the ONE who cares most and deserves, the beneficent, the merciful, the main architect of everything.



Ashik Iqbal Sheikh

Contents

Synopsis	xxxii
List of Figures	xxxii
List of Tables	xlvi
1 Introduction	1
1.1 Quantum Chromodynamics (QCD)	2
1.1.1 Two Novel Properties of QCD	3
1.1.2 The QCD Phase Diagram	4
1.2 Deconfined QCD Matter at Laboratory	6
1.3 Experimental Signatures of QGP	7
1.3.1 Strangeness Enhancement	8
1.3.2 J/ψ Suppression	8
1.3.3 Jet Quenching	9
1.3.4 Other Signatures	10
1.4 Heavy Quark Jet	10
1.5 Goal of this Thesis	12
1.6 Outline of this Thesis	13

2	Heavy Quark Propagation in the QGP	15
2.1	Production of Heavy Quarks in Heavy-Ion Collisions	16
2.1.1	Leading Order(LO) pQCD Calculation	16
2.1.2	Nuclear Shadowing Effect in p-A and A-A Collisions	18
2.2	Model for QGP Evolution and Initial Condition	20
2.2.1	A Simplistic 1D Expansion	20
2.2.2	Hydrodynamic Evolution	22
2.3	Heavy Quark Dynamics	22
2.3.1	Fokker-Planck Equation	23
2.3.2	Langevin Equation	25
2.4	Heavy Quark Energy Loss	26
2.4.1	Collisional Energy Loss	26
2.4.2	Radiative Energy Loss	28
2.5	Heavy Quark Hadronization to Heavy Mesons	31
2.5.1	Fragmentation	31
2.5.2	Coalescence	35
3	The Chromo-Electromagnetic Field Fluctuations and Heavy Quarks	37
3.1	The Chromo-Electromagnetic Field Fluctuations in the QGP	37
3.2	Heavy Quark Energy Gain	38
3.3	Effect of the Chromo-Electromagnetic Field Fluctuations on Drag and Diffusion Coefficient of Heavy Quarks	45
3.4	Effect of the Chromo-Electromagnetic Field Fluctuations on Heavy Flavour Sup- pression as Observed in the ALICE and CMS experiment	49
3.5	Effect of the Chromo-Electromagnetic Field Fluctuations on J/ψ Suppression . . .	53

3.6	Effect of the Chromo-Electromagnetic Field Fluctuations on η/s of the QGP . . .	57
4	The LHC and the ALICE Detector	61
4.1	The Large Hadron Collider (LHC)	61
4.2	A Large Ion Collider Experiment (ALICE)	63
4.2.1	ALICE Tracking System	65
4.2.2	Particle Identification	68
4.2.3	Electromagnetic Calorimeter (EMCal)	70
4.2.4	VZERO (V0) Detector	71
4.2.5	TZERO (T0) Detector	72
5	Measurement of Inclusive b-Jets in p-Pb Collisions	73
5.1	Datasets and Monte Carlo Productions	74
5.1.1	Production Cycles	74
5.1.2	PYTHIA+EPOS Simulations	75
5.2	Analysis Strategy	78
5.2.1	Event Selection	79
5.2.2	Track Selection	79
5.2.3	Jet Reconstruction	80
5.2.4	The b -Jet Candidate Identification (Secondary Vertex Tagging)	81
5.3	Data Quality Assurance (QA)	82
5.3.1	Tracks and Jets	82
5.3.2	QA of SV Tagging Cuts	84
5.4	Corrections	86
5.4.1	The b-Jet Tagging Efficiency	88

5.4.2	Purity of the Tagged b-Jet Sample	91
5.4.3	Hybrid Purity	94
5.5	Unfolding Procedure	103
5.5.1	Unfolding of the Measured Spectra	104
5.6	Systematic Uncertainties	114
5.6.1	Tagging Systematics	114
5.6.2	POWHEG Scale Variations and Hybrid Purity Systematics	115
5.6.3	Unfolding Systematics	116
5.6.4	Choice of the Background Estimation Method	116
5.6.5	Tracking Efficiency	117
5.6.6	Track Momentum Smearing	118
5.6.7	Secondary Tracks Admixture	120
5.7	Results and Discussions	124
5.7.1	The b-Jet Cross Section with Systematics	124
5.7.2	Comparison of b-Jet Cross Section with NLO pQCD Calculations	126
6	Summary	129
	Appendix A	133
A.1	Jet Reconstruction Algorithm	134
A.2	POWHEG+PYTHIA	136
A.2.1	Interfacing POWHEG with PYTHIA	137
A.2.2	POWHEG Settings	137
A.2.3	POWHEG Systematics	139
A.3	Optimization of Tagging Cuts	145

A.3.1 Optimum Range for Tagging Cuts	149
A.4 Invariant Mass Templates	149
A.4.1 Data-Driven Purity Template Fits	149

Synopsis



Homi Bhabha National Institute

Synopsis of PhD Thesis

- 1. Name of the Student: ASHIK IKBAL SHEIKH**
- 2. Name of the Constituent Institution: Variable Energy Cyclotron Centre, Kolkata**
- 3. Enrolment No. : PHYS04201404006**
- 4. Title of the Thesis: Study of Inclusive b-Jet Production in ALICE Experiment at LHC**
- 5. Board of Studies: Physical Sciences**

Quantum Chromodynamics (QCD) is the non-abelian gauge theory (where gluon plays the role of gauge boson) that governs the interactions between colour charges (quarks and gluons) via the strong interaction. The QCD has a unique property called the asymptotic freedom which suggests that at very high temperature and density the interactions between the partons inside hadrons become so weak that the partons are no longer confined within the hadrons rather move in the extended volume, i.e., the partons get deconfined. Such new deconfined phase of QCD matter is called Quark-Gluon Plasma (QGP). Some lattice QCD based calculations show that the quark-hadron phase transition occurs at temperature $T_c \sim 170$ MeV. It is believed that our universe has under gone such transition after a few microsecond of the Big Bang, and the core of some compact astrophysical objects like neutron stars may contain this deconfined QCD matter at high baryon density and low temperature. This makes the study of such deconfined QCD matter of immense interest. The currently known way to produce this deconfined state of QCD matter at laboratory is to collide beams of heavy-ions at ultra-relativistic energies. The ultra-relativistic heavy-ion collisions produce extremely hot (temperature in excess of 10^{12} K) and dense (energy density above $1 \text{ GeV}/fm^3$) deconfined matter, the QGP. The experimental facilities in operation

are the Relativistic Heavy-Ion Collider (RHIC) at the Brookhaven National Laboratory (BNL) and the Large Hadron Collider (LHC) at the European Organization for Nuclear Research (CERN). The main goals of these experimental facilities are to create this QGP medium in laboratory and characterize the produced medium. Various experimental signatures have been observed in the favour of the existence of the QGP medium. The main signatures are Strangeness enhancement, Quarkonia suppression, Jet quenching, Dilepton production etc.

Amongst many, one of the crucial probes to characterize the QGP medium is the heavy quark jets. The heavy quarks (mainly charm (c) and bottom (b)) have some interesting properties which make them excellent probes to study the QGP: the heavy quarks are mainly produced in the primordial hard scatterings in the collisions and hence they encounter the full space-time evolution of the medium which suggests that they might preserve a memory of their interaction history. Being heavy, the thermal production of heavy quarks is negligible which ensures that the initial production of heavy quarks becomes frozen at very beginning of the collisions. Immediately after the production of heavy quarks during the collisions, they will propagate and shower into collimated spray of particles, called heavy-flavor tagged jets (c -jets or b -jets, depending upon the fragmenting parton). The heavy-flavor tagged jets can shed light on the fundamental thermodynamic and transport properties of the QGP. The heavy quarks are expected to lose energy in QGP differently compared to the light quarks, significantly at the lower and intermediate transverse momentum regions. Therefore, the jet quenching effects depend on the flavor or mass of the fragmenting parton which is most pronounced for b -jets [1, 2]. The experimental efforts have been made to measure the heavy-flavor tagged jets by CMS [3, 4] and ATLAS [5] collaborations at the LHC.

Furthermore, the energy loss suffered by the heavy quarks throughout their path of propagation is reflected in the relative suppression of heavy-flavor hadrons[6, 7, 8, 9]. Heavy quarks lose energy by colliding with the light partons of the thermal background (QGP) and by radiating gluons, *viz.*, bremsstrahlung process due to the deceleration of the heavy quarks. The QGP is a statistical system of coloured partons that are moving randomly. Since quarks and gluons have colour charge, they produce colour electromagnetic field called “Chromo-Electromagnetic Field”, during their random motions. In other words, the QGP is a statistical ensemble of mobile coloured charge particles, which can be characterised by stochastic colour field fluctuations. These field fluctuations generally couple to the external perturbations and would affect the response of the medium. In general, these field fluctuations are not considered when heavy quark

energy losses are calculated in the QGP. The effect of these chromo-electromagnetic field fluctuations in the QGP cause energy gain of heavy quarks of all momenta, significantly at lower momentum [10]. This is due to the fact that the statistical change in the energy of the propagating heavy quarks takes place when the chromo-electromagnetic field fluctuations cause the fluctuations in the velocities of heavy quarks. This energy gain results in reduction of the total energy loss. The magnitudes of transport coefficients (drag and diffusion coefficients) of heavy quarks are determined by the interaction of the heavy quarks with the medium partons. Hence, field fluctuations have an important effect on heavy quark transport coefficients and heavy-flavor nuclear modification factor (R_{AA}). Besides that, the shear viscosity to entropy density ratio (η/s) of the QGP medium is also affected by the field fluctuations.

This dissertation includes the phenomenological study of chromo-electromagnetic field fluctuations in the QGP medium and the measurements of reconstructed inclusive bottom quark jet (b -jet) production in p-Pb collisions at $\sqrt{s_{NN}} = 5.02$ TeV in the ALICE experiment at the LHC.

For the phenomenological studies, we have considered an isentropic cylindrical expansion [11] of the QGP medium and obtain the temperature (T) as a function of proper time (τ) as, $T^3\tau = \text{const.}$ The collisional [12, 13] and radiative [14, 15, 16] energy loss of heavy quarks are calculated as a function of proper time. The calculated energy loss is then averaged over the temperature evolution of the QGP medium. The energy gain due to field fluctuations has also been calculated in similar way. In this spirit, we use energy loss $-dE/dx$ to estimate the drag (A) and diffusion (B) coefficients of heavy quarks as, $A = \frac{1}{p} \left(-\frac{dE}{dx} \right)$ and $B = T \left(-\frac{dE}{dx} \right)$. In addition to that, the η/s of the QGP medium has been calculated as [17]:

$$\frac{\eta}{s} \approx 1.25 \frac{T^3}{\hat{q}}, \quad (1)$$

where T is the temperature of the medium and \hat{q} is the transport coefficient which is defined as square of the average exchanged momentum between the heavy quark and bath particles per unit length. We use $\hat{q} = 4B$, where B is the diffusion coefficients of heavy quarks. The nuclear modification factor, R_{AA} for heavy-flavor mesons is computed as:

$$R_{AA}(p_T, b_1, b_2) = \frac{\frac{d^2\sigma_{PbPb}(p_T, b_1, b_2)}{dp_T^2 dy}}{\int_{b_1}^{b_2} d^2b T_{AA} \frac{d^2\sigma_{pp}(p_T)}{dp_T^2 dy}}. \quad (2)$$

where, b_1 and b_2 are the impact parameters corresponding to a given centrality of collision and

T_{AA} is the nuclear overlap function (obtained from Glauber model).

We have found that these fluctuations result a reduction of the drag and diffusion coefficients [18], as these fluctuations cause heavy quarks to gain energy. We have also observed that the value of η/s of the QGP medium increases with the inclusion of these fluctuations [18] and make the calculation of η/s closer to the value obtained in lattice QCD (LQCD) and functional renormalization group calculations. The calculated R_{AA} of the heavy-flavor mesons can describe the measured R_{AA} of D -mesons and B -mesons at CMS and ALICE experiments within their uncertainties, when the effect of these fluctuations is included along with the energy loss processes [19, 20]. We have also found significant effect of these fluctuations on experimentally observed J/ψ suppression at the RHIC and LHC energies [21]. We emphasize that the chromo-electromagnetic field fluctuations are found to play an important role on the propagation of the heavy quark jets in the QGP vis-a-vis the nuclear modification factor of heavy-flavor particles and on η/s of the QGP medium.

The main focus of this dissertaion is to measure the bottom quark jet (b -jet) production in the ALICE experiment at the LHC. In order to do that, we have analyzed the ALICE minimum bias data of p-Pb collisions at $\sqrt{s_{NN}} = 5.02$ TeV, recorded in Run-2 in the year of 2016. In this analysis, the ALICE sub-detectors involved are: Inner Tracking System (ITS), Time Projection Chamber (TPC), V0 and T0. The V0 detector serves as minimum bias triggers and helps in primary vertex reconstruction. The T0 detector provides fast timing signals in ALICE trigger system and TOF detector. The secondary vertex reconstruction is done by ITS. The charged particle tracks are reconstructed using ITS and TPC.

The LHC has explored several algorithms to tag heavy quark jets in the experiments. All of the algorithms rely on the properties of hadrons containing heavy quarks, i.e., their displaced secondary vertices (SVs), large impact parameters of the tracks in the SV, large invariant mass of SV, etc. For b -jet identification, the ALICE detector at the LHC has excellent particle tracking capabilities which allows to identify displaced SVs of B-hadron decays inside the jet. The SVs due to B-hadron decays are displaced from the primary vertex (PV) and hence called displaced secondary vertex (DSV). The distance from PV to the DSV is very different for B-hadrons than charm hadrons or mesons. This property of B-hadron DSV allows us to discriminate b -jets from other flavor jets.

In this analysis method, firstly, the charged tracks are selected with selection criteria $p_{T,tracks} > 0.15$ GeV/ c and $|\eta| < 0.9$ for jet reconstruction. Then, with the selected tracks, the jets are re-

constructed (with jet resolution parameter, $R = 0.4$) by the anti- k_T jet finding algorithm from FastJet package. Since, the jets are produced via hard scatterings in the QCD processes, the reconstructed jets in the experiments are affected by the background particles (i.e., the particles that are not produced from the hard processes). In order to get the signal jets, the backgrounds must be subtracted. The background subtraction is performed by running the k_T jet finding algorithm and removing the two high p_T k_T -jets since they might be the signal jets. Now with the k_T -jets, background density is calculated by taking the median of k_T -jet p_T divided by k_T -jet area. Furthermore, the backgrounds from one jet to another jet may fluctuate which smear the measurements. Thus, one needs to take into account the background fluctuations and it is done by Random Cone (RC) algorithm. This RC algorithm throws random cones in the $\eta - \phi$ space and counts the number of tracks inside the cone to add their p_T values, provided the RC does not overlap with the signal jet. Now with these background subtracted reconstructed jets, the SVs inside these jets are searched by taking 3 tracks from the jet constituents. The distances of these reconstructed SVs from PV are calculated and the distances are called decay lengths (L_{xy} or $SL_{xy} = L_{xy}/\sigma_{L_{xy}}$, normalized decay lengths where $\sigma_{L_{xy}}$ is the uncertainty in L_{xy}). The jets with SVs are the b -jet candidates. Further confirmation for the b -jet is achieved by studying the properties of reconstructed SVs, SL_{xy} and SV dispersion ($\sigma_{SV} = \sqrt{d_1^2 + d_2^2 + d_3^2}$, where $d_{1,2,3}$ are the distances of three tracks from the SV), and correcting the tagged jets for tagging efficiency (ϵ_b) and purity (P_b) as: $N_{b-jets} = N_{tagged-jets} \times (P_b/\epsilon_b)$. The ϵ_b is obtained from Monte Carlo simulations (PYTHIA+EPOS) and P_b is obtained from POWHEG+PYTHIA simulations as well as from the secondary vertex mass template fitting. The POWHEG (POsitive Weight Hardest Emission Generator) is a Monte Carlo event generator for heavy quark pair production at NLO.

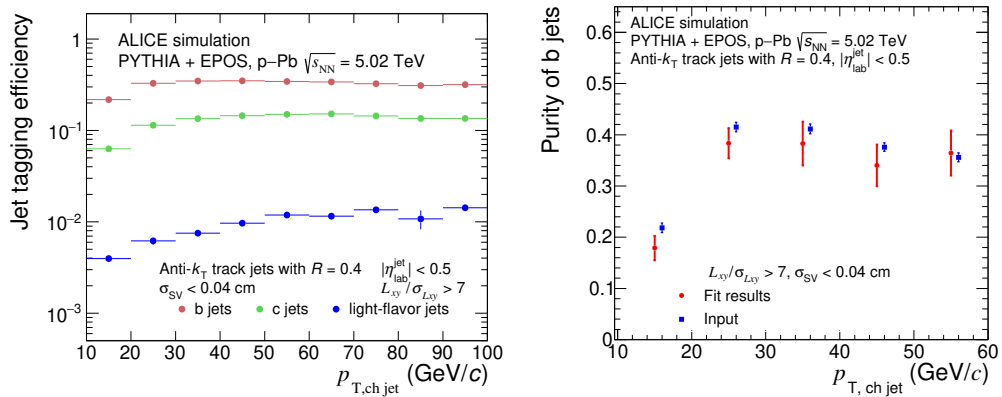


Figure 1: Left: Jet tagging efficiency for $SL_{xy} > 7$ and $\sigma_{SV} < 0.04$ as a function of charged jet p_T . Right: Purity of b -jets for $SL_{xy} > 7$ and $\sigma_{SV} < 0.04$ as a function of charged jet p_T .

Fig. 1 shows jet tagging efficiency (left) and purity of b -jets (right) for the displaced secondary vertex topological cuts $SL_{xy} > 7$ and $\sigma_{SV} < 0.04$ cm as a function of charged jet p_T . The jet tagging efficiency for b -jets is higher compared to the other flavor jets in this DSV tagging method. The b -jet purity for the same topological cuts is obtained by performing the fits of the secondary vertex mass templates and the result is consistent with that of obtained from PYTHIA+EPOS simulation.

Finally the tagged b -jet spectrum is corrected for the detector effects. Because the measurements are affected due to the detectors used in the experiment. In order to correct for the detector effects, we have performed the unfolding of the measured b -jet spectra by the iterative methods, Bayesian and Singular Value Decomposition (SVD) methods. We have compared the measurements for b -jets with NLO pQCD calculations (POWHEG).

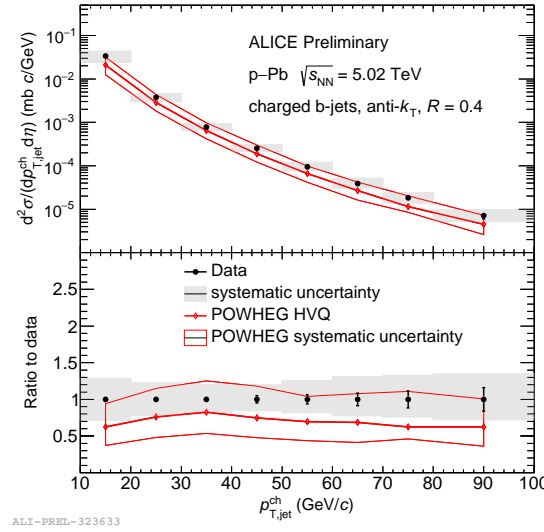


Figure 2: Upper panel: The measured b -jet cross-section as a function of charged jet p_T . Lower panel: The ratio of the measured b -jet spectra with the NLO pQCD calculations (POWHEG).

In Fig. 2, we have shown the measured b -jet spectra as a function of jet p_T and the comparison with NLO pQCD calculations (POWHEG). The measured b -jet spectra is in agreement with the NLO pQCD calculations within the experimental and theoretical uncertainties.

In summary, we find that the chromo-electromagnetic field fluctuations play an important role to explain the experimentally observed heavy flavour suppression at the RHIC and LHC energies. These fluctuations also causes the increment of the values of η/s of the QGP medium that are consistent with the LQCD and functional renormalization group calculations. The inclusive b -jet production cross-section has been measured in p-Pb collisions at $\sqrt{s_{NN}} = 5.02$ TeV in ALICE experiment at the LHC. The experimental measurements are quite consistent with the NLO pQCD calculations within their uncertainties.

References

- [1] J. Huang, Z.-B. Kang and I. Vitev, Phys. Lett. B **726** (2013) 251.
- [2] Z.-B. Kang, J. Reiten, I. Vitev and B. Yoon, Phys. Rev. D. **99** (2019) 034006.
- [3] CMS Collaboration, JINST **8** (2013) P04013; Phys. Rev. Lett. **113** (2014) 132301; Phys. Lett. B **754** (2016) 59.
- [4] CMS Collaboration, Phys. Lett. B **772** (2017) 306.
- [5] ATLAS Collaboration, Eur. Phys. J. C **71** 1846 (2011); Phys. Lett. B **706** 295 (2012); ATLAS-CONF-2010-042.
- [6] ALICE Collaboration, JHEP 1603 (2016) 081.
- [7] CMS Collaboration CMS-PAS-HIN-15-005.
- [8] CMS Collaboration CMS-PAS-HIN-16-001.
- [9] CMS Collaboration, Phys. Rev. Lett. **119** (2017) 152301.
- [10] P. Chakraborty, M. G. Mustafa and M. H. Thoma, Phys. Rev. C **75** (2007) 064908.
- [11] V. Kumar, P. Shukla and R. Vogt, Phys. Rev. C **92** (2015) 024908.
- [12] E. Brateen and M. H. Thoma, Phys. Rev. D **44** (1991) R2625.
- [13] S. Peigne and A. Peshier, Phys. Rev. D **77** (2008) 114017.
- [14] S. Wicks, W. Horowitz, M. Djordjevic and M. Gyulassy, Nucl. Phys. A **784** (2007) 426; Nucl. Phys. A **783** (2007) 493; M. Djordjevic and M. Gyulassy, Nucl. Phys. A **733** (2004) 265.
- [15] M. Gyulassy, P. Levai and I. Vitev, Phys. Rev. Lett. **85** (2000) 5535.
- [16] R. Abir, U. Jamil, M. G. Mustafa and D. K. Srivastava, Phys. Lett. B **715** (2012) 183.
- [17] A. Majumder, B. Muller and X. N. Wang, Phys. Rev. Lett. **99** (2007) 192301.
- [18] Ashik Ikbal Sheikh and Zubayer Ahammed, Nucl. Phys. A, **986**, (2019) 48.
- [19] Ashik Ikbal Sheikh, Zubayer Ahammed, Prashant Shukla and Munshi G. Mustafa, Phys. Rev. C **98**, (2018) 034915.

[20] Ashik Ikbal Sheikh and Zubayer Ahammed, arXiv:1902.02477.

[21] Ashik Ikbal Sheikh and Zubayer Ahammed, arXiv:1902.06989.

Publications in Refereed Journals:

a. Published

1. "Effect of the chromo-electromagnetic field fluctuations on heavy quark propagation in a deconfined hadronic medium at energies available at the CERN Large Hadron Collider"
Ashik Ikbal Sheikh, Zubayer Ahammed, Prashant Shukla and Munshi G. Mustafa
Phys. Rev. C **98**, (2018) 034915.
2. "Impact of the chromo-electromagnetic field fluctuations on transport coefficients of heavy quarks and shear viscosity to entropy density ratio of quark-gluon plasma"
Ashik Ikbal Sheikh and Zubayer Ahammed
Nucl. Phys. A **986**, (2019) 48.

b. Communicated

1. "Heavy flavour Langevin diffusion with the chromo-electromagnetic field fluctuations in the quark-gluon plasma",
Ashik Ikbal Sheikh and Zubayer Ahammed
arXiv:1902.02477.
2. "The role of the stochastic color field fluctuations on J/ψ suppression in ultra-relativistic heavy-ion collisions",
Ashik Ikbal Sheikh, Zubayer Ahammed and Munshi G. Mustafa
arXiv:1902.06989.

Other Publications:

ALICE Analysis Note

1. "Inclusive b -jet tagging using the displaced secondary vertex method in p-Pb collisions at $\sqrt{s_{NN}} = 5.02$ TeV"

Ashik Ikbal Sheikh, Artem Isakov, Róbert Vértési, Filip Krizek, Elena Bruna and Zubayer Ahammed,
ANA 913 (<https://alice-notes.web.cern.ch/node/913>)

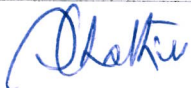



a. Conference/Symposium

1. "Optimization of secondary vertex based b-jet tagging algorithm with ALICE at the LHC"
Ashik Ikbal Sheikh, Zubayer Ahammed and Elena Bruna
Proceedings of the DAE-BRNS Symp. on Nucl. Phys. **61**, (2016) 792.
2. "Effect of initial state beam parton energy loss in Drell-Yan production for proton-nucleus collisions"
Ashik Ikbal Sheikh and Partha Pratim Bhaduri
Proceedings of the DAE-BRNS Symp. on Nucl. Phys. **62**, (2017) 878.
3. "The nuclear modification factor of D and B mesons in a field fluctuating quark-gluon plasma at LHC energies"
Ashik Ikbal Sheikh, Zubayer Ahammed and Munshi G. Mustafa
PoS(BEAUTY2018) 062, (2018).
4. "Heavy quarks and chromo- electromagnetic field fluctuations: The Drag, Diffusion coefficient and Nuclear modification factor"
Ashik Ikbal Sheikh, Zubayer Ahammed and Munshi G. Mustafa
Journal of Physics: Conf. Series **1137**, (2019) 012049.


Signature of Student:

Date: 15/05/2019

Doctoral Committee:

S. No.	Name	Designation	Signature	Date
1.	Prof. Subhasis Chattopadhyay	Chairman		15/5/19
2.	Prof. Zubayer Ahammed	Guide/Convener		15-5-19
3.	Prof. Chandana Bhattacharya	Member 1		15.5.2019
4.	Prof. Munshi Golam Mustafa	Member 2		15/05/19

List of Figures

1.1	The running coupling constant $\alpha_s(Q^2)$ as a function of momentum transfer Q , determined from varieties of processes. This figure is taken from Ref.[4].	3
1.2	Normalized energy density(normalized by T^4) as a function of temperature T , calculated by Lattice QCD. This figure is taken from Ref. [7].	4
1.3	Illustration of the QCD phase diagram in the temperature-baryonic chemical potential plane. Credit for the diagram goes to Ref [8].	5
1.4	Sketch of a relativistic heavy-ion collisions. Taken from the website of IEBE-VISHNU of Ohio State University [9].	7
1.5	Sketch of jet quenching in a relativistic heavy-ion collisions.	9
2.1	An illustration of nuclear shadowing effect. This figure is taken from Ref.[72]	19
2.2	The Peterson fragmentation function [106] (for $c \rightarrow D^0$ -meson) and Dadfar fragmentation function [107] (for $c \rightarrow J/\psi$ -meson).	32
2.3	The NLO calculation of p_T -differential cross section of D -meson in pp collisions at $\sqrt{s} = 2.76$ TeV [105]. The experimental data are taken from ALICE collaboration [108].	33
2.4	The LO calculations of p_T -differential cross section of D^0 -meson (left plot) and B^+ -meson (right plot) in pp collisions at $\sqrt{s} = 5.02$ TeV [68], compared with the experimental measurements of CMS collaboration [109, 110].	34

2.5	The calculation of p_T -differential cross section of prompt J/ψ -meson in pp collisions at $\sqrt{s} = 2.76$ TeV. The experimental data are taken from ALICE collaboration [111].	34
3.1	The energy loss of charm (left plot) and bottom (right plot) quark inside QGP medium as a function of momentum, obtained using collisional (PP)[88], radiative (AJMS)[104] energy loss and fluctuations[80].	42
3.2	Fractional energy loss of charm (left plot) and bottom (right plot) quark inside QGP due to fluctuations, collisions (PP) and radiations (AJMS) as a function of momentum. The path length considered here is $L = 5$ fm.	43
3.3	Fractional energy gain of a charm quark with momentum, $p = 5, 10$ and 20 GeV inside the QGP medium due to fluctuations, as a function of T . The path length considered here is $L = 5$ fm.	44
3.4	The drag coefficient of a charm quark inside the QGP medium as a function of time (left plot) and momentum (right plot), obtained for different energy loss schemes (BT [86] and DGLV [98, 99]) along with the effect of fluctuations [80].	47
3.5	The diffusion coefficient of a charm quark inside the QGP medium as a function of time (left plot) and momentum (right plot), obtained for different energy loss schemes(BT [86] and DGLV [98, 99]) and along with the effect of fluctuations [80].	48
3.6	The nuclear modification factor R_{AA} of D^0 -meson with collisional (PP) and radiative (AJMS) energy loss along with the effect of fluctuations as a function of transverse momentum p_T for $(0 - 10)\%$ centrality in Pb-Pb collisions at $\sqrt{s_{NN}} = 2.76$ TeV. The experimental data are taken from the measurements of ALICE [129] and CMS experiments [130].	50

3.7	The nuclear modification factor R_{AA} of D^0 -meson with collisional(PP) and radiative(AJMS) energy loss along with the effect of fluctuations as a function of transverse momentum p_T for $(0 - 100)\%$ centrality in Pb-Pb collisions at $\sqrt{s_{NN}} = 2.76$ TeV. The experimental data are taken from the measurement of CMS experiment [130].	50
3.8	The nuclear modification factor R_{AA} of D^0 -meson with collisional (PP) and radiative (AJMS) energy loss along with the effect of field fluctuations as a function of transverse momentum p_T for $(0 - 100)\%$ centrality in Pb-Pb collisions at $\sqrt{s_{NN}} = 5.02$ TeV. The experimental data are taken from the measurements of CMS experiment [109].	52
3.9	The nuclear modification factor R_{AA} of B^+ -meson with collisional (PP) and radiative (AJMS) energy loss along with the effect of field fluctuations as a function of transverse momentum p_T for $(0 - 100)\%$ centrality in Pb-Pb collisions at $\sqrt{s_{NN}} = 5.02$ TeV. The experimental data are taken from the measurements of CMS experiment [110].	52
3.10	Spatial diffusion coefficient as a function of normalized temperature compared to lattice QCD calculations [143], dressed perturbative QCD(DpQCD), quasi-particle models(QPM) [145], and Bayesian analysis [144].	55
3.11	The nuclear modification factor R_{AA} of J/ψ mesons with the effect of fluctuations as a function of p_T in Pb-Pb collisions for $0 - 100\%$ centrality at $\sqrt{s_{NN}} = 2.76$ TeV. The experimental measurements are taken from CMS Collaboration [137].	55
3.12	The nuclear modification factor R_{AA} of J/ψ mesons with the effect of fluctuations as a function of p_T in Pb-Pb collisions at $\sqrt{s_{NN}} = 2.76$ TeV, compared with the ALICE data [135].	56

3.13	Left Plot: The nuclear modification factor R_{AA} of J/ψ mesons with the effect of fluctuations as a function of N_{part} in Pb-Pb collisions at $\sqrt{s_{NN}} = 2.76$ TeV. The experimental measurements are taken from CMS Collaboration [137]. Right Plot: The nuclear modification factor R_{AA} of J/ψ mesons with the effect of fluctuations as a function of N_{part} in Au-Au collisions at $\sqrt{s_{NN}} = 200$ GeV. The experimental data are taken from PHENIX Collaboration [133].	57
3.14	The viscosity to entropy density ratio (η/s) as a function of T/T_c , is compared with the results obtained by LQCD calculations[148, 149, 150] and functional renormalization group calculations[151]. Here critical temperature T_c is taken 155 MeV. . .	59
5.1	. Detector-level inclusive p_T spectrum of charged jets with resolution parameter, $R = 0.4$ as obtained from the MC simulations analyzed with and without outlier rejection. Jet p_T is corrected for the mean underlying event (UE) density. Input sample of jets had UE density uncorrected jet p_T greater than 5 GeV/c.	77
5.2	Probability distribution of UE density in inclusive events. The MC distribution corresponds to PYTHIA+EPOS detector-level simulation.	80
5.3	A sketch of a b -jet.	82
5.4	Distribution of hybrid tracks as a function of pseudorapidity for real data and PYTHIA+EPOS detector-level simulations. Distributions are normalized by their integral. Left: inclusive tracks, Middle: tracks with $p_T > 3$ GeV/c, Right: $p_T > 10$ GeV/c.	83
5.5	Distribution of hybrid tracks as a function of azimuth for real data and PYTHIA+EPOS detector-level simulations. Distributions are normalized by their integral. Left: inclusive tracks, Middle: tracks with $p_T > 3$ GeV/c, Right: $p_T > 10$ GeV/c.	83

5.6	Left: Inclusive p_T spectrum of hybrid tracks from real data and PYTHIA+EPOS detector-level simulations. The distributions are normalized by their integral. Right: Reconstruction efficiency of hybrid tracks as obtained from PTYHIA+EPOS simulations.	83
5.7	Distribution of charged anti- k_T $R = 0.4$ jets as a function of pseudorapidity for real data and PYTHIA+EPOS detector-level simulations. Distributions are normalized by their integral. Left: inclusive tracks, Right: $p_T > 10$ GeV/ c	84
5.8	Distribution of charged anti- k_T $R = 0.4$ jets as a function of azimuth for real data and PYTHIA+EPOS detector-level simulations. Distributions are normalized by their integral. Left: inclusive tracks, Right: $p_T > 10$ GeV/ c	84
5.9	Inclusive p_T spectrum of charged anti- k_T $R = 0.4$ jets from real data and PYTHIA+EPOS detector-level simulations. The distributions are normalized by their integral. . . .	85
5.10	Distribution of SL_{xy} (no cut on σ_{SV}) in real data and in PYTHIA+EPOS detector-level simulations. Distributions are normalized by their integral.	85
5.11	Distribution of SL_{xy} for $\sigma_{SV} < 0.03$ cm in real data and in PYTHIA+EPOS detector-level simulations. Distributions are normalized by their integral.	86
5.12	Distribution of SV dispersion (no cut on SL_{xy}) in real data and in PYTHIA+EPOS detector-level simulations. Distributions are normalized by their integral.	87
5.13	Distribution of SV dispersion for SV passing the cut $SL_{xy} > 7$ in real data and in PYTHIA+EPOS detector-level simulations. Distributions are normalized by their integral.	87

5.14	Left: Example of raw inclusive p_T spectra of b jets for $SL_{xy} > 7$ and varying cut on σ_{SV} . Bin width is 1 GeV/ c . Right: Rebinned raw spectrum for $SL_{xy} > 7$ and $\sigma_{SV} < 0.03$ cm which is used as input to unfolding. The numbers show the number of counts in given bin.	88
5.15	b -jet tagging efficiency as a function of jet p_T for $SL_{xy} > 5$ and 7 and different choices of the σ_{SV} cut.	89
5.16	Mistagging efficiency of c -jet and light-flavor jet versus b -jet tagging efficiency for a fixed $\sigma_{SV} < 0.04$ cm cut and several choices of SL_{xy} ($> 3, 4, 5, 6, 7, 8, 9, 10$).	90
5.17	b -jet tagging purity as a function of jet p_T for $SL_{xy} > 5, 7$ and 9 and different choices of the σ_{SV} cut. The purity is assessed with the default POWHEG settings.	92
5.18	Ratio of b -jet tagging purity to b -jet tagging efficiency as a function of jet p_T for $SL_{xy} > 5, 7$ and 9 and different choices of the σ_{SV} cut. The purity is assessed with the default POWHEG settings.	92
5.19	Fit of the simulated detector-level SV invariant mass distributions with smoothened MC templates. The cuts on SV are $\sigma_{SV} < 0.04$ cm and $SL_{xy} > 7$. The bottom part of each panel shows the ratio of data to the fit.	95
5.20	MC closure test result: purity of the selected detector-level b -jet candidate sample as obtained from the template fit method and the corresponding true detector-level b -jet purity. The cuts on SV are mentioned in legend.	96
5.21	Comparison of data-driven template-fit method and POWbc b -jet purities for different σ_{SV} cuts.	97
5.22	Comparison of data-driven template-fit method and POWbc b -jet purities for different SL_{xy} cuts.	98

5.23	Left: The distribution of χ_i^2/N_i values for each combination of tagging cuts and POWHEG settings. Right: The χ^2/N distribution of the combined tests when all tagging cuts are taken simultaneously into account for each POWHEG settings. . .	99
5.24	χ_i^2 values (left) and N_i values (right) obtained for the Default POWHEG setup. . .	100
5.25	χ_i^2 values (left) and N_i values (right) obtained for the POWHEG setup with default charm settings, beauty factorization scale 0.5 and beauty renormalization scale 2. .	101
5.26	χ_i^2 values (left) and N_i values (right) obtained for the POWHEG setup with charm and beauty factorization scales 0.5 and renormalization scales 2.	101
5.27	Result of hybrid purity tests. The χ^2/N values are shown for each POWHEG setting. Settings consistent with data-driven results are marked red. Settings failing the test are blue.	102
5.28	Purity of the b-jet candidates selected with a cut on $SL_{xy} > 7$ and $\sigma_{SV} < 0.03$ cm. Comparison of the data driven template fit method (red data points) and POWHEG based method (blue data points).	102
5.29	Left: δp_T distribution as obtained by random cone method from events with a SV. Middle: The corresponding δp_T matrix having a bin size of $1 \text{ GeV}/c \times 1 \text{ GeV}/c$. Right: Comparison of δp_T distribution from inclusive events and from events with a SV.	105
5.30	Left: Distribution of particle-level b -jets which is used to normalize the response matrix. Middle: Instrumental response matrix for b -jets. Right: Instrumental response matrix of b -jets converted to probability matrix. Both matrices have a bin size of $1 \text{ GeV}/c \times 1 \text{ GeV}/c$. All data are based on PYTHIA filtered simulation. . .	106

5.31	Left: Combined response matrix for b -jets which is obtained by Eq. (5.14). The matrix has a bin size of $1 \text{ GeV}/c \times 1 \text{ GeV}/c$. Middle: The same matrix after rebinning (5.12) and (5.13). Right: The re-binned matrix converted to probability.	106
5.32	Comparison of correction factors by the PYTHIA-filtered detector matrix multiplied with deltapt matrix to EPOS+PYTHIA matrix. The effect on the unfolded spectrum is smaller than this.	107
5.33	Results of the first unfolding closure test. Upper left: comparison of the raw, unfolded, refolded and prior b -jet spectrum. Upper right: d vector components based on which we choose the regularization parameter to be 5. Bottom left: Ratio of the folded spectrum to the input raw spectrum corrected for SV tagging efficiency and purity. Bottom right: Ratio of unfolded spectrum to the true spectrum. In the bottom panels, different data sets correspond to different choices of the regularization parameter.	109
5.34	Results of the second unfolding closure test with the true b -jet prior. Meaning of the individual panels is analogous to Fig. 5.33.	110
5.35	Results of the third unfolding closure test done with the Bayesian unfolding method. Meaning of the individual panels is analogous to Fig. 5.33.	111
5.36	SVD unfolding the corrected b -jet spectrum with different regularization parameters (i). Meaning of the individual panels is analogous to Fig. 5.33.	112
5.37	Bayesian unfolding the corrected b -jet spectrum with different regularization parameters (i).	113
5.38	Effect of tagging cut variations on the analysis. We plot the ratio of the spectrum derived by the chosen tagging cut over the principal analysis. The left panel shows SL_{xy} and the right panel shows σ_{SV}	115

5.39	Effect of some unfolding variations on the analysis. We plot the ratio of the spectrum derived by the chosen SVD unfolding settings cut over the principal analysis. The left panel shows prior variations and the right panel shows the choice of k_{SVD} . . .	117
5.40	Left: The relative resolution of p_T^{-1} for hybrid tracks as a function of track p_T in p-Pb collisions at $\sqrt{s_{NN}} = 5.02$ TeV. Right: The corresponding mean relative resolution of p_T^{-1} for hybrid tracks as a function of track p_T . The red line represents parameterization of the trend by a smooth function.	118
5.41	$1/p_T$ spectra of negatively charged tracks for 36 azimuthal slices. The x -axis corresponds to track inverse transverse momentum ($1/p_T$) and the y -axis gives the number of entries. The solid red line represents a fit of the data with the power-law (5.16).	119
5.42	Extracted values of the B parameter for positively and negatively charged tracks in each of the 36 azimuthal slices shown in Fig. 5.41.	119
5.43	Top panels: Instrumental response matrices obtained with the toy MC simulation based on PYTHIA8 Tune5. The particle-level $1/p_T$ is smeared either with σ_{1/p_T} from Fig. 5.40 (top left) or with σ_{1/p_T} increased by the RMS of B (top right). The bottom panels show the corresponding matrices after folding with the δp_T matrix.	121
5.44	Ratio of the fully corrected b -jet spectra obtained using a response matrix that accounts for momentum smearing described by σ_{1/p_T} from Fig 5.40 and the response matrix for which the value of σ_{1/p_T} is increased by the RMS of B	121
5.45	DCA distributions of charged hybrid tracks in p-Pb data. The real data are fitted with a sum two simulated templates corresponding to the DCA distribution of physical primaries and the DCA distribution of secondary tracks.	122

5.46	Left: Distribution of fractions of jet p_T carried by secondary tracks versus jet p_T . Right: Projection of the distribution in one jet p_T bin on the y -axis.	122
5.47	Left: Fit of the fully unfolded b -jet spectrum by (5.18). Right: Ratio of parametrizations (5.18) for $\xi = 1$ and $\xi = 1.013$ which gives the estimated systematic uncertainty on b -jet spectrum due to different secondary track admixture in real data and in the MC.	124
5.48	The b -jet cross section from Run2 LHC16q and LHC16t $\sqrt{s_{NN}} = 5.02$ TeV p-Pb collisions, together with the systematic contributions.	125
5.49	Upper panel: The measured b -jet cross-section as a function of charged jet p_T . Lower panel: The ratio of the measured b -jet spectra with the NLO pQCD calculations (POWHEG).	126
A.1	Production cross section of c quark pair for mass variation of c quark, in mid rapidity as a function of transverse momentum, p_T (left) and their ratio as a function of p_T (right).	140
A.2	Same as Fig.A.1, but for b quark pair.	140
A.3	c quark pair production cross section in mid rapidity as a function of p_T . The cross section is obtained for factorization scale variation with renormalization scale 0.5 (left) and 2 (right).	141
A.4	Ratio of c quark pair production cross section. The ratio is between cross section from factorization scale 0.5 and 2 with the default value for renormalization scale value 0.5 (left) and 2 (right).	141
A.5	Same as Fig.A.3, but for b quark.	142
A.6	Same as Fig.A.4, but for b quark. The left panel is for renormalization scale 0.5 and right panel is for renormalization scale 2.	142

A.7	c quark pair production cross section in mid rapidity as a function of p_T . The cross section is obtained for renormalization scale variation with factorization scale 0.5 (upper left) and 2 (upper right) and their ratio for factorization scale 0.5 (lower left) and 2 (lower right).	143
A.8	Same as Fig.A.7, but for b quark.	144
A.9	$p_{T,jet}$ -integrated 2D distributions of SL_{xy} and σ_{SV} , as well as efficiencies and suppression factors of SL_{xy} && σ_{SV} cuts.	146
A.10	Cut behavior on SL_{xy} distributions for b -jets (red), c -jets (blue) and light flavor jets (black), with different $p_{T,jet}$ selections (left to right, $p_{T,jet}$ -inclusive, $5 < p_{T,jet} < 20$ GeV/ c , $20 < p_{T,jet} < 40$ GeV/ c , $40 < p_{T,jet} < 60$ and $60 < p_{T,jet} < 100$ GeV/ c . Top row is distributions, middle row is efficiency and bottom row is the suppression factor of a $SL_{xy} > x$ cut placed at a given x position.	147
A.11	Cut behavior on σ_{SV} distributions for b -jets (red), c -jets (blue) and light flavor jets (black), after an applied $SL_{xy} > 3$ cut, with different $p_{T,jet}$ selections (left to right, $p_{T,jet}$ -inclusive, $5 < p_{T,jet} < 20$ GeV/ c , $20 < p_{T,jet} < 40$ GeV/ c , $40 < p_{T,jet} < 60$ and $60 < p_{T,jet} < 100$ GeV/ c . Top row is distributions, middle row is efficiency and bottom row is the suppression factor of a σ_{SV} cut placed at a given x position. . .	148
A.12	Cut behavior on σ_{SV} distributions for b -jets (red), c -jets (blue) and light flavor jets (black), after an applied $SL_{xy} > 5$ cut, with different $p_{T,jet}$ selections (left to right, $p_{T,jet}$ -inclusive, $5 < p_{T,jet} < 20$ GeV/ c , $20 < p_{T,jet} < 40$ GeV/ c , $40 < p_{T,jet} < 60$ and $60 < p_{T,jet} < 100$ GeV/ c . Top row is distributions, middle row is efficiency and bottom row is the suppression factor of a σ_{SV} cut placed at a given x position. . .	149

A.13 Cut behavior on σ_{SV} distributions for b -jets (red), c -jets (blue) and light flavor jets (black), after an applied $SL_{xy} > 7$ cut, with different $p_{T,jet}$ selections (left to right, $p_{T,jet}$ -inclusive, $5 < p_{T,jet} < 20$ GeV/ c , $20 < p_{T,jet} < 40$ GeV/ c , $40 < p_{T,jet} < 60$ and $60 < p_{T,jet} < 100$ GeV/ c . Top row is distributions, middle row is efficiency and bottom row is the suppression factor of a σ_{SV} cut placed at a given x position. . .	150
A.14 Fit of the detector-level SV invariant mass distributions with smoothened MC templates. The cuts on SV were $\sigma_{SV} < 0.03$ cm and $L_{xy}/\sigma_{L_{xy}} > 5$. The bottom part of each panel shows the ratio of data to the fit.	151
A.15 Fit of the detector-level SV invariant mass distributions with smoothened MC templates. The cuts on SV were $\sigma_{vertex} < 0.04$ cm and $L_{xy}/\sigma_{L_{xy}} > 5$. The bottom part of each panel shows the ratio of data to the fit.	152
A.16 Fit of the detector-level SV invariant mass distributions with smoothened MC templates. The cuts on SV were $\sigma_{SV} < 0.03$ cm and $L_{xy}/\sigma_{L_{xy}} > 6$. The bottom part of each panel shows the ratio of data to the fit.	153
A.17 Fit of the detector-level SV invariant mass distributions with smoothened MC templates. The cuts on SV were $\sigma_{SV} < 0.04$ cm and $L_{xy}/\sigma_{L_{xy}} > 6$. The bottom part of each panel shows the ratio of data to the fit.	154
A.18 Fit of the detector-level SV invariant mass distributions with smoothened MC templates. The cuts on SV were $\sigma_{SV} < 0.02$ cm and $L_{xy}/\sigma_{L_{xy}} > 7$. The bottom part of each panel shows the ratio of data to the fit.	155
A.19 Fit of the detector-level SV invariant mass distributions with smoothened MC templates. The cuts on SV were $\sigma_{SV} < 0.04$ cm and $L_{xy}/\sigma_{L_{xy}} > 7$. The bottom part of each panel shows the ratio of data to the fit.	156

List of Tables

2.1	Parameters for medium evolution.	21
5.1	List of runs from the LHC16q and LHC16t periods [167] used in this analysis. Run numbers are the numbers assigned to each run of the LHC machine during the process of data collection.	75
5.2	The analyzed MC data sets. The number of events generated in each hard bin is denoted as $N_{\text{events,hb}}^{\text{raw}}$. The corresponding number of events after physics selection is labeled $N_{\text{events,hb}}^{\text{phys.sel.}}$	76
5.3	The total number of input events and the total number of rejected events in hard bins for $p_{T,\text{chjet}} > 4\hat{p}_T$	76
5.4	The total number of input events and the total number of rejected events in hard bins for $p_{T,\text{chjet}} > 3\hat{p}_T$	77
5.5	List of POWHEG settings with defaults highlighted.	115
5.6	Estimated systematic uncertainties of b -jet cross-section, in percentage (%).	125

Chapter 1

Introduction

Ever since the beginning of human being, the mankind have been wondering and looking for an understanding of the composition of matter. Gradually the development of modern science happened. In 1911, Ernest Rutherford did his famous experiment of the scattering of α -particle in thin gold foil and discovered the atomic nucleus. After that, the discovery of the neutron completed the main structure of atomic nucleus. Further more, people did the Deep Inelastic Scattering (DIS) of electrons from proton target. This DIS experiment concluded the composite nature of proton which led to the existence of quarks.

In Particle Physics, the Standard Model (SM) talks about the elementary particles and their interactions in the universe. In SM, there are three generations of leptons (electron, muon, tau) and three generations of quarks (spin-half fermions); four interaction bosons (with spin 1); and the most recently confirmed Higgs boson (with spin 0) which is responsible for the generation of masses of all these elementary particles [1, 2, 3]. The interactions between these elementary elements are classified into three fundamental forces: the electromagnetic force, the weak force and the strong force. All the visible matter around us, even our bodies, are made of quarks, gluons and electrons along with the help of the fundamental forces which hold them together in an atom.

The interactions between quarks/gluons are governed by strong force which is described by the Quantum Chromodynamics (QCD).

In this dissertation, we would like to study the properties of a particular type of QCD system (extremely hot and dense) that may exist in the $\sim 10^{-11}s$ old baby universe after the Big Bang. In order to create and study such hot baby universe in the laboratory, we collide beams of ultra-relativistic heavy nuclei and observe the produced particles. In particular, we will use heavy quarks (charm and bottom) as probe of this QCD system and acquire knowledge of the strong interaction and the evolution history of our baby universe. We will discuss later in more details.

1.1 Quantum Chromodynamics (QCD)

The Quantum Chromodynamics (QCD) is a non-abelian gauge theory (where gluon plays the role of gauge boson) that governs the interactions between color charges (quarks and gluons) via the strong interaction. Unlike QED, the QCD coupling constant is function of momentum transfer, Q , and hence it is called the running coupling constant, α_s . The running coupling constant, α_s is obtained at leading order as,

$$\alpha_s(Q^2) = \frac{12\pi}{(11N_c - 2N_f) \log(Q^2/\Lambda_{QCD}^2)} \quad (1.1)$$

where, N_f is the number of quark flavors, N_c is the number of color charges and $\Lambda_{QCD} \sim 1 \text{ fm}^{-1}$, is the QCD scale parameter.

Fig.1.1 shows the running coupling constant $\alpha_s(Q^2)$ as a function of momentum transfer Q where α_s is compared with several independent experimental estimates covering a wide range of Q . The non-abelianity of QCD ensures the two novel properties of QCD: Confinement and Asymptotic freedom.

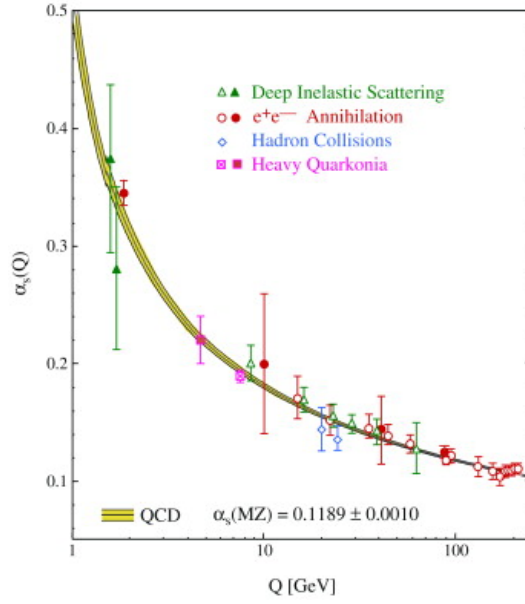


Figure 1.1: The running coupling constant $\alpha_s(Q^2)$ as a function of momentum transfer Q , determined from varieties of processes. This figure is taken from Ref.[4].

1.1.1 Two Novel Properties of QCD

Confinement

As the momentum transfer (Q^2) approaches towards Λ_{QCD}^2 value from above, the value of the QCD coupling constant α_s increases (see Eq.1.1). In other words, at low momentum transfer in QCD interactions, i.e., at large distance, the QCD coupling strength becomes large. This ensures the non-existence of a free quark rather the existence of color singlet hadronic bound state. This property is called the quark confinement. This property gives the theoretical grounds to explain hadron production in all kinds of high energy particle collisions experiments. Specially, it is the basis of jet production in high energy collisions and it will be discussed later.

Asymptotic Freedom

As per the expression of the QCD coupling constant α_s , Eq.1.1, for large momentum transfer (Q^2), the value of α_s becomes very small. This means, for large momentum transfer, the interaction

between quarks becomes weak as the quarks get closer to one another. This is known as the asymptotic freedom of QCD [5, 6].

1.1.2 The QCD Phase Diagram

Ordinary hadronic matter is the bound state of quarks and gluons, and exists at low temperature and pressure. The quarks and gluons are confined within the hadrons. The concept of asymptotic freedom immediately suggests that at very high temperature and density the interactions between the partons inside hadrons become so weak that the partons are no longer confined within the hadrons rather move in the extended volume, i.e., the hadrons get deconfined. Such new deconfined phase of matter is called Quark-Gluon Plasma (QGP). This is a clear indication of a change of hadronic phase to the partonic phase.

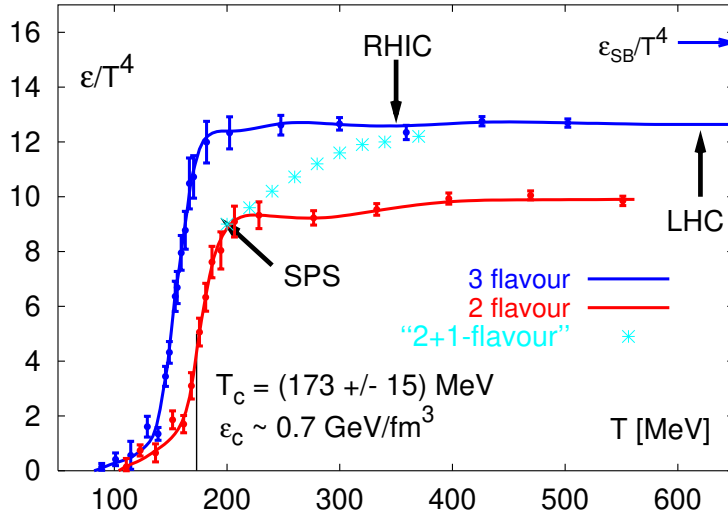


Figure 1.2: Normalized energy density(normalized by T^4) as a function of temperature T , calculated by Lattice QCD. This figure is taken from Ref. [7].

Lattice QCD calculations show that this deconfined phase of quarks and gluons can exist if the energy density of the system is increased. Fig. 1.2 displays energy density as a function of the temperature, calculated by Lattice QCD for different quark flavors. A rapid increase of the energy

density of matter is observed around a critical temperature, $T_c = 170$ MeV. This is interpreted as an increase in the number of degrees of freedom (hadrons to quarks and gluons). At high temperature limit, the energy density follows the Stefan-Boltzmann (SB) formula which is indicated by the arrow on right top of Fig. 1.2.

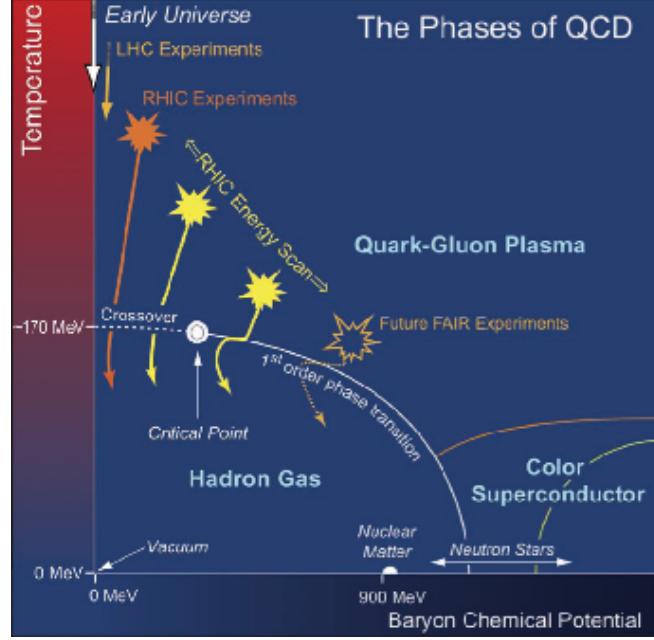


Figure 1.3: Illustration of the QCD phase diagram in the temperature-baryonic chemical potential plane. Credit for the diagram goes to Ref [8].

Fig.1.3 illustrates the QCD phase diagram labeled with energy regimes explored by different experiments. Here it is shown that at low temperature and low baryonic chemical potential, there is hadron gas in which the quarks and gluons are confined. The possible occurrence of deconfined QCD matter is observed at two extreme scenarios. The deconfined matter observed at high temperature and low baryonic chemical potential is similar to the early universe. The LHC and RHIC experiments are designed to study this type of QCD matter. At low temperature and high chemical potential, the QCD matter exists is similar to the core of the neutron star. Upcoming CBM experiment (FAIR at GSI, Germany) is dedicated for this region. At very high chemical potential and very low temperature quarks may form cooper pairs and a new phase, color

superconducting phase may exist. In this dissertation, the main focus will be on the low baryonic chemical potential and high temperature regime of the phase diagram which is explored by the LHC experiments and the high energy RHIC experiments.

1.2 Deconfined QCD Matter at Laboratory

The deconfined QCD matter is obtained under the condition of very high temperature and density as discussed above. The only currently known way to produce this deconfined state of QCD matter at laboratory is to collide beams of heavy-ions at ultra-relativistic energies. Such ultra-relativistic heavy-ion collisions produce extremely hot (temperature in excess of 10^{12} K) and dense (energy density above $1 \text{ GeV}/fm^3$) deconfined matter, the QGP. The experimental facilities in operation are the Relativistic Heavy-Ion Collider (RHIC) at the Brookhaven National Laboratory (BNL) and the Large Hadron Collider (LHC) at the European Organization for Nuclear Research (CERN). At the RHIC, Au, Cu and U nuclei are collided at center of mass energy per nucleon pair $\sqrt{s_{NN}} = 200$ GeV and, at LHC, Pb nuclei are collided at center of mass energy per nucleon pair $\sqrt{s_{NN}} = 2.76$ and 5.02 TeV to create the QGP matter.

The hot and deconfined nuclear matter produced in the relativistic heavy-ion collision experiments evolves through several stages. It has been sketched in Fig. 1.4. Two Lorentz contracted nuclei approach each other with almost the speed of light and collide. During the collisions, the overlap zone becomes highly compressed and large amount of energies are dumped in that small region. As a result of that, large number of new particles with different momenta are produced. A short time ($\sim 1 \text{ fm}/c$), called the pre-equilibrium stage is required for these particles to interact among themselves and drive the system towards local thermal equilibrium state, i.e., to form a QGP matter. The detailed mechanisms of the pre-equilibrium stage and its thermalization are still unknown. After the pre-equilibrium stage, the QGP state sets in and a rapid hydrodynamic

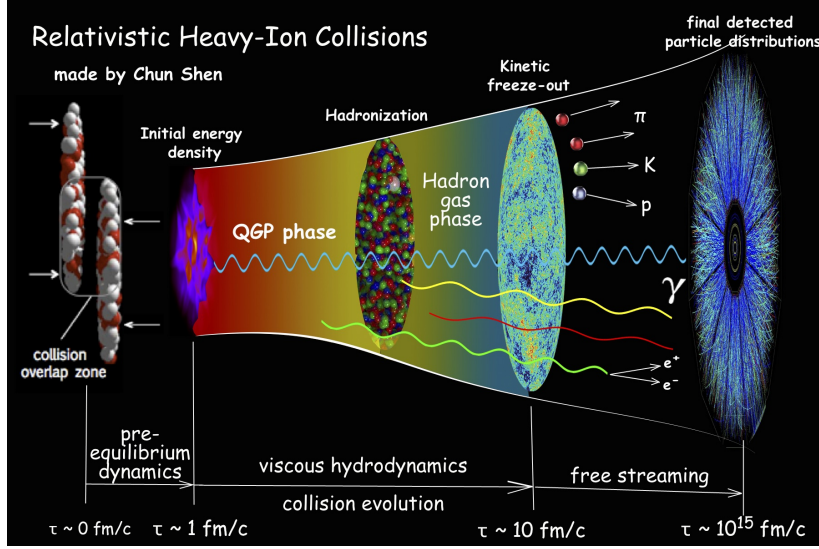


Figure 1.4: Sketch of a relativistic heavy-ion collisions. Taken from the website of IEBE-VISHNU of Ohio State University [9].

expansion begins due to the large internal pressure in the QGP. During the expansion, energy density as well as temperature of the QGP medium decreases. When the temperature drops below $T_c(\sim 160\text{MeV})$, the deconfined partons hadronize and revert back to a hadron gas phase, where the produced hadrons interact themselves via elastic and inelastic processes. Gradually the temperature decreases further and a certain value the inelastic processes get stopped. The particle species becomes fixed at this point and this is referred to as chemical freeze-out. The elastic processes get stopped as well after further expansion and cooling. This is referred to as kinetic freeze-out. After this point, free streaming of the particles is observed until they are detected in the particle detectors.

1.3 Experimental Signatures of QGP

The QGP medium produced in the relativistic heavy-ion collision experiments survives for a very short duration of time as discussed earlier, which makes impossible to study this phase of matter directly. Final-state particles are detected in the detectors. Various signatures have been observed

to confirm the existence of this transient state of matter. Few of them are discussed below.

1.3.1 Strangeness Enhancement

The mass of strange quark (s) is ~ 96 MeV and no valence strange quarks are present in the initial colliding nucleons. On the other hand, a large number of gluons are present in the QGP. Thermal production of s quarks happens via gluon fusion process ($g + g \rightarrow s + \bar{s}$). However strange mesons can be produced in the hadronic phase. The thermal production of s quarks is significantly enhanced in the QGP phase compared to the hadronic phase [10, 11]. This is one of the signatures of the QGP observed experimentally in SPS [12], RHIC [13] and LHC [14] energies.

1.3.2 J/ψ Suppression

J/ψ is a bound state of charm quark (c) and anti charm quark (\bar{c}) produced in the early stage of the nuclear collisions. The potential between c and \bar{c} pair in free space can be obtained as [15],

$$V(r) = -\frac{Q}{4\pi r} + \kappa r \quad (1.2)$$

where the first term refers to the long-range Coulomb like potential and the second term refers to the confining linear potential with κ being the string tension.

Now the $c\bar{c}$ bound state potential (Eq.1.2) in the QGP medium gets modified due to the color screening effect and vanishing of the linear term in the potential occurs. Since κ vanishes at high temperature, the only interaction remains at high temperature is the long-range Coulomb like potential with modification due to Debye screening,

$$V(r) = -\frac{Q}{4\pi r} e^{-r/\lambda_D}, \quad (1.3)$$

where λ_D is the Debye screening length, inversely proportional to the temperature. This is because the plasma density around $c\bar{c}$ pair is larger for larger temperature. Therefore the $c\bar{c}$ bound state potential becomes weak, i.e., $c\bar{c}$ pairs are screened due to such medium. This $c\bar{c}$ bound state will no more be a bound state when $\lambda_D < r_B$, with r_B is the Bohr radius. This is a signature of the presence of the QGP state. It has been first observed at the SPS [16] then later confirmed at RHIC [17, 18] and LHC [19, 20]. However the possibility of thermal recombination of $c\bar{c}$ in higher collisional energies makes the study more complex.

1.3.3 Jet Quenching

In high energy collisions, hard scatterings between the partons (mostly in the early stage) produce high momentum partons. These high momentum partons shower into collimated spray of particles, called jets. If the jets propagate through the medium formed after collision, they will suffer energy loss due to the interaction with medium partons. This energy loss causes the high momentum jets to be quenched. This was first suggested by Bjorken [21].

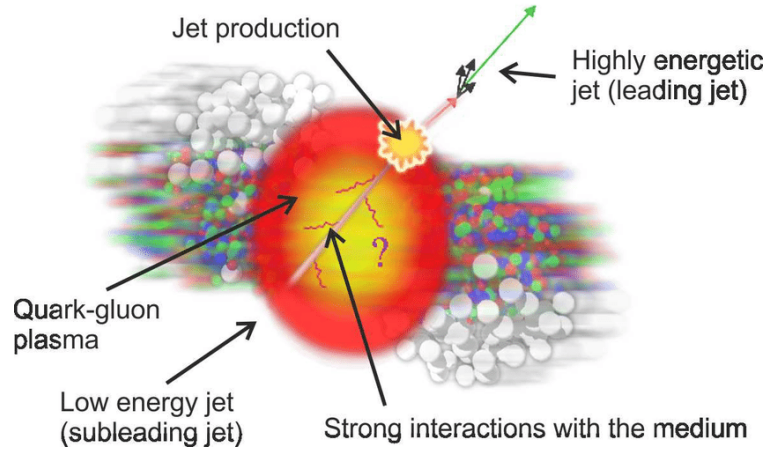


Figure 1.5: Sketch of jet quenching in a relativistic heavy-ion collisions.

The jets are always emitted back-to-back due to momentum conservation. Now if it is so happened that one jet is produced at the edge of the medium (near side jet) another one in the

deep inside the medium (away side jet) as shown in Fig.1.5, then the away side jet will travel more distance inside the medium compared to the near side jet. As a consequence of this, away side jet will be quenched more. The experimental results from RHIC [22, 23] and LHC [24, 25] confirm the phenomena of quenching through the suppression of inclusive high p_T hadron production.

1.3.4 Other Signatures

The other important signatures of the QGP medium formation are: two-particle correlations [26], collective phenomena like identified particle spectra [27], anisotropic flow [28], multiplicity dependent particle production [29] etc.

1.4 Heavy Quark Jet

Jet production in high energy collisions is one of the important milestone perturbative Quantum Chromodynamics (pQCD) processes [30]. Jet observables serve as the precision tests of QCD. The differential jet production cross section is factorized by convoluting the parton distribution functions (PDFs), the hard kernels, and the semi-inclusive jet functions (SiJFs), or the fragmentation functions to jet: [31]:

$$\begin{aligned} \frac{d\sigma_{pp \rightarrow J+X}}{dp_T d\eta} = & \frac{2p_T}{s} \sum_{a,b,c} \int_{x_a^{\min}}^1 \frac{dx_a}{x_a} f_a(x_a, \mu) \int_{x_b^{\min}}^1 \frac{dx_b}{x_b} f_b(x_b, \mu) \\ & \times \int_{z_{\min}}^1 \frac{dz_c}{z_c^2} \frac{d\hat{\sigma}_{ab \rightarrow c}(\hat{s}, p_T/z_c, \hat{\eta}, \mu)}{dvdz} J_{J/c}(z_c, w_J \tan(R'/2), m_Q, \mu) , \end{aligned} \quad (1.4)$$

where $d\hat{\sigma}_{ab \rightarrow c}(\hat{s}, p_T, \hat{\eta}, \mu)/dvdz$ denotes the hard function for the sub-process $ab \rightarrow c$, $f_{a,b}$ represents the PDF for parton a or b , and $J_{J/c}$ is the jet function which describes the probability of a parton c with transverse momentum p_T/z_c (where $z_c = p_T/p_T^c < 1$, with p_T^c is the transverse momentum of the fragmenting parton c and p_T is the transverse momentum of jet J) to fragment into a

jet J with transverse momentum p_T . The \hat{s} and $\hat{\eta}$ are partonic center-of-mass energy and parton rapidity respectively. The function $J_{J/c}$ depends on the fragmenting quark mass m_Q , jet energy w_J , the factorization scale μ and $R' = R/\cosh(\eta)$ (from the jet reconstruction algorithm). The function $J_{J/c}$ has been calculated up to next-to-leading order (NLO) for light quark jets [32, 33] as well as heavy quark jets [34].

In heavy-ion collisions, it is expected that QGP is produced, and the propagation of energetic partons produces showers of particles in this QGP medium which get quenched due to the presence of the medium. This is known as jet quenching as discussed in the earlier section. When the particle showers are initiated by the initially produced heavy quarks (charm (c) and bottom (b)) then the resulting showers are called the heavy flavor-tagged jets (c -jet and b -jet). The heavy flavor-tagged jets have some important properties which can shed light on the fundamental thermodynamic and transport properties of the QGP. The heavy quarks, being heavy, are expected to lose energy differently compared to the light quarks, significantly at the lower and intermediate transverse momentum regions. Therefore, the jet quenching effects depend on the flavor of the fragmenting parton which is most pronounced for b -jets [35, 36].

Apart from that, the heavy quarks have some interesting properties which make them excellent probes to study the QGP diagnostics:

- The heavy quarks are mainly produced in the primordial hard scatterings in the collisions and hence they encounter the full space-time evolution of the medium which suggests that they might preserve a memory of their interaction history. They do not constitute the bulk of the QGP medium rather they act as impurities in the medium. Hence their motions can be described by the theory of Brownian motion which can be treated in the ambit of Langevin dynamics under soft scattering approximations.
- In high energy collisions, the heavy quarks are considered heavy for a twofold reasons: Firstly,

from typical particle physics point of view, the mass of the heavy quarks, $M_Q \gg \Lambda_{QCD}$ (where Λ_{QCD} is the typical momentum scale of QCD) which makes possible the evaluation of cross section up to NLO; secondly, from plasma physics point of view, $M_Q \gg T$ (T being the typical temperature of the QGP medium formed at RHIC and LHC) therefore it may be expected the heavy quarks to decouple from the medium and also a negligible thermal production.

- The thermalization time scale for heavy quarks (τ_Q) is larger than that of light quarks (τ_f) by a factor of $M_Q/T \sim 5 - 20$ [37, 38, 39, 40]. The light quark thermalization time scale is $\tau_{lf} \sim 0.3 - 1 \text{ fm}/c$ and the life time of the QGP, $\tau_{QGP} \sim 5 \text{ fm}/c$. So, τ_Q may be comparable to or even larger than the QGP lifetime. This ensures that probability of thermalization of heavy quarks is very less.

The heavy flavor studies are, therefore, of great importance in the field of relativistic heavy-ion collisions research [38, 39, 40, 41, 42, 43, 44, 45, 46, 47, 48, 49, 50, 51, 52, 53, 54, 55, 56, 57, 58, 59, 60, 61, 62, 63]. The experimental efforts have also been made to measure the heavy-flavor tagged jets by CMS [64, 65] and ATLAS [66] collaborations of LHC.

1.5 Goal of this Thesis

The importance of the study of heavy flavors and heavy flavor-tagged jets in heavy-ion collision has been discussed in the earlier section. Keeping these in mind, in this dissertation, we will stress upon the fully reconstructed inclusive bottom(b)-jet production in p-Pb collisions at $\sqrt{s_{NN}} = 5.02$ TeV in the ALICE experiment at the LHC. The b -jet production cross-section as a function of transverse momentum has been measured. The measured cross-section is compared with the NLO pQCD calculations. This is the primary motivation of this dissertation.

As discussed in Sec.1.3.3, the strong suppression of single particles/jets observed in the high energy heavy-ion collisions is explained in terms of parton energy loss through parton-medium interaction. This suppression of produced particles is one of the indication of medium formation in the high energy heavy-ion collision experiments. Hence, beside b -jet production cross-section measurement, this thesis presents phenomenological studies of heavy flavor particle (D -mesons, B -mesons and J/ψ) productions and suppressions as observed in the experiments at the LHC.

1.6 Outline of this Thesis

This thesis is organized as follows: In Chapter 2, heavy quark production in high energy collisions and propagation in the QGP medium has been discussed. The model for QGP medium evolution is described here. Along with that, a brief summary of heavy quark energy loss and hadronization have also been discussed.

In Chapter 3, we have discussed the chromo electro-magnetic field fluctuations present in the QGP medium. The effect of these fluctuations is important and has a great impact on the heavy quark propagation, heavy flavor suppression and shear viscosity to entropy density ratio of the QGP medium. They will also be discussed in this chapter.

The Chapter 4 is dedicated to discuss the ALICE experimental setup at the LHC. This chapter also covers the discussions about the different sub-detectors used in this experiment.

The main focus of this thesis is the measurement of b -jets produced in the ALICE experiment. In Chapter 5, we have discussed the measurement procedure in great details. We have also discussed the results of the measurements and the comparisons with the NLO pQCD calculations. Finally, the Chapter 6 is devoted to the summary of the works done in this thesis.

Chapter 2

Heavy Quark Propagation in the QGP

Heavy quarks are of special interest in order to probe the hot and deconfined QCD matter produced in the ultra-relativistic heavy-ion collisions as discussed in the earlier chapter. We will start this chapter by discussing how the heavy quark pairs are produced in the ultra-relativistic heavy-ion collisions. Then we will focus on their dynamics and energy loss in the hot and dense QGP medium.

This chapter is organized as follows: We first discuss the heavy quark production in heavy-ion collisions. Then in [Sec.2.2](#), the model for QGP medium evolution is discussed in short. In [Sec.2.3](#), we focus on the heavy quark dynamics in the QGP medium and energy losses by heavy quarks in [Sec.2.4](#). The [Sec.2.5](#) is devoted to describe how heavy quarks are hadronized into heavy flavor mesons.

2.1 Production of Heavy Quarks in Heavy-Ion Collisions

Heavy quarks are mostly produced in the primordial hard scatterings in the elementary or relativistic heavy-ion collisions. They are mainly produced by gluon-gluon fusion ($gg \rightarrow Q\bar{Q}$) and quark anti-quark annihilations ($q\bar{q} \rightarrow Q\bar{Q}$) [67]. The production cross section of these processes can be calculated upto next-to-leading order (NLO) by employing the perturbative QCD (pQCD) techniques. Nevertheless, there may exist other instruments of heavy quark production, i.e., productions due to interactions between the very high p_T partons themselves or with the thermalized partons. This is beyond the discussion of this thesis.

2.1.1 Leading Order(LO) pQCD Calculation

The leading order (LO) processes for heavy quark production are, $gg \rightarrow Q\bar{Q}$ and $q\bar{q} \rightarrow Q\bar{Q}$. These LO processes for pp collisions can be written as,

$$p(P1) + p(P2) \rightarrow Q(p1) + \bar{Q}(p2) + X \quad (2.1)$$

The cross section for the process in Eq. 2.1 reads as [68],

$$\frac{d^2\sigma}{dp_T^2 dy} = \frac{1}{S} \sum_{i,j} \int \frac{dx_1}{x_1} \left(-\frac{1}{t_1} \right) f_i^p(x_1, Q^2) f_j^p(x_2, Q^2) \sigma_{ij}(s, t_1, u_1) \quad (2.2)$$

where i and j are the interacting partons; $f_i^p(x_1, Q^2)$, $f_j^p(x_2, Q^2)$ are the parton distribution functions (PDFs) in nucleons, x_1 and x_2 are the momentum fractions of the nucleons carried by the interacting partons and Q^2 being the scale of momentum transfer. Here, $s = x_1 x_2 S$, $t_1 = x_1 T_1$ and $u_1 = x_2 U_1$ are the partonic variables where $S = (P_1 + P_2)^2$, $T_1 = (P_1 - p_1)^2 - M_Q^2$ and $U_1 = (P_1 - p_2)^2 - M_Q^2$, with M_Q being the mass of heavy quark. Here σ_{ij} is the Born cross sections, have been calculated up to LO as [69, 70]:

$$\sigma_{ij} = \frac{1}{64\pi} K_{ij} \times \sum |M_{ij}|^2 . \quad (2.3)$$

Here, K_{ij} is the color averaging factor. It is $1/(N^2 - 1)^2$ for the gluon-gluon fusion process and is $1/N^2$ for the quark-antiquark annihilation process. For the gluon-gluon fusion, the square of the amplitude averaged over the initial gluon polarization and color is given by [69],

$$\begin{aligned} \sum |M_{gg}|^2 &= 2 g^4 \left(C_O B_O + C_K B_K + C_{QED} B_{QED} \right) , \\ C_O &= N(N^2 - 1) , \quad C_K = (N^2 - 1)N^{-1} \quad \text{and} \quad C_{QED} = 0 , \\ B_{QED} &= \frac{t_1}{u_1} + \frac{u_1}{t_1} + \frac{4m^2 s}{t_1 u_1} \left(1 - \frac{m^2 s}{t_1 u_1} \right) , \\ B_O &= \left(1 - 2 \frac{t_1 u_1}{s^2} \right) B_{QED} \quad \text{and} \quad B_K = -B_{QED} . \end{aligned} \quad (2.4)$$

The square of the amplitude averaged over the initial quark/antiquark spins and color for the quark-antiquark annihilation process is given as [70],

$$\sum |M_{q\bar{q}}|^2 = 4 g^4 N C_F \left(\frac{t_1^2 + u_1^2}{s^2} + \frac{2m^2}{s} \right) . \quad (2.5)$$

Here, $g(= \sqrt{4\pi\alpha})$ is the dimensionless coupling constant. $C_F(= (N^2 - 1)/(2N))$ is the color factor corresponding to the fundamental representation of the quarks.

We have used next-to-leading order (NLO) CT10 parton density functions [71] for the calculation of heavy quark production cross section in pp collisions.

2.1.2 Nuclear Shadowing Effect in p-A and A-A Collisions

The parton distribution function $f(x, Q^2)$ is the probability of finding a parton (valence/sea quark or gluon) in a nucleon with a fractional momentum x ; where x is the ratio between the momentum of the parton and that of the nucleon and Q^2 being the scale of momentum transfer. The heavy quark production cross section in pp collisions is obtained by convoluting the cross sections at parton level with these PDFs, as can be seen in Eq. 2.2.

These nucleon PDFs get modified when the nucleons reside as bound within a nucleus. Such modifications of the nucleon PDFs are called “nuclear shadowing effect” or “cold nuclear matter effect”.

The bound proton NLO PDFs $f_i^A(x, Q^2)$ for each parton flavor i is defined as [72],

$$f_i^A(x, Q^2) \equiv R_i^A(x, Q^2) f_i^{\text{CTEQ6.1M}}(x, Q^2), \quad (2.6)$$

where $R_i^A(x, Q^2)$ signifies the nuclear modification to the free proton PDF $f_i^{\text{CTEQ6.1M}}$. This $R_i^A(x, Q^2)$ function may be parametrized as follows,

$$R_i^A(x) = \begin{cases} a_0 + (a_1 + a_2 x)[\exp(-x) - \exp(-x_a)] & x \leq x_a \\ b_0 + b_1 x + b_2 x^2 + b_3 x^3 & x_a \leq x \leq x_e \\ c_0 + (c_1 - c_2 x)(1 - x)^{-\beta} & x_e \leq x \leq 1, \end{cases} \quad (2.7)$$

where $a_i, b_i, c_i, \beta, x_a$ and x_e are parameters depend on nuclei species(A). $R_i^A(x, Q^2)$ is continuous and it has vanishing first derivatives at matching points x_a and x_e . This property of $R_i^A(x, Q^2)$ ensures the elimination of 6 parameters out of original 13 parameters. The rest 7 parameters will be expressed in terms of the following 6 parameters together with self-evident elucidations:

- y_0 Height to which shadowing levels as $x \rightarrow 0$
 x_a, y_a Position and height of the antishadowing maximum
 x_e, y_e Position and height of the EMC minimum
 β Slope factor in the Fermi-motion part,

Note that the parameter c_0 is fixed to $c_0 = 2y_e$.

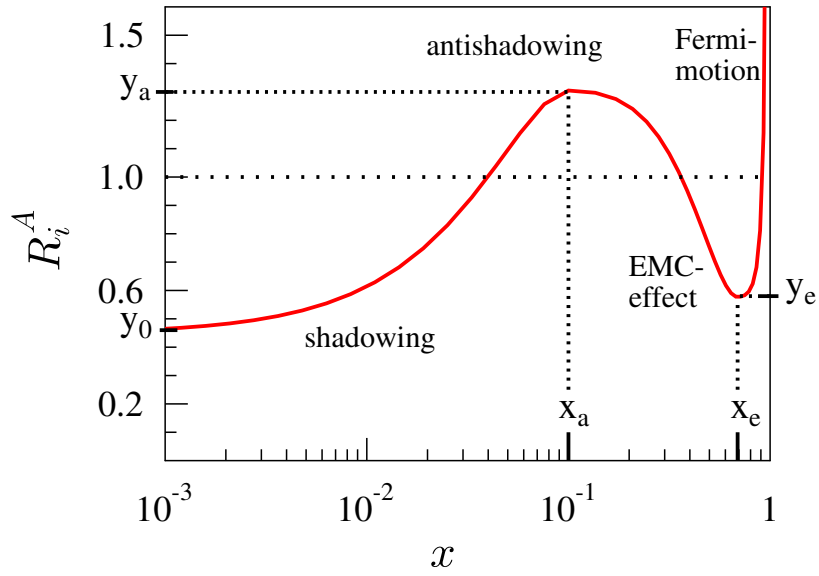


Figure 2.1: An illustration of nuclear shadowing effect. This figure is taken from Ref.[72]

Fig. 2.1 illustrates the nuclear shadowing effect [72]. In small x region, the probability for a parton in one nucleon to see the partons in another nucleon in a nucleus might be reduced after its interaction with the previous one, i.e., probing the structure of a nucleon can be shadowed by its neighbors in the nucleus. That is why the low x region of Fig. 2.1 is called shadowing region. Therefore, the probe particle sees less partons in the small x region, due to energy and momentum conservation of the target nucleon, there must exist an enhancement of the parton distribution in the larger x region. This is termed as “anti-shadowing effect”. A scale violation of the nuclear structure function is observed in $0.2 < x < 0.7$ which is called “EMC effect”. After the region of

EMC effect, a rise of $R_i^A(x, Q^2)$ is expected due to the nucleon-nucleon interaction in a nucleus. This can be viewed as a fermi gas.

In our work, for heavy-ion collisions, the shadowing effect is taken into account by using the spatially dependent EPS09 [72] nPDF sets. The differential cross section of heavy quark production, including the nuclear shadowing effect corresponding to a given centrality class between impact parameters b_1 and b_2 , is calculated.

2.2 Model for QGP Evolution and Initial Condition

2.2.1 A Simplistic 1D Expansion

As the heavy quark loses energy during its passage through the QGP medium, one needs to estimate the path length it is traversing inside the medium. We consider a heavy quark, which is being produced at a point (r, θ) in heavy ion collisions and propagates at an angle θ with respect to \hat{r} in the transverse plane. So, the path length L covered by the heavy quark inside the medium is given by [73]:

$$L(r, \theta) = \sqrt{R^2 - r^2 \sin^2 \theta} - r \cos \theta. \quad (2.8)$$

where R is the radius of the colliding nuclei. The average distance travelled by the heavy quark inside the plasma is

$$\langle L \rangle = \frac{\int_0^R r dr \int_0^{2\pi} L(r, \theta) T_{AA}(r, b) d\theta}{\int_0^R r dr \int_0^{2\pi} T_{AA}(r, b) d\theta}, \quad (2.9)$$

where the nuclear overlap function, $T_{AA}(r, b)$, at an impact parameter b , obtained from Glauber Model calculation as, $T_{AA}(r, b) = \rho(|\vec{r}|) \rho(|\vec{r} - \vec{b}|)$ (with $\rho(|\vec{r}|)$ is the density of nucleus assumed to be a sharp sphere with radius $R = 1.1A^{1/3}$ fm). The effective path length of heavy quark having

transverse mass m_T and transverse momentum p_T in the QGP of life time τ_f is obtained as,

$$L_{\text{eff}} = \min[\langle L \rangle, \frac{p_T}{m_T} \times \tau_f]. \quad (2.10)$$

The evolution of the system for each centrality bin is assumed to be governed by an isentropic cylindrical expansion as described in Ref. [74]. As the medium expands, the temperature of the medium (T) decreases with proper time (τ) as, $T^3\tau = \text{constant}$. This is simplistic model for the QGP medium evolution. The entropy conservation condition $s(T)V(\tau) = s(T_0)V(\tau_0)$ is used to obtain the temperature as a function of proper time. The equation of state obtained by Lattice QCD and hadronic resonance gas formulation has been used.

The initial volume corresponding to a given centrality is obtained by $V(\tau_0) = \pi[R_{tr}(N_{part})]^2\tau_0$. The transverse size $R_{tr}(N_{part})$ for a given centrality with number of participant (N_{part}) is obtained as $R_{tr}(N_{part}) = R\sqrt{N_{part}/2A}$, where A is the mass number of the colliding nucleus [74].

The energy loss as a function of proper time is calculated which is then averaged over the temperature evolution for each centrality bin. The results will be shown in the next chapter (Chapter.3). The initial and freeze-out times are taken as $\tau_0 = 0.3$ fm and $\tau_f = 6$ fm, respectively same as used in Ref. [68]. Various parameters used in our calculations for different centrality classes such as impact parameter $\langle b \rangle$, N_{part} , $\langle L \rangle$ and initial temperature T_0 are given in Table 2.1.

$\sqrt{s_{NN}}$ (TeV)	2.76	2.76	5.02
Centrality class (%)	0-10	0-100	0-100
$\langle b \rangle$ (fm)	3.44	9.68	9.65
N_{part}	356	113	114
$\langle L \rangle$ (fm)	5.73	4.16	4.18
T_0 GeV	0.467	0.436	0.469

Table 2.1: Parameters for medium evolution.

2.2.2 Hydrodynamic Evolution

In heavy-ion collisions, the produced hot and dense strongly interacting QCD medium is in the pre-equilibrium phase before it reaches local thermalization. Generally, the QCD medium undergoes rapid thermalization at time around $\tau_0 = 0.6 \text{ fm}$ and the hydrodynamic evolution begins.

In this work, the hydrodynamic evolution is understood by $(3 + 1)$ -dimensional relativistic viscous hydrodynamics, vHLLE [75]. We assume initial time $\tau_0 = 0.6 \text{ fm}$, critical temperature $T_c = 150 \text{ MeV}$, shear viscosity $\eta/s = 0.08$ and bulk viscosity $\zeta/s = 0.04$ in the hadronic phase for Au-Au and Pb-Pb collisions. We use optical Glauber initial state for this hydrodynamic evolution. It provides the space-time history of the flow velocity and temperature of the evolving medium. This information of space-time history is used in performing the heavy flavor Langevin simulation (will be discussed in Sec.2.3.2).

2.3 Heavy Quark Dynamics

The bulk medium produced in relativistic heavy-ion collisions consists of mainly light quarks and gluons. The heavy flavor quarks may play a crucial role in understanding the properties of such medium because they do not constitute the bulk part of the system. The perturbative QCD (pQCD) calculations [76, 77] imply that the heavy quark thermalization time is larger than the light parton thermalization time scale, which suggests that the heavy quarks are not in equilibrium with the QGP medium, and hence the heavy quarks qualify to execute Brownian motion in the heat bath of light quarks and gluons. This is analogous to the evolution of pollen grains on the background of water molecules, where water molecules are in equilibrium and the pollen grains execute Brownian motion in the water.

2.3.1 Fokker-Planck Equation

We consider a heavy quark of momentum p and energy E , executing the Brownian motion in a thermal bath of light quarks and gluons. The Boltzmann transport equation is employed to describe such motions which reads as,

$$\left(\frac{\partial}{\partial t} + \frac{p}{E} \frac{\partial}{\partial x} + F \frac{\partial}{\partial p} \right) f(x, p, t) = \left(\frac{\partial f}{\partial t} \right)_{\text{coll}} \quad (2.11)$$

where $f(x, p, t)$ is the phase space distribution function (here it is for heavy quarks). Under the assumptions that the plasma is uniform and there is no external force present, the collision term on the right side of Eq.2.11 is approximated as [78, 79],

$$\frac{\partial f}{\partial t} = \left(\frac{\partial f}{\partial t} \right)_{\text{coll}} = \frac{\partial}{\partial p_i} \left(A_i(p) f + \frac{\partial}{\partial p_i} [B_{ij}(p) f] \right) \quad (2.12)$$

with

$$A_i = \int d^3p \omega(p, k) k_i \quad (2.13)$$

$$B_{ij} = \int d^3p \omega(p, k) k_i k_j \quad (2.14)$$

and the function $\omega(p, k)$ is given by,

$$\omega(p, k) = g_j \int \frac{d^3q}{(2\pi)^3} f'(q) v \sigma_{p, q \rightarrow p-k, p+k} \quad (2.15)$$

where f' implies phase space distribution for light quarks and gluons, v denotes relative velocity between two collision partners, σ and g are the cross section and statistical degeneracy factor respectively. It is assumed here that the coefficients in the first two terms in the expansion of

Eq.2.12 are similar in magnitude.

Under these assumptions, the Boltzmann equation reduces to the Landau kinetic equation which is a integro-differential equation:

$$\frac{\partial f}{\partial t} = \frac{\partial}{\partial p_i} \left(A_i(p)f + \frac{\partial}{\partial p_i} [B_{ij}(p)f] \right) \quad (2.16)$$

The Eq.2.16 reduces to a linear partial differential equation (referred to as Fokker-Plank (FP) equation) when the distribution functions of one of the collision partners are replaced by their equilibrium Fermi-Dirac or Bose-Einstein distributions in the expressions of A_i and B_{ij} . The quantities A_i and B_{ij} are related to the usual drag and diffusion coefficients, which we denote as A and B respectively. i.e., $A_i \rightarrow pA$. So, one can write the FP equation as [78],

$$\frac{\partial f}{\partial t} = \frac{\partial}{\partial p_i} \left(pA(p)f + \frac{\partial}{\partial p_i} [B(p)f] \right), \quad (2.17)$$

which can be used to study the evolution of heavy quarks in the QGP medium. During the propagation through the QGP, the heavy quarks lose energy via elastic collisions and bremsstrahlung gluon radiations. Along with that, heavy quarks gain energy due to the statistical field fluctuations of the QGP medium (see Ref. [80] for the details) which reduces the total energy loss of the heavy quarks. Therefore, the estimation of drag (A) and diffusion (B) coefficients should include these energy losses along with the energy gain. This will be discussed in more details in the next chapter (Chapter 3).

2.3.2 Langevin Equation

The Fokker-Planck equation is solved by stochastic Langevin equation [37, 38, 39, 81]:

$$dx_i = \frac{p_i}{E} dt \quad (2.18)$$

$$dp_i = -\gamma p_i dt + \rho_i \sqrt{2D} dt \quad (2.19)$$

where dx_i and dp_i refer to the updates of the position and momentum of the heavy quark in each time step dt with $i = x, y$, and z denotes the three components in Cartesian coordinates. We have assumed here a diagonal form for the diffusion matrix as used in the past by several authors [39, 40, 62]. ρ_i is the standard Gaussian noise variable which is distributed randomly according to,

$$w(\rho) = \frac{1}{(2\pi)^{3/2}} \exp(-\rho^2/2) \quad (2.20)$$

The random variable ρ_i satisfies the relation, $\langle \rho_i \rangle = 0$ and $\langle \rho_i \rho_j \rangle = \delta(t_i - t_j)$.

In the following, we work on the pre-point discretization scheme. We use the equilibrium condition which takes the simple form of fluctuation-dissipation theorem, $D = \gamma ET$, where γ and D are the drag and diffusion coefficient respectively, that govern the interaction between the heavy quark and the medium, $E = \sqrt{p^2 + M_Q^2}$ is the energy of the heavy quark. It is to be noted here that the estimation for γ and D in the QGP medium is not yet a settled issue. The γ is related to energy loss, $-dE/dx$ of the heavy quark propagating in the QGP medium. We have estimated the drag coefficient, γ , for heavy quark by using $\gamma = \frac{1}{p}(-\frac{dE}{dx})$ [82, 83]. The γ in Langevin dynamics generally contains the collisional processes. Since radiative processes are also important

mechanisms for energy loss, we have taken care of the radiative processes through γ and defined an effective γ as $\gamma = \gamma_{coll} + \gamma_{rad}$, where γ_{coll} (γ_{rad}) is associated with collisional (radiative) processes. We have used this effective γ in our calculation of Langevin diffusion of heavy quarks. We have checked that in long time limit, the heavy quark phase space distribution function converges to the equilibrium Boltzmann-Juttner function $e^{-E/T}$. We have estimated the diffusion coefficient in the low momentum limit ($p \rightarrow 0$) of drag coefficient, called space diffusion coefficient (D_s) and compared with different model calculations (Quasi-particle model, Dressed pQCD model, LQCQ and Bayesian approach). This will be discussed further in the Sec. 3.5 of Chapter 3.

The Langevin equations, Eq.2.18 and Eq.2.19, are valid for a static medium. In our context, for the evolving medium we perform a Lorentz boost to each heavy quark into the local rest frame of the fluid cell through which it propagates and the position and momentum are updated according to Eq.2.18 and Eq.2.19. After that, we boosted back to the laboratory rest frame to obtain the heavy quark phase space coordinates. In our simulation, we stop the Langevin evolution when temperature of the background medium drops to 150 MeV, where particle spectra are calculated in statistical emission model [84]. We will show the calculated results for heavy flavor nuclear modification factor (R_{AA}) in the next chapter (Chapter 3).

2.4 Heavy Quark Energy Loss

2.4.1 Collisional Energy Loss

One of the important mechanism in which heavy quarks may lose energy inside the QGP is through elastic collisions. The calculation of collisional energy loss per unit length dE/dx has been reported in the past by several authors [85, 86, 87, 88].

Brateen and Thoma (BT) Formalism:

The heavy quarks, while propagating through the QGP medium, collide elastically with the particles of the medium and lose energy. The collisional energy loss per unit length ($-dE/dx$) has been calculated in the past by several authors [85, 86, 87, 88]. Brateen and Thoma [86] performed the most detailed calculation of $-dE/dx$ which was based on their previous QED calculation of $-dE/dx$ for muons [89]. The expression for $-dE/dx$ in the QGP medium of temperature T for a relativistic heavy quark with mass M_Q and energy $E \ll M_Q^2/T$ reads as [86],

$$-\frac{dE}{dx} = \frac{8\pi\alpha_s^2 T^2}{3} \left(1 + \frac{n_f}{6}\right) \left(\frac{1}{v} - \frac{1-v^2}{2v^2} \ln \frac{1+v}{1-v}\right) \times \ln \left(2^{n_f/(6+n_f)} B(v) \frac{ET}{m_g M_Q}\right), \quad (2.21)$$

where $\alpha_s = 0.3$ is the strong coupling constant, $B(v)$ is a smooth function of velocity (v) of heavy quark which can be taken approximately as 0.7, $m_g = \sqrt{(1+n_f/6)gT/3}$, is thermal gluon mass and $g = \sqrt{4\pi\alpha_s}$ and n_f is the number of active quark flavors in the QGP medium. In the ultra-relativistic region i.e., $E \gg M_Q^2/T$, the expression for $-dE/dx$ becomes [86]

$$-\frac{dE}{dx} = \frac{8\pi\alpha_s^2 T^2}{3} \left(1 + \frac{n_f}{6}\right) \ln \left(2^{n_f/2(6+n_f)} 0.920 \frac{\sqrt{ET}}{m_g}\right) \quad (2.22)$$

Peigne and Peshier (PP) Formalism:

The calculation of Brateen and Thoma [86] for dE/dx is based on an assumption that the momentum exchange q in elastic collisions is very less than the energy of the heavy quark E , i.e., $q \ll E$. But this is not an appropriate assumption in the domain $E \gg M^2/T$, where M is the mass of the heavy quark and T is the temperature of the medium. The improved differential energy loss expression, valid for $E \gg M^2/T$, has been obtained by Peigne and Pashier [88] as

$$\frac{dE}{dx} = \frac{4\pi\alpha_s^2 T^2}{3} \left[\left(1 + \frac{n_f}{6}\right) \log\left(\frac{ET}{\mu_g^2}\right) + \frac{2}{9} \log\left(\frac{ET}{M^2}\right) \right] + \frac{4\pi\alpha_s^2 T^2}{3} c(n_f), \quad (2.23)$$

where, $\mu_g^2 = 4\pi\alpha_s T^2 (1 + n_f/6)$ is the square of Debye screening mass, n_f , is the number of active quark flavors and $c(n_f) \approx 0.146n_f + 0.05$ and $\alpha_s = 0.3$ is the strong coupling constant.

2.4.2 Radiative Energy Loss

Gluon radiation from a fast parton is the dominant and hence essential mechanism of energy loss inside the QGP. The energy loss due to gluon radiation was first estimated in Ref. [90]. Latter many authors [82, 91, 92, 93, 94, 95, 96, 97, 98, 99, 100, 101, 102, 103, 104, 105] also calculated the radiative energy loss with many important factors.

Reaction Operator Formalism (DGLV):

The energy loss by gluon radiation from light quark jets in powers of gluon opacity (L/λ) (where λ is the mean free path and L is the path length traversed in the medium) has been calculated by using reaction operator formalism [99]. This formalism was then extended to obtain the energy loss by gluon radiation from heavy quarks and simplified for the first order of opacity expansion [98].

The average energy loss due to gluon radiation from a heavy quark, obtained by the reaction operator formalism is written as [105],

$$\frac{\Delta E}{L} = E \frac{C_F \alpha_s}{\pi} \frac{1}{\lambda} \int_{\frac{m_g}{E+p}}^{1 - \frac{M_Q}{E+p}} dx \int_0^\infty \frac{4\mu_g^2 q^3 (X \ln Y + Z)}{\left(\frac{4Ex}{L}\right)^2 + (q^2 + \beta^2)^2} dq, \quad (2.24)$$

where

$$\beta^2 = m_{gt}^2(1-x) + M_Q^2 x^2, \lambda^{-1} = \rho_g \sigma_{Qg} + \rho_q \sigma_{Qq} \quad (2.25)$$

with $\rho_g = 16T^3 \frac{1.202}{\pi^2}$ and $\rho_q = 9n_f T^3 \frac{1.202}{\pi^2}$ are the densities of quarks and gluons in the QGP medium respectively where $\sigma_{Qq} = \frac{9\pi\alpha_s^2}{2\mu_g^2}$ and $\sigma_{Qg} = \frac{4}{9}\sigma_{Qq}$. Here $C_F = 4/3$ which determines the coupling strength between the heavy quark and gluon and $m_{gt} = \mu_g/\sqrt{2}$ is the transverse gluon mass.

The functions X , Y and Z are given by the following relations:

$$X = \frac{2\beta^2}{f_\beta^3}(\beta^2 + q^2) \quad (2.26)$$

$$Y = \frac{(\beta^2 + K)(\beta^2 Q_\mu^- + Q_\mu^+ Q_\mu^+ + Q_\mu^+ f_\beta)}{\beta^2(\beta^2(Q_\mu^- - K) - Q_\mu^- K + Q_\mu^+ Q_\mu^+ + f_\beta f_\mu)} \quad (2.27)$$

$$Z = \frac{1}{2q^2 f_\beta^2 f_\mu} [\beta^2 \mu_g^2 (2q^2 - \mu_g^2) + \beta^2 (\beta^2 - \mu_g^2) K + Q_\mu^+ (\beta^4 - 2q^2 Q_\mu^+) + f_\mu (\beta^2 (\mu_g^2 - \beta^2 - 3q^2) + 2q^2 Q_\mu^+) + 3\beta^2 q^2 Q_k^-] \quad (2.28)$$

Where, $K = k_{max}^2 = 2px(1-x)$, $Q_\mu^\pm = q^2 \pm \mu_g^2$, $Q_k^\pm = q^2 \pm k_{max}^2$, $f_\beta = f(\beta, Q_\mu^+, Q_\mu^-)$ and $f_\mu = f(\mu_g, Q_k^+, Q_k^-)$ with $f(x, y, z) = \sqrt{x^4 + 2x^2 y + z^2}$.

Abir, Jamil, Mustafa and Srivastava (AJMS) Formalism:

The radiative energy loss with various ingredients and kinematical conditions has been estimated in the literature [92, 93, 94, 95, 96, 97, 98, 100, 102, 103, 104]. In Refs.[92, 93] the soft gluon

emission from heavy quarks was estimated which was found to suppress as compared to the case of the light quarks due to the mass effect, known as dead cone effect. The radiative energy loss induced by the medium due to the dead cone effect was limited only to the forward direction. In Ref. [94], some of the constraints imposed in the work of Refs. [92, 93] (e.g., the gluon emission angle and the scaled mass of the heavy quark with its energy) were relaxed and a generalised dead cone was obtained which led to a very compact expression for the gluon emission probability off a heavy quark. Based on the generalised dead cone approach and the gluon emission probability [94], AJMS [104] computed the heavy quark radiative energy loss^[1] as

$$\frac{dE}{dx} = 24\alpha_s^3 \rho_{QGP} \frac{1}{\mu_g} (1 - \beta_1) \left(\sqrt{\frac{1}{(1 - \beta_1)} \log\left(\frac{1}{\beta_1}\right) - 1} \right) \mathcal{F}(\delta), \quad (2.29)$$

with

$$\mathcal{F}(\delta) = 2\delta - \frac{1}{2} \log \left(\frac{1 + \frac{M^2}{s} e^{2\delta}}{1 + \frac{M^2}{s} e^{-2\delta}} \right) - \left(\frac{\frac{M^2}{s} \sinh(2\delta)}{1 + 2\frac{M^2}{s} \cosh(2\delta) + \frac{M^4}{s^2}} \right), \quad (2.30)$$

where

$$\delta = \frac{1}{2} \log \left[\frac{1}{(1 - \beta_1)} \log \left(\frac{1}{\beta_1} \right) \left(1 + \sqrt{1 - \frac{(1 - \beta_1)}{\log \frac{1}{\beta_1}}} \right)^2 \right]. \quad (2.31)$$

and ρ_{QGP} is the density of the QGP medium which acts as a background containing the target partons. If ρ_q and ρ_g are the density of quarks and gluons respectively in the medium, then the

¹Later a kinematical correction was made in Ref.[105].

ρ_{QGP} is given by

$$\rho_{QGP} = \rho_q + \frac{9}{4}\rho_g, \quad (2.32)$$

$$\beta_1 = \frac{\mu_g^2}{CET}, \quad (2.33)$$

$$C = \frac{3}{2} - \frac{M^2}{4ET} + \frac{M^4}{48E^2T^2\beta_0} \log \left(\frac{M^2 + 6ET(1 + \beta_0)}{M^2 + 6ET(1 - \beta_0)} \right), \quad (2.34)$$

$$\beta_0 = \sqrt{1 - \frac{M^2}{E^2}}. \quad (2.35)$$

2.5 Heavy Quark Hadronization to Heavy Mesons

The heavy quarks, after evolving in the QGP medium (discussed in Sec.2.3), exit the medium when the local temperature of the medium falls below the critical temperature T_c through the process of hadronization into their hadronic bound states. They may hadronize by the process of fragmentation or coalesce with the light quarks/anti-quarks. The later process is called "coalescence".

2.5.1 Fragmentation

Overwhelming high momentum heavy quarks tend to fragment into lower momentum partons among which the heavy flavor bound state can be formed. This process is called "fragmentation" and can be understood by the fragmentation function. The fragmentation function $D(z)$ gives the probability for a parton with momentum p to form a hadron with momentum zp , where $0 < z < 1$.

In our work, we use the Peterson fragmentation function [106] for fragmentation of c quarks into

D -mesons and b quarks into B -mesons. For c quarks to J/ψ fragmentation, we use LO calculation of the fragmentation function as calculated by Dadfar et. al. [107]. The form of the Peterson fragmentation function reads as [106],

$$D(z) = \frac{N}{z[1 - (1/z) - \epsilon_Q/(1 - z)]^2}, \quad (2.36)$$

where N is the normalization constant fixed by summing over all hadrons containing the fragmenting heavy quark,

$$\sum \int dz D(z) = 1 \quad (2.37)$$

We use the parameter ϵ as $\epsilon_c = 0.016$ for charm quarks and $\epsilon_b = 0.0012$ for bottom quarks in our calculation. For other details of the production and fragmentation of heavy quarks we refer the readers to Refs. [68].

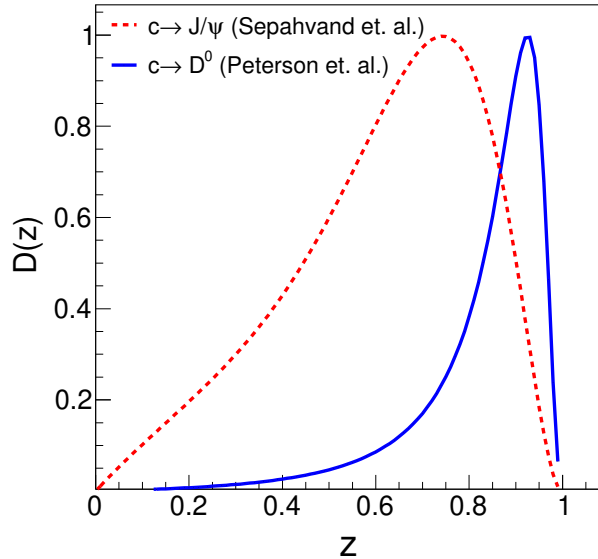


Figure 2.2: The Peterson fragmentation function [106] (for $c \rightarrow D^0$ -meson) and Dadfar fragmentation function [107] (for $c \rightarrow J/\psi$ -meson).

In Fig. 2.2, we show the Peterson and Dadfar fragmentation function as function of z (momen-

tum fraction between the parent heavy quark and the daughter heavy meson) for charm quark fragmenting into D^0 -meson and J/ψ -meson respectively. The fragmentation probability ($D(z)$) increases as z increases from zero and reaches a pick value after that $D(z)$ decreases as z further increases. Finally the heavy flavor hadron spectra can be obtained by convoluting the heavy quark production cross section with the fragmentation function.

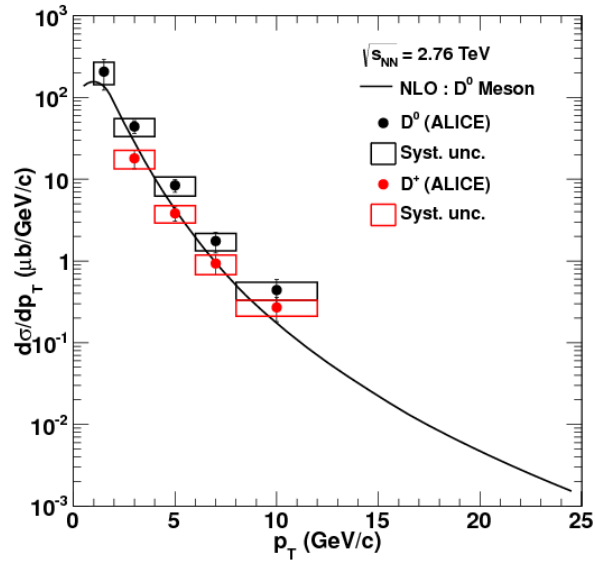


Figure 2.3: The NLO calculation of p_T -differential cross section of D -meson in pp collisions at $\sqrt{s} = 2.76$ TeV [105]. The experimental data are taken from ALICE collaboration [108].

In Fig. 2.3, we show the NLO pQCD calculations of p_T -differential cross section of D -meson as a function of p_T in pp collisions at $\sqrt{s} = 2.76$ TeV. To obtain the calculated cross section for D -meson, we convolute the charm quark production cross section (discussed in Sec. 2.1) with the Peterson fragmentation function. We compare the calculation with ALICE measurements of p_T -differential differential cross section of D^0 and D^+ mesons [108]. The calculation can describe the measurements quite well within the uncertainties.

Figure 2.4 displays the pQCD calculation of p_T -differential prduction cross section of D^0 and B^+ -meson as a function of p_T in pp collisions at $\sqrt{s} = 5.02$ TeV, compared with the experimental

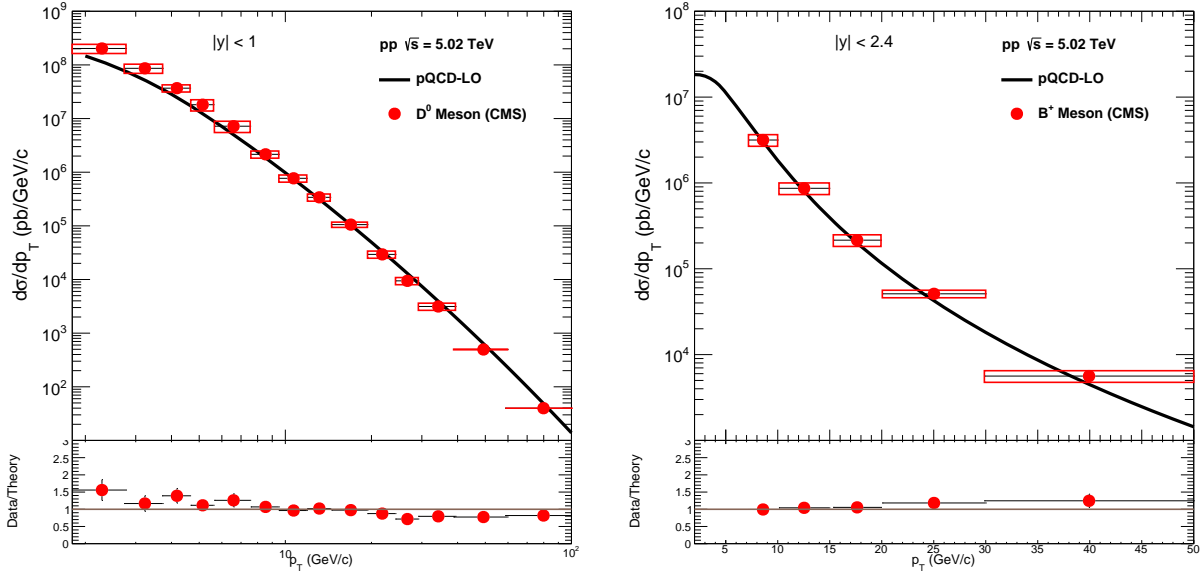


Figure 2.4: The LO calculations of p_T -differential cross section of D^0 -meson (left plot) and B^+ -meson (right plot) in pp collisions at $\sqrt{s} = 5.02$ TeV [68], compared with the experimental measurements of CMS collaboration [109, 110].

measurements of CMS collaboration [109, 110]. The experimental data is described well by the calculation within the uncertainties.

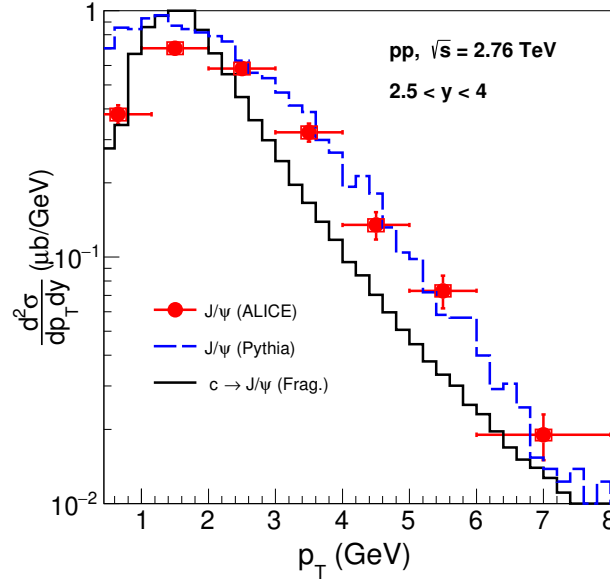


Figure 2.5: The calculation of p_T -differential cross section of prompt J/ψ -meson in pp collisions at $\sqrt{s} = 2.76$ TeV. The experimental data are taken from ALICE collaboration [111].

In Fig. 2.5, we depict the calculation of p_T -differential production cross section of prompt

J/ψ -meson in pp collisions at $\sqrt{s} = 2.76$ TeV, compared with ALICE measurements [111] and PYTHIA [112] prediction. For the calculation of J/ψ -meson production cross section, we convolute the charm quark production cross section with the Dadfar [107] fragmentation function for $c \rightarrow J/\psi$ -meson. The calculation can not describe the experimental data properly. This is because of the fact that charm quark fragmenting to J/ψ -meson is not the dominant process for J/ψ production. This fragmentation prescription is valid for very high p_T region. The dominant process for prompt J/ψ production is the gluon-gluon fusion. However, the mechanisms are not fully understood. There are several models for J/ψ production like Colour Evaporation Model, NRQCD Model etc. PYTHIA event generator can predict the J/ψ production very well, as it includes the dominant processes. This is the main drawback in the works shown in Chapter 3 for J/ψ production and suppression.

2.5.2 Coalescence

Here we discuss, the hadronization of the heavy quarks by coalescing the heavy quark with the light quarks from the QGP medium. Note that this coalescence mechanism does not need the thermalization of the coalescing partons. This approach was began to use for light hadrons [113, 114, 115, 116], and later applied to heavy flavors [117, 118, 119] also for partonic jet hadronization [120].

The momentum distribution of hadrons formed by the coalescence mechanism reads as [121],

$$\frac{d^2 N_H}{dP_T^2} = g_H \int \prod_{i=1}^n \frac{d^3 p_i}{(2\pi)^3 E_i} p_i \cdot d\sigma_i f_{q_i}(x_i, p_i) f_H(x_1..x_n, p_1..p_n) \delta^{(2)} \left(P_T - \sum_{i=1}^n p_{T,i} \right) \quad (2.38)$$

where,

g_H Statistical factor to make a colorless hadron from the spin 1/2

quark and antiquark

n Number of quarks to combine; 2 for meson and 3 for baryon

$d\sigma_i$ An element of a space-like hypersurface

f_{qi} Quark/anti-quark distribution functions

and f_H refers Wigner function, describes the coordinate and momentum distribution of quarks/anti-quarks in a hadron or meson and also describes the probability for partons to combine to form a meson or hadron. This coalescence process of heavy flavor particle formation will be incorporated in future and is beyond the discussion in this dissertation.

To summarize this chapter, we have discussed the heavy quark production and fragmentation in heavy-ion collisions. The models to describe the QGP medium formed in the collisions have been described. We have also discussed the detailed dynamics of the heavy quarks in the QGP medium and how they lose energy during their path of motion.

Chapter 3

The Chromo-Electromagnetic Field Fluctuations and Heavy Quarks

We will start this chapter by introducing the Chromo-Electromagnetic Field present in the QGP medium and how this field fluctuates. As a result of these field fluctuations, the heavy quarks propagating in the QGP medium gain energy and this has been discussed in Sec.3.1. The effects of these fluctuations on drag and diffusion coefficient of heavy quarks, heavy flavor suppressions and shear viscosity to entropy density ratio (η/s) of QGP medium have been studied in Sec.3.3, Sec.3.4 and Sec.3.6 respectively.

3.1 The Chromo-Electromagnetic Field Fluctuations in the QGP

QGP is a hot and dense deconfined state of QCD matter produced in the relativistic heavy-ion collisions. The QGP medium constituents i.e., light quarks and gluons move randomly inside the QGP volume and resemble Brownian motion. Since quarks and gluons have color charge, they produce color electromagnetic field during their random motions. This color electromagnetic field

is termed as "Chromo-Electromagnetic Field". The produced color field is fluctuating in nature and is a function of local space-time. In other words, the QGP is a statistical ensemble of mobile colored charge particles, which can be characterised by omnipresent stochastic fluctuations. These field fluctuations generally couple to the external perturbations and would affect the response of the medium. The response of the medium to these perturbations can be expressed through the suitable correlation functions of the microscopically fluctuating variables.

In case of the QED plasma, similar type of field fluctuations (here the field is electromagnetic field) are observed and the effect of such electromagnetic field fluctuations during the passage of charged particles through a non-relativistic classical QED plasma has been calculated by several authors [122, 123, 124, 125, 126, 127]. The chromo-electromagnetic field fluctuations in the QGP have a great impact on heavy quark propagation in the QGP medium. These fluctuations lead to energy gain of heavy quarks of all momenta but is more pronounced for the lower momentum ones [80] which are discussed below.

3.2 Heavy Quark Energy Gain

Upon passing through the QGP, heavy quark loses part of its energy because of the interactions with the QGP medium particles. These energy losses are calculated if it is assumed that the energy lost by the heavy quark per unit time is small compared to the energy of the heavy quark itself, and therefore, the change in velocity of the heavy quark during the motion may be neglected. When an energetic parton (either light or heavy) propagates in QGP, a retarding force acts on the parton in the plasma due to the chromo-electric field generated by the parton itself while moving. The energy-loss of the parton is obtained through the work done by this retarding force that acts on the parton and is determined within the linear response theory in terms of the dielectric tensor

of the medium. Therefore the energy losses of the parton per unit time are,

$$\frac{dE}{dt} = Q^a \vec{v} \cdot \vec{\mathcal{E}}^a|_{\vec{r}=\vec{v}t}, \quad (3.1)$$

where Q^a is the charge, \vec{v} is velocity of the parton and $\vec{\mathcal{E}}^a$ is the field, taken at the location (\vec{r}, t) of the parton.

Nevertheless, the Eq.3.1 does not take into account the chromo-electric field fluctuations and the particle recoil in the plasma. To include these effects, one needs to perform two kind of averaging [80]: (a) an ensemble average with respect to the equilibrium density matrix and (b) a time average over random fluctuations in plasma. This averaging is applicable to high energy jets of both the light and heavy quarks in the QGP.

After accommodating these effects, the energy losses of the parton per unit time are given by [123],

$$\frac{dE}{dt} = \left\langle Q^a \vec{v} \cdot \vec{\mathcal{E}}_t^a(\vec{r}(t), t) \right\rangle, \quad (3.2)$$

where $\langle \dots \rangle$ represents the statistical averaging operation. The electric field $\vec{\mathcal{E}}_t^a$ in Eq.3.2 consists of the induced field (which is obtained by Maxwell's equations and the equation of continuity) and a spontaneously generated microscopic field (which is a random function of position and time).

Let us pick a sufficiently large time interval Δt as compared with the period of the random fluctuations of the electromagnetic field in the plasma (τ_2), but small as compared with the time during which the particle motion changes in an essential manner (τ_1). i.e.,

$$\tau_1 \gg \Delta t \gg \tau_2 \quad (3.3)$$

Since the particle trajectory differs only slightly from a straight line during this time interval Δt ,

the particle velocity and the field acting on the particle at time $t = t_0 + \Delta t$ may be represented approximately as [123],

$$\vec{v}(t) = \vec{v}_0 + \frac{1}{E_0} \int_{t_0}^t dt_1 Q^a \vec{\mathcal{F}}_t^a(\vec{r}_0(t_1), t_1) \quad (3.4)$$

where E_0 is the initial parton energy and $\vec{\mathcal{F}}_t^a = \vec{\mathcal{E}}_t^a + \vec{v} \times \vec{\mathcal{B}}_t^a$, where $\vec{\mathcal{B}}_t^a$ is the magnetic field consists of an induced and a microscopic part as in the case of electric field,

$$\vec{\mathcal{E}}_t^a(\vec{r}(t), t) = \vec{\mathcal{E}}_t^a(\vec{r}_0(t), t) + \frac{Q^b}{E_0} \int_{t_0}^t dt_1 \int_{t_0}^{t_1} dt_2 \times \sum_j \mathcal{E}_{j,t}^b(\vec{r}_0(t_2), t_2) \frac{\partial}{\partial r_{0j}} \vec{\mathcal{E}}_t^a(\vec{r}_0(t), t) \quad (3.5)$$

where, $\vec{r}_0(t) = \vec{r}_0(t_0) + \vec{v}_0(t - t_0)$.

Substituting Eq.3.4 and Eq.3.5 into Eq.3.2, we obtain the following expression for the mean change in energy of the moving parton per unit time,

$$\begin{aligned} \frac{dE}{dt} &= \left\langle Q^a \vec{v}_0 \cdot \vec{\mathcal{E}}_t^a(\vec{r}_0(t), t) \right\rangle_\beta \\ &+ \frac{Q^a Q^b}{E_0} \int_0^t dt_1 \left\langle \vec{\mathcal{E}}_t^b(\vec{r}_0(t_1), t_1) \cdot \vec{\mathcal{E}}_t^a(\vec{r}_0(t), t) \right\rangle_\beta \\ &+ \frac{Q^a Q^b}{E_0} \int_0^t dt_1 \int_0^{t_1} dt_2 \left\langle \sum_j \mathcal{E}_{t,j}^b(\vec{r}_0(t_2), t_2) \right. \\ &\times \left. \frac{\partial}{\partial r_{0j}} \vec{v}_0 \cdot \vec{\mathcal{E}}_t^a(\vec{r}_0(t), t) \right\rangle_\beta. \end{aligned} \quad (3.6)$$

where, $\langle \dots \rangle_\beta$ denotes the ensemble average. Evidently, the mean value of the fluctuating part of the field equals zero, hence $\left\langle \vec{\mathcal{E}}_t(\vec{r}(t), t) \right\rangle_\beta$ is the chromo-electric field produced by the particle itself in the plasma. Therefore, the first term in Eq.3.6 characterizes the customary polarization energy losses of the moving parton. The second and third terms in Eq.3.6 correspond to the

statistical change in the energy of the moving parton, associated with the fluctuations of the chromo-electromagnetic field in the plasma, as well as the fluctuations in velocity of the parton itself under the effect of this field. The second term in Eq.3.6 determines the dynamic friction of the parton due to the presence of space-time correlations between the fluctuating fields, while the third term determines the average change in the energy of the moving particle due to the correlation between the fluctuations in the velocity of the parton and the fluctuations in the electrical field in the plasma. The presence of such correlations leads to a statistical magnification of the energy of the moving parton. Now the statistical magnification of the parton energy can be obtained in terms of the spectral density of field fluctuations as [80];

$$\left. \frac{dE}{dt} \right|_{\text{fl}} = \frac{C_F \alpha_s}{16\pi^3 E} \int d^3k \left[\frac{\partial}{\partial \omega} \left\langle \omega \tilde{\mathcal{E}}_L^2 \right\rangle_{\beta} + \left\langle \tilde{\mathcal{E}}_T^2 \right\rangle_{\beta} \right]_{\omega=\vec{k} \cdot \vec{v}} \quad (3.7)$$

where $\left\langle \tilde{\mathcal{E}}_L^2 \right\rangle$ and $\left\langle \tilde{\mathcal{E}}_T^2 \right\rangle$ denote the longitudinal and transverse field fluctuations, respectively. Eq.3.7 can also be recast as [80];

$$\left. \frac{dE}{dt} \right|_{\text{fl}} = \frac{C_F \alpha_s}{8\pi^2 E v^3} \int_0^{k_{\text{max}} v} d\omega \coth \frac{\beta \omega}{2} F(\omega, k = \omega/v) + \frac{C_F \alpha_s}{8\pi^2 E v} \int_0^{k_{\text{max}}} dk k \int_0^{kv} d\omega \coth \frac{\beta \omega}{2} G(\omega, k), \quad (3.8)$$

where $F(\omega, k) = 8\pi\omega^2 \text{Im} \epsilon_L / |\epsilon_L|^2$ and $G(\omega, k) = 16\pi \text{Im} \epsilon_T / |\epsilon_T - k^2/\omega^2|^2$ and $v_0 = v$.

It is important to note here, since the spectral density of field fluctuations $\left\langle \tilde{\mathcal{E}}_{L/T}^2 \right\rangle$ are positive for positive frequencies by definition, according to Eq.3.8 the parton energy will grow due to interactions with the fluctuating fields in the plasma. i.e., the above expression (Eq.3.8) gives the mean energy absorbed from the plasma per unit time by the propagating parton.

The leading-log (LL) contribution of this energy gain per unit path length of a heavy quark

propagating in the plasma is obtained [80] as;

$$\left(\frac{dE}{dx}\right)_{\text{fl}}^{\text{LL}} = 2\pi C_F \alpha_s^2 \left(1 + \frac{n_f}{6}\right) \frac{T^3}{Ev^2} \ln \frac{1+v}{1-v} \ln \frac{k_{\text{max}}}{k_{\text{min}}}, \quad (3.9)$$

where, $k_{\text{min}} = \mu_g$ is Debye mass and $k_{\text{max}} = \min \left[E, 2q(E+p)/\sqrt{M^2 + 2q(E+p)} \right]$ with $q \sim T$ is the typical momentum of the thermal partons. One can physically interpret the energy gain of the heavy quark as due to the absorption of gluons during its propagation.

We study the effect of these fluctuations on heavy quark propagation in the QGP medium. We calculate the energy gain as well as energy losses (collisional and radiative energy losses are described in the previous chapter, Sec.2.4) of a propagating heavy quark in QGP medium. For the evolution of the medium, we use simplistic 1D expansion as discussed in the previous chapter (Sec.2.2).

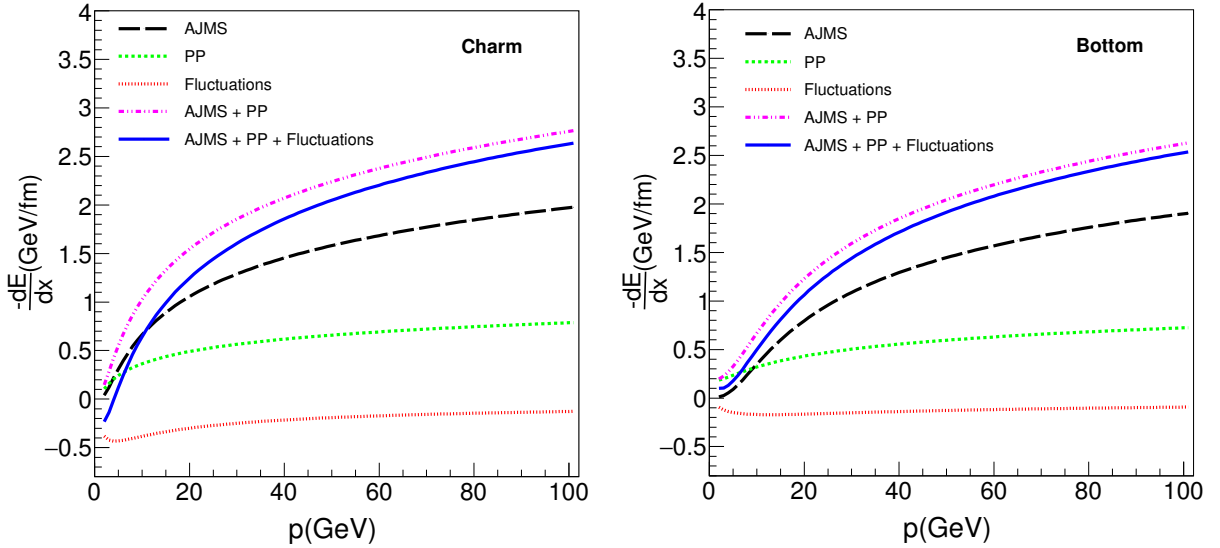


Figure 3.1: The energy loss of charm (left plot) and bottom (right plot) quark inside QGP medium as a function of momentum, obtained using collisional (PP)[88], radiative (AJMS)[104] energy loss and fluctuations[80].

In Fig. 3.1 (taken from our work [128]), we display the various contributions to the differential energy loss of charm and bottom quark, respectively. Also the differential contribution due to

the effect of field fluctuations is included in both figures. Our choices of parameters are: $n_f = 2$, $\alpha_s = 0.3$, charm quark mass, $M_c = 1.25$ GeV and bottom quark mass, $M_b = 4.2$ GeV. It is observed that the energy loss increases as momentum of quarks increases but rate of increment is higher at lower momentum region. It is also seen that the AJMS differential radiative energy loss always dominates over that of PP collisional energy loss for charm quark whereas for bottom quark, the differential PP collisional energy loss dominates the AJMS differential radiative energy loss upto momentum 10 GeV, beyond which the AJMS radiative energy takes over. The differential energy loss ($-dE/dx$) is negative due to the field fluctuations which implies energy gain due to the absorption of gluon by heavy quark. This energy gain due to the field fluctuations is found to be significant in the momenta range (4 – 20) GeV. This energy gain is relatively more for charm quark compared to bottom quark.

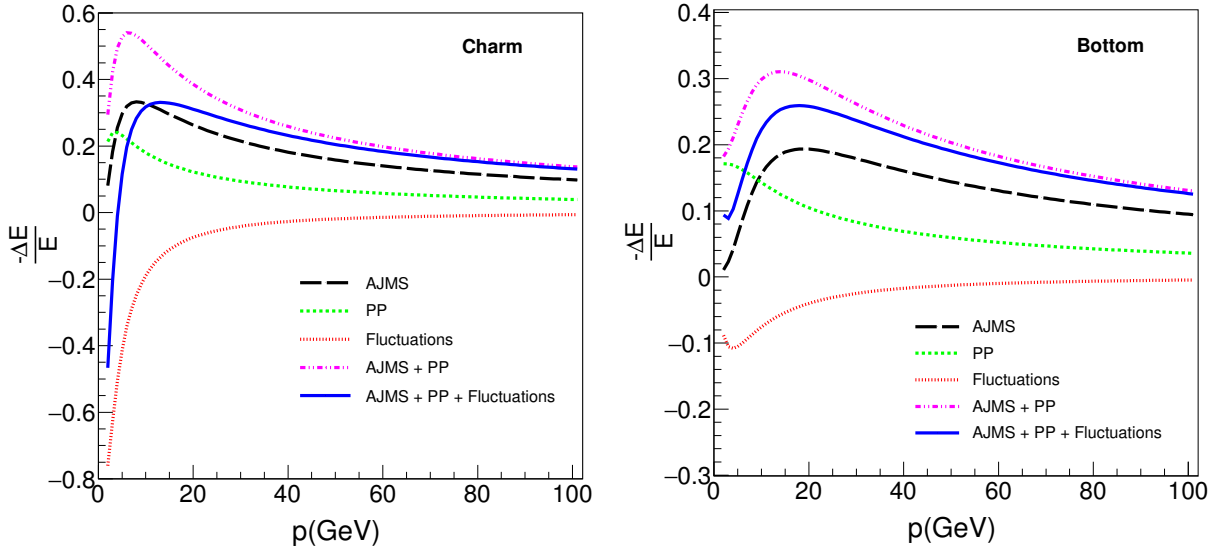


Figure 3.2: Fractional energy loss of charm (left plot) and bottom (right plot) quark inside QGP due to fluctuations, collisions (PP) and radiations (AJMS) as a function of momentum. The path length considered here is $L = 5$ fm.

Fig. 3.2 (taken from our work [128]) display the fractional energy loss from collisional and radiative processes, and also the energy gain due to the field fluctuations for charm and bottom quarks, respectively. It is clear from both the figures that the energy gain for heavy quarks is

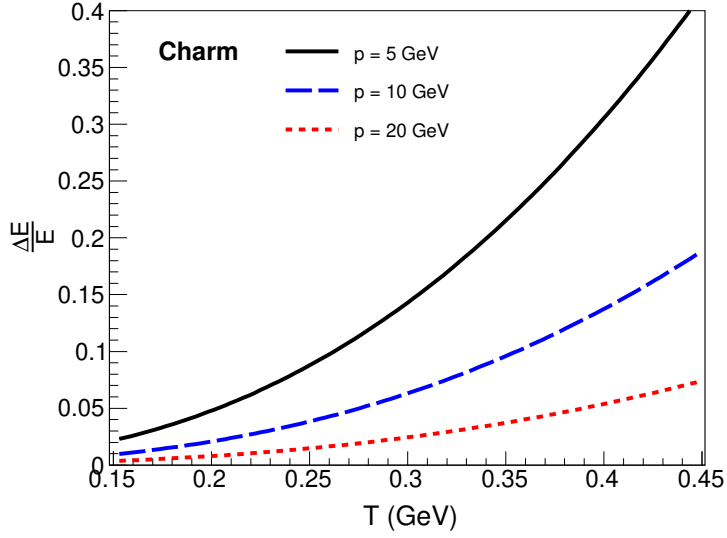


Figure 3.3: Fractional energy gain of a charm quark with momentum, $p = 5, 10$ and 20 GeV inside the QGP medium due to fluctuations, as a function of T . The path length considered here is $L = 5$ fm.

relatively more at the lower momentum region ($4 - 40$ GeV) than that in higher momentum (> 40 GeV) region. This means that the field fluctuations and thus the energy gain becomes substantial only in the low velocity limit of heavy quark. This gets more clearer in Fig. 3.3 which displays the fractional energy gain of a charm quark with momentum, $p = 5, 10$ and 20 GeV inside the QGP medium due to field fluctuations as a function of T . The fractional energy gain is more for the charm quark with lower momentum. The effect of these field fluctuations is to reduce the total energy loss of a heavy quark up to a certain value of momentum beyond which their contribution gradually diminishes as seen in Fig. 3.2.

3.3 Effect of the Chromo-Electromagnetic Field Fluctuations on Drag and Diffusion Coefficient of Heavy Quarks

During the propagation through the QGP, the heavy quarks lose energy via elastic collisions and bremsstrahlung gluon radiations. Along with that, heavy quarks gain energy due to the statistical field fluctuations of the QGP medium (see Ref. [80] for the details) which reduces the total energy loss of the heavy quarks. As a consequence of that, the heavy quarks are dragged and diffused in the medium. Therefore, the estimation of drag (A) and diffusion (B) coefficients should include these energy losses as well as the energy gain processes.

In this spirit, we use $-dE/dx$ to estimate the drag and diffusion coefficients of heavy quarks. A_{Coll} and B_{Coll} are drag and diffusion coefficient for collisional process. Similarly we define A_{Rad} and B_{Rad} , (A_{Fl} and B_{Fl}) for radiative, (field fluctuations) process. The effective drag and diffusion coefficients are defined as $A = A_{Coll} + A_{Rad} + A_{Fl}$ and $B = B_{Coll} + B_{Rad} + B_{Fl}$ respectively. The net $-dE/dx$ is used to calculate the effective drag and diffusion coefficients. It should be mentioned here that the transport coefficients (A and B) in FP equation (as discussed in Sec. 2.3.1, Eq.2.17) usually evaluated for the collisional processes. Here, we also consider the fluctuations and radiative processes with the view in mind that though the invariant amplitude of three body scattering can be expressed in terms of two body scattering, the fluctuations, collisional and radiative processes take place inside the thermal medium independently. However, the collisional, radiative and fluctuations processes are not entirely independent, that is, the collisional and fluctuations processes may influence the radiative one and vice-versa, therefore strictly speaking $-dE/dx$ and hence the transport coefficients for collisional, radiative and fluctuations processes should not be added to obtain the net energy loss or net value of the transport coefficients. However, in the absence any rigorous method, we add them up to obtain the effective transport coefficients. This is a good

approximation for the work done here for the LHC because the radiative loss is large compared to the collisional loss at the LHC energies.

The effect of effective drag and diffusion on the heavy quark of momentum p in the QGP of temperature T can be defined as [82, 83],

$$A = \frac{1}{p} \left(-\frac{dE}{dx} \right)_{Coll+Rad+Fl} \quad (3.10)$$

$$B = T \left(-\frac{dE}{dx} \right)_{Coll+Rad+Fl} \quad (3.11)$$

respectively. These effective transport coefficients are important quantities containing the dynamics of energy loss and gain processes of the heavy quarks in the QGP medium. One can average out A and B over momentum, implying that the dynamics is dominated by the energy loss and gain processes in the heat bath.

Usually A and B are functions of momentum p and temperature T . We use power-law distribution and differential energy loss calculations BT [86] and DGLV [98, 99] (discussed in Chapter 2) to perform the momentum averaging of A and B . To sample the initial transverse momentum of charm quarks, we use the following power-law parametrization [58]:

$$\frac{dN}{d^2p_T} \propto \frac{1}{(p_T^2 + \Lambda^2)^n} \quad (3.12)$$

where, $\Lambda = 2.1$ and $n = 3.9$. The time dependence in A and B comes from assuming the temperature T is decreasing with time as the system expands cylindrically in isentropic nature. For time averaging of A and B , we calculate A and B from energy loss for different times during the expansion of the system and then averaging them over the entire evolution of the system.

In Fig. 3.4 (taken from our work [152]), the variation of drag coefficients (A) of a charm quark

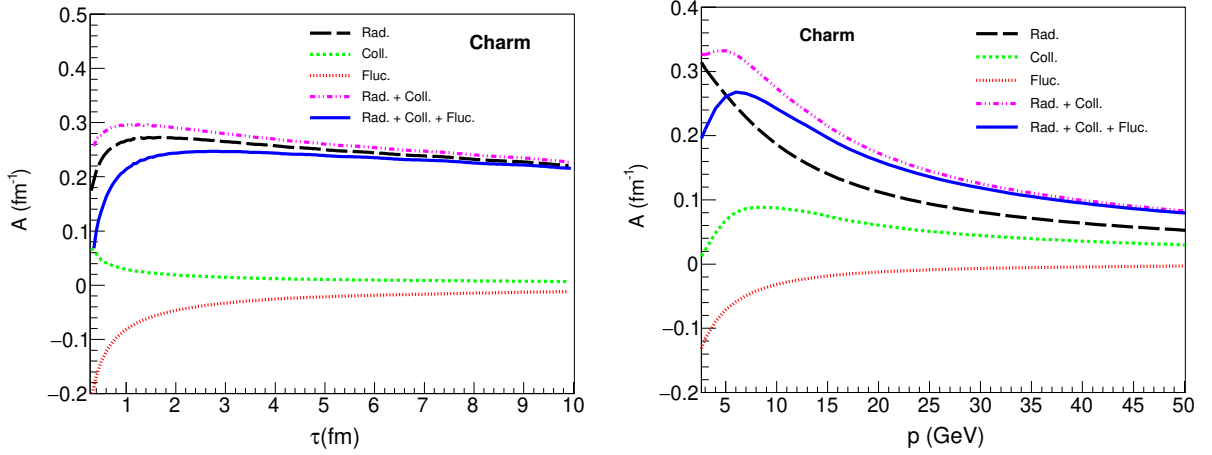


Figure 3.4: The drag coefficient of a charm quark inside the QGP medium as a function of time (left plot) and momentum (right plot), obtained for different energy loss schemes (BT [86] and DGLV [98, 99]) along with the effect of fluctuations [80].

with time and charm quarks momentum have been depicted. The values of A are positive and decrease with time and momentum where only the energy loss processes have been considered. For the field fluctuations, as these fluctuations cause charm quarks to gain energy, the values of A are negative. We also observe that the contribution of radiative energy loss is large compared to the collisional one which is consistent with the findings of Das et. al. [83]. The total contribution of radiative and collisional losses ($Coll. + Rad.$) are large enough whereas the inclusion of the effect of field fluctuations decreases the total drag coefficient ($Coll. + Rad.$) and we call it effective drag coefficient ($Coll. + Rad. + Fluc.$). The reduction of drag coefficient is more at the lower momentum region ($p < 25$ GeV) since the fluctuations are significant at lower momentum as discussed earlier. At $p > 25$ GeV region, the effect of the fluctuations on drag coefficient is negligibly small.

Once the drag coefficient is averaged out over momentum using the properties of heat bath (as discussed earlier), the diffusion coefficient can also be averaged out over momentum since it is derivable from the drag coefficient through Einstein's relation. Fig. 3.5 (taken from our work [152]) displays the diffusion coefficients (B) of a charm quark as a function of time and charm quarks momentum respectively. We observe that the values of B are positive and decrease with time and

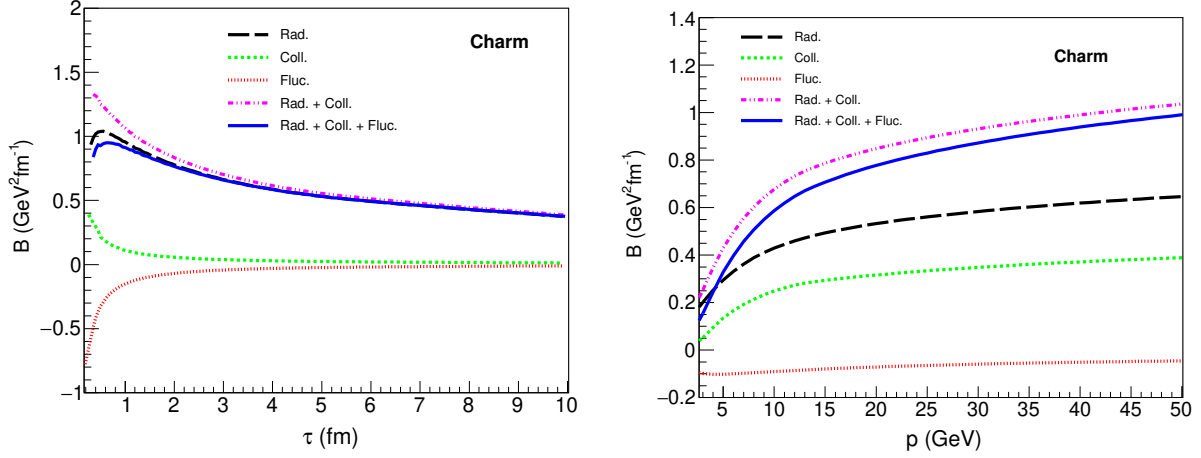


Figure 3.5: The diffusion coefficient of a charm quark inside the QGP medium as a function of time (left plot) and momentum (right plot), obtained for different energy loss schemes (BT [86] and DGLV [98, 99]) and along with the effect of fluctuations [80].

increase with momentum when only the energy loss processes are considered. The values of B are negative for field fluctuations because the charm quarks gain energy due to field fluctuations. In principle, B should not be negative, as it is a measure of thermal average of the square of momentum transfer weighted by the square of invariant amplitude. The negative values of B due to fluctuations only are by our convention. When heavy quarks lose energy in the bulk medium, the momentum transfer from heavy quarks to the bulk medium occurs and hence the positive B values are obtained. Since fluctuations cause the heavy quarks to gain energy, the momentum transfer from the bulk medium to heavy quarks happens. Hence, we denote the B values for fluctuations only as negative to make understand that the fluctuations will decrease the total B . There is no as such physical meaning attached with negative B . It results a reduction of total diffusion coefficient ($Coll. + Rad.$) to an effective diffusion coefficient, $B_{eff} (Coll. + Rad. + Fluc.)$ which is less compared to $Coll. + Rad.$ case.

3.4 Effect of the Chromo-Electromagnetic Field Fluctuations on Heavy Flavour Suppression as Observed in the ALICE and CMS experiment

In order to study the heavy flavor suppression, it is required to calculate the heavy quark production cross sections both for proton-proton (pp) and heavy-ion (A-A) collisions. It has been obtained by using factorization with elementary cross sections calculated upto Leading Order (LO) and Next-to-Leading Order (NLO) CT10 parton density functions [71] for pp collisions as described in Sec.2.1 of Chapter.2. For A-A collisions, the shadowing effect is taken into account by using the spatially dependent EPS09[72] sets. The differential cross section including nuclear shadowing effect corresponding to a given centrality class between impact parameters b_1 and b_2 is calculated. Then the spectrum in Pb-Pb collisions can be obtained by shifting the calculated differential cross section by the momentum loss Δp_T . We consider the simplistic 1D expansion for the QGP medium evolution as described in Sec.2.2.1 of Chapter.2. For fragmentation of c quarks into D -mesons and b quarks into B -mesons, the Peterson fragmentation function[106] with parameters $\epsilon_c = 0.016$ for c quarks and $\epsilon_b = 0.0012$ for b quarks are used. For other details of the production and fragmentation of heavy quarks we refer the readers to Refs. [68].

Finally the nuclear modification factor R_{AA} is computed as:

$$R_{AA}(p_T, b_1, b_2) = \frac{\frac{d^2\sigma_{PbPb}(p_T, b_1, b_2)}{dp_T^2 dy}}{\int_{b_1}^{b_2} d^2b T_{AA} \frac{d^2\sigma_{pp}(p_T)}{dp_T^2 dy}}. \quad (3.13)$$

where, b_1 and b_2 are the impact parameters corresponding to a given centrality of collision and T_{AA} is the nuclear overlap function.

The Figs3.6 and 3.7 display the nuclear modification factor R_{AA} as a function of p_T for D^0 -

meson in Pb-Pb collisions for (0 – 10)% and (0 – 100)% centralities, respectively considering both collisional and radiative energy loss along with the energy gain due to the field fluctuations. The results are also compared with ALICE [129] and CMS data [130].

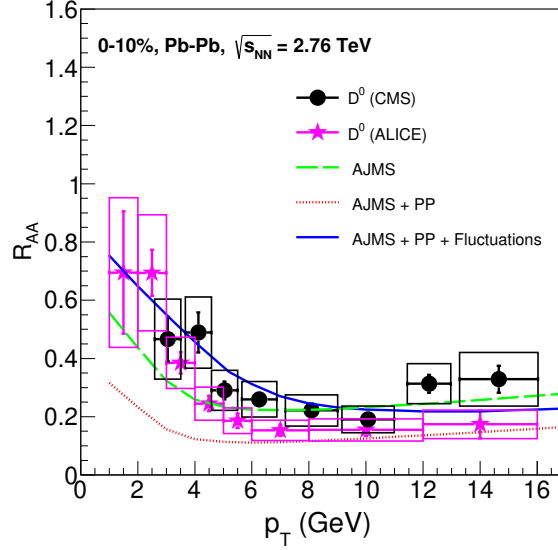


Figure 3.6: The nuclear modification factor R_{AA} of D^0 -meson with collisional (PP) and radiative (AJMS) energy loss along with the effect of fluctuations as a function of transverse momentum p_T for (0 – 10)% centrality in Pb-Pb collisions at $\sqrt{s_{NN}} = 2.76$ TeV. The experimental data are taken from the measurements of ALICE [129] and CMS experiments [130].

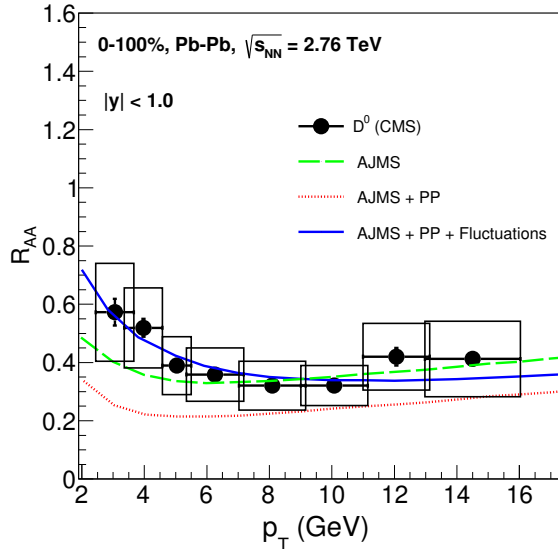


Figure 3.7: The nuclear modification factor R_{AA} of D^0 -meson with collisional(PP) and radiative(AJMS) energy loss along with the effect of fluctuations as a function of transverse momentum p_T for (0 – 100)% centrality in Pb-Pb collisions at $\sqrt{s_{NN}} = 2.76$ TeV. The experimental data are taken from the measurement of CMS experiment [130].

We observe that only radiative energy loss (AJMS) or the collisional energy loss (PP) along with the radiative energy loss can not explain the data properly. As seen that the radiative loss along with the collisional energy loss overestimate the data in entire p_T range whereas only the radiative one alone can describe the data for the transverse momentum $p_T > 10$ GeV. This is because the radiative energy loss has dominant contribution compared to that of the collisional one. When the energy gain due to the chromo-electromagnetic field fluctuations are included in addition to both the collisional and the radiative losses the measured data are well described in the entire p_T range. We *emphasize* that the chromo-electromagnetic field fluctuations are found to play an important role on the propagation of the heavy quark jets in a QGP vis-a-vis the nuclear modification factor of heavy flavored hadrons.

Fig. 3.8 displays the nuclear modification factor R_{AA} of D^0 -meson as a function of p_T , for (0 – 100)% centrality in Pb-Pb collisions at $\sqrt{s_{NN}} = 5.02$ TeV, obtained using collisional (PP), radiative (AJMS) energy loss and effect of field fluctuations in Pb-Pb collisions at $\sqrt{s_{NN}} = 5.02$ TeV. The experimental data are taken from the CMS collaboration [109]. Again the radiative energy loss (AJMS) alone can describe the data above transverse momentum 10 GeV but the R_{AA} spectra in full p_T range can be described when the effect of fluctuations is taken into consideration.

In Fig. 3.9 the nuclear modification factor R_{AA} , for B^+ -meson in Pb-Pb collisions at $\sqrt{s_{NN}} = 5.02$ TeV is displayed considering both collisional and radiative energy loss along with the effect of the field fluctuations and is compared with CMS data [110]. The radiative energy loss itself produces a small suppression but when the collisional one is added, it gives more suppression than the suppression measured by CMS experiment. Importantly, the inclusion of the energy gain due to the chromo-electromagnetic field fluctuations in addition to both the radiative and collisional losses, the suppression is found to be very close to the measured data within their uncertainties.

We would like to mention that the theoretical uncertainties may appear due to following reasons:

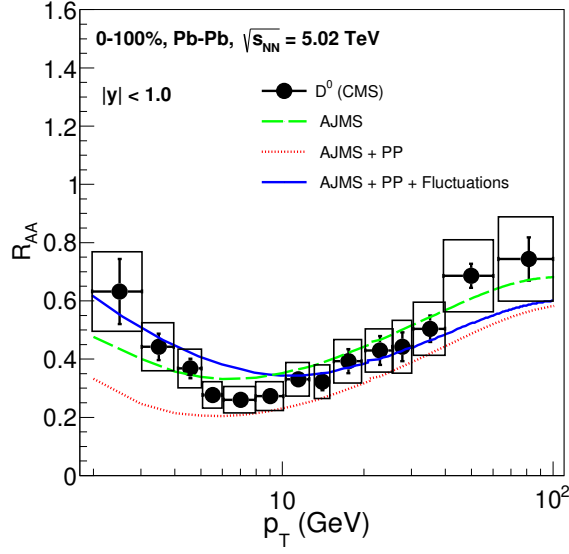


Figure 3.8: The nuclear modification factor R_{AA} of D^0 -meson with collisional (PP) and radiative (AJMS) energy loss along with the effect of field fluctuations as a function of transverse momentum p_T for (0 – 100)% centrality in Pb-Pb collisions at $\sqrt{s_{NN}} = 5.02$ TeV. The experimental data are taken from the measurements of CMS experiment [109].

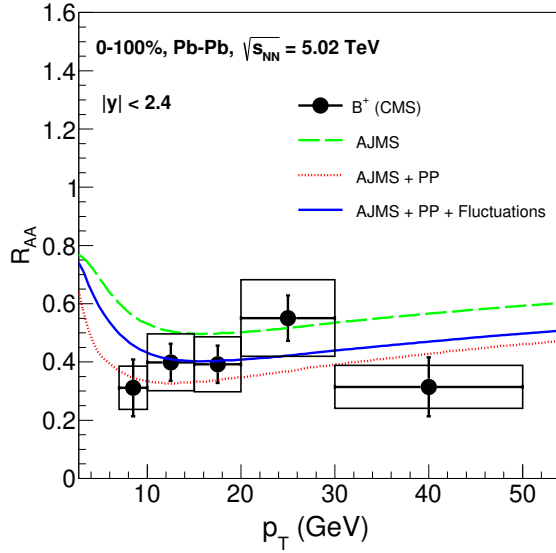


Figure 3.9: The nuclear modification factor R_{AA} of B^+ -meson with collisional (PP) and radiative (AJMS) energy loss along with the effect of field fluctuations as a function of transverse momentum p_T for (0 – 100)% centrality in Pb-Pb collisions at $\sqrt{s_{NN}} = 5.02$ TeV. The experimental data are taken from the measurements of CMS experiment [110].

- i) The thermalization of hot and dense matter is an unsettled issue which causes an uncertainty in the initial conditions. The initial time, τ_0 , may vary between 0.1 and 0.5 fm/c which

effectively causes variation in the initial temperature, T_0 and thus in the effective temperature of the medium.

- ii) Semiclassical approximation has been used to calculate the mean energy loss, which has been shown to be equivalent to the Hard Thermal Loop approximation based on the weak coupling limit [85, 86, 88, 104]. It also corresponds to neglecting the non-Abelian terms in the QCD equations of motion.
- iii) We assume a constant momentum and temperature independent coupling constant instead of running coupling.
- iv) The parton distribution and fragmentation function involve uncertainties affecting the shape of the pp spectra which in turn would affect the R_{AA} .

3.5 Effect of the Chromo-Electromagnetic Field Fluctuations on J/ψ Suppression

The J/ψ suppression due to the color screening effect has been considered as one of the most conclusive experimental evidence of the QGP formation. Several measurements of J/ψ production have been reported over the last couple of years [131, 132, 133, 134, 135, 136, 137, 138]. However the results of J/ψ production at LHC energies [135, 136, 137, 138] compelled intense discussions on the regeneration of J/ψ [139, 140] apart from cold nuclear matter effects (CNM) [141]. While invoking these effects, other effects, importantly the chromo-electromagnetic field fluctuations were ignored.

We have studied the effect of the chromo-electromagnetic field fluctuations on J/ψ suppression in relativistic heavy-ion collisions. We consider charm quarks produced in the primordial hard scattering (as described in Chapter 2, Sec 2.1) and executing Langevin diffusion in the QGP as

discussed in Sec 2.3.2 of Chapter 2. The initial production points of charm quarks are distributed according to the nuclear overlap function of the colliding nuclei using Glauber model approach. For further details, we refer to the Ref. [52]. For the evolution of the QGP medium, we follow (3+1)-D viscous hydrodynamics, vHLLE [75], discussed in Sec 2.2.2 of Chapter 2. After the Langevin diffusion of the charm quarks under this hydrodynamic background, hadronization of the charm quarks to J/ψ occurs. The hadronization is done by the Leading Order (LO) calculation of fragmentation function as calculated in Ref. [107].

Finally, we form the nuclear modification factor, defined as:

$$R_{AA} = \frac{dN^{AA}/dp_T}{N_{coll}dN^{pp}/dp_T} \quad (3.14)$$

where, N_{coll} is the number of binary nucleon-nucleon collisions for a given centrality class, obtained from Glauber model calculations.

In order to ensure that the estimation of drag (γ) and diffusion (D) coefficients in our Langevin framework is consistent with other model calculations of γ and D , we estimated the space diffusion coefficient (D_s) in the low momentum limit ($p \rightarrow 0$) of γ as, $D_s = T/M * \gamma(p \rightarrow 0)$. In Fig.3.10 (taken from our work [142]), we show the dimensionless quantity $2\pi T D_s$ for charm quark as a function of T/T_c , compared with lattice calculations [143], Bayesian analysis [144] and quasiparticle model (QPM) [145] calculations. It is seen that our estimation of $2\pi T D_s$ is consistent with other calculations.

It is important to mention here that the prominent process of prompt J/ψ production in high energy collisions is the gluon-gluon fusion. Though the mechanism is not fully understood. Here we have not considered this process in the calculation of J/ψ production in our model. Also, we have not considered the regeneration phenomena for J/ψ production from charm quark (anti-quark).

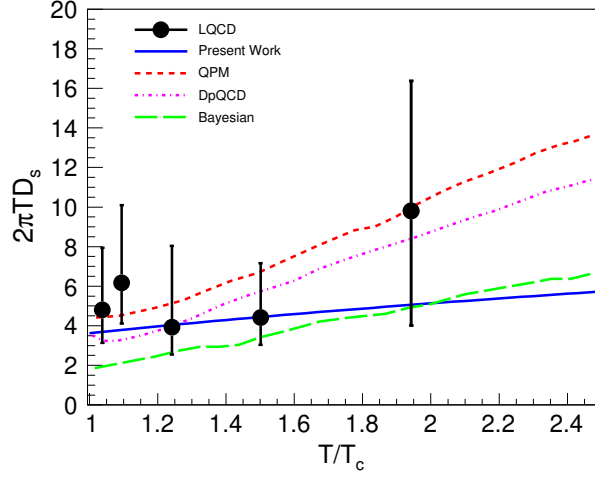


Figure 3.10: Spatial diffusion coefficient as a function of normalized temperature compared to lattice QCD calculations [143], dressed perturbative QCD(DpQCD), quasi-particle models(QPM) [145], and Bayesian analysis [144].

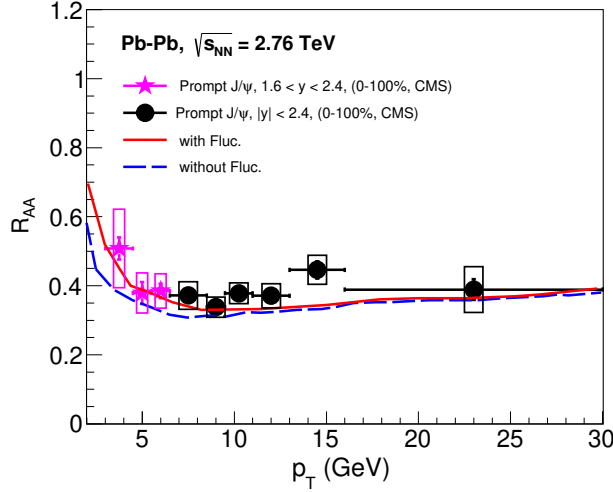


Figure 3.11: The nuclear modification factor R_{AA} of J/ψ mesons with the effect of fluctuations as a function of p_T in Pb-Pb collisions for 0 – 100% centrality at $\sqrt{s_{NN}} = 2.76$ TeV. The experimental measurements are taken from CMS Collaboration [137].

The nuclear modification factor, R_{AA} for J/ψ as a function of transverse momentum p_T is shown in Fig.3.11 (taken from our work [142]) with and without considering chromo-electromagnetic field fluctuations. Significant contribution of chromo-electromagnetic field fluctuations is observed at

lower transverse momentum region. The estimated R_{AA} is in good agreement with the measured experimental results [137] by CMS collaboration.

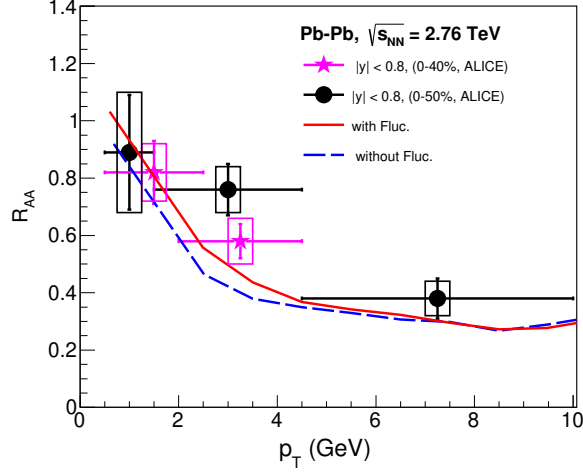


Figure 3.12: The nuclear modification factor R_{AA} of J/ψ mesons with the effect of fluctuations as a function of p_T in Pb-Pb collisions at $\sqrt{s_{NN}} = 2.76$ TeV, compared with the ALICE data [135].

In Fig.3.12 (taken from our work [142]), we show the results for 0 – 40% and 0 – 50% centrality class data as measured by ALICE collaboration at mid-rapidity [135]. The estimated R_{AA} with chromo-electromagnetic field fluctuations reproduces the measured experimental data. The energy gain due to field fluctuations occurs as gluons are absorbed during their propagation. This energy gain due to field fluctuations is more prominent in the low p_T region. This is consistent with the observed comparison with the data.

In Fig.3.13 (taken from our work [142]), we show the calculated R_{AA} as a function of number of participant nucleons in Pb-Pb collisions at $\sqrt{s_{NN}} = 2.76$ TeV and Au-Au collisions at $\sqrt{s_{NN}} = 200$ GeV. The results from CMS and PHENIX experiment are also compared. It is observed that the estimated values of R_{AA} with field fluctuations are in good agreement with the data within their uncertainties in Pb-Pb collisions at $\sqrt{s_{NN}} = 2.76$ TeV. In case of Au-Au collisions at $\sqrt{s_{NN}} = 200$ GeV, the experimental data can be described without considering chromo-electromagnetic field

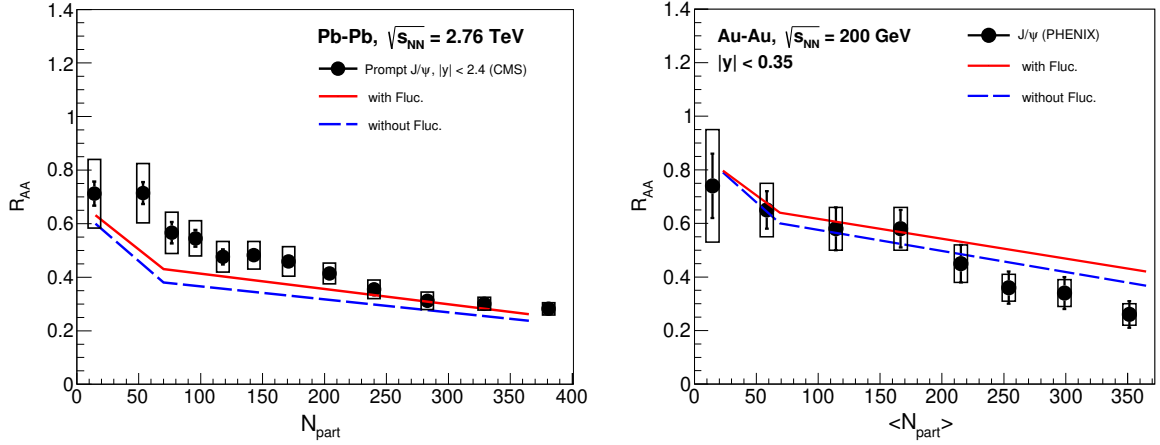


Figure 3.13: Left Plot: The nuclear modification factor R_{AA} of J/ψ mesons with the effect of fluctuations as a function of N_{part} in Pb-Pb collisions at $\sqrt{s_{NN}} = 2.76$ TeV. The experimental measurements are taken from CMS Collaboration [137].

Right Plot: The nuclear modification factor R_{AA} of J/ψ mesons with the effect of fluctuations as a function of N_{part} in Au-Au collisions at $\sqrt{s_{NN}} = 200$ GeV. The experimental data are taken from PHENIX Collaboration [133].

fluctuations.

The chromo-electromagnetic field fluctuations play an important role and probably one can closely explain the measured experimental data at $\sqrt{s_{NN}} = 200$ GeV at RHIC and $\sqrt{s_{NN}} = 2.76$ TeV at LHC energy without invoking regeneration phenomena.

3.6 Effect of the Chromo-Electromagnetic Field Fluctuations on η/s of the QGP

Viscosity measures the resistance of a fluid deformed either by tensile stress or shear stress. The less viscosity causes greater fluidity. In order to characterize QGP, amongst many, η/s is one of the important quantity. It is an important dimensionless measure of how imperfect or dissipative the QGP is.

A heavy quark with certain momentum while propagating through the QGP medium encounters the medium partons and hence the momentum exchange occurs with the medium partons. The

momentum exchange results minimization of momentum gradient in the system. Hence, it is related to the shear viscous coefficients of the system which drives the system towards a reduced momentum gradient. The expression of η/s has been calculated in Ref. [146], which reads as:

$$\frac{\eta}{s} \approx 1.25 \frac{T^3}{\hat{q}}, \quad (3.15)$$

where T is the temperature of the medium and \hat{q} is the transport coefficient which is defined as square of the average exchanged momentum between the heavy quark and bath particles per unit length. During the interaction of heavy quark with bath particles, the momentum diffusion occurs in the medium which is expressed through the diffusion coefficient B . Here we have used Eq.3.11 to estimate the B of charm quark. For energy loss in using Eq.3.11, we have used BT [86] collisional and DGLV [98, 99] radiative energy loss as discussed in Sec.2.4 of Chapter.2. The diffusion coefficient and \hat{q} , both are directly related to the square of the momentum transfer and hence \hat{q} is proportional to diffusion coefficient which is more often used in the diffusion equation as discussed in Ref.[146, 59]. The \hat{q} in Eq.3.15 is defined for gluon [146]. We have considered the color factor difference while relating the charm quark diffusion coefficient B with \hat{q} . The relation between B and \hat{q} is $B = \hat{q}/4$. Eq.3.15 has been used to estimate η/s of the QGP medium in the light of heavy quarks energy loss by Mazumder et. al.[147]. In this work, we estimate η/s from Eq.3.15, where \hat{q} is obtained from the effective diffusion coefficient which takes into account the effect of the field fluctuations.

In Fig. 3.14 (taken from our work [152]), we display η/s as a function of T/T_c when the charm quarks undergo both collisional and radiative processes along with the chromo-electromagnetic field fluctuations which cause the charm quarks to gain energy. We observe that the effect of such fluctuations increases the values of η/s of the QGP. The obtained values of η/s are close to the LQCD calculations[148, 149, 150] and findings of functional renormalization group technique[151]

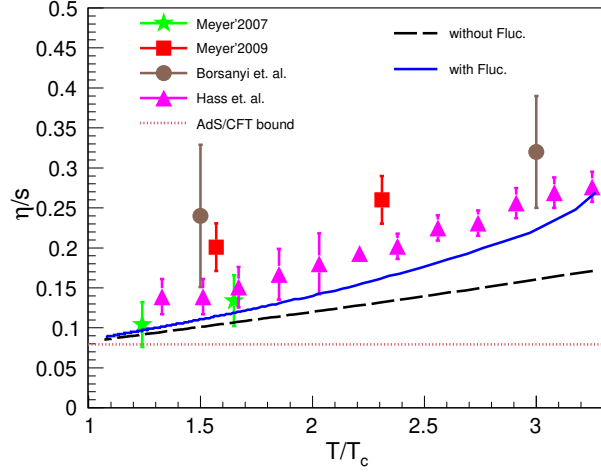


Figure 3.14: The viscosity to entropy density ratio (η/s) as a function of T/T_c , is compared with the results obtained by LQCD calculations[148, 149, 150] and functional renormalization group calculations[151]. Here critical temperature T_c is taken 155 MeV.

within their uncertainties when we include the effect of field fluctuations into account.

AdS/CFT calculations give a lower bound of η/s , which is $\frac{\eta}{s} \geq \frac{1}{4\pi}$. The obtained η/s values go slightly below this AdS/CFT lower bound near T_c which might be unphysical. It is hard to characterize the QGP near critical point. However it is worth mentioning that the theoretical uncertainties may appear in our calculations due to thermalization of the medium which may occur due to uncertainties in initial conditions. Mean energy loss calculations used here is based on semi-classical approximation which is equivalent to the Hard Thermal Loop approximation on the basis of weak coupling limit. The non-Abelian terms in the QCD equations of motion is also ignored here. Thus the uncertainty in the estimation of η/s from the energy loss calculation may arise.

The energy loss encountered by an energetic parton in a QGP medium reveals the dynamical properties of that medium in view of jet quenching of high energy partons. This is usually reflected in the transverse momentum spectra and nuclear modification factor of mesons which are measured in heavy ion experiments. For the phenomenology of the heavy quarks jet quenching, the field fluctuations in the QGP medium were not considered in the literature before.

To summarize this chapter, we have considered the energy gain of high energy heavy quarks due to field fluctuations along with the energy losses caused by the collisions and gluon radiations during the propagation of heavy quarks inside the QGP medium. It is observed that the effect of the fluctuations reduces the drag and diffusion coefficients compared to the total contributions from collisions and gluon radiations. The radiative loss is dominant over the collisional counter part in drag and diffusion coefficients. The nuclear modification factors R_{AA} for D -mesons and B -mesons in Pb-Pb collisions at $\sqrt{s_{NN}} = 2.76$ TeV and $\sqrt{s_{NN}} = 5.02$ TeV are calculated by including both the types of energy losses and the field fluctuations effect. We note that the radiative energy loss alone can describe the D -mesons suppressions at higher transverse momentum. Nevertheless, the nuclear modification factors for both D and B mesons are found to agree quite well with those data in the entire p_T range measured by CMS and ALICE experiments at the LHC energies, if the energy gain due to the field fluctuations is taken into account in addition to the collisional and radiative loss in the medium. We have also calculated the R_{AA} for J/ψ in Au-Au collisions at $\sqrt{s_{NN}} = 200$ GeV and in Pb-Pb collisions at $\sqrt{s_{NN}} = 2.76$ TeV. It is observed that the effect of the field fluctuations can describe the experimental measurements for J/ψ suppression at RHIC and LHC energies. It is also important to note that the effect of the fluctuations has significant impact on η/s of the QGP medium. These fluctuations increase the values of η/s . The obtained values of η/s close to the LQCD and functional renormalization group calculations when the effect of the fluctuations are taken into account. Therefore, the effect of field fluctuations in hot and dense QGP medium is found to play an important role in the propagation of heavy quarks in describing the experimental data for heavy quarks quenching and also to shed light on the transport coefficients e.g., η/s of the QGP medium.

Chapter 4

The LHC and the ALICE Detector

4.1 The Large Hadron Collider (LHC)

The Large Hadron Collider (LHC) at CERN, world's largest and most powerful particle collider, has been installed in a tunnel with a circumference of about 27 km and 50-170 m underground at the Swiss-French border near Geneva city [153]. It can accelerate protons and nuclei at the ultra-relativistic energies and let them collide.

In Fig.4.1, we show a schematic view of the LHC accelerator chain. The particles in two parallel beam pipes travel in two opposite directions. The parallel beam pipes intersect each other at four interaction points (IPs) called collision points. The detectors are installed in experimental caverns at these four collision points: ALICE [154], ATLAS [155], CMS [156] and LHCb [157]. The ALICE experiment is dedicated to study the early universe related to BigBang; the ATLAS and CMS experiments are more specialized to the discovery and precision measurement of new particles like the Higgs boson, Standard Model and Beyond Standard Model particles; the LHCb is a more specialized experiment to be focused on CP violation.

A complex chain of pre-accelerators (Fig.4.1) is used where the protons and ions undergo

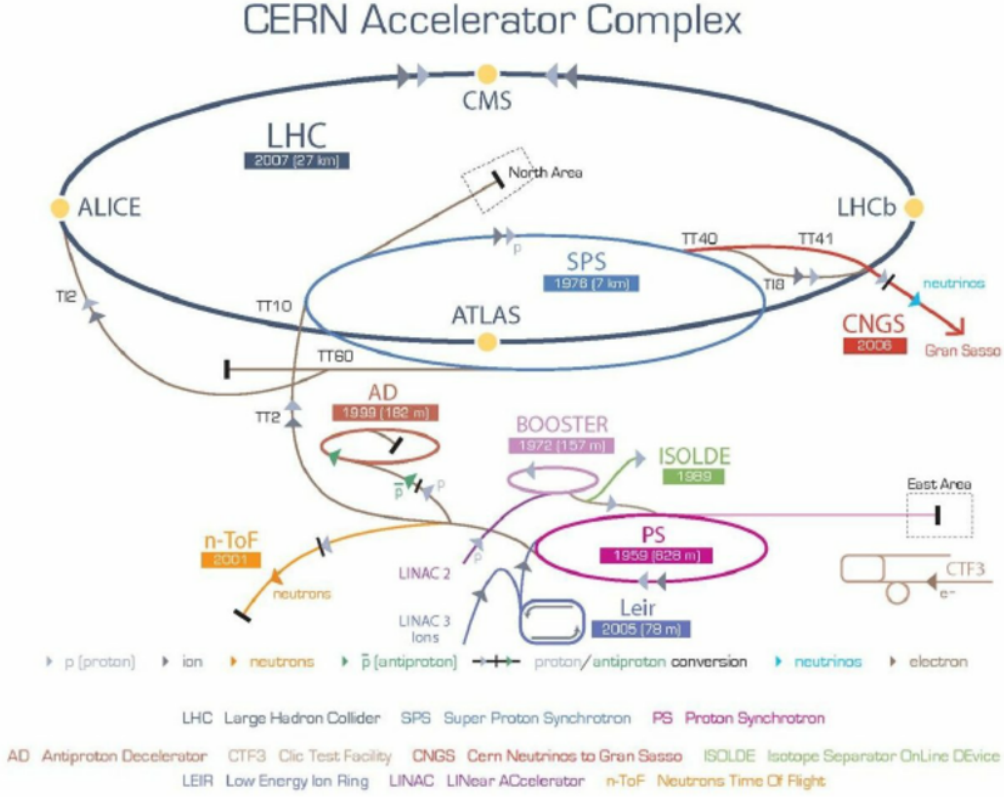


Figure 4.1: Sketch of the LHC accelerator complex and experiments [158].

several pre-acceleration steps before being injected into the main LHC ring. The protons are first accelerated in a linear accelerator (LINAC 2) up to the energy of 50 MeV. After that the protons are subsequently passed to the Proton Synchrotron Booster (PSB), the Proton Synchrotron (PS), and the Super Proton Synchrotron (SPS) where they are accelerated up to the energy of 450 GeV. Finally they are injected to the main LHC ring where the energy is ramped up to the desired energy of collisions. On the other hand, the lead (Pb) ions are first accelerated by a linear accelerator (LINAC 3) up to the energy of 4.2 MeV/n (nucleon). After that the Pb ions are pre-accelerated subsequently in the Low Energy Ion Ring (LEIR), the PS, and the SPS. Finally the Pb ions are filled into the LHC main ring and accelerated up to desired energy of collisions.

4.2 A Large Ion Collider Experiment (ALICE)

ALICE is a dedicated heavy-ion experiment, designed to study the deconfined QCD medium which is believed to present in the early universe, just after BigBang. Besides the heavy-ion program, ALICE has also performed the proton-proton and proton-nucleus asymmetric collisions to shed light on several QCD topics and to understand the results from heavy-ion collisions. In order to achieve its physics goals, ALICE should have a good detector system which must be able to precisely determine particle p_T over a wide range (0.15 - 100 GeV/c), accurate particle identification down to low p_T , maintain its performance in a high-multiplicity environment, etc.

Keeping these in mind, ALICE attributes a central barrel tracking detector at mid-rapidity, a forward muon spectrometer and a variety of other detectors. The detector system is immersed in a longitudinal magnetic field $B = 0.5$ T, produced by solenoid magnet, which bends particle trajectories to measure their momentum. Figure 4.2 shows a schematic view of the ALICE detector system where each sub-detectors are labelled by numbers.

THE ALICE DETECTOR

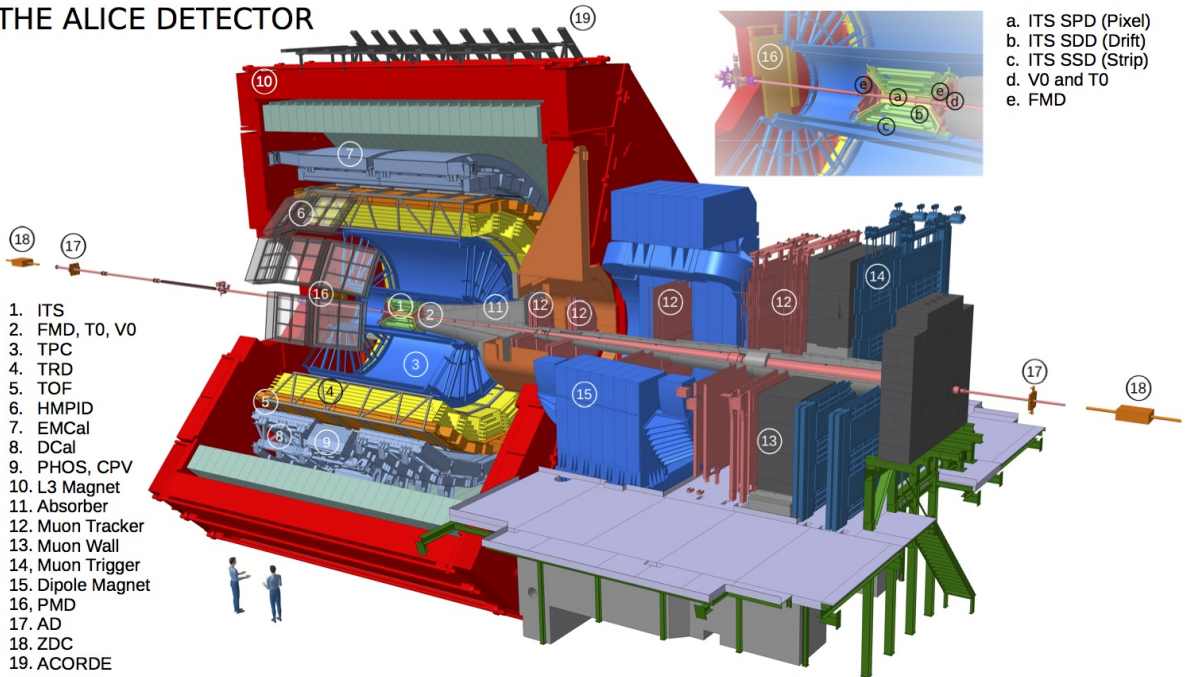


Figure 4.2: A schematic view of the ALICE detector [159].

In a typical high energy collision experiment, the produced particles are identified by the characteristic signatures they leave in the detector setup while passing through the detector. The different sub-detectors are arranged sequentially from the collision point outwards in such a way that the particles first face the tracking system, then a calorimeter (electromagnetic (EM) and/or hadronic) and finally a muon system. The main ALICE tracking system consists of an Inner Tracking System (ITS) of 6 silicon layers used for primary and secondary vertex determination, followed by a large-volume gaseous detector, Time Projection Chamber (TPC), surrounding the ITS. Beside tracking, the ITS and TPC have excellent particle identification (PID) capabilities. After TPC, two full-azimuth PID detectors are present: one is Transition Radiation Detector (TRD) which is used for electron identification and another one is Time-Of-Flight (TOF) detector, used for identification of pion, kaon and proton. The high p_T (3 - 5 GeV/ c) particle identification is done with the High-Momentum Particle Identification Detector (HMPID) which measures the Cherenkov light patterns generated by fast particles. The Photon Spectrometer (PHOS) is an electromagnetic calorimeter which is a small-acceptance and high-granularity detector designed for the precise measurement of photons. The large acceptance calorimeter is the Electromagnetic Calorimeter (EMCal), used also for jet reconstruction and identification of electrons, photons and neutral pions (π^0). Another calorimeter called Di-jet Calorimeter arm (DCal), similar to EMCal, has been installed on the opposite side of the EMCal to perform the jet correlation measurements.

The Zero Degree Calorimeters (ZDC) are located about 113 m away on both sides of the interaction point in order to access the collision centrality, measure the number of spectators. The Time Zero (T0) detector, consisting of two arrays of Cherenkov counters, measures the starting time of a collision which is then used in TOF to calculate particles time-of-flight. It can also give approximate position of primary vertex (with a precision ± 1.5 cm). VZERO (V0) detector is a small angle detector, composed of two arrays of scintillators (V0A and V0C). The V0A and

V0C serve as minimum bias triggers and help in the determination of centrality. The Forward Multiplicity Detector (FMD) and Photon Multiplicity Detector (PMD) measures the charged-particle multiplicity and photon multiplicity respectively, in the forward-rapidity region. The muon spectrometer (MCH) is used to identify muons for open heavy flavor and quarkonia measurements in the pseudo-rapidity range of $-4 < \eta < -2.4$. It consists of a dipole magnet, an absorber, a tracking chambers, a muon filter and trigger chambers (MTR).

The analysis presented in this thesis, i.e., the heavy-flavor (here, mainly b -jet) jet measurement, uses the charged tracks that are detected by the tracking system (ITS and TPC). With these charged tracks, ITS is used to reconstruct the decay topology, through the determination of the primary and secondary vertices. The TPC dE/dx and TOF information is used for PID. For trigger purpose and primary vertex estimation, the T0 and V0 detector is used. The further details of the sub-detectors used in this thesis work is presented in the following sections.

4.2.1 ALICE Tracking System

Inner Tracking System (ITS)

The ITS is one the most important ALICE central barrel detector is placed close to the beam axis. The main tasks of ITS are to localize the primary vertex with a resolution better than $100 \mu\text{m}$, to reconstruct the secondary vertices from the shortly lived particles like hyperons, B and D meson decays and tracking of charged particles (with $p_T < 200 \text{ MeV}/c$) which traverse the dead zones of the TPC. It also improves the momentum and angle resolution of particles measured by TPC. Along with that, it allows to measure dE/dx for the particle identification in the low p_T region.

It is composed of six cylindrical layers of silicon detectors (pixel, drift and strip detectors) placed coaxially around the beam pipe, covering the central rapidity region ($|\eta| < 0.9$). The six cylindrical layers are grouped into three pairs as shown in Fig.4.3: two layers of each, the Silicon

Pixel Detector (SPD), Silicon Drift Detector (SDD) and Silicon Strip Detectors (SSD).

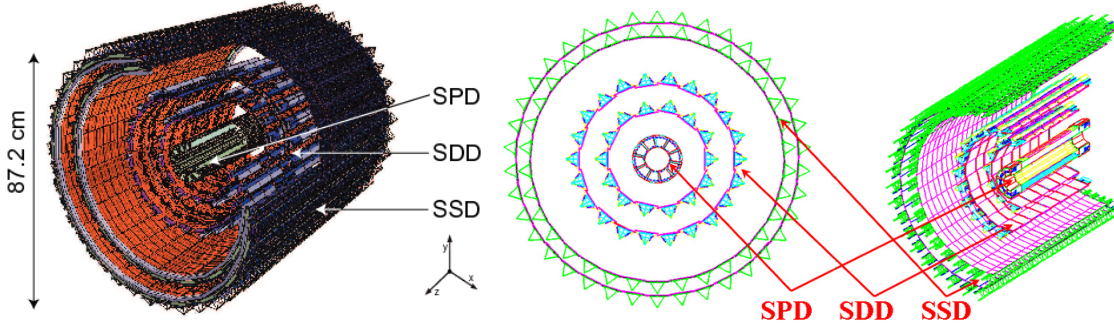


Figure 4.3: A general layout of the ALICE Inner Tracking System (ITS) [160].

The innermost and most crucial layers, the SPD (covers $|\eta| < 2$) is located at an average distance of 3.9 cm and 7.6 cm from the beam axis, respectively. It operates in a region of very high track density, 50 tracks/cm² and very high radiation levels. Each SPD module contains a two-dimensional sensor matrix of reverse-biased silicon detector diodes. For large acceptance coverage and high granularity, there are almost 9.8 million pixel cells.

The SDD is the two intermediate layers of the ITS, located at average radii of 15.0 cm and 23.9 cm respectively from beam axis. The SDD sensor is divided into two drift regions, where electrons move in opposite directions. The biasing of the collecting region is kept independent of the drift voltage by using a second bias supply. The charges are collected in each drift region with the anodes. The two-dimensional points of a track passing through the detector are reconstructed by the drift time of the charges in one direction and the anode segmentation in other direction. On the other hand, the signal measured by the SDD is proportional to the energy deposited by the particles which makes the measurement of specific energy loss dE/dx of the particle which is useful for the particle identification in low p_T region.

The SSD, two outermost layers of the ITS, located at average radii of 38 cm and 43 cm respectively from beam axis. Each SSD module is composed of a 1536-strip double-sided silicon sensor. It provides two-dimensional measurement of the track position. It also performs dE/dx

measurements for particle identification in the non-relativistic region along with the measurements provided by the SDD.

Time Projection Chamber (TPC)

The ALICE TPC, a large volume gas detector, is the main tracking device of the ALICE detector setup. It performs tracking, momentum measurement of charged particles, particle identification by measuring energy loss dE/dx and secondary vertex determination of strange particle decays.

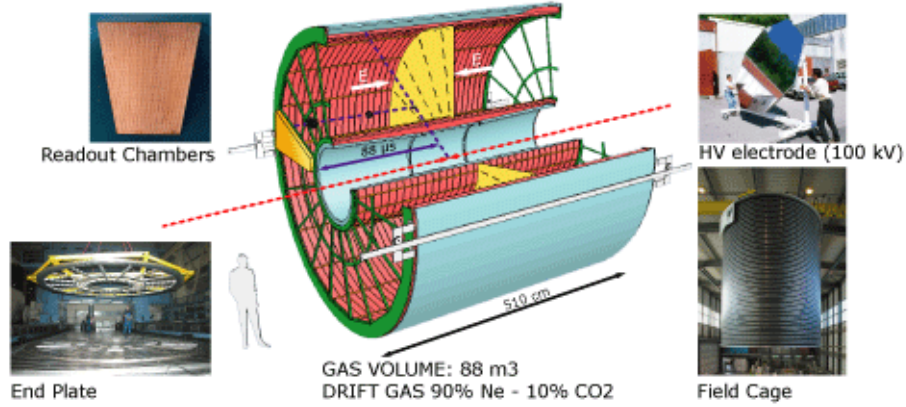


Figure 4.4: The 3D layout of ALICE TPC [161].

Fig.4.4 depicts the 3D layout of ALICE TPC. Its construction is: it is 510 cm long along beam pipe, with an inner and outer radius of 90 cm and 250 cm respectively. The total inner volume (88 m^3) is full of a gas mixture (mainly 90/10 of Ne- CO_2) – which is the actual detector volume. It covers a pseudo-rapidity range of $|\eta| < 0.9$ and full range of azimuth. In order to obtain a good position resolution, TPC field cage provides stability and extremely precise positioning of the end-cap read-out pads.

The central electrode in the TPC is charged to 100 kV, which separates the TPC-drift volume into two segments and creates an electric field of 400 V/cm parallel to the beam line directed

towards the membrane. When a charged particle passes through the detector active volume, it ionizes the gas volume along its trajectory. The electrons liberated in the process of ionisation drift towards the end-plates along the beam axis at an average drift velocity of 2.7 cm/s. The end-plates are equipped with Multi-Wire Proportional Chambers (MWPCs) segmented into 72 readout pads. The x-y positions of the tracks are obtained from the hit points on the anode-pads at the end-plates. The z-coordinates of the tracks are reconstructed based on the information of drift velocity and arrival time of the liberated electrons at the anode plane relative to some external reference (say collision time of the beams). Thus the x, y and z positions of the tracks are measured, and the position resolution is about 800-1100 μm in the transverse plane and 1100-1250 μm along the z-direction.

4.2.2 Particle Identification

Energy loss dE/dx measurement in the TPC:

The measurement of specific energy loss of charged particles (dE/dx) in the detector active volume can be done from the charge collected in TPC read-out pads. The dE/dx of charged particle travelling through a medium is well described by Bethe-Block formula [162]. This dE/dx of particles along the trajectory is measured by the magnitude of the signals induced by the particles. A typical rigidity (momentum/charge) dependence dE/dx spectrum has different bands corresponding to different masses viz. the different particles.

For an example, Fig.4.5 shows the measurement of dE/dx in pp collisions at $\sqrt{s} = 7$ TeV. It is observed that, at $p \lesssim 1$ GeV/ c , the particles are distinguished on a track-by-track basis. At higher momenta, particles are separable on a statistical basis with multi-Gaussian fits. This method offers the measurement of p_T spectra of identified particle up to ~ 20 GeV/ c .

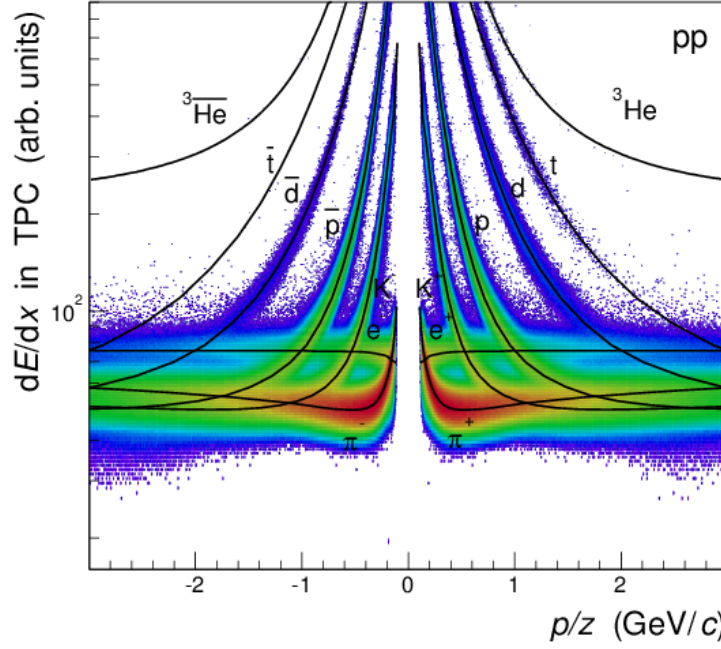


Figure 4.5: Specific energy loss (dE/dx) as a function of rigidity (momentum/charge) for TPC tracks from pp collisions at $\sqrt{s} = 7$ TeV. The solid lines refers to the Bethe-Block curve [163].

Time Of Flight (TOF):

In order to identify particles in the intermediate p_T , ALICE uses the technique of time-of-flight measurement. It is based on the measurement of flight time (t) taken by a particle to traverse a known distance along the track trajectory. With a given momentum and known distance, mass of the particle can be calculated. The use of Multi-gap Resistive Plate Chambers (MRPCs) makes possible the TOF measurement of the flight time of individual particles with a very good precision (~ 100 ps). The start time for the TOF is taken from T0 detector (arrays of Cherenkov counters). The TOF has the particle identification capabilities in the intermediate p_T (0.5 - 2 GeV/ c) for pion and kaons, and up to 4 GeV/ c for protons.

Fig.4.6 shows the performance of the TOF detector. It measures the particle velocity (β) as a function of rigidity (momentum (p)/charge (z)). This shows the separation among the particles as a function of momentum.

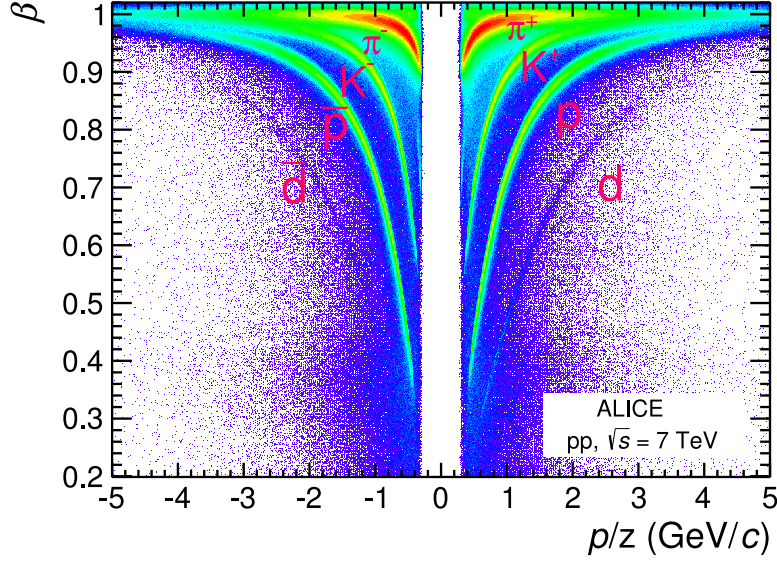


Figure 4.6: Particle velocity (β) as a function of rigidity (momentum/charge), measured by TOF detector from pp collisions at $\sqrt{s} = 7$ TeV [164].

4.2.3 Electromagnetic Calorimeter (EMCal)

The ALICE EMCal is the lead-scintillator sampling calorimeters with large acceptance. It is designed to measure direct photons and decay photons (decay predominantly from π^0 and η mesons and neutral hadrons), electrons and positron over a large range in energy. The working principle of the calorimeter is that the electrons, positrons and photons produce electromagnetic showers in the calorimeter and deposit their energies. Now photons can be distinguished from electrons, positrons by extrapolating the charged particle tracks from tracking system to the EMCal, since photons leave no track in the tracking systems. Also the direct photons can be distinguishable from decay photons by analyzing the transverse shape of the electromagnetic shower.

The detection of neutral hadrons via decay photons in the EMCal provides a more precise measurement of the jet energy scale. So the charge measurements get improved by adding the neutral constituents. Though the full jet measurement is beyond of this dissertation. Also EMCAL along with DCAL makes hadron-jet and/or jet-jet high precision correlation measurements. Further-

more, the EMCal can identify electrons by determining the ratio p/E (where p is the momentum, measured by the tracking system and E is the energy, measured by the calorimeter).

4.2.4 VZERO (V0) Detector

The V0 detector is a forward detector consisting of two arrays of 32 scintillator counters set on the both sides of the interaction point, called V0A and V0C. The scintillating light is collected by photomultipliers (PMTs) through Wave-Length Shifting (WLS) fibres. The V0A and V0C are located at 330 cm and 90 cm away from the primary vertex respectively. They cover the pseudo-rapidity ranges of $2.8 < \eta < 5.1$ (V0A) and $-3.7 < \eta < -1.7$ (V0C) which has been displayed in Fig.4.7.

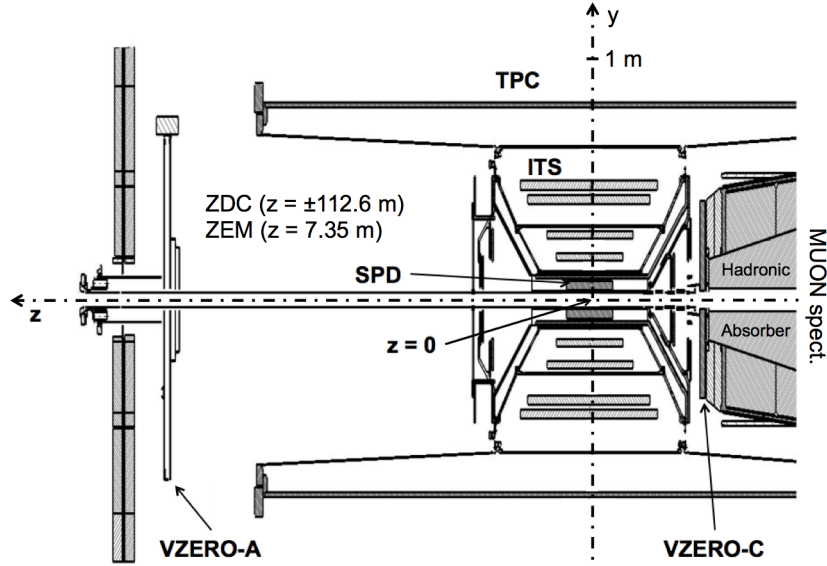


Figure 4.7: Position of the two V0 detectors in the ALICE detector setup [165].

The V0 detector is dedicated to provide a minimum bias trigger for the central barrel detectors. It also discriminates the beam-gas interactions by correlating V0A and V0C timing. Furthermore, it estimates the collision centrality and event plane by V0A and V0C amplitudes as well as it measures the charged particle multiplicity density.

4.2.5 TZERO (T0) Detector

The T0 detector consists of arrays (T0A and T0C) of photomultipliers (PMTs) equipped with Cherenkov radiators, located on the opposite sides of the interaction point. The T0 covers the pseudo-rapidity coverages of $4.5 < \eta < 5$ and $-3.3 < \eta < -2.9$. The position of the T0 detector inside ALICE detector setup has been shown in Fig.4.8. T0 provides fast timing signals which is used in the L0 trigger for ALICE. It also supplies a wake-up call for TRD and to deliver collision time reference for TOF detector. Besides that, T0 can provide approximate vertex position (with a precision ± 1.5 cm) and a very crude estimation of event multiplicity.



Figure 4.8: Position of the T0 detector inside ALICE detector setup [166].

Chapter 5

Measurement of Inclusive b-Jets in p-Pb Collisions

In ultra-relativistic high energy collisions, the heavy quarks are produced in the early stages via hard scattering of partons. Like light quarks or gluons, heavy quarks fragment into jets, called heavy-flavor tagged jets. In experiment, the heavy quark content of a jet can be identified by looking for the presence of heavy-flavor hadrons inside the jet. The hadrons containing heavy quarks have sufficient lifetimes ($\sim 10^{-12}$ s), so they travel some distances (\sim few mm) before decaying. The properties of their decay vertices allow us to identify heavy-flavor tagged jets.

The CMS [64, 65] and ATLAS [66] collaborations have measured the heavy-flavor jet production and suppression in heavy-ion collisions. In this chapter, we focus on the measurements of bottom-tagged jets (b -jet) in p-Pb collisions at $\sqrt{s_{NN}} = 5.02$ TeV in ALICE experiment. The proton-nucleus (p-A) collisions are essential to understand the effects that take place in the cold nuclear matter, which serve as a baseline for the measurements done in nucleus-nucleus collisions. Usual measurements of heavy flavor mesons (D , B) reconstructed either directly or via their decay electrons (HFe) provide important information about the jet quenching and collective motion of c

and b quarks (R_{AA} and v_2) within the medium. Reconstruction of jets containing a heavy quark provides in addition the information about the flavor dependence of the fragmentation mechanism. Partonic energy loss is expected to be mass dependent and the corresponding effects should be pronounced for partons with low transverse momentum p_T . Therefore, at the low p_T region, b -jet energy loss might be significantly different from that of light quark jets. The previous measurements of b -jets done in the CMS [64] and ATLAS [66] collaborations are in the high p_T region. At low p_T region, there are no measurements of b -jets in CMS and ATLAS collaborations. The ALICE detectors have excellent particle tracking capabilities in the lower momentum region which allow to identify b -jets relatively up to lower p_T region where the mass dependent energy loss might be pronounced.

This chapter is organized as follows: In Sec. 5.1, we describe the datasets and Monte Carlo productions. Sec. 5.2 describes the the analysis setup and Sec. 5.3 presents the quality assurance of the analysed data. In Sec. 5.4 and Sec. 5.5, we discuss the b -jet tagging efficiency and purity corrections and the de-convolution procedure to correct the measured b -jet spectrum for detector and background effects. Sec. 5.6 is devoted to the systematic uncertainty studies. Finally, we describe the results and the comparison of the results to the NLO pQCD predictions in Sec. 5.7.

5.1 Datasets and Monte Carlo Productions

5.1.1 Production Cycles

In this analysis, we use Run2 p-Pb data at $\sqrt{s_{NN}} = 5.02$ TeV, collected by the ALICE experiment. Details of the corresponding production cycles are given in Table 5.1.

Table 5.1: List of runs from the LHC16q and LHC16t periods [167] used in this analysis. Run numbers are the numbers assigned to each run of the LHC machine during the process of data collection.

Run list	Run number
LHC16q_pass1_CENT_woSDD LHC16q_pass1_FAST	265525, 265521, 265501, 265500, 265499, 265435, 265427, 265426, 265425, 265424, 265422, 265421, 265420, 265419, 265388, 265387, 265385, 265384, 265383, 265381, 265378, 265377, 265344, 265343, 265342, 265339, 265338, 265336, 265334, 265332, 265309
LHC16t_pass1_CENT_woSDD LHC16t_pass1_FAST	267166, 267165, 267164, 267163

5.1.2 PYTHIA+EPOS Simulations

We have used PYTHIA+EPOS Monte Carlo (MC) production anchored in the LHC16q and LHC16t run periods. The simulated events are processed with the detailed model of ALICE detector response based on GEANT3. These MC simulations are used for efficiency and data-driven purity corrections as well as for performance studies. Here PYTHIA is used to calculate the hard processes and EPOS simulates the underlying events (UE). A part of the used MC data sets were generated with enhanced b and c quark production. Further, the MC data for distinguish FAST and woSDD trigger conditions are given in Table. 5.2. When analyzing the events, we have not found any difference between FAST and woSDD data sets. Thus these data sets are merged together.

Simulated events that do not include instrumental effects are labeled as “particle-level”. The MC simulation where particle-level events have passed through a detailed model of the ALICE detector based on GEANT3 and are reconstructed with the same procedures that are used for real data are labeled as “detector-level”.

The simulations are done in six p_T bins:

bin ID	1	2	3	4	5	6
\hat{p}_T [GeV/c]	5-10	10-18	18-30	30-50	50-70	≥ 70

Table 5.2: The analyzed MC data sets. The number of events generated in each hard bin is denoted as $N_{\text{events,hb}}^{\text{raw}}$. The corresponding number of events after physics selection is labeled $N_{\text{events,hb}}^{\text{phys.sel.}}$.

Subset	Enhancement	$N_{\text{events,hb}}^{\text{raw}} (\times 10^6)$	$N_{\text{events,hb}}^{\text{phys.sel.}} (\times 10^6)$
LHC17h6a2_cent_woSDD	bbbar	1.77	1.55
LHC17h6b2_FAST	bbbar	1.79	1.57
LHC17h6c2_cent_woSDD	ccbar	1.79	1.56
LHC17h6d2_FAST	ccbar	1.79	1.57
LHC17h6e2_cent_woSDD	–	6.24	5.46
LHC17h6f2_FAST	–	6.25	5.47

Removal of outliers:

PYTHIA+EPOS MC productions suffer from rare events generated in low \hat{p}_T bins which come with a large weight. These events result in spikes (outliers) in inclusive p_T spectra of charged jets. We introduced an outlier rejection function that removes all events where p_T of a charged jet ($p_{T,jet}^{\text{ch}}$) exceeds a multiple of \hat{p}_T (PYTHIA internal bias on the hardness of the process). An effect of this rejection on the detector-level inclusive p_T spectrum of charged jets can be seen in Fig. 5.1. The total number of events rejected like that in the MC data have been shown in Table. 5.3 and Table. 5.4.

Table 5.3: The total number of input events and the total number of rejected events in hard bins for $p_{T,chjet} > 4\hat{p}_T$.

Hard bin	bbbar		ccbar		jet-jet	
	LHC17h6a2_cent_noSDD LHC17h6b2_FAST $N_{\text{events,hb}}^{\text{raw}}$	Rejected	LHC17h6c2_cent_noSDD LHC17h6d2_FAST $N_{\text{events,hb}}^{\text{raw}}$	Rejected	LHC17h6e2_cent_noSDD LHC17h6f2_FAST $N_{\text{events,hb}}^{\text{raw}}$	Rejected
1		569		701		2447
2		36		33		74
3	3.5×10^6	2	3.5×10^6	1	1.2×10^7	3
4		0		0		0
5		0		0		0
6		0		0		0

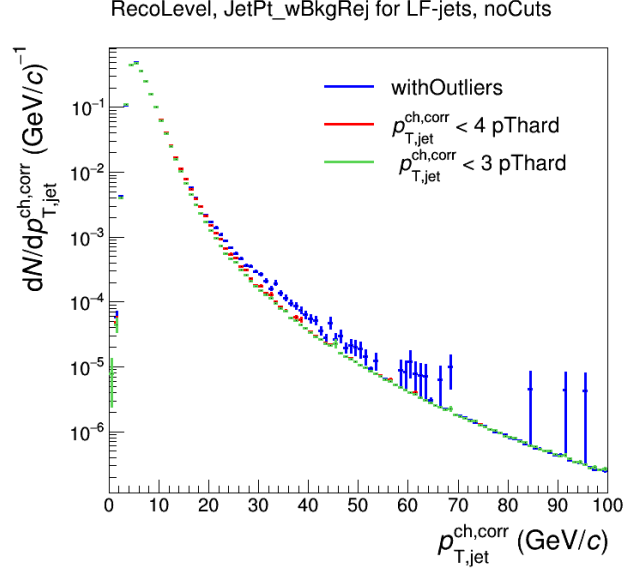


Figure 5.1: . Detector-level inclusive p_T spectrum of charged jets with resolution parameter, $R = 0.4$ as obtained from the MC simulations analyzed with and without outlier rejection. Jet p_T is corrected for the mean underlying event (UE) density. Input sample of jets had UE density uncorrected jet p_T greater than $5 \text{ GeV}/c$.

Table 5.4: The total number of input events and the total number of rejected events in hard bins for $p_{T, chjet} > 3\hat{p}_T$.

Hard bin	bbbar		ccbar		jet-jet	
	LHC17h6a2_cent_noSDD LHC17h6b2_FAST		LHC17h6c2_cent_noSDD LHC17h6d2_FAST		LHC17h6e2_cent_noSDD LHC17h6f2_FAST	
	$N_{\text{events,hb}}^{\text{raw}}$	Rejected	$N_{\text{events,hb}}^{\text{raw}}$	Rejected	$N_{\text{events,hb}}^{\text{raw}}$	Rejected
1	3.5×10^6	2387	3.5×10^6	3036	1.2×10^7	11109
2		120		127		284
3		9		8		11
4		0		0		0
5		0		0		0
6		0		0		0

5.2 Analysis Strategy

The analysis consists of the following major steps:

1. Data are reconstructed from the LHC16t and LHC16q periods, and the jets are reconstructed from reconstructed tracks.
2. The b -jet candidates are tagged using topological variables, in order to extract the raw detector-level b -tagged jet spectrum, $N_b^{tagged}(p_{T,jet}^{ch,det})$ (raw yields vs. detector-level charged jet transverse momentum, $p_{T,jet}^{ch,det}$).
3. Corrections for b -jet tagging efficiency (ϵ_b) and purity (P_b) are established as a function of $p_{T,jet}^{ch,det}$. The ϵ_b is determined using MC (PYTHIA+EPOS) simulation. The P_b is determined using a hybrid method based both on POWHEG (POsitive Weight Hardest Emission Generator) simulations and a data-driven approach. The raw b -tagged jet spectrum, N_b^{tagged} is corrected for the ϵ_b and P_b to get the actual b -jet spectrum as:

$$N_b(p_{T,jet}^{ch,det}) = N_b^{tagged}(p_{T,jet}^{ch,det}) \times \frac{P_b(p_{T,jet}^{ch,det})}{\epsilon_b(p_{T,jet}^{ch,det})} \quad (5.1)$$

4. The corrected spectrum is unfolded and normalized to obtain the b -jet cross-sections as a function of the particle-level charged jet transverse momentum, $p_{T,jet}^{ch}$. The correction for reconstruction is inherent in this step. The response matrix used in unfolding consists of the detector response and a matrix that describes jet momentum smearing due to local background fluctuations (δp_T). The detector matrix is established by reconstructing pure PYTHIA events with the analysis task. The δp_T matrix is obtained from real data using the random cone method.

All the above steps are discussed in details below:

5.2.1 Event Selection

Events are selected with the minimum bias trigger `AliVEvent::kINT7` which requires a time coincidence of the trigger signals from V0A and V0C scintillator arrays. Position of the primary vertex along the beam direction is constrained to $|z_{\text{vtx}}| < 10$ cm which ensures uniform efficiency and acceptance for tracks in the pseudo-rapidity range $|\eta_{\text{track}}| < 0.9$. The total number of events in each hard bin prior and after physics selection is quoted in Table 5.2.

5.2.2 Track Selection

The analysis uses tracks selected by the filter bits $(1 << 4) | (1 << 9)$ which provides uniform distribution of tracks in azimuth. Pseudo-rapidity of accepted tracks is constrained to $|\eta_{\text{track}}| < 0.9$.

The filter bit $(1 << 4) | (1 << 9)$ contains following track cuts:

- `MinNClustersTPC(50)` (Minimum number of cluster in TPC = 50)
- `MaxChi2PerClusterTPC(3.5)` (Maximum χ^2 value per cluster in TPC = 3.5)
- `RequireTPCRefit(kTRUE)` (TPC refit is required)
- `MaxDCAToVertexXY(2.4)` (Maximum distance of closest approach (DCA) in the XY plane to the primary vertex = 2.4 cm)
- `MaxDCAToVertexZ(3.2)` (Maximum distance of closest approach (DCA) to the primary vertex = 3.2 cm)
- `DCAToVertex2D(kTRUE)` (Distance of closest approach (DCA) to the primary vertex is calculated in 2D)
- `RequireITSRefit(kTRUE)` (ITS refit is required)

5.2.3 Jet Reconstruction

The jets are reconstructed from the selected charged tracks using the infrared and collinear safe anti- k_T algorithm with a resolution parameter of $R = 0.4$ using the p_T -recombination scheme as implemented in the FastJet package [168]. The inclusive charged jets have been measured in ALICE experiment for p-Pb collisions at $\sqrt{s_{NN}} = 5.02$ TeV (see, Ref. [169]). The detailed jet finding algorithm is discussed in Appendix A.1. Area of the ghost particles is set to 0.005. The transverse momentum of jet constituents is constrained to $0.15 < p_T < 100$ GeV/ c . The pseudorapidity of analyzed jets is limited to $|\eta_{\text{jet}}| < 0.5$. UE density uncorrected p_T (jet) of b -jet candidates is constrained to the range $5 < p_{T,\text{jet}}^{\text{raw}} < 200$ GeV/ c .

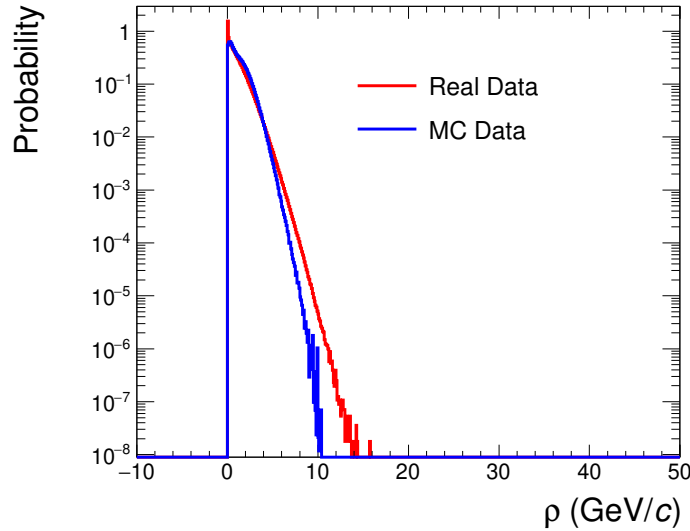


Figure 5.2: Probability distribution of UE density in inclusive events. The MC distribution corresponds to PYTHIA+EPOS detector-level simulation.

The transverse momentum $p_{T,\text{jet}}^{\text{raw}}$ of reconstructed jets at the particle as well as the detector-level is corrected for the average contribution of the UE using the formula,

$$p_{T,\text{jet}}^{\text{reco}} = p_{T,\text{jet}}^{\text{raw}} - \rho A_{\text{jet}}, \quad (5.2)$$

where A_{jet} denotes jet area and ρ is the mean UE density. The mean UE density is estimated on the event-by-event basis employing the CMS modification of the standard area based method [170]:

$$\rho = \frac{A_{\text{physical jets}}}{A_{\text{all jets}}} \times \text{median}_{k_T \text{ physical jets}} \left\{ \frac{p_{T,jet}^{raw}}{A_{\text{jet}}} \right\} \quad (5.3)$$

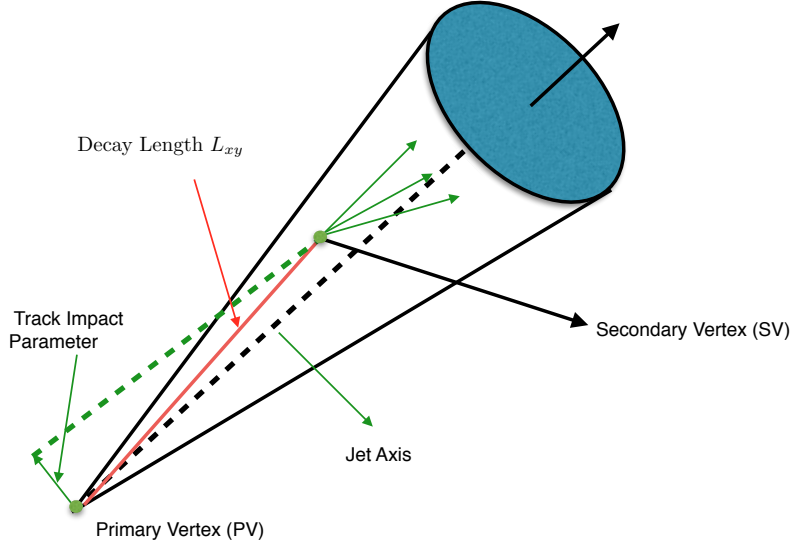
where $A_{\text{physical jets}}$ denotes the total area of jets that contain real tracks and $A_{\text{all jets}}$ is the total area covered by real jets and ghost jets. The median is calculated from k_T jets which have a resolution parameter of $R = 0.4$ and which contain real tracks. Two leading k_T jets are removed while calculating the median, since they might be the signal jets. Fig 5.2 shows a comparison of inclusive ρ distribution from measured data and detector-level simulation.

5.2.4 The b-Jet Candidate Identification (Secondary Vertex Tagging)

On the detector level, a b -jet candidate is identified by means of reconstruction of a displaced secondary vertex (SV) within the jet. The SV is reconstructed from jet constituents and is required to have 3 tracks. If several SV candidates are found, the analysis considers only the most displaced SV within the jet. A sketch of a b -jet is shown in Fig. 5.3.

Discriminating variables exploit properties of beauty-hadron decays determined by their long lifetimes and large masses. The following variables can be used to find b -jet candidates:

- $SL_{xy} = L_{xy}/\sigma_{L_{xy}} > \text{cut on significance}$, where L_{xy} is the projection of the distance of the reconstructed SV from the primary vertex on the XY plane and $\sigma_{L_{xy}}$ is the resolution of L_{xy} . The distributions of L_{xy} on a given p_T are characteristic to each flavor. However, there is a pronounced p_T dependence of L_{xy} variable. The significance SL_{xy} shows much less dependence on p_T , at least if the cut is not too low. Therefore it is favorable to use SL_{xy} instead of L_{xy} to achieve a relatively constant efficiency and purity in p_T .

Figure 5.3: A sketch of a b -jet.

- $\sigma_{SV} < \text{cut on SV resolution}$, where the SV resolution is calculated as,

$$\sigma_{SV} = \sqrt{\sum_{i=1}^3 d_i^2},$$

where d_i are the closest approaches of the tracks (used to reconstruct SV) to the SV in 3D.

As it turns out, σ_{SV} has a discrimination power only if a cut on SL_{xy} is applied.

5.3 Data Quality Assurance (QA)

5.3.1 Tracks and Jets

Figs. 5.4, 5.5 and 5.6 show a comparison of basic hybrid track η , ϕ and p_T distributions from the real data and the corresponding PYTHIA+EPOS detector-level simulation. Similar distributions for inclusive jets are presented in Figs. 5.7, 5.8, and 5.9. In general, we see good agreement between MC and the measured data. The right panel in Fig. 5.6 shows track reconstruction efficiency as obtained from the PYTHIA+EPOS MC simulation.

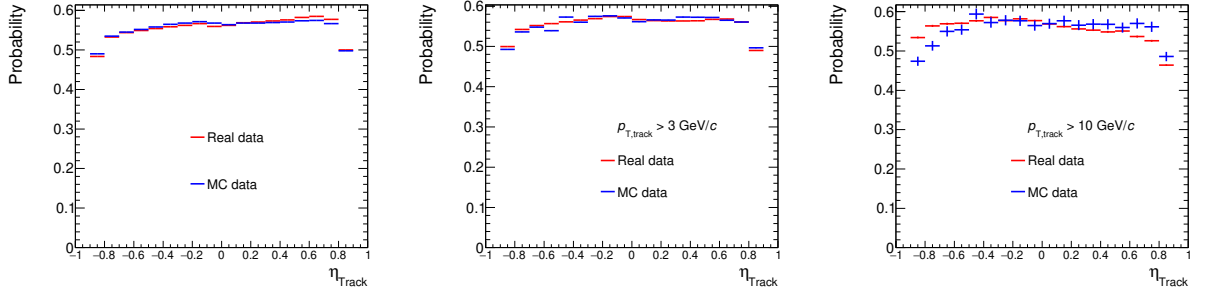


Figure 5.4: Distribution of hybrid tracks as a function of pseudorapidity for real data and PYTHIA+EPOS detector-level simulations. Distributions are normalized by their integral. Left: inclusive tracks, Middle: tracks with $p_T > 3 \text{ GeV}/c$, Right: $p_T > 10 \text{ GeV}/c$.

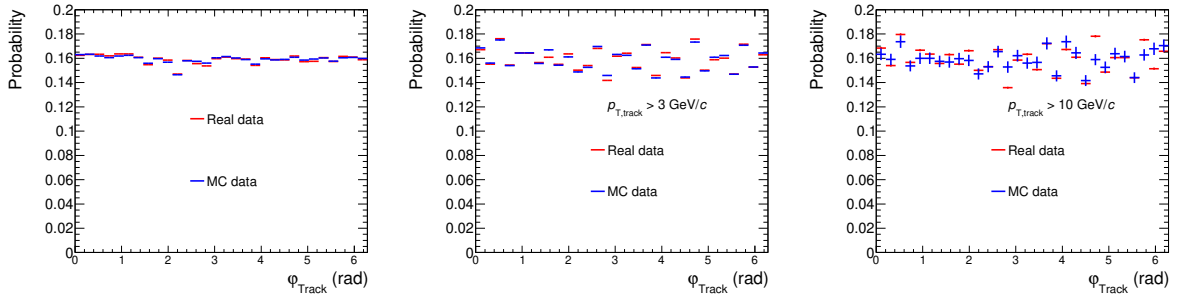


Figure 5.5: Distribution of hybrid tracks as a function of azimuth for real data and PYTHIA+EPOS detector-level simulations. Distributions are normalized by their integral. Left: inclusive tracks, Middle: tracks with $p_T > 3 \text{ GeV}/c$, Right: $p_T > 10 \text{ GeV}/c$.

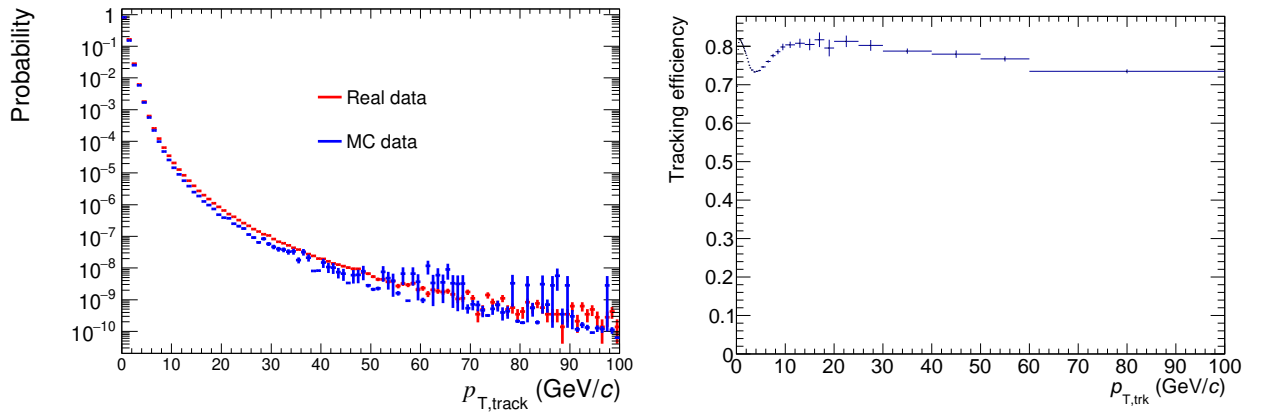


Figure 5.6: Left: Inclusive p_T spectrum of hybrid tracks from real data and PYTHIA+EPOS detector-level simulations. The distributions are normalized by their integral. Right: Reconstruction efficiency of hybrid tracks as obtained from PYTHIA+EPOS simulations.

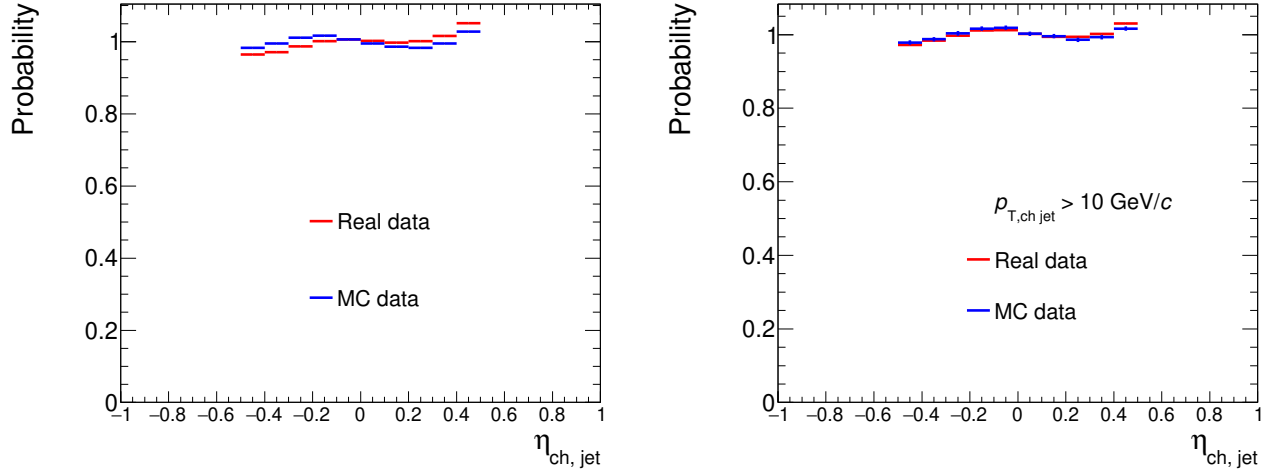


Figure 5.7: Distribution of charged anti- k_T $R = 0.4$ jets as a function of pseudorapidity for real data and PYTHIA+EPOS detector-level simulations. Distributions are normalized by their integral. Left: inclusive tracks, Right: $p_T > 10$ GeV/ c .

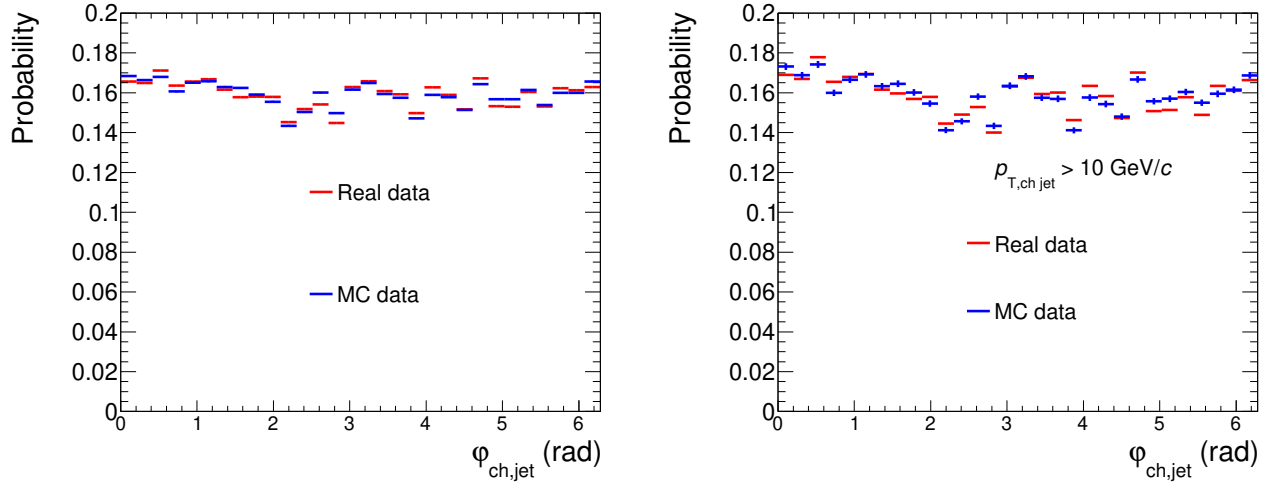


Figure 5.8: Distribution of charged anti- k_T $R = 0.4$ jets as a function of azimuth for real data and PYTHIA+EPOS detector-level simulations. Distributions are normalized by their integral. Left: inclusive tracks, Right: $p_T > 10$ GeV/ c .

5.3.2 QA of SV Tagging Cuts

Figs. 5.10, 5.11, 5.12 and 5.13 show a comparison of SL_{xy} and σ_{SV} distributions from the real data and from the detector-level of the PYTHIA+EPOS simulation. Definition of the topological cuts on SV can be found in Sec. 5.2.4.

In general, the MC adequately describes the trends seen in the data. However, certain differences

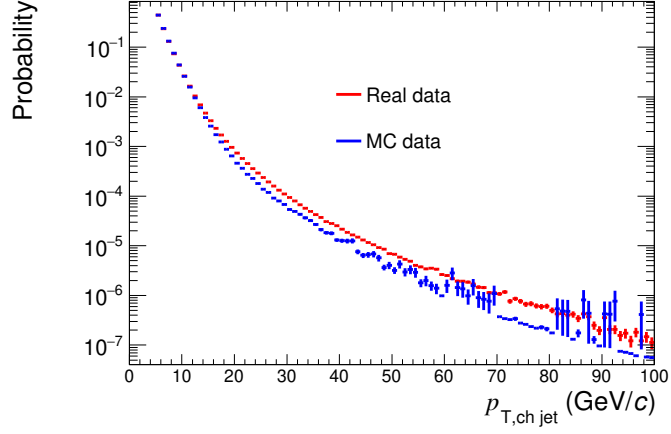


Figure 5.9: Inclusive p_T spectrum of charged anti- k_T $R = 0.4$ jets from real data and PYTHIA+EPOS detector-level simulations. The distributions are normalized by their integral.

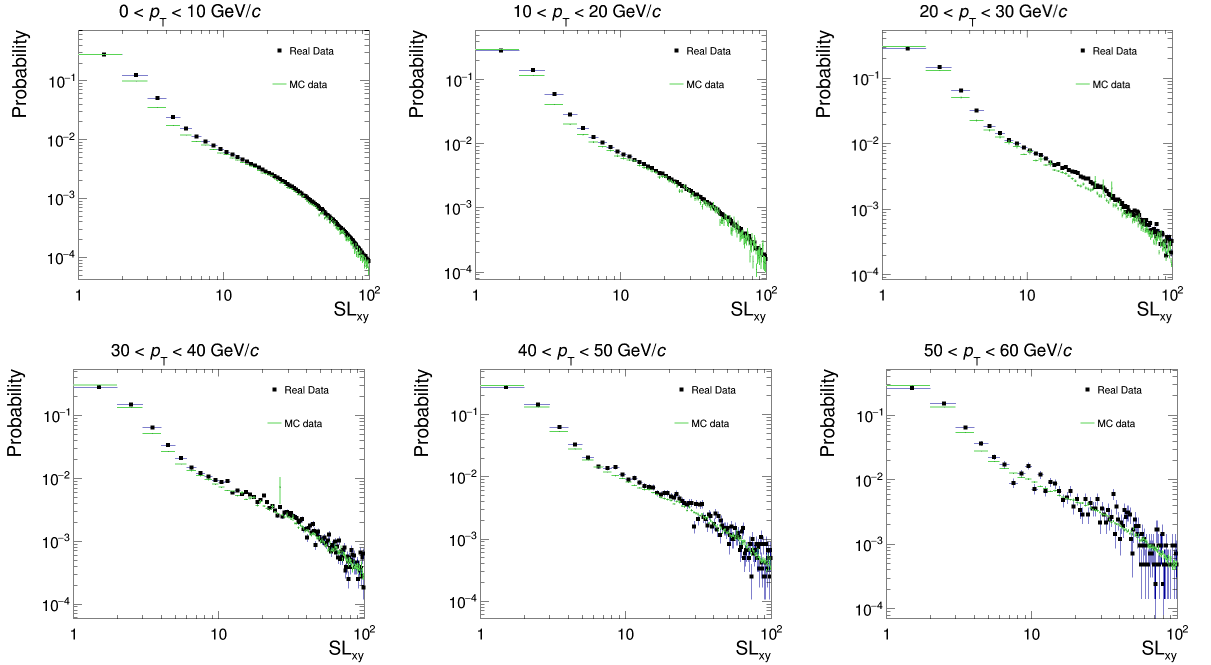


Figure 5.10: Distribution of SL_{xy} (no cut on σ_{SV}) in real data and in PYTHIA+EPOS detector-level simulations. Distributions are normalized by their integral.

can be seen. Problematic regions include low SL_{xy} values ($SL_{xy} \leq 3$) and low σ_{SV} values ($\sigma_{SV} \leq 0.02$ cm, after the application of the SL_{xy} cut). The topological cuts are optimized such that those regions are avoided. In addition, we avoid the regions of rapidly changing signal-to-background ratios (See Appendix A.3). The final fully corrected results are fairly independent of

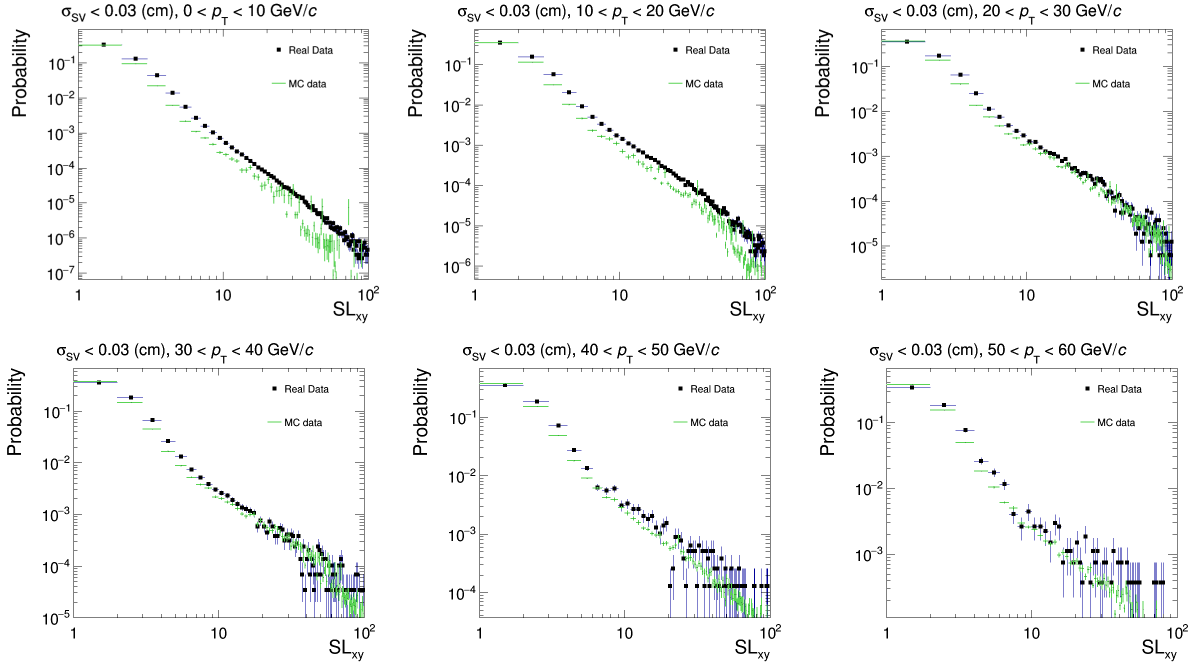


Figure 5.11: Distribution of SL_{xy} for $\sigma_{SV} < 0.03$ cm in real data and in PYTHIA+EPOS detector-level simulations. Distributions are normalized by their integral.

the choice of the tagging cuts. The rest of the variations are within statistical uncertainties by far (Sec. 5.6.1). The only exception is the spectrum obtained with the $\sigma_{SV} < 0.02$ cm cut that shows a deviating trend, but still within one σ . This difference is considered as systematics.

5.4 Corrections

The tagging procedure is performed by using the topological cuts (SL_{xy} and σ_{SV}) as discussed in Sec. 5.2. Each set of cut on SL_{xy} and σ_{SV} gives different performances of the tagging algorithm. The tagging efficiency and the purity are dependent on these cuts and we will discuss this later. It is clear that some optimizations for the tagging cuts are required for the analysis. In order to find the best working point of tagging cuts for significance (or signal-to-background ratio), we carried out one and two-dimensional studies. These are discussed in details at the Appendix A.3. The tagging cuts chosen for the principal analysis are $SL_{xy} > 7$ and $\sigma_{SV} < 0.03$ cm.

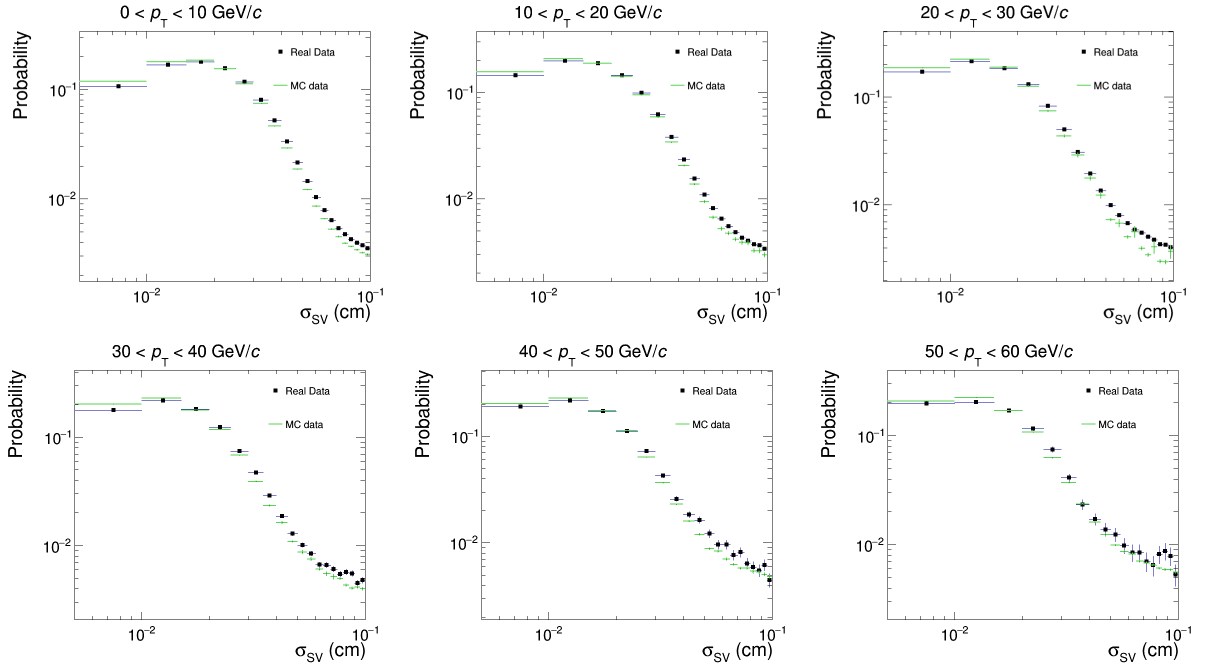


Figure 5.12: Distribution of SV dispersion (no cut on SL_{xy}) in real data and in PYTHIA+EPOS detector-level simulations. Distributions are normalized by their integral.

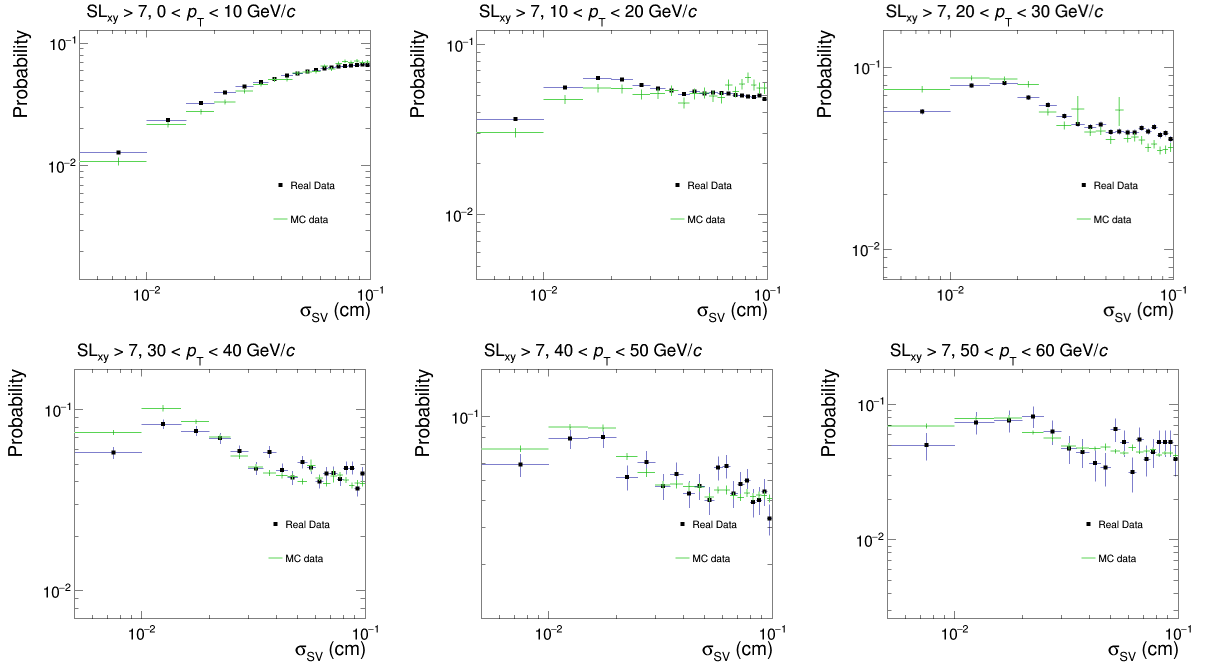


Figure 5.13: Distribution of SV dispersion for SV passing the cut $SL_{xy} > 7$ in real data and in PYTHIA+EPOS detector-level simulations. Distributions are normalized by their integral.

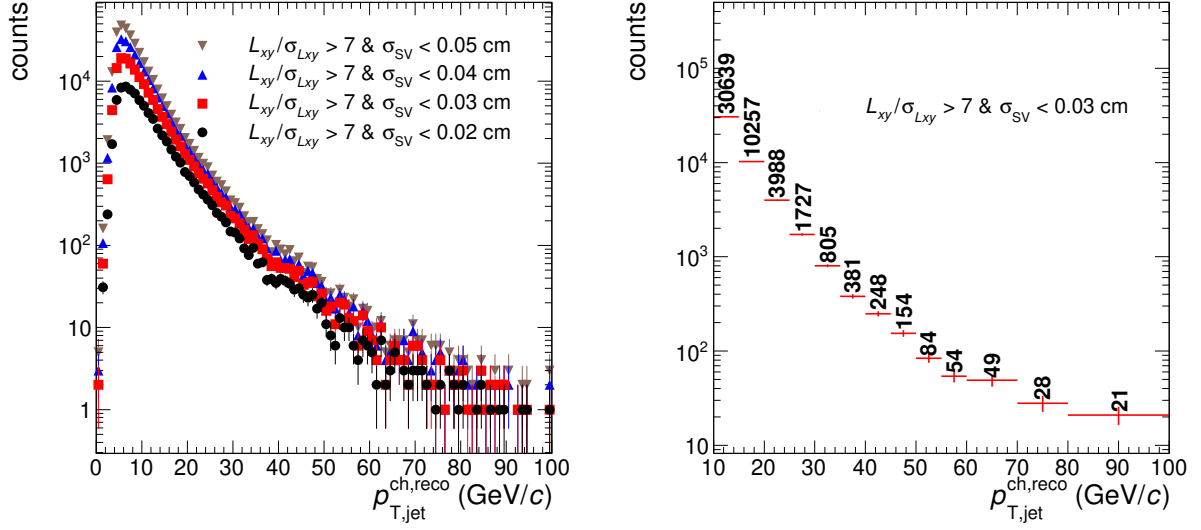


Figure 5.14: Left: Example of raw inclusive p_T spectra of b jets for $SL_{xy} > 7$ and varying cut on σ_{SV} . Bin width is 1 GeV/c. Right: Rebinned raw spectrum for $SL_{xy} > 7$ and $\sigma_{SV} < 0.03$ cm which is used as input to unfolding. The numbers show the number of counts in given bin.

Fig. 5.14 shows examples of raw inclusive p_T spectra of b -jet candidates before correction for the b -jet tagging efficiency and purity. Now, the spectra of b -jet can be obtained from b -jet candidates after correcting for tagging efficiency and purity using Eq. 5.1.

The b -jet tagging efficiency and purity are discussed in the following sections:

5.4.1 The b -Jet Tagging Efficiency

The efficiency ε_b of the b -jet tagging is estimated based on the detector-level simulation as,

$$\varepsilon_b(p_{T,jet}^{reco}) = \frac{N_{b\text{ jets}}^{\text{selected}}}{N_{b\text{ jets}}^{\text{all}}}, \quad (5.4)$$

where $N_{b\text{ jets}}^{\text{all}}$ is the total number of detector-level true b -jets before imposing any topological cut on the parameters of the SV (σ_{SV} and SL_{xy}) and $N_{b\text{ jets}}^{\text{selected}}$ denotes the number of b -jets after applying the topological cuts (σ_{SV} and SL_{xy}). The mistagging efficiency (mistagging rate) for this analysis is the efficiency of mistakenly tagged a jet as b -jet which is actually c -jet or light flavor jet.

In other words, mistagging efficiency is c -jet or light flavor jet tagging efficiency. The estimation of mistagging efficiency is important since higher mistagging rate increases the contamination due to other flavor jets in the tagged b -jet sample and affects the purity of b -jet sample.

The b -jet tagging efficiencies for different cut selections are shown in Fig. 5.15. The Fig. 5.16 presents mistagging efficiency of c -jet and light-flavor jet versus b -jet tagging efficiency.

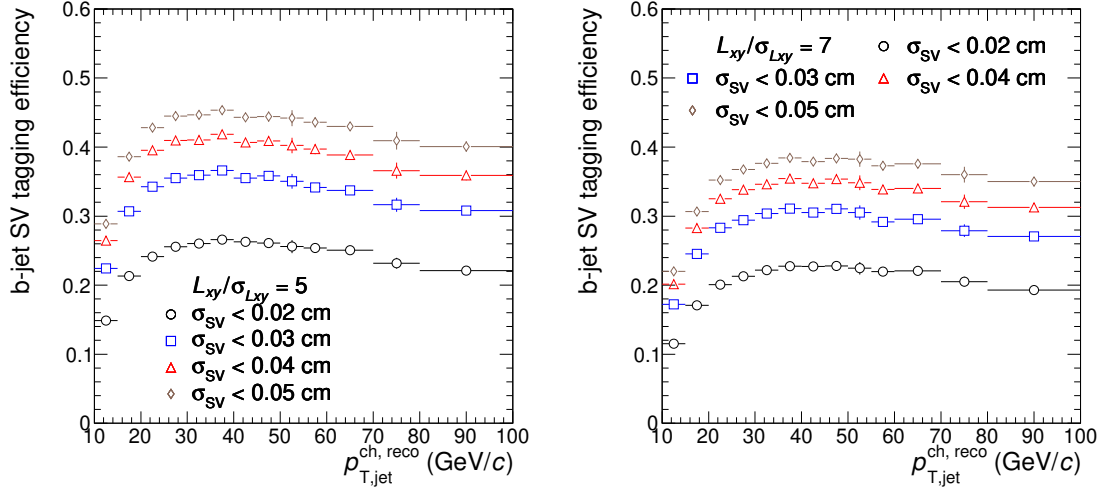


Figure 5.15: b -jet tagging efficiency as a function of jet p_T for $SL_{xy} > 5$ and 7 and different choices of the σ_{SV} cut.

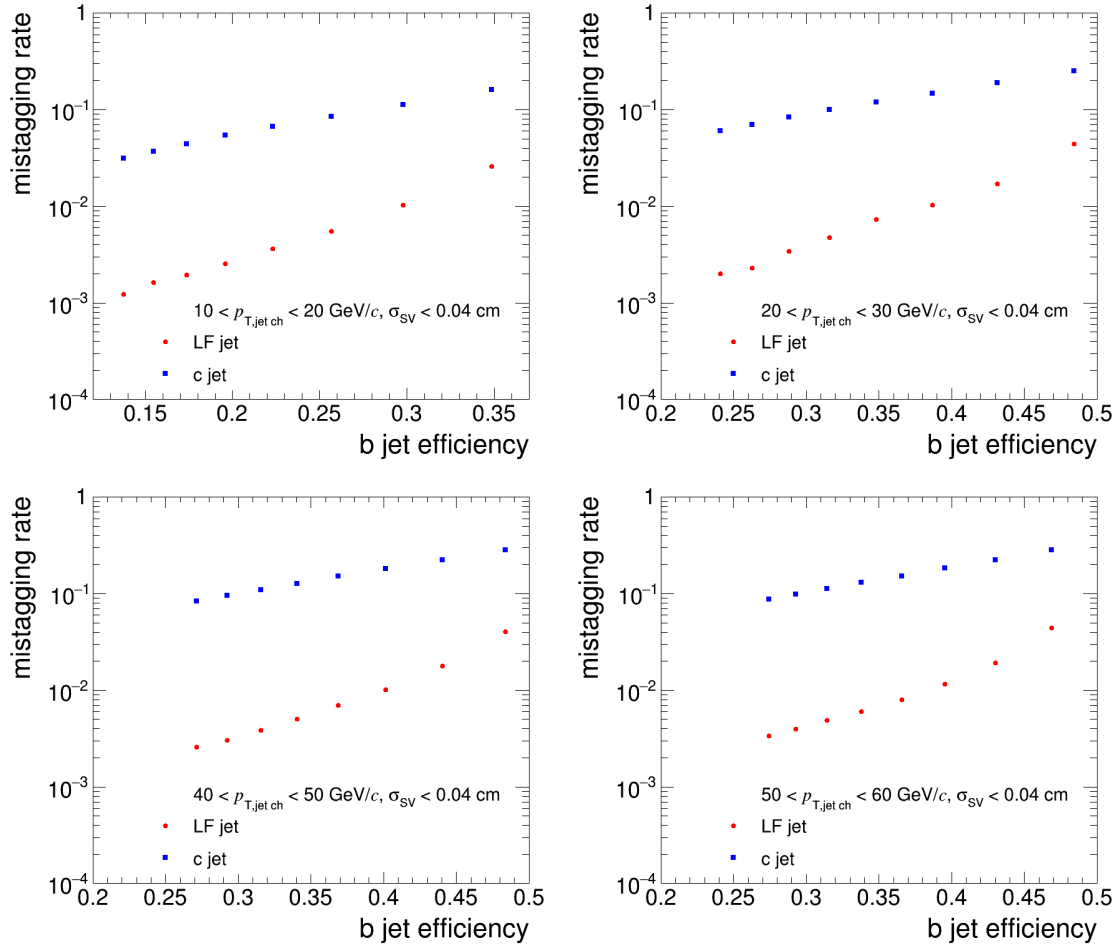


Figure 5.16: Mistagging efficiency of c -jet and light-flavor jet versus b -jet tagging efficiency for a fixed $\sigma_{SV} < 0.04$ cm cut and several choices of SL_{xy} ($> 3, 4, 5, 6, 7, 8, 9, 10$).

5.4.2 Purity of the Tagged b -Jet Sample

POWbc Method:

Purity of a tagged b -jet sample gives the fraction of detector-level true b -jets among all detector-level jets that are tagged as b -jets. In our analysis, the purity of tagged b -jet sample is obtained based on a POWHEG+PYTHIA MC simulation. POWHEG [171, 172, 173] is a NLO model that calculates hard QCD processes. Details of POWHEG events are given in the Appendix. A.2.

In our approach, b -jet and c -jet particle-level spectra are first generated by POWHEG+PYTHIA. Each of these spectra is then folded with the corresponding response matrix that accounts for local background fluctuations (δp_T matrix) and instrumental effects (detector jet response matrix obtained for b -jets or c -jets from the PYTHIA filtered simulations). In this way, the particle-level spectrum is converted to the corresponding detector-level spectrum. Subsequently, the purity of the b -jet sample is calculated as,

$$P_b = \frac{N_b \epsilon_b}{N_b \epsilon_b + N_c \epsilon_c + N_{lf} \epsilon_{lf}}, \quad (5.5)$$

where, ϵ_b , ϵ_c , and ϵ_{lf} are the SV tagging efficiencies for b -jets, c -jets and light flavor jets, respectively, obtained from the PYTHIA+EPOS simulations (LHC17h6a2+LHC17h6b2, LHC17h6c2+LHC17h6d2 and LHC17h6e2+LHC17h6f2). The numbers of b -jets and c -jets, obtained from POWHEG+PYTHIA simulations and expressed in terms of cross sections, are denoted as N_b and N_c , respectively. The number of light-flavor jets, N_{lf} , is obtained by subtracting the N_b and N_c from the raw inclusive jet p_T spectra from the real data (LHC16q and LHC16t) which is again expressed in terms of cross-section.

Fig. 5.17 shows the purity of b -jets obtained by the SV tagging as a function of jet p_T . The estimated purities are by construction, dependent on the SV tagging efficiencies. This correlation

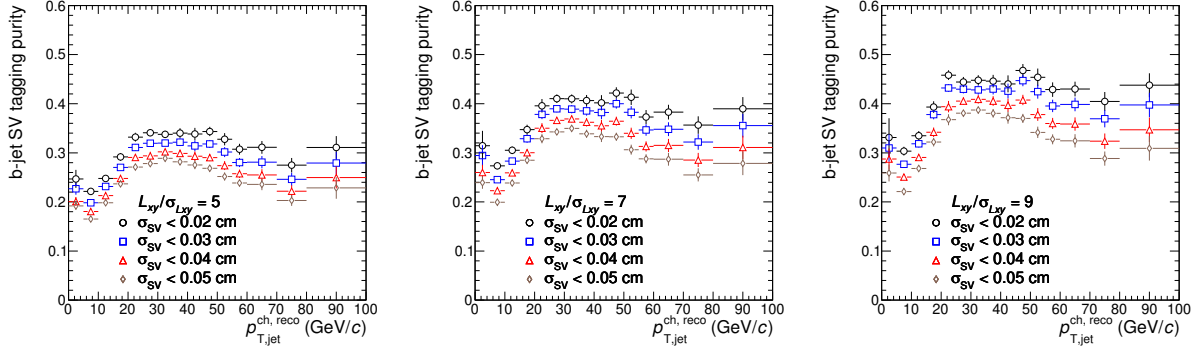


Figure 5.17: b -jet tagging purity as a function of jet p_T for $SL_{xy} > 5, 7$ and 9 and different choices of the σ_{SV} cut. The purity is assessed with the default POWHEG settings.

has to be taken into account when evaluating the ratio P_b/ε_b in Eq. (5.1). The ratio is shown in

Fig. 5.18.

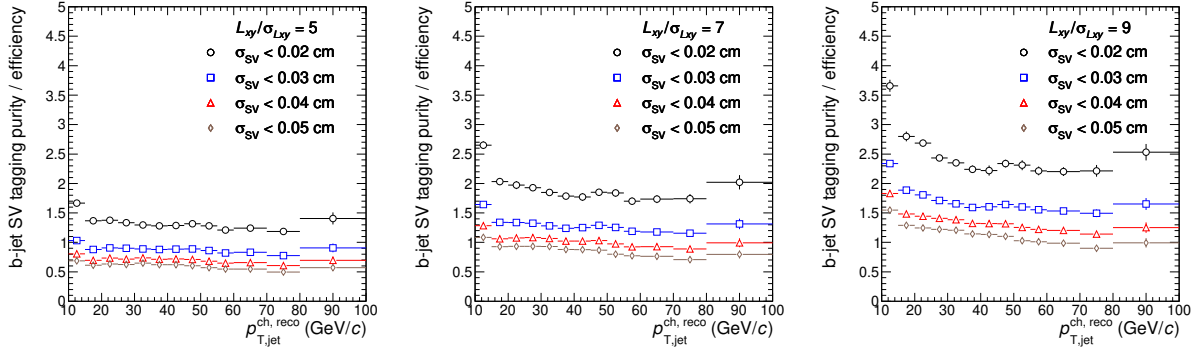


Figure 5.18: Ratio of b -jet tagging purity to b -jet tagging efficiency as a function of jet p_T for $SL_{xy} > 5, 7$ and 9 and different choices of the σ_{SV} cut. The purity is assessed with the default POWHEG settings.

SV Invariant Mass Template Fit Method:

The template fit method is based on parameterization of the measured SV invariant mass distribution by a sum of simulated invariant mass distributions that correspond to b -jets, c -jets and light-flavor jets. These templates are obtained from the detector-level MC by applying the same sets of cuts as for the raw data. If the measured invariant mass distribution is normalized to a

unit integral, it can be parameterized as,

$$n_{\text{SV}}(M_{\text{inv}}) = P_{\text{b}} \cdot \mathcal{B} + P_{\text{c}} \cdot \mathcal{C} + P_{\text{lf}} \cdot \mathcal{L}, \quad (5.6)$$

where $n_{\text{SV}}(M_{\text{inv}})$ is the fraction of SVs measured in the given invariant mass bin. The b -jets, c -jets and light-flavor jets templates normalized to a unit integral are denoted as \mathcal{B} , \mathcal{C} and \mathcal{L} . The purity of b -jets is denoted by P_{b} and the parameters P_{c} and P_{lf} correspond to the contamination of the selected sample of b -jet candidates by c -jets and light-flavor jets. The normalization condition for these amplitudes can be expressed as,

$$1 = P_{\text{b}} + P_{\text{c}} + P_{\text{lf}}.$$

In order to fit the SV invariant mass distribution by Eq. (5.6), we use TMinuit where the minimized function is

$$\chi^2 = \sum_{i=1}^{\text{n bins}} \frac{(n_{\text{SV},i} - P_{\text{b}} \cdot \mathcal{B}_i - P_{\text{c}} \cdot \mathcal{C}_i - P_{\text{lf}} \cdot \mathcal{L}_i)^2}{\sigma_{n_{\text{SV},i}}^2 + (\sigma_{\mathcal{B},i} \cdot P_{\text{b}})^2 + (\sigma_{\mathcal{C},i} \cdot P_{\text{c}})^2 + (\sigma_{\mathcal{L},i} \cdot P_{\text{lf}})^2}.$$

Here the index i denotes the consecutive number of bin in the invariant mass distribution. The statistical uncertainties of the measured data and MC templates in the given bin are denoted with σ and are distinguished with the corresponding subscripts. Note that in this way, the TMinuit fit takes into account statistical uncertainties of the templates and can be used also for the cases when the statistical uncertainties of the raw data are non-Poissonian, e.g., when the measured data are obtained from a detector-level MC simulation as a sum over hard bins. Let us also point out that neither of the above mentioned features can be incorporated by the otherwise frequently used RooFit method which is based on the maximum-likelihood estimator.

MC SV Invariant Mass Templates Fit and Closure Test:

Fig. 5.19 shows a fit of the detector-level SV invariant mass distributions with the smoothened MC templates. More template fits for different cut settings are presented in Sec. A.4.1. The extracted purities as a function of $p_{T,jet}^{reco}$ are presented in Fig. 5.20. The results are compared with the true b -jet purity which is estimated based on PYTHIA+EPOS detector-level MC simulation. The b -jet purity in template fit method shows a good agreement with the true (MC based) b -jet purity as shown in Fig. 5.20.

5.4.3 Hybrid Purity

Purity is estimated based on two methods: the POWHEG-based method (POWbc) and the data-driven method. Both rely on simulations to some extents. However, in the POWHEG case, fundamental physics comes from the simulation which has a significant scale uncertainty¹. On the other hand, the data-driven method which is based on fitting of the SV invariant mass distribution by templates relies only on accurate description of decay kinematics of b , c and light-flavor hadrons and detector responses by PYTHIA+EPOS simulations. It does not depend on the corresponding production cross-sections. Therefore we trust the latter more. A serious disadvantage of the template fitting is that, it is very statistics dependent method. Therefore a hybrid method is developed, where we treat the different POWHEG settings as models and test them against the template fit results to statistically determine whether a model with given settings (factorization scale, renormalization scale, etc. for heavy quark pair production in POWHEG, discussed in A.2.3) can possibly be correct.

¹There is some logical circularity in that we aim to determine the b spectrum, and at the same time we evaluate purities using the b spectrum from simulations without any nuclear modification. Any such method works only as long as the nuclear modification is within the uncertainty on the input spectrum. In our case this is exactly what happens, as a large uncertainty is present in the simulated b spectrum and the uncertainty entering the purity is later restricted by using the Hybrid method. In principle, a way around the core problem is to express the b spectrum with the inclusive and tagged spectra and the efficiencies, thus eliminating this circularity. We call this the POWb method. This one could not be used because it amplifies statistical uncertainties too much.

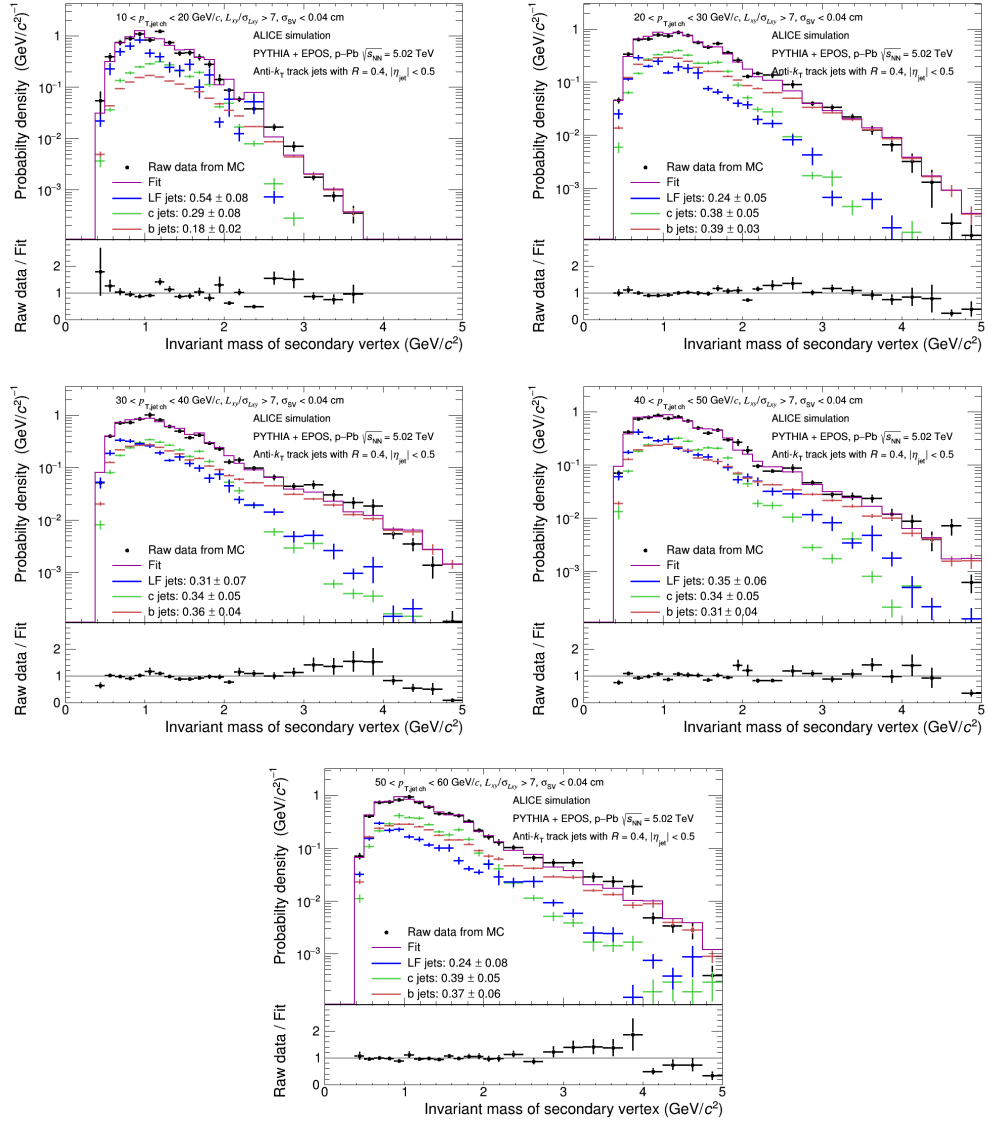


Figure 5.19: Fit of the simulated detector-level SV invariant mass distributions with smoothened MC templates. The cuts on SV are $\sigma_{SV} < 0.04$ cm and $SL_{xy} > 7$. The bottom part of each panel shows the ratio of data to the fit.

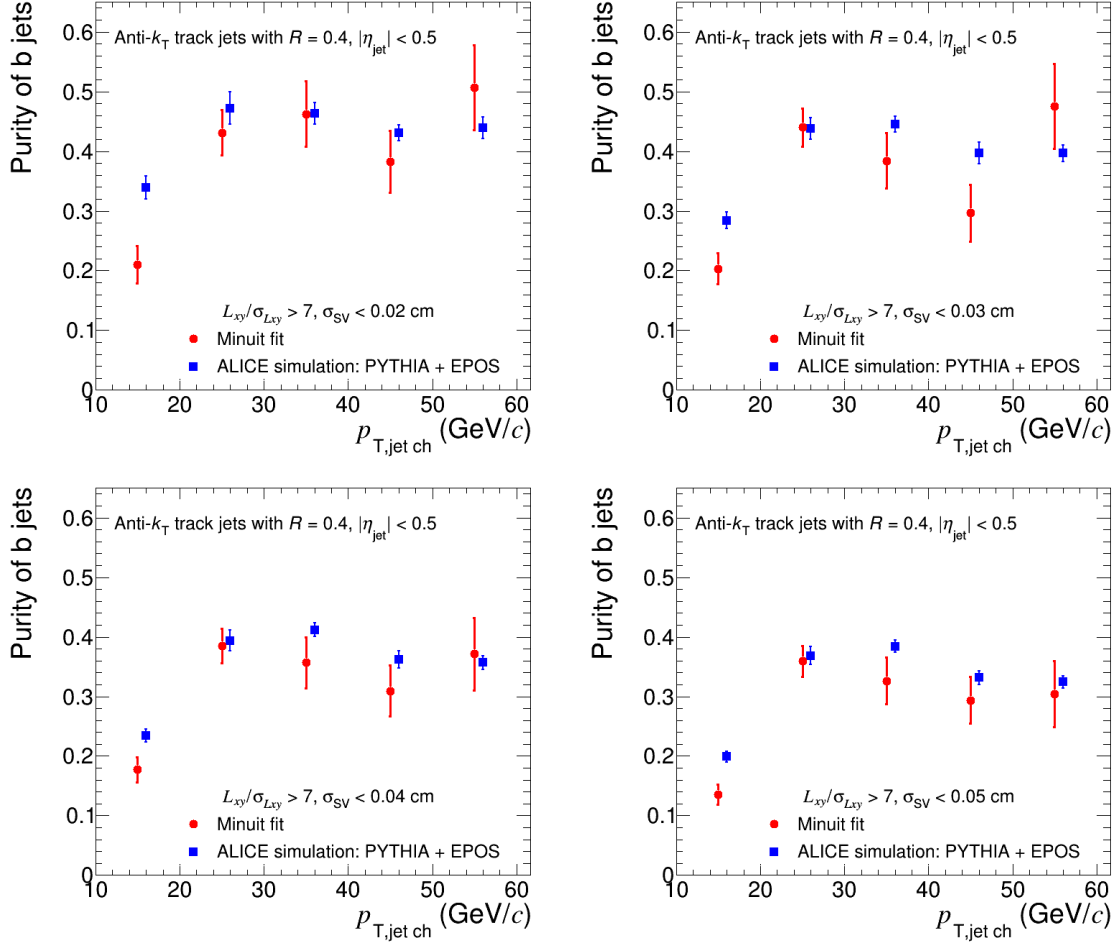


Figure 5.20: MC closure test result: purity of the selected detector-level b -jet candidate sample as obtained from the template fit method and the corresponding true detector-level b -jet purity. The cuts on SV are mentioned in legend.

Single χ^2 Test:

The data-driven and POWbc purities are compared for any combination of the tagging cuts $\sigma_{SV} < x$ and $SL_{xy} > y$, where $x \in \{0.02, 0.03, 0.04, 0.05\}$ cm and $y \in \{5, 6, 7, 8, 9\}$. A comparison of b -jet sample purity as a function of $p_{T,jet}^{reco}$ as obtained from the POWbc and template fit methods is shown in Figs. 5.21 and 5.22. The $\sigma_{SV} < 0.03$ cm and $SL_{xy} > 7$ cuts are varied respectively, and the other is kept fixed. Here the default POWHEG settings (renormalization and factorization scales are unity for both charm and beauty, default quark masses) for POWbc method are used. For the sake of brevity, we do not show the individual cross-variations.

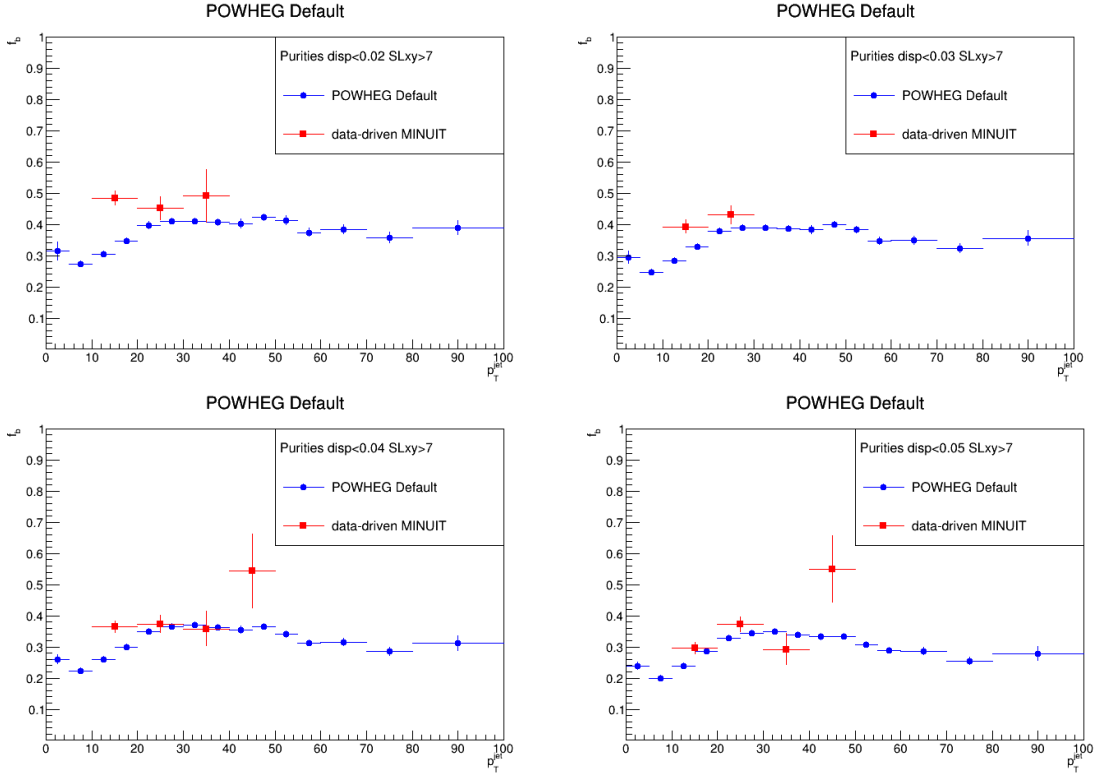


Figure 5.21: Comparison of data-driven template-fit method and POWbc b -jet purities for different σ_{SV} cuts.

As one can observe, there is a slight, but systematic deviation between the POWHEG Default curves, as the POWHEG curve tends to undershoot the data-driven points. Although the method appears robust for the choice of the tagging cuts. This gives us confidence that the two methods

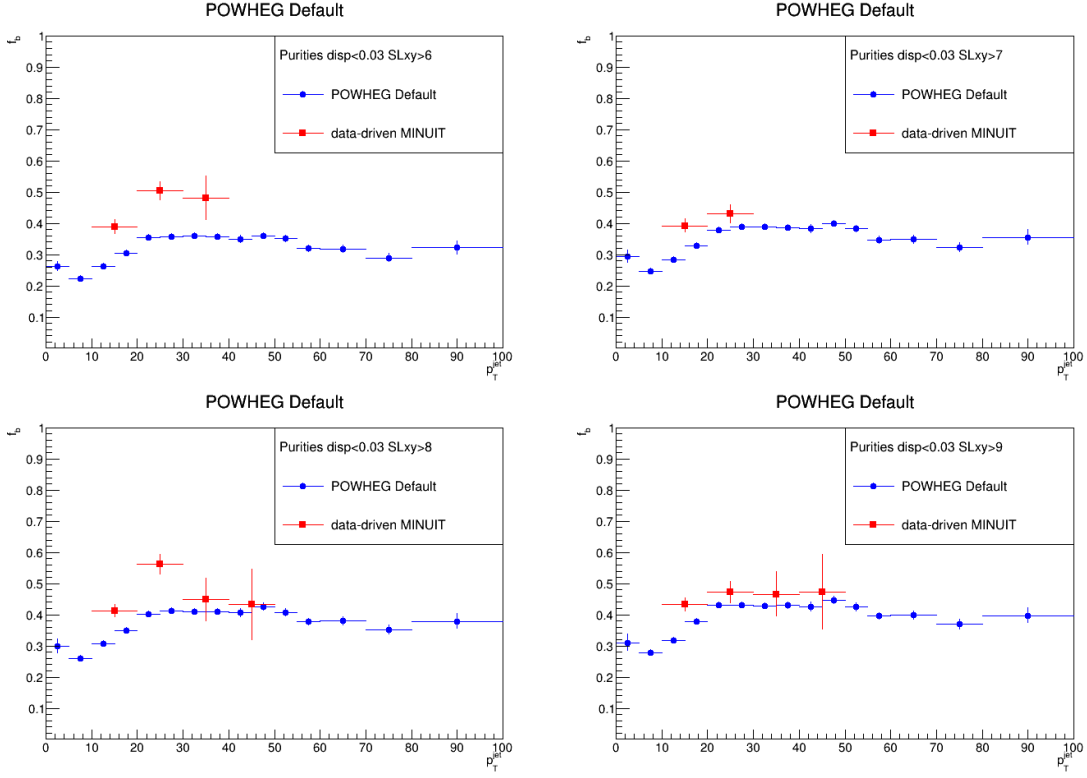


Figure 5.22: Comparison of data-driven template-fit method and POWb c b -jet purities for different SL_{xy} cuts.

work consistently with each other.

In order to quantitatively compare data-driven and POWb c purities, the latter is re-binned from 5 GeV/ c into 10 GeV/ c bins and scaled by 0.5. Only those data-driven points are considered where there is a convergent fit. Data points with values and errors less than 10^{-5} are ignored. Then the χ^2 is calculated as,

$$\chi^2 = \sum_{bins} \frac{(f_b^{\text{POWbc}} - f_b^{\text{data-driven}})^2}{\sigma_{\text{POWbc}}^2 + \sigma_{\text{data-driven}}^2}. \quad (5.7)$$

Let us note that the contribution of σ_{POWbc} is negligible. Since there is no input to the model based on data (no fit is carried out, just consistency checks), the number of points N is taken as the number of degrees of freedom. The distribution of χ_i^2/N_i for all combinations of POWHEG settings and tagging cuts is shown in Fig. 5.23 (left panel). It roughly follows the expected shape

of an χ^2 curve.

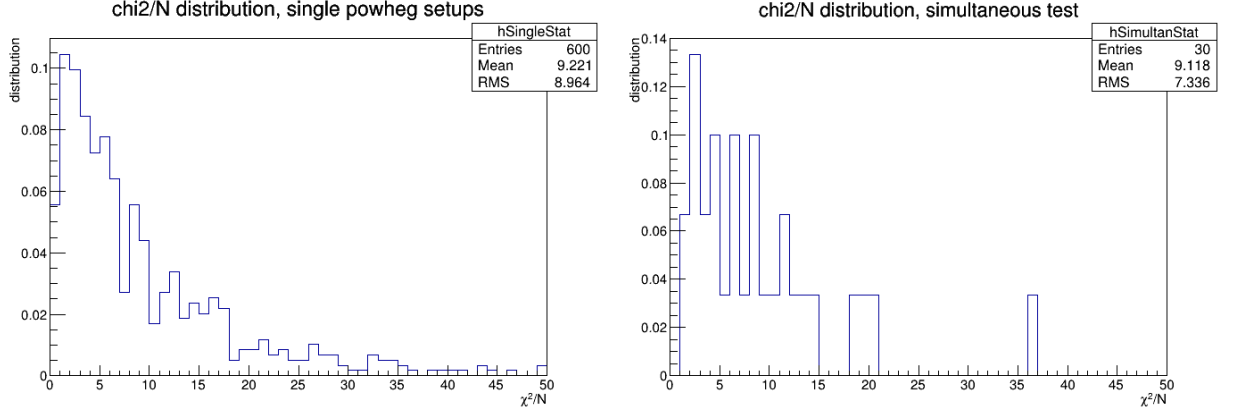


Figure 5.23: Left: The distribution of χ_i^2/N_i values for each combination of tagging cuts and POWHEG settings. Right: The χ^2/N distribution of the combined tests when all tagging cuts are taken simultaneously into account for each POWHEG settings.

Combined χ^2 Test:

For each of the POWHEG scale settings, we consider all χ_i^2 values corresponding to different choices of the tagging cuts. We derive the combined discriminator value as,

$$\chi^2/N = \sum_i (\chi_i^2) / \sum_i (N_i), \quad (5.8)$$

where the index i runs over the possible tagging cut configurations. The resulting distribution of χ^2/N is shown in the right panel of Fig. 5.23. As an example, the values of the constituent χ_i^2 and the N_i values are shown as a form of a 2D histogram for the Default POWHEG setting in Fig. 5.24. The 2D histograms for the two other examples are in Figs. 5.25 and 5.26.

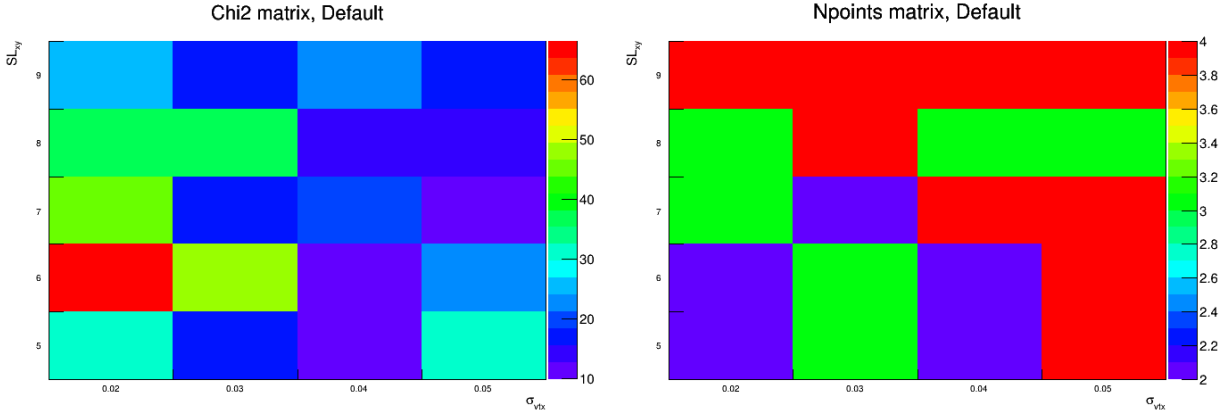


Figure 5.24: χ_i^2 values (left) and N_i values (right) obtained for the Default POWHEG setup.

As an arbitrary, but sensible criterion any POWHEG setting with two-digit χ^2/N is rejected. Note that POWHEG with Default settings shows a marginal agreement with $\chi^2/N \approx 10$. The results of this test are shown in Fig. 5.27. The restrictions provided by the data-driven method are tremendous when one compares the corresponding systematics on the spectrum obtained by the hybrid method and by the POWbc method without restrictions.

The purity for $SL_{xy} > 7$ and $\sigma_{SV} < 0.03$ cm, both from data-driven and POWHEG based method is compared in Fig. 5.28. Here we have considered the scale uncertainties of POWHEG

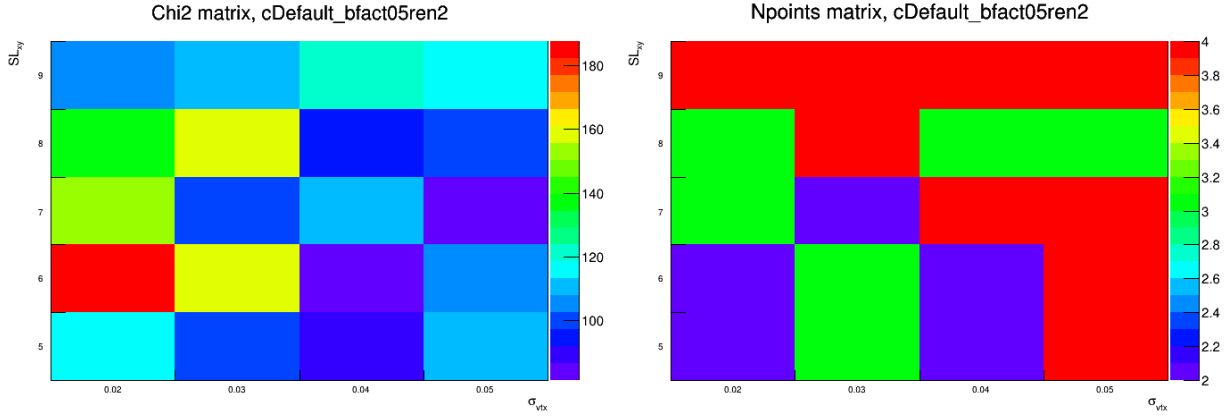


Figure 5.25: χ_i^2 values (left) and N_i values (right) obtained for the POWHEG setup with default charm settings, beauty factorization scale 0.5 and beauty renormalization scale 2.

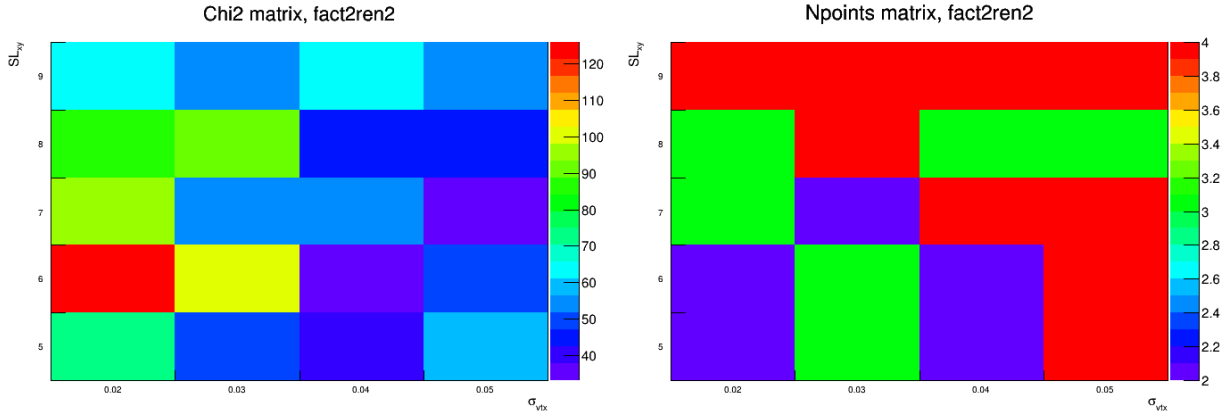


Figure 5.26: χ_i^2 values (left) and N_i values (right) obtained for the POWHEG setup with charm and beauty factorization scales 0.5 and renormalization scales 2.

and obtained the spread of the accepted POWHEG based purity variation as shown by the shaded band in the Fig. 5.28. Both estimations are consistent with each other.

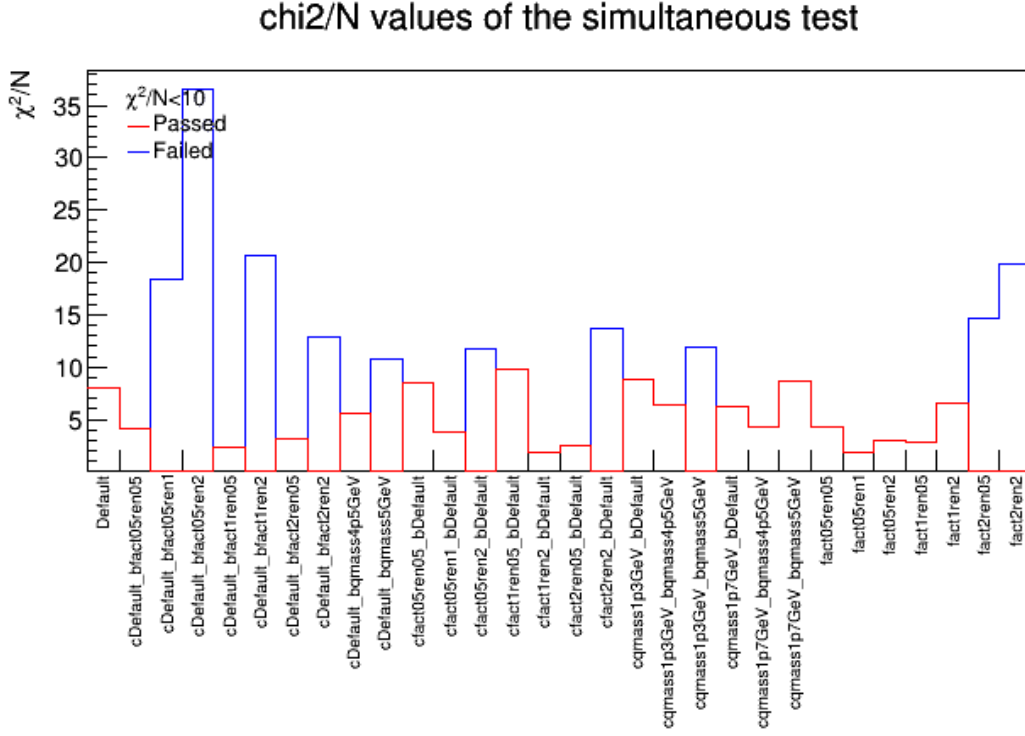


Figure 5.27: Result of hybrid purity tests. The χ^2/N values are shown for each POWHEG setting. Settings consistent with data-driven results are marked red. Settings failing the test are blue.

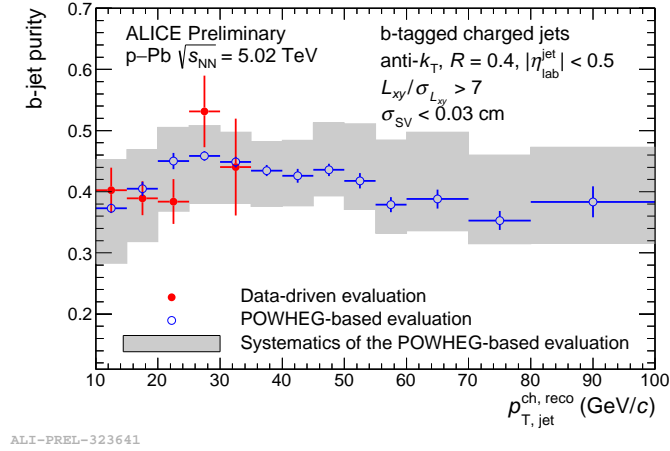


Figure 5.28: Purity of the b-jet candidates selected with a cut on $SL_{xy} > 7$ and $\sigma_{SV} < 0.03$ cm. Comparison of the data driven template fit method (red data points) and POWHEG based method (blue data points).

5.5 Unfolding Procedure

The spectrum of b -jets obtained by SV tagging and corrected by the corresponding purity/efficiency ratio is still affected by distortions stemming from two main factors, *i*) instrumental effects and *ii*) local background fluctuations w.r.t. the mean UE density. These two effects smear the “true” b -jet spectrum and have to be corrected which are done via an unfolding procedure. In general, it is assumed that relation between some measured spectrum $m(y)$ and the corresponding true spectrum $t(y)$ is linear and can be written as,

$$m(y) = \int A(x, y)t(x)dx, \quad (5.9)$$

where $A(x, y)$ is the so-called response function. In our case, x and y denote particle-level and detector-level jet p_T . For spectra with finite size bins, the above equation can be rewritten as a matrix equation

$$m_j = \sum_i A_{ji} t_i, \quad (5.10)$$

where A denotes the so-called response matrix. To solve this equation for t , first we have to know the response matrix A and its inversion. If the inversion of A exists, we could write

$$t_i = \sum_j A_{ij}^{-1} m_j. \quad (5.11)$$

However, A suffers from statistical fluctuations and is often singular. Therefore, in order to solve Eq. (5.10) for t one has to use unfolding method based on iteration. Basic unfolding methods are implemented in the RooUnfold [174] package. We will use the most common methods based on the Bayesian theorem [175] and the SVD decomposition [176]. The ingredients used for the unfolding are listed below.

5.5.1 Unfolding of the Measured Spectra

Inputs to the unfolding are as follows:

- **Raw spectra** of b -jet candidates corrected for SV tagging efficiency and purity, see Sec. 5.4.

These spectra are re-binned using the binning scheme

$$10, 15, 20, 25, 30, 35, 40, 45, 50, 55, 60, 70, 80, 100 \quad \text{GeV/c.} \quad (5.12)$$

- **Prior spectrum** is the b -jet spectrum from PYTHIA+POWHEG simulation with the default POWHEG settings. The binning scheme for the prior is

$$5, 10, 15, 20, 25, 30, 40, 50, 60, 70, 80, 100, 200 \quad \text{GeV/c.} \quad (5.13)$$

Note that the first and last bin are used as underflow and overflow bins, hence any physics conclusion should not be drawn from the first and last bin of the prior spectrum. They will not appear in the final spectrum.

- **Response matrix** which gives the relation between the measured spectrum and the particle level spectrum is assumed to be factorizable as a product of a matrix δp_T that describes momentum smearing due to local UE fluctuations and a matrix M which describes instrumental effects,

$$A(p_{T,jet}^{part}, p_{T,jet}^{reco}) = \delta p_T(p_{T,jet}^{det}, p_{T,jet}^{reco}) \times M(p_{T,jet}^{part}, p_{T,jet}^{det}). \quad (5.14)$$

Here $p_{T,jet}^{part}$ denotes original true jet p_T , $p_{T,jet}^{det}$ is the jet p_T smeared by instrumental effects and $p_{T,jet}^{reco}$ is the jet p_T smeared by local UE fluctuations.

The δp_T matrix is obtained from the δp_T distribution which is measured by the random cone

method in events with a SV, see Fig. 5.29. The SV is required to fulfil $SL_{xy} > 7$. The random cone method calculates δp_T based on the formula,

$$\delta p_T = \sum_{\text{tracks in cone}} p_{T,\text{track}} - \pi R^2 \rho, \quad (5.15)$$

where $R = 0.4$ is a cone size of the jets. The measured δp_T distribution is shown in Fig. 5.29. In order to suppress statistical fluctuations in the tail of the distribution, the data are fitted with a sum of two exponential functions. In the region $\delta p_T > 7 \text{ GeV}/c$, measured data are replaced by the fit. The distribution is then normalized by its integral and used to construct the δp_T matrix.

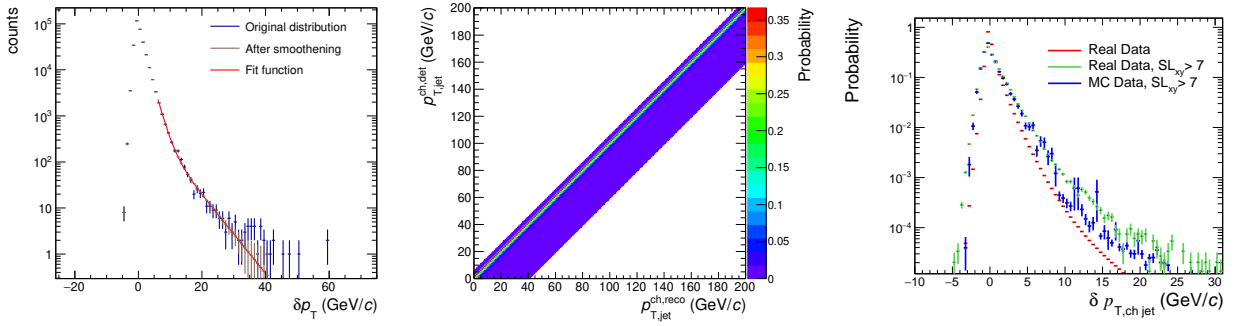


Figure 5.29: Left: δp_T distribution as obtained by random cone method from events with a SV. Middle: The corresponding δp_T matrix having a bin size of $1 \text{ GeV}/c \times 1 \text{ GeV}/c$. Right: Comparison of δp_T distribution from inclusive events and from events with a SV.

The instrumental response matrices for b -jets, c -jets and light-flavor jets are obtained from the PYTHIA-filtered simulation. The response matrix for b -jets is shown in Fig. 5.30. It is generated from the MC datasets with enhanced b quark fraction (LHC17h6a2, LHC17h6b2). The instrumental response matrices for c -jets and light-flavor jets are obtained from PYTHIA-filtered (LHC17h6e2, LHC17h6f2) events.

Fig. 5.31 shows the combined response matrix for b -jets as calculated from Eq. (5.14). This matrix is used for our primary analysis (PA). As systematic variation, we are using also b -jet response matrix obtained directly from PYTHIA+EPOS simulation which takes into account local

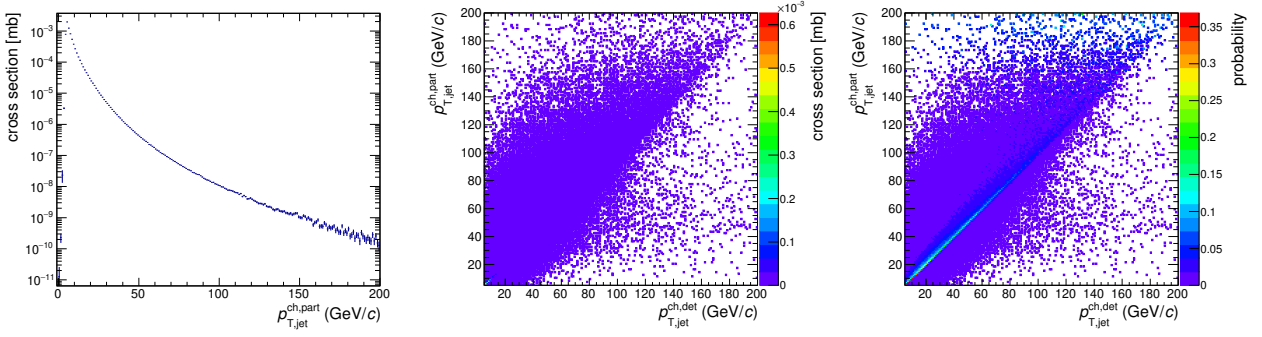


Figure 5.30: Left: Distribution of particle-level b -jets which is used to normalize the response matrix. Middle: Instrumental response matrix for b -jets. Right: Instrumental response matrix of b -jets converted to probability matrix. Both matrices have a bin size of $1 \text{ GeV}/c \times 1 \text{ GeV}/c$. All data are based on PYTHIA filtered simulation.

background fluctuations as described by EPOS. Choice of the jet response matrix affects also the correction on SV tagging purity and efficiency, as illustrated by the Fig. 5.32. It is to be noted that in p-Pb, the fluctuation by background smearing has a relatively small effect compared to the detector response. The effect stays below 20% even at low p_T and it is negligible towards higher p_T values.

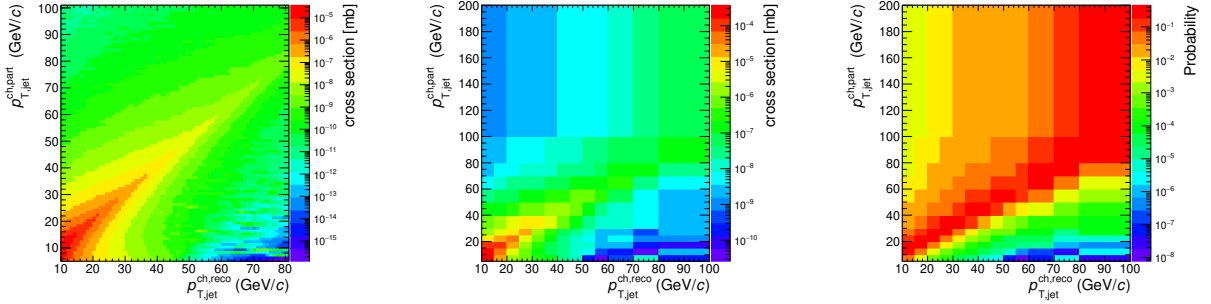


Figure 5.31: Left: Combined response matrix for b -jets which is obtained by Eq. (5.14). The matrix has a bin size of $1 \text{ GeV}/c \times 1 \text{ GeV}/c$. Middle: The same matrix after rebinning (5.12) and (5.13). Right: The re-binned matrix converted to probability.

MC Closure Tests of the Unfolding Procedure:

The first closure test used the following settings:

- Raw spectrum of b -jet candidates, obtained by applying SV tagging selections in events from

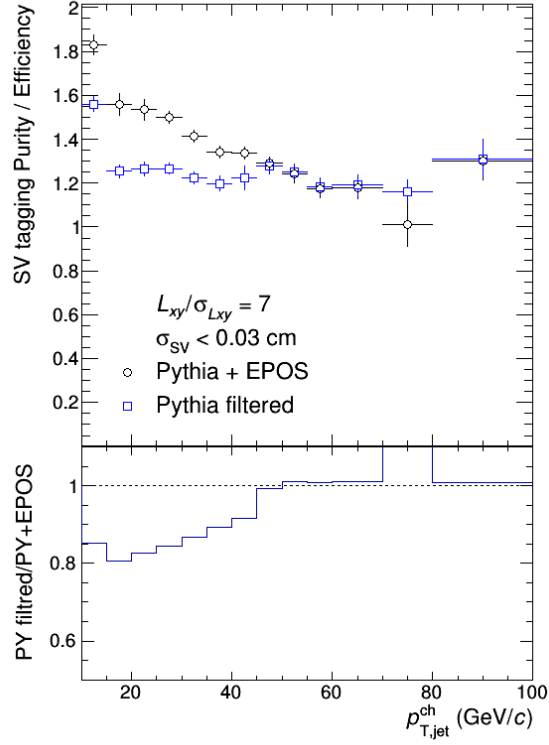


Figure 5.32: Comparison of correction factors by the PYTHIA-filtered detector matrix multiplied with deltapt matrix to EPOS+PYTHIA matrix. The effect on the unfolded spectrum is smaller than this.

the PYTHIA+EPOS MC sample.

- True spectrum is the particle-level b -jet spectrum from the same PYTHIA+EPOS sample.
- Prior spectrum is a b -jet spectrum obtained from the POWHEG+PYTHIA simulation with default settings.
- δp_T matrix is created based on a δp_T distribution obtained from the PYTHIA+EPOS sample.
- Instrumental response matrix is generated from the MC datasets with enhanced b quark production (LHC17h6a2, LHC17h6b2), i.e. the same matrix that is used for the real data unfolding.
- SV tagging efficiency and purity corrections are taken from the PYTHIA+EPOS sample (i.e.

they are the ideal ones).

- SVD unfolding.

Results of this closure test are shown in Fig. 5.33. The unfolded spectrum is obtained for the regularization parameter $i = 5$. It is within $\approx 5\%$ from the true spectrum except of the last bin. Agreement in the first two bins can be further improved if the particle-level binning (5.13) would started from 4 GeV/ c .

The second closure test uses the same settings as the first one, but the unfolding prior is the true b -jet spectrum. Results of this closure test are shown in Fig. 5.34. Indeed, in this case we see a bit better agreement between the true spectrum and the unfolded solution.

The third closure test uses the same settings as the first one, but the unfolding is done with the Bayesian method. Results of this closure test are shown in Fig. 5.35. Also here the agreement would further improve if one would use the true spectrum as a prior or if the particle-level binning would start from 4 GeV/ c .

Unfolding of the Measured b -Jet Spectrum:

Our primary analysis is done with the tagging cuts $SL_{xy} > 7$ and $\sigma_{SV} < 0.03$ cm. The QA plots for the unfolding with the primary analysis settings are shown in Figs 5.36 and 5.37 for the SVD and Bayesian methods, respectively. From the plots one can see that the convergences are stable for regularization parameters $i \geq 4$. In the SVD case, this choice is also supported by the d -vector distribution. Refolding of the unfolded solution provides a compatible spectrum to the raw data. All its points are far within 2σ (statistical errors on the raw spectrum), and all but one are within 1σ . No serious oscillations are present. The default regularization parameters are therefore chosen as $i_{\text{SVD}} = 5$ and $i_{\text{Bayes}} = 5$. The default primary analysis method for the spectrum unfolding is SVD. As systematics, regularization parameter is varied from 4 to 6 and we have used other

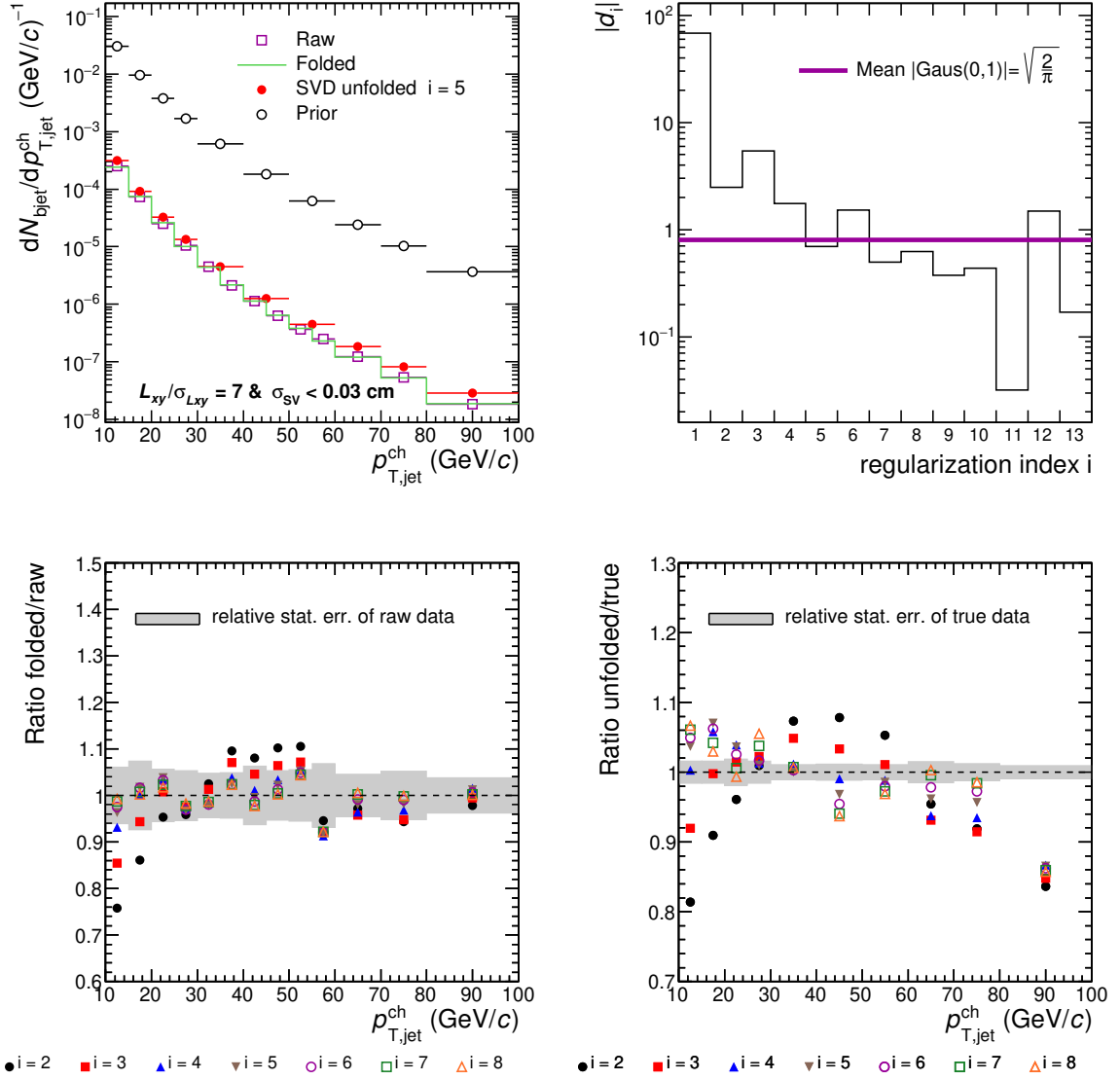


Figure 5.33: Results of the first unfolding closure test. Upper left: comparison of the raw, unfolded, refolded and prior b -jet spectrum. Upper right: d vector components based on which we choose the regularization parameter to be 5. Bottom left: Ratio of the folded spectrum to the input raw spectrum corrected for SV tagging efficiency and purity. Bottom right: Ratio of unfolded spectrum to the true spectrum. In the bottom panels, different data sets correspond to different choices of the regularization parameter.

POWHEG+PYTHIA variations (excluding cross-variations) as prior.

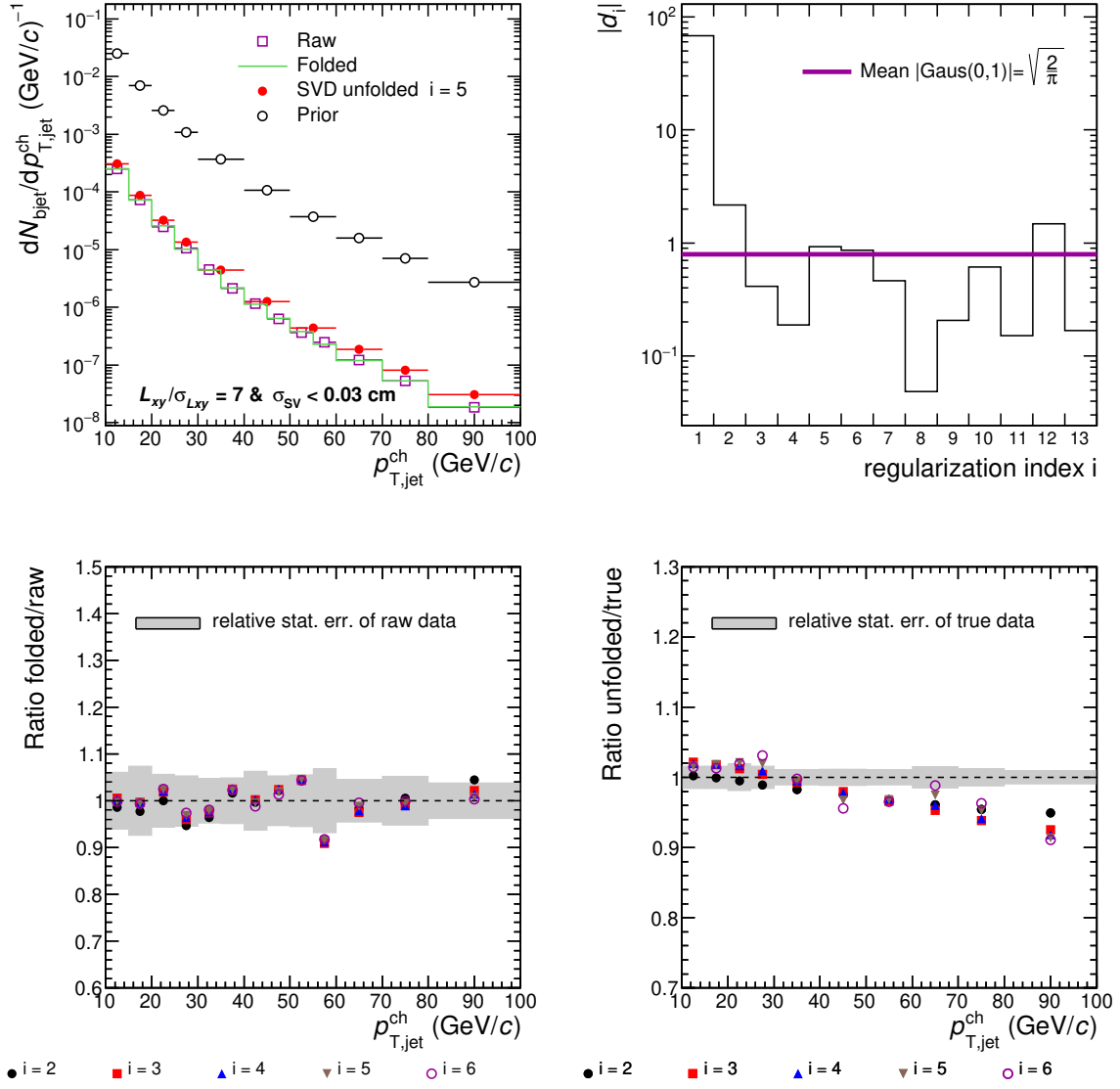


Figure 5.34: Results of the second unfolding closure test with the true b -jet prior. Meaning of the individual panels is analogous to Fig. 5.33.

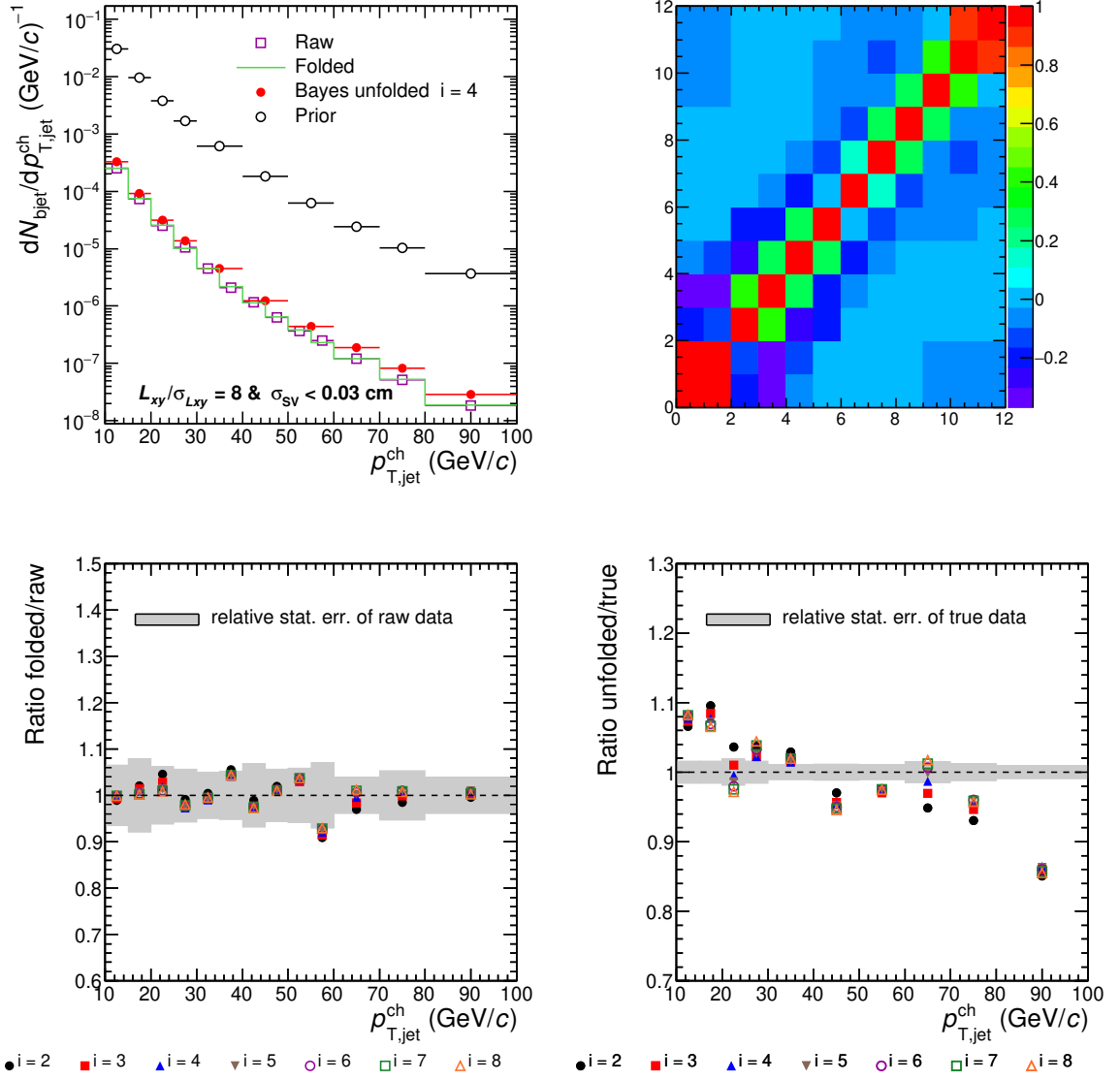


Figure 5.35: Results of the third unfolding closure test done with the Bayesian unfolding method. Meaning of the individual panels is analogous to Fig. 5.33.

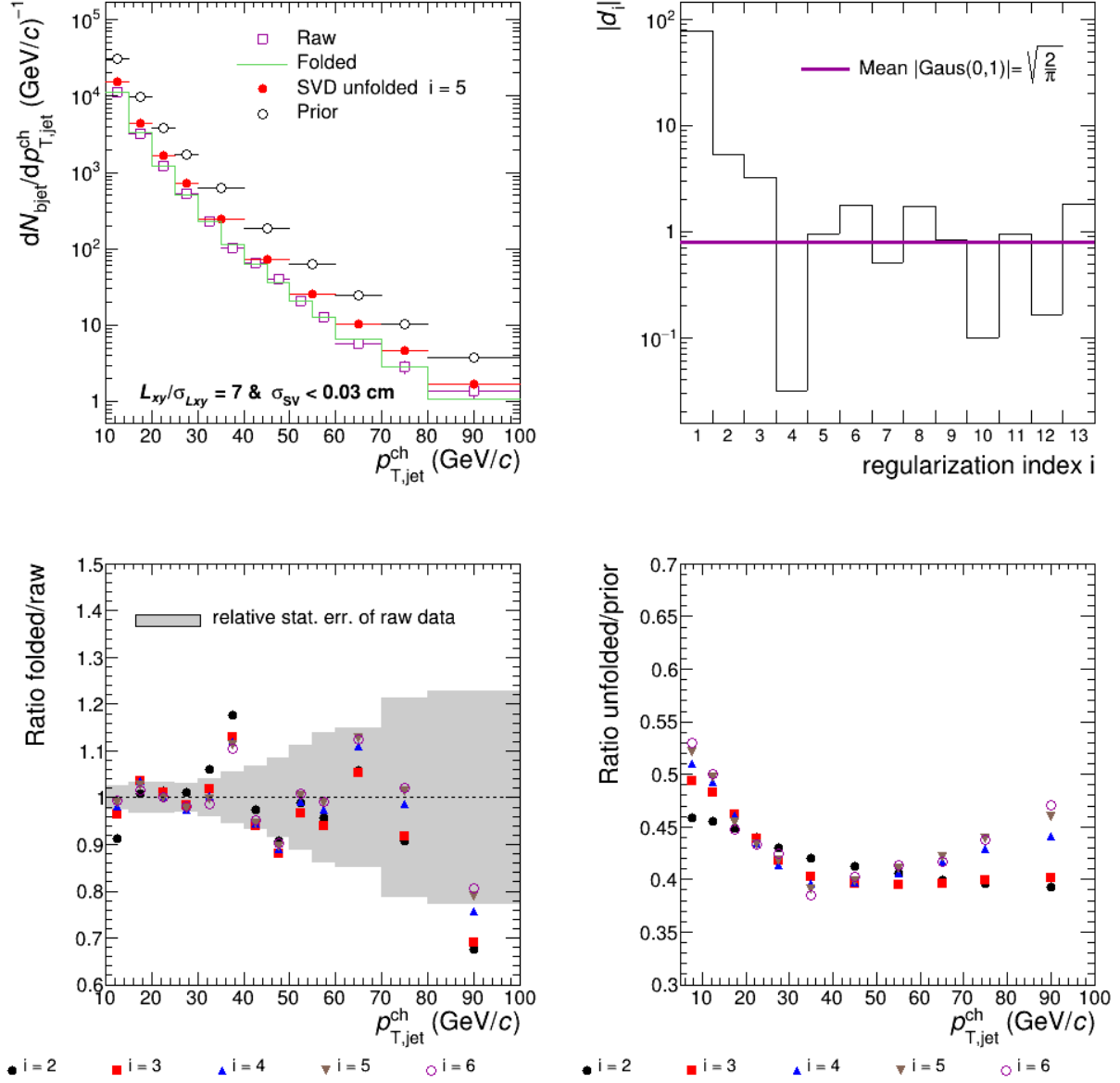


Figure 5.36: SVD unfolding the corrected b -jet spectrum with different regularization parameters (i). Meaning of the individual panels is analogous to Fig. 5.33.

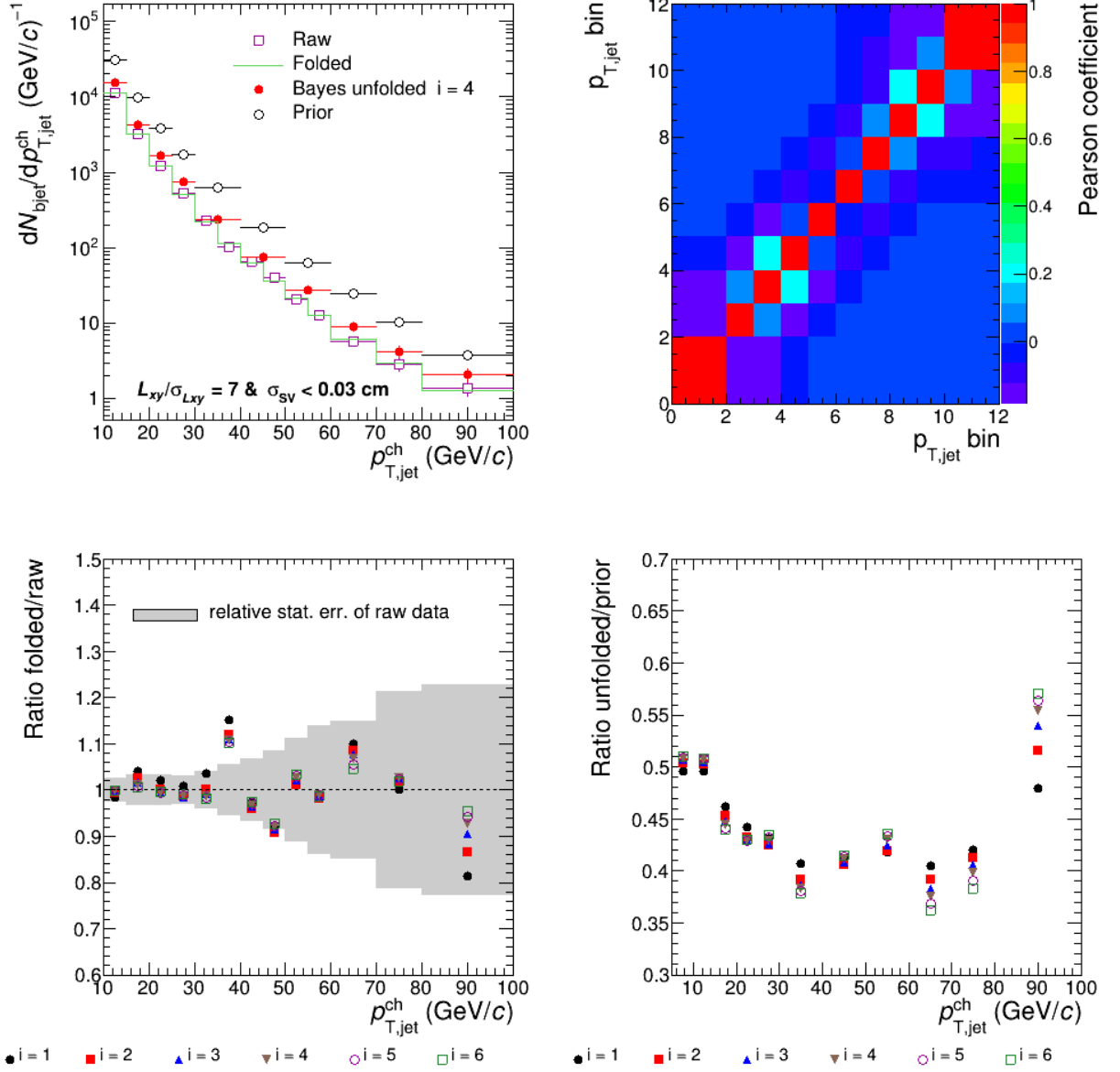


Figure 5.37: Bayesian unfolding the corrected b -jet spectrum with different regularization parameters (i).

5.6 Systematic Uncertainties

The systematic uncertainties are important since changing the analysis parameters within reason causes deviations of the measured observables. Analysis parameters are to be understood as numerical values as well as analysis techniques. The jet analysis is relatively complex and especially the tracking efficiency in the detector and the unfolding procedure are the main sources of uncertainties. So, the evaluation of systematic uncertainties is an integral part of the analysis. Besides that, since it is a jet flavor tagging analysis, another source of the systematic uncertainty would come from the tagging procedure itself. There might have some other sources of systematic uncertainties, like in the estimations of purity. All these uncertainties are discussed in details below. These items are considered independent and summed up quadratically in the result.

5.6.1 Tagging Systematics

The tagging cuts chosen for the principal analysis are $SL_{xy} > 7$ and $\sigma_{SV} < 0.03$ cm. The tagging systematics is determined by changing the SL_{xy} cut-off from 7 to 5, 6, or 8, and σ_{SV} cut-off from 0.03 cm to 0.02, 0.04 or 0.05 cm. One cut is varied at a time. The full correction and unfolding process are then repeated with the chosen set of the cuts. A summary of how these variations affect the spectrum are shown in Fig. 5.38. The analysis is very stable against the tagging variations, as all the points are consistent with unity within uncertainties. There is a slight trend in the case of $\sigma_{SV} < 0.02$ cm, culminating in a $\approx 15\%$ non-significant discrepancy at high $p_{T,jet}$. This can be explained by slight inaccuracies in the description of data by the PYTHIA+EPOS MC, that is amplified by the rapidly changing distributions of σ_{SV} around $\sigma_{SV} < 0.02$ cm, as shown in Appendix A.3. To stay on the safe side, we include this choice in the systematics. Since the variations of the tagging cuts are not independent, the envelope of the corrected spectrum variations is considered as systematics, representing a worst-case scenario.

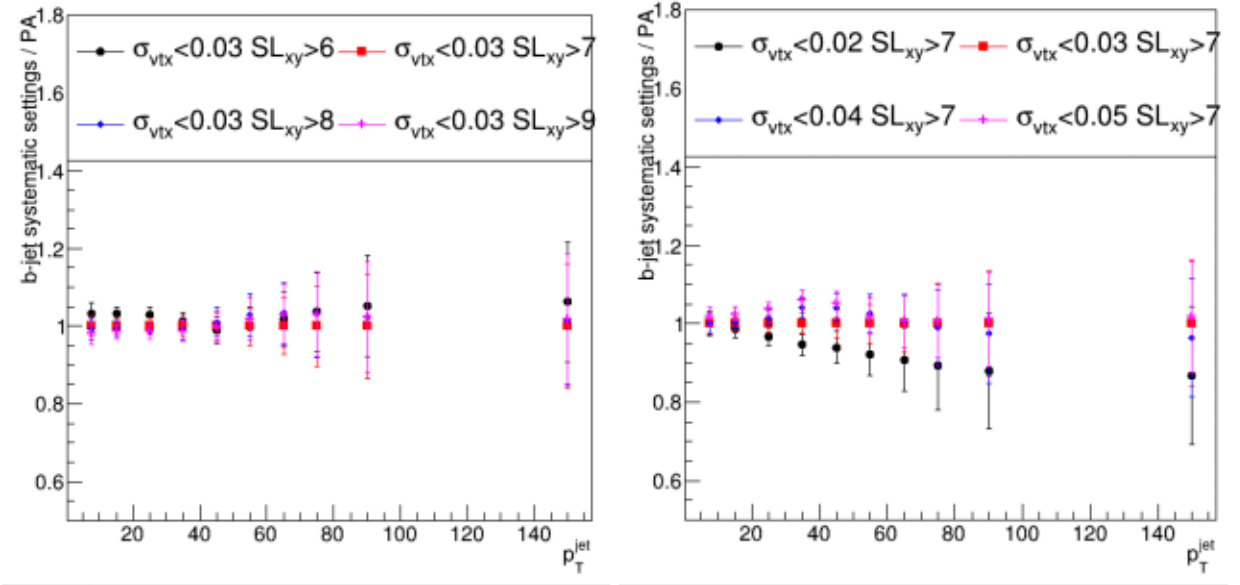


Figure 5.38: Effect of tagging cut variations on the analysis. We plot the ratio of the spectrum derived by the chosen tagging cut over the principal analysis. The left panel shows SL_{xy} and the right panel shows σ_{SV} .

5.6.2 POWHEG Scale Variations and Hybrid Purity Systematics

Details of the POWHEG+PYTHIA simulations we have used are discussed in Appendix A.2. Here we briefly recap the way POWHEG scale uncertainties are taken into account and propagated into the purity. The list of varied parameters in POWHEG are in Table 5.5. There are 30 possibilities

Table 5.5: List of POWHEG settings with defaults highlighted.

parameter	explanation (see more in Appendix A.2)	values
m_c	charm quark mass	1.3 1.5 1.7
m_b	beauty quark mass	4.5 4.75 5.0
cfact	charm factorization scale	0.5 1 2
cren	charm renormalization scale	0.5 1 2
bfact	beauty factorization scale	0.5 1 2
bren	charm renormalization scale	0.5 1 2

altogether, allowing cross-variations of renormalization and factorization scales. The extraction of systematics from the hybrid purity determination is outlined in Sec. 5.4.3. The list of statistically accepted scale variations are shown in Fig. 5.27.

5.6.3 Unfolding Systematics

As described in Sec. 5.5, the principal analysis uses SVD unfolding with regularization parameter $k_{SVD} = 5$ and prior from the default POWHEG settings. There are several tests with different choices of priors, binning and range, choice of response matrices and regularization parameters, described in Ref. [177]. We have used two independent implementation methods, one is described here and the other one in Ref. [178] for consistency checks. As systematic variations, we have settled with the following:

- SVD method is changed to Bayesian with $k_{Bayes} = 5$;
- The prior is changed from default POWHEG spectrum to all POWHEG spectra as described in Appendix A.2;
- SVD regularization parameters are varied from 4 through 6 to 7;

We show how the prior variations as well as the choice of regularization parameter affect the spectrum in Fig. 5.39. The comparison of unfolding methods are detailed in Sec. 5.5. These variations are not considered as independent and therefore they are not summed up. Instead, the total range of systematic uncertainties are determined based on the envelope of the outcoming results.

5.6.4 Choice of the Background Estimation Method

Although the background estimation is closely related to unfolding, we consider this as an independent uncertainty, since the unfolded spectrum is also affected. By default, as a response matrix, we consider the PYTHIA-filtered detector matrix multiplied by the normalized matrix of background fluctuations, as described in Sec. 5.5. Alternatively, the background matrix is constructed from the EPOS+PYTHIA matrix that inherently contains background. In Fig. 5.32, the effect on the

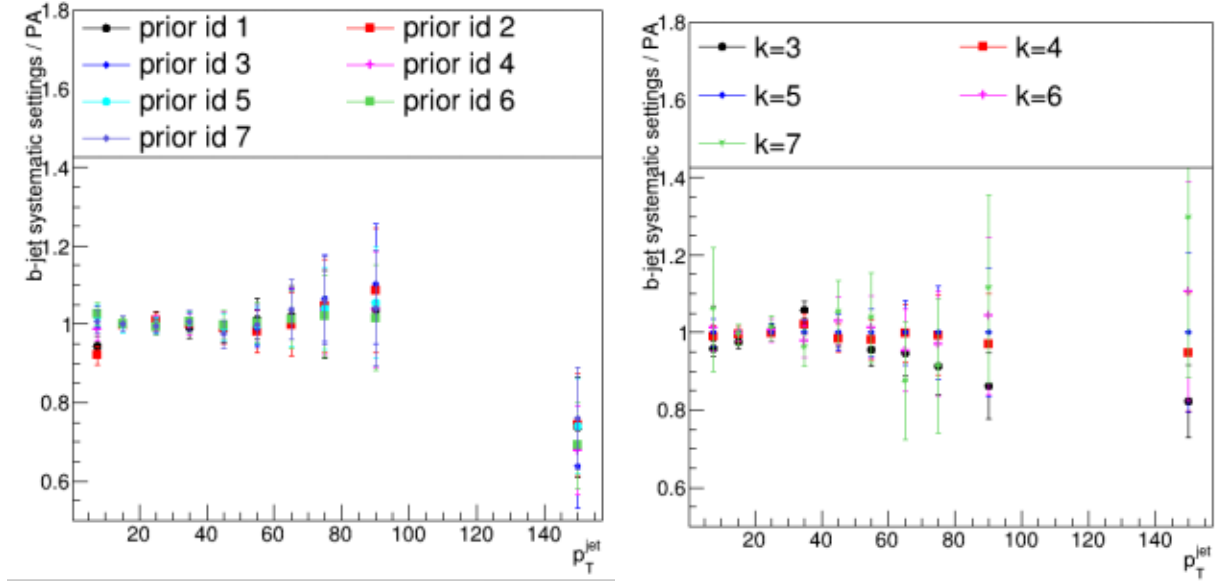


Figure 5.39: Effect of some unfolding variations on the analysis. We plot the ratio of the spectrum derived by the chosen SVD unfolding settings cut over the principal analysis. The left panel shows prior variations and the right panel shows the choice of k_{SVD} .

detector-level purities/efficiencies has been shown.

5.6.5 Tracking Efficiency

Influence of the track reconstruction inefficiency on the fully corrected b -jet spectrum is investigated following the approach used for the inclusive jet spectra [179]. The uncertainty on the track reconstruction efficiency is assumed to be 4% as per the Ref [169]. The tracking efficiency in simulation is therefore uniformly lowered by 4% and an alternative instrumental matrix is obtained. The analysis is repeated with this assumption, ie. the extraction of the correction factors is repeated from MC as well as the raw jet spectra. The correction factors and the unfolding of the b -jet spectra is obtained with this alternative response matrix to the primary analysis spectrum which is resulting the systematic uncertainty due to tracking efficiency.

5.6.6 Track Momentum Smearing

The momentum resolution of measured hybrid tracks estimated from the space-point residuals to the track fit stored in the covariance matrix can be found in Fig. 5.40. In the analysis note [180], one discusses how to estimate the corresponding systematic uncertainty on p_T spectrum of charged tracks. Here we follow the same approach and assess what will be its effect on the b -jet spectrum.

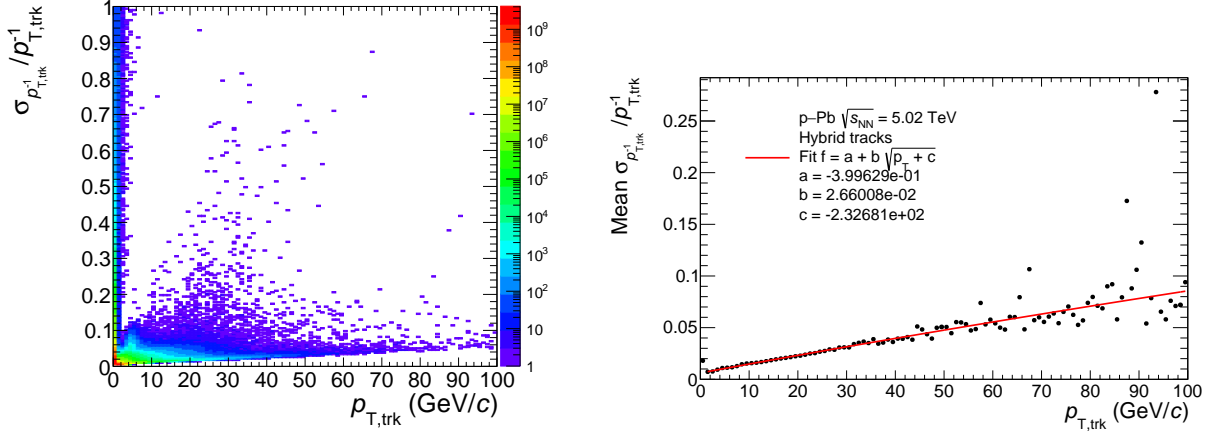


Figure 5.40: Left: The relative resolution of p_T^{-1} for hybrid tracks as a function of track p_T in p-Pb collisions at $\sqrt{s_{NN}} = 5.02$ TeV. Right: The corresponding mean relative resolution of p_T^{-1} for hybrid tracks as a function of track p_T . The red line represents parameterization of the trend by a smooth function.

We divided the full azimuthal angle into 36 slices. In each slice, $1/p_T$ spectrum of positively (negatively) charged tracks is fitted using a power-law function

$$y(p_T^{-1}) = A(p_T^{-1} - B)^{-n}, \quad (5.16)$$

where A , B and n are parameters of the fit. The fit is done in the range 8 - 20 GeV/ c , see Fig. 5.41.

The fitted B values for positive and negative tracks are shown in Fig. 5.42. The mean B values for negative (positive) tracks is 0.0036 (0.0033) and the B RMS is 0.0077 (0.006). Further it is assumed that RMS of B is independent of track p_T . The RMS value of B then represents the systematic uncertainty of the σ_{1/p_T} obtained from the covariance matrix, shown in Fig. 5.40.

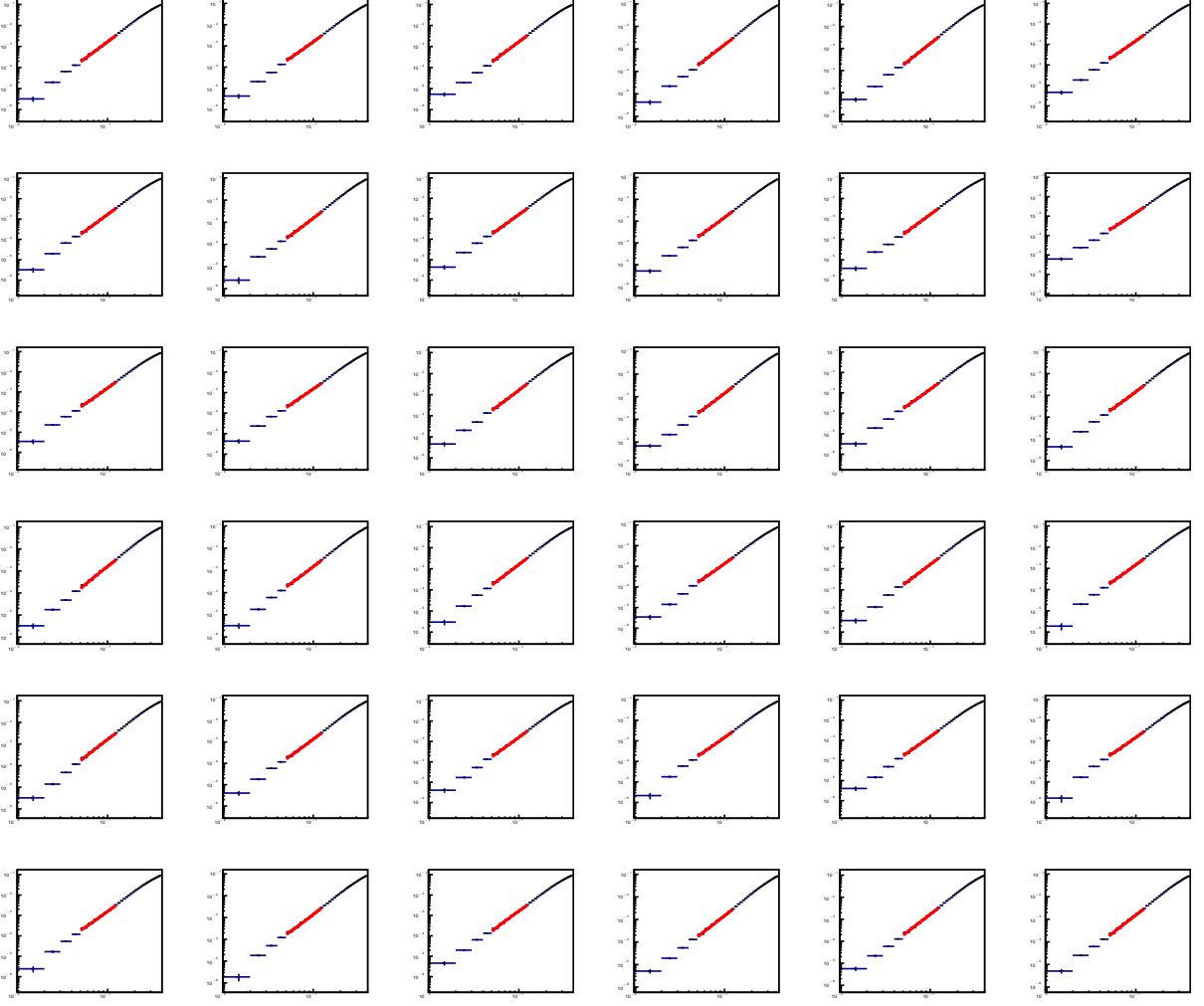


Figure 5.41: $1/p_T$ spectra of negatively charged tracks for 36 azimuthal slices. The x -axis corresponds to track inverse transverse momentum ($1/p_T$) and the y -axis gives the number of entries. The solid red line represents a fit of the data with the power-law (5.16).

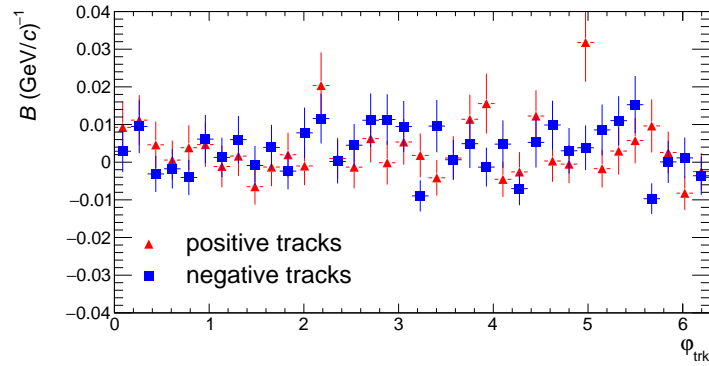


Figure 5.42: Extracted values of the B parameter for positively and negatively charged tracks in each of the 36 azimuthal slices shown in Fig. 5.41.

The resulting systematic uncertainty on the b -jet spectrum is investigated by means of a toy MC simulation. The toy MC simulation used PYTHIA8 with Tune 5 to generate pp collisions at $\sqrt{s} = 5.02$ TeV with the nucleon-nucleon center-of-mass system rapidity shift of $y_{NN} = -0.465$. Generated tracks are filtered using the track reconstruction efficiency given by Fig. 5.6. Subsequently, their transverse momentum is smeared based on (i) σ_{1/p_T} obtained from Fig. 5.40 or (ii) σ_{1/p_T} increased by the RMS of $B = 0.0077$ (added together in quadrature). Both sets of tracks are used to reconstruct anti- k_T jets and to fill the corresponding instrumental response matrices, see Fig. 5.43. The matrices are further folded with the δp_T matrix from Fig. 5.29 and are used to unfold the measured b -jet spectra. The difference between the resulting b -jet spectra is then taken as the systematic uncertainty, see Fig. 5.44. Uncertainty in track p_T smearing affects the b -jet spectra on the level of 5%.

5.6.7 Secondary Tracks Admixture

The reconstructed jet momentum is shifted due to admixture of secondary tracks. The primary analysis accounts for this shift using the instrumental response matrix shown in Fig. 5.30. The matrix is based on the PYTHIA filtered simulation. In order to check, to what extent does our simulation describe the fractions of physical primaries and secondary tracks in the p-Pb data, we have analyzed the distance of closest approach (DCA) distributions of reconstructed hybrid tracks to the primary vertex, see Fig. 5.45. The simulation provides DCA templates for physical primaries and secondary tracks. These templates are used to fit the measured p-Pb DCA distribution. Free parameters of the fit are the scaling factors of the templates. From the fit we see that the ratio of the number of secondary tracks to the number of all reconstructed tracks is by 29.9% higher in the measured p-Pb data relative to the pp simulation.

Further, from the PYTHIA filtered simulation we estimated a fraction of jet p_T which is carried

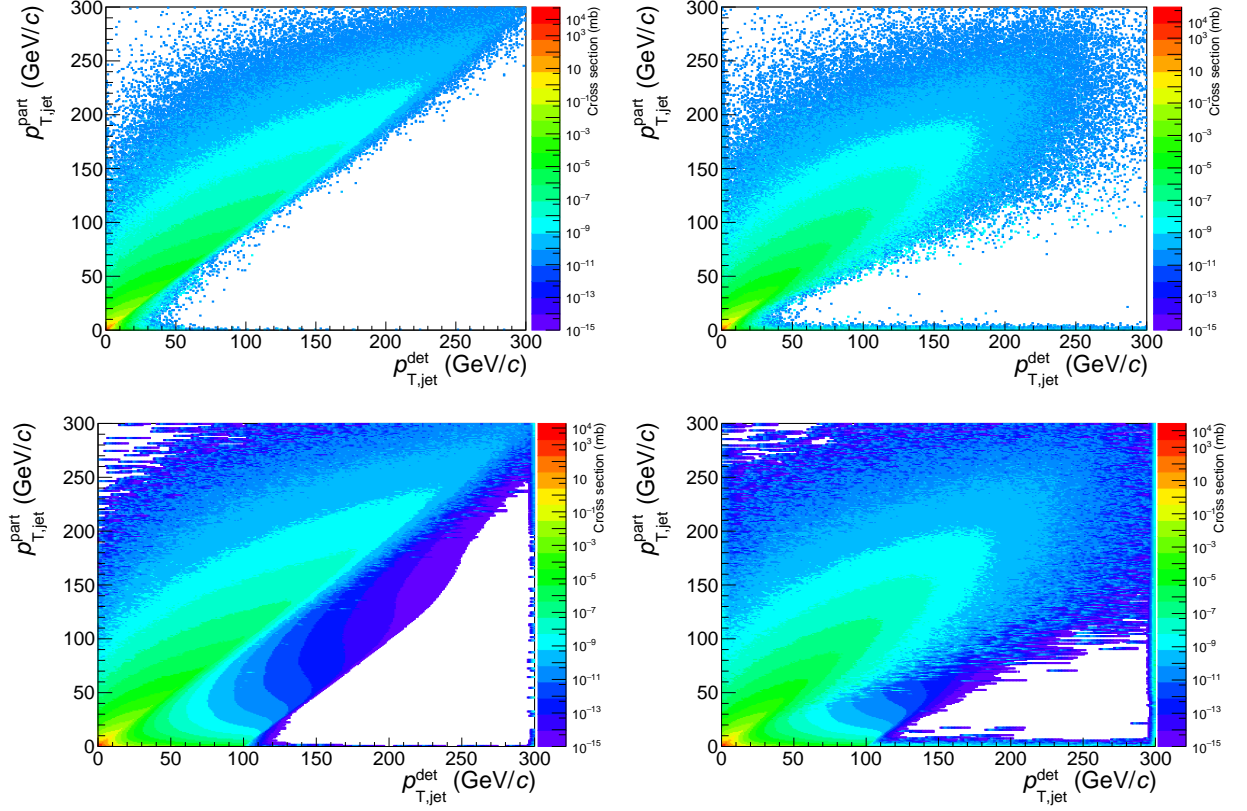


Figure 5.43: Top panels: Instrumental response matrices obtained with the toy MC simulation based on PYTHIA8 Tune5. The particle-level $1/p_T$ is smeared either with σ_{1/p_T} from Fig. 5.40 (top left) or with σ_{1/p_T} increased by the RMS of B (top right). The bottom panels show the corresponding matrices after folding with the δp_T matrix.

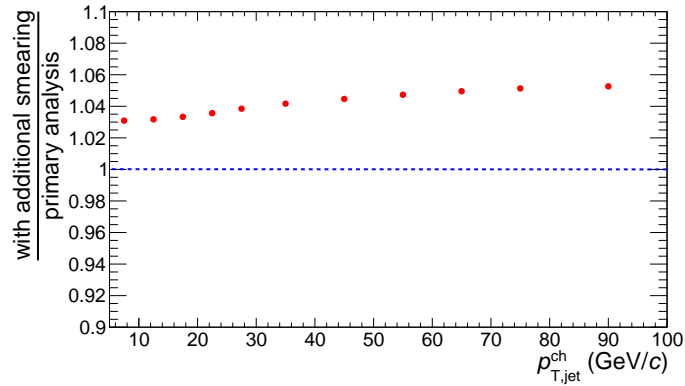


Figure 5.44: Ratio of the fully corrected b -jet spectra obtained using a response matrix that accounts for momentum smearing described by σ_{1/p_T} from Fig 5.40 and the response matrix for which the value of σ_{1/p_T} is increased by the RMS of B .

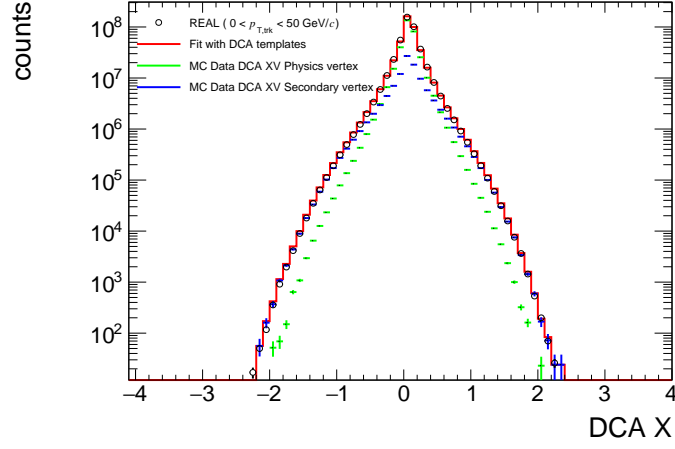


Figure 5.45: DCA distributions of charged hybrid tracks in p-Pb data. The real data are fitted with a sum two simulated templates corresponding to the DCA distribution of physical primaries and the DCA distribution of secondary tracks.

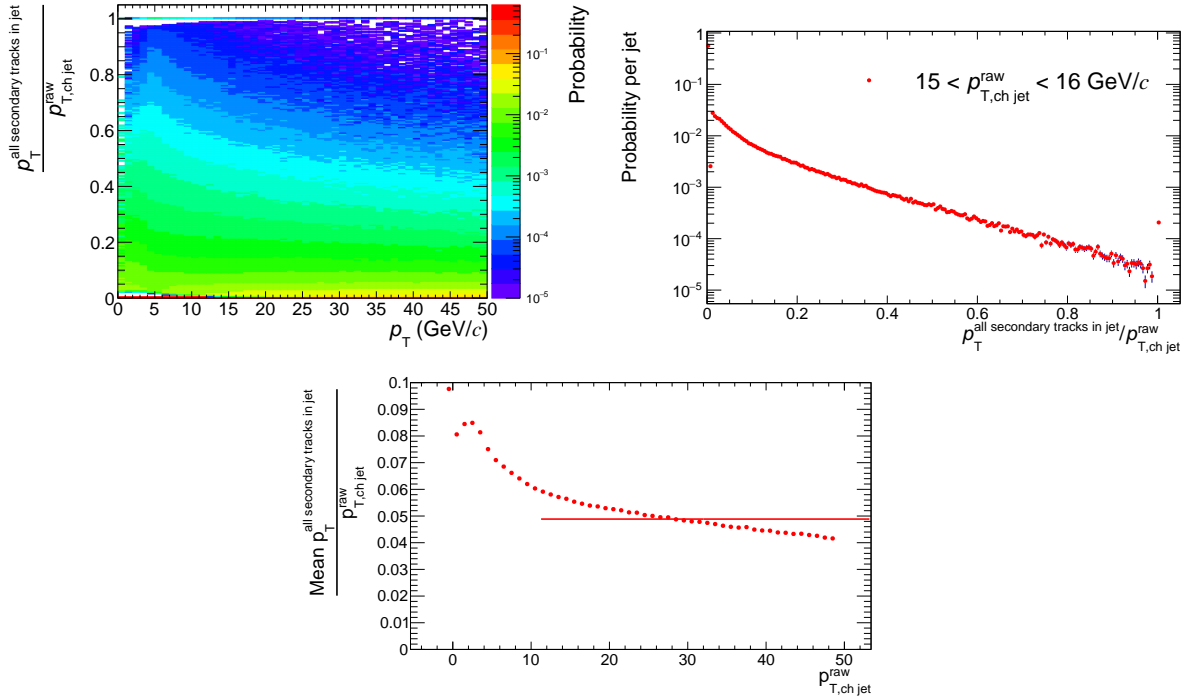


Figure 5.46: Left: Distribution of fractions of jet p_T carried by secondary tracks versus jet p_T . Right: Projection of the distribution in one jet p_T bin on the y -axis.

by secondary tracks, i.e., for each inclusive jet in a given p_T range, we sum up transverse momenta of its non-physical primary jet constituents and divide this number by the corresponding $p_{T,jet}^{raw}$. An example of the resulting distribution for $15 < p_{T,chjet} < 16$ GeV/ c jets is shown in the upper panel of Fig. 5.46. The very first data point on the left represents the jets which are formed by physical primaries only. The more one moves to the right, the more the p_T fraction carried by secondary tracks in a jet grows. The lower panel in Fig. 5.46 then shows the mean fraction of $p_{T,chjet}$ which is carried by non-physical primary tracks in an inclusive charged jet of given $p_{T,chjet}$. For anti- k_T jets with $R = 0.4$ and $p_{T,chjet} > 15$ GeV/ c this fraction is about 4.7%. Let us remind that the instrumental response matrix accounts for the corresponding jet transverse momentum shift. From the above discussed DCA fits, it is inferred that there is 29.9% more secondary tracks in the p-Pb data relative to PYTHIA filtered simulation. We assume that the fraction of jet p_T carried by secondary tracks should be also 29.9% larger, i.e. $1.299 \times 4.7\% = 6.1\%$. Hence, the relation between the unfolded jet p_T , which accounts for the 4.7% shift only, and the true jet p_T , which should correct for the shift of 6.1%, is expected to be

$$p_{T,jet}^{unfolded} = \xi \cdot p_{T,jet}^{true}, \quad (5.17)$$

where the ξ parameter corrects for the larger secondary track fraction, $\xi = 1.061/1.047 = 1.013$.

Systematic uncertainty of the fully corrected b -jet spectra which can be attributed to the difference between the secondary track abundances in the simulation and in the measured p-Pb data is estimated in the following way. The fully corrected b -jet distributions are fitted with a sum of exponentials

$$f(p_{T,jet}) = \sum_i a_i \cdot \exp[\xi \cdot p_{T,jet}/b_i] \quad (5.18)$$

where a_i and b_i are parameters of the fit and $\xi = 1.013$, see the left panel in Fig. 5.47. In each

spectrum bin, we evaluate an integral of the fit function (5.18) and an integral of a function (5.18) that has the same a and b but where $\xi = 1$. The ratio of these two integrals is the resulting systematic uncertainty, see the right panel in Fig. 5.47.

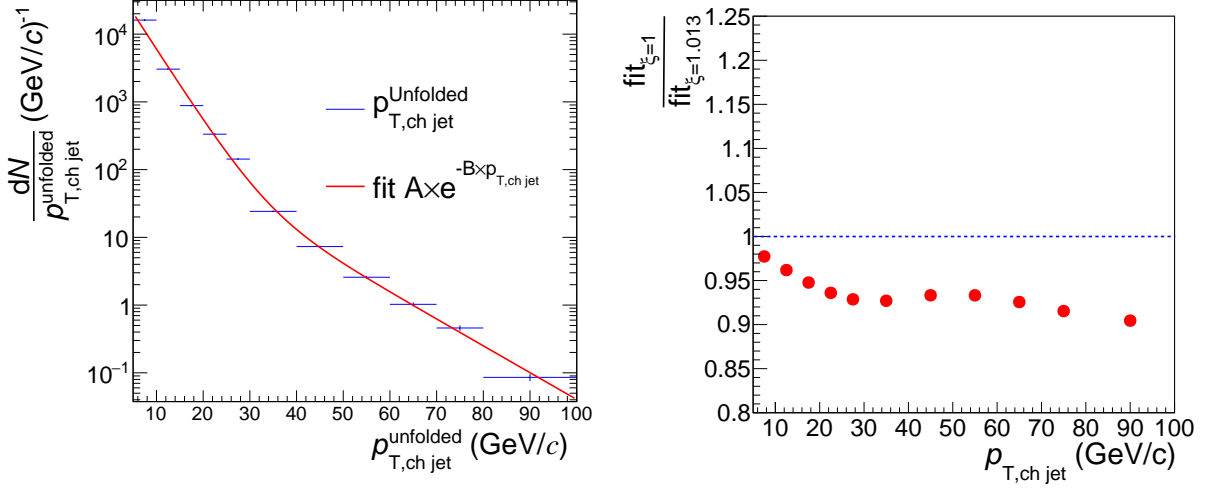


Figure 5.47: Left: Fit of the fully unfolded b -jet spectrum by (5.18). Right: Ratio of parametrizations (5.18) for $\xi = 1$ and $\xi = 1.013$ which gives the estimated systematic uncertainty on b -jet spectrum due to different secondary track admixture in real data and in the MC.

5.7 Results and Discussions

5.7.1 The b-Jet Cross Section with Systematics

The spectrum is corrected and unfolded using raw counts. Therefore we have calculated the cross-section as,

$$\sigma_{b-jet} = Y \sigma_{pPb}^{inel} / N \quad (5.19)$$

where Y is the measured yield in counts, $N = 6.0205018 \times 10^8$ is the number of events processed, and $\sigma_{pPb}^{inel} = 2090$ mb is the p-Pb inelastic cross section. The POWHEG simulations, intended for pp collisions, are scaled with $A = 208$ to make them p-Pb like. The results and systematics are shown in Fig. 5.48. A recent measurement of the p-Pb inelastic cross-section has been performed

in Ref. [181]. The corresponding scaling uncertainty is approx. 4%, which is not included in these measurements. The estimations of all sources of the systematic uncertainties are listed in the Table.5.6.

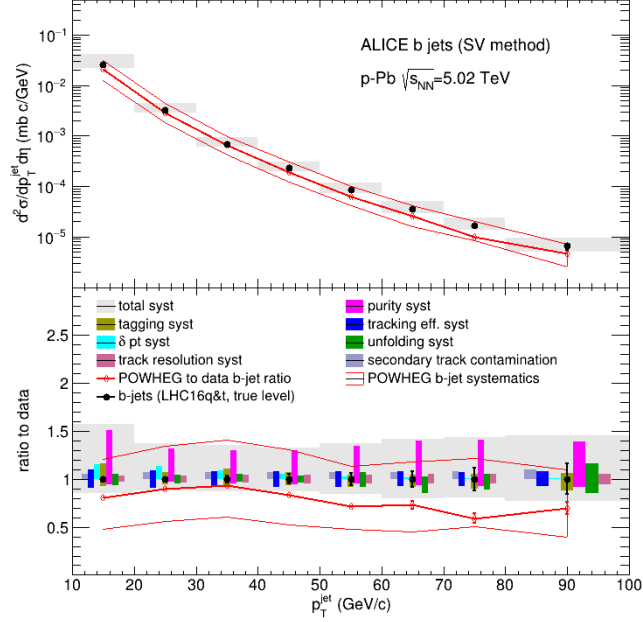


Figure 5.48: The b -jet cross section from Run2 LHC16q and LHC16t $\sqrt{s_{NN}} = 5.02$ TeV p-Pb collisions, together with the systematic contributions.

Table 5.6: Estimated systematic uncertainties of b -jet cross-section, in percentage (%).

p_T (GeV)	tracking eff.	δp_T	tagging	purity	unfolding	track resol.	sec.trk. contam.	total syst.
10–20	−9.2/ + 9.2	−0/ + 16	−4.7/ + 9.1	−25/ + 18	−8.5/ + 5.6	−3.3/ + 3.3	−0/ + 4.1	−28/ + 29
20–30	−8.6/ + 8.6	−0/ + 15	−3.2/ + 3.4	−17/ + 9.6	−7.6/ + 7.4	−3.8/ + 3.8	−0/ + 5.7	−22/ + 23
30–40	−7.8/ + 7.8	−0/ + 10	−5/ + 6.2	−14/ + 10	−3/ + 6.6	−4.2/ + 4.2	−0/ + 5.9	−17/ + 20
40–50	−7.9/ + 7.9	−0/ + 5.4	−4.3/ + 3.1	−11/ + 15	−4.4/ + 3.6	−4.5/ + 4.5	−0/ + 5.4	−16/ + 20
50–60	−7.7/ + 7.7	−0/ + 3	−6.3/ + 4.8	−11/ + 22	−9.6/ + 6.3	−4.7/ + 4.7	−0/ + 5.3	−18/ + 26
60–70	−7.2/ + 7.2	−0/ + 1.8	−7.3/ + 5.4	−14/ + 29	−13/ + 2.6	−5/ + 5	−0/ + 6	−22/ + 31
70–80	−6.6/ + 6.6	−0/ + 0.96	−9/ + 4.9	−15/ + 30	−14/ + 5.7	−5.1/ + 5.1	−0/ + 6.8	−24/ + 33
80–100	−6.5/ + 6.5	−0/ + 0.23	−11/ + 5.9	−16/ + 29	−18/ + 15	−5.3/ + 5.3	−0/ + 7.8	−28/ + 35

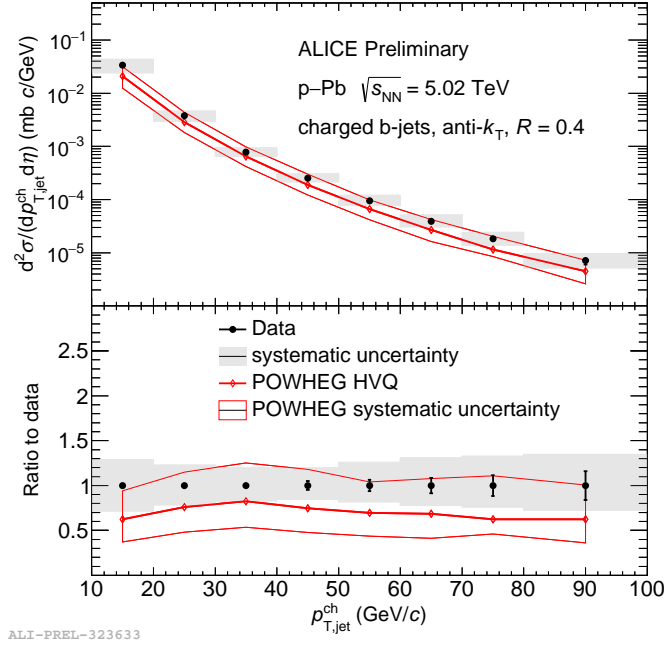


Figure 5.49: Upper panel: The measured b -jet cross-section as a function of charged jet p_T . Lower panel: The ratio of the measured b -jet spectra with the NLO pQCD calculations (POWHEG).

5.7.2 Comparison of b -Jet Cross Section with NLO pQCD Calculations

The p_T -differential production cross section for b -jets reconstructed from charged particles in minimum bias p-Pb collisions at $\sqrt{s_{NN}} = 5.02$ TeV is shown in Fig. 5.49 for the resolution parameter $R = 0.4$. We have compared the measured b -jet cross-section with NLO pQCD calculations (POWHEG+PYTHIA). The measured b -jet cross-section is in agreement with the NLO pQCD calculations within the experimental and theoretical uncertainties as seen in the ratio (data over calculation) plot in the lower panel of Fig. 5.49.

Summarizing this chapter, the b -jet production cross section has been measured for p-Pb collisions at $\sqrt{s_{NN}} = 5.02$ TeV and compared with the NLO pQCD calculations. The b -jet production cross section is found to be compatible with NLO pQCD calculations at the same energy. The identification of b -jets among the reconstructed charged jets is done by finding the displaced secondary vertices within the jets which exploits the long life time of B-hadrons. The

tagged jets are corrected for the tagging efficiency and purity. They are further corrected for the detector effects via unfolding. Finally the systematic uncertainty estimations are done for the measurement. The great uniqueness of this measurement is the low p_T reach. The b -jet production cross section has been measured from 10 GeV/ c ($p_T^{chjet} > 10$ GeV/ c) which is very much challenging. The previous measurements of CMS and ATLAS collaborations were for the higher p_T region (beyond 50 GeV/ c). Our measured b -jet production cross section could be used to study the cold nuclear matter effect for p-Pb collisions, specially at the lower momentum region. The cold nuclear matter effect is important to understand for the study of the impact of the hot nuclear matter (QGP) effect on heavy flavor jets, significantly at the lower momentum region where the mass dependent energy loss is prominent. This is the beauty of the b -jet measurement in ALICE at the lower momentum region.

Chapter 6

Summary

In this thesis, we have presented the measurement of reconstructed inclusive bottom quark jet (b -jet) production in p-Pb collisions at $\sqrt{s_{NN}} = 5.02$ TeV in the ALICE experiment at the LHC. However, we have also studied the effect of chromo-electromagnetic field fluctuations on heavy quark jet propagation in the QGP medium.

We have analyzed the ALICE minimum bias data in p-Pb collisions at $\sqrt{s_{NN}} = 5.02$ TeV, recorded in Run-2 in the year of 2016. The measurement of b -jet production in p-Pb collisions addresses several key points like pQCD production cross-section, cold nuclear matter effect and base line for nucleus-nucleus collisions. Apart from these, the b -jet measurement in p-Pb collisions are interesting to investigate the interplay between heavy quark jets and the nuclear environment.

In this analysis, the jet reconstruction has been performed by using the currently most prevalent jet finding algorithm at the LHC: the anti- k_T algorithm, which is implemented in the FastJet package. For jet reconstruction, we have used the charged tracks reconstructed with the ALICE tracking system. The secondary vertices are found within these reconstructed jets (with resolution parameter, $R = 0.4$) and the properties (large decay lengths) of the secondary vertices are used to tag the b -jets among other flavor jets. We have optimized the topological cuts (SL_{xy} and σ_{SV})

related to the secondary vertices based on b -jet tagging efficiency and mistagging rate, and the optimized cuts chosen for the principal analysis are $SL_{xy} > 7$ and $\sigma_{SV} < 0.03$ cm. The other variations of these optimized cuts are taken as systematic uncertainties related to the tagging procedure. The b -tagged jets are obtained after correcting the tagged jets for tagging efficiency and purity. The tagging efficiency is obtained from PYTHIA+EPOS MC simulation. The purity is obtained in two methods: MC method (POWbc) based on MC simulation and data driven method based on the template fitting of invariant mass at the secondary vertices. The closure tests for the mass template fitting have also been shown. The purities obtained in these two methods are consistent with each other. Keeping these in mind, we have developed a hybrid method for the purity using a χ^2 test. The other correction techniques, mainly the background correction and the unfolding for detector effects have been applied to obtain fully corrected theory-comparable b -jets. An event-wise background density are subtracted in the jet-by-jet basis, taking into account the jet area. The backgrounds from one jet to another jet may fluctuate which smear the measurements. The background fluctuations are estimated by Random Cone (RC) algorithm. The background fluctuations have been taken into account in the unfolding procedure. The unfolding of the measured b -jet spectra is performed by the iterative methods, Bayesian and Singular Value Decomposition (SVD) methods. We have also estimated the systematic uncertainties for this measurement. The main sources of the systematic uncertainties are related to unfolding, tracking efficiency, tagging procedure and purity estimation.

The corrected measurement for p_T -differential b -jet cross section is compared with the NLO pQCD calculations (POWHEG). The POWHEG is a Monte Carlo event generator for heavy quark pair production at NLO. The measured b -jet spectra is in agreement with the NLO pQCD calculations within the experimental and theoretical uncertainties.

This measurement of b -jet is very much relevant in high energy collisions, particularly for

the mass dependent study in terms of production, fragmentation and energy loss in the partonic medium. The energy loss encountered by an energetic parton in a QGP medium reveals the dynamical properties of that medium in view of jet quenching of high energy partons. This is usually reflected in the transverse momentum spectra and nuclear modification factor of mesons which are measured in heavy-ion experiments. For the phenomenology of the heavy quarks jet quenching, the field fluctuations in the QGP medium were not considered in the literature before. In this thesis, we have also reported the propagation of high energy heavy quarks by including the energy gain due to field fluctuations along with the energy loss caused by the collisions and gluon radiations inside the QGP medium. We found significant effect of these fluctuations in explaining the experimentally observed heavy flavor suppression at the RHIC and LHC energies. We have also observed that these field fluctuations affect η/s of the QGP medium. The effect of field fluctuations in hot and dense QGP medium is found to play an important role in the propagation of heavy quark jets.

Appendix A

A.1 Jet Reconstruction Algorithm

A jet is defined by the jet reconstruction algorithm used to group final state particles into jet candidates. A robust jet finding algorithm would find the same jet with the same p_T regardless of the details of the fragmentation and would thus be collinear safe. It should also be infrared safe, i.e., the jet finding algorithm will find the same jets, even in the presence of a large number of soft partons. Therefore a robust jet finding algorithm should be collinear safe as well as infrared safe. The most commonly used jet finding algorithms in high energy heavy-ion collisions are the anti- k_T and k_T algorithm which are implemented in the FastJet package [168] and are infrared and collinear safe.

The anti- k_T jet finding algorithm is a sequential recombination, which does the grouping of particles into jet candidates and the algorithm is repeated unless and until all particles in an event become part of a jet. The steps are the followings:

1. Calculate the distance between every pair of particles (i^{th} and j^{th} particles) as

$$d_{ij} = \min(1/p_{T,i}^2, 1/p_{T,j}^2) \frac{\Delta R_{ij}^2}{R^2} \quad (\text{A.1})$$

and

$$d_i = 1/p_{T,i}^2 \quad (\text{A.2})$$

where $R = \sqrt{\Delta\phi^2 + \Delta\eta^2}$ (with $\Delta\phi$ and $\Delta\eta$ are the distances from the jet axis in azimuth and pseudorapidity respectively) is the jet resolution parameter; $\Delta R_{ij} = \sqrt{(\phi_i - \phi_j)^2 + (\eta_i - \eta_j)^2}$; $p_{T,i}$, $p_{T,j}$ are the transverse momenta, η_i , η_j are the pseudorapidities and ϕ_i , ϕ_j are the azimuthal angles of the i^{th} and j^{th} particles.

2. Compare the two distances d_{ij} and d_i . If $d_{ij} < d_i$, combine these particles into one jet

candidate, adding their energies and momenta, and return to the first step.

3. If $d_i < d_{ij}$, i^{th} particle is a final state jet candidate. Remove it from the list and return to the first step. Iterate until no particles remain left in the list.

The anti- k_T algorithm has some notable features. It finds the minimum of the distance d_{ij} , which is smallest for pairs of high- p_T particles. Hence it starts clustering high- p_T particles first into jets and forms a jet around these particles.

Unlike anti- k_T algorithm, the k_T jet finding algorithm starts clustering low- p_T particles first into jets and hence used in the estimation of background event density which is important to subtract from the raw jets to get the pure signal jets.

A.2 POWHEG+PYTHIA

Next-to-leading order (NLO) QCD computations become the standard tools for phenomenological studies at lepton and hadron colliders since the last two decades. QCD tests have been mainly performed by comparing NLO computations with experimental measurements after correcting the experimental measurements for detector effects. The Shower Monte Carlo (SMC) programs include dominant QCD effects at the leading logarithmic (LL) level, but unfortunately they do not have NLO accuracy. Thus when a precision measurement is needed, to be compared with an NLO calculation, it is not possible to directly compare the measurements with the SMC output. The output of SMC simulation is used on the one hand to correct the data for detector effects and on the other to correct NLO theory calculations to account non-perturbative effects. It is clear that SMC programs should be improved to NLO accuracy and thus provide a large amount of QCD corrections available. The problem of merging NLO calculations with SMC simulations is basically that of avoiding overcounting, since the SMC programs do implement approximate NLO corrections already. The first acceptable solution to the overcounting problem was given by MC@NLO [182]. The basic idea of this method is to subtract the approximated cross section, which is implemented in the SMC, from the exact NLO cross section. In general, the exact NLO cross section minus the SMC subtraction terms does not need to be positive. So, MC@NLO can generate events with negative weights. Therefore another method is used to determine the NLO matrix elements to be interfaced with any SMC and provides positive event weights. NLO calculations for the hard process are obtained with the POWHEG (Positive Weight Hardest Emission Generator) [171, 172, 173] method which gives the positive weighted events.

The general features of POWHEG are,

- i. Hardest emission is generated first with NLO accuracy.

- ii. Positive weighted events are generated.
- iii. Interface with any SMC program.
- iv. Infrared-safe observables have NLO accuracy and collinear emission are summed at the LL level .
- v. Double logarithmic region (i.e. soft and collinear gluon emission) is treated correctly if the SMC code used for showering has this capacity.

A.2.1 Interfacing POWHEG with PYTHIA

Interfacing the POWHEG output with an angular ordered SMC generator is important enough as we have described earlier in Sec.A.2. Here we interface POWHEG with PYTHIA6 [112] SMC program which also serves the purpose of hadronization of the initially hardest emission partons.

The interfacing is done with AliGenPythia class as implemented in AliRoot software package. First, POWHEG processes are initiated then the output of POWHEG is linked to the PYTHIA6 by using “SetProcess” function of AliGenPythia class. After that, target, projectile and range of other observables like rapidity, momentum , etc. have been set. Finally one can pass the PYTHIA output with some detector simulation. This last is optional, depends on the requirement.

A.2.2 POWHEG Settings

In order to generate the NLO calculations and the hardest emission events one needs the correct settings in the steering file powheg.input. The settings according to our investigations of b -jets are given here. We generate heavy flavor pair ($c\bar{c}$ and $b\bar{b}$) using the following settings in the input file:

- numevts 10000 ! number of events to be generated
- ih1 1 ! hadron 1 (1 for protons, -1 for antiprotons)

- ih2 1 ! hadron 2 (1 for protons, -1 for antiprotons)
- lhans1 11000 ! pdf set for hadron 1 (LHA numbering)
- lhans2 11000 ! pdf set for hadron 2 (LHA numbering)
- ebeam1 2510 ! energy of beam 1
- ebeam2 2510 ! energy of beam 2
- qmass 1.5 ! mass of heavy quark in GeV/c^2 (qmass = 1.5 GeV/c^2 for c quark mass and 4.75 GeV for b quark mass)

The above block gives the numbers of events, type, parton distribution function and energy of the colliding partons.

One can also set the QCD factorization and renormalization scale as following:

- facscfact 1 ! factorization scale factor: $\text{mufact}=\text{muref}*\text{facscfact}$
- rensfact 1 ! renormalization scale factor: $\text{muren}=\text{muref}*\text{rensfact}$

The other parameters we have used are:

- ncall1 50000 ! number of calls for initializing the integration grid
- itmx1 5 ! number of iterations for initializing the integration grid
- ncall2 100000 ! number of calls for computing the integral and finding upper bound
- itmx2 5 ! number of iterations for computing the integral and finding upper bound
- foldcsi 5 ! number of folds on x integration
- foldy 5 ! number of folds on y integration

- foldphi 1 ! number of folds on phi integration
- nubound 500000 ! number of bbarra calls to setup norm of upper bounding function
- iymax 1 ! j= 10, normalization of upper bounding function in iunorm X iunorm square in y, $\log(m_{2qq})$
- ixmax 1 ! j= 10, normalization of upper bounding function in iunorm X iunorm square in y, $\log(m_{2qq})$
- xupbound 2 ! increase upper bound for radiation generation

A.2.3 POWHEG Systematics

We studied $c\bar{c}$ and $b\bar{b}$ pair production with variations of several parameters in the POWHEG input file. We varied the mass of c and b quarks and factorization and renormalization scale from their default values. In each and every case of different scale variation, we found a considerable change in the cross section of heavy quark pair production.

Heavy Quarks Mass Variation

We varied c quark mass from $1.5 \text{ GeV}/c^2$ (default value) to $1.3 \text{ GeV}/c^2$ and $1.7 \text{ GeV}/c^2$ and b quark mass from $4.75 \text{ GeV}/c^2$ (default value) to $4.5 \text{ GeV}/c^2$ and $5 \text{ GeV}/c^2$. Please keep a note here that we kept the other parameters fixed while varying the mass of the heavy quark pairs in the POWHEG input file.

In Figs. A.1 and A.2, we show cross section of c and b quark pair production as a function of p_T respectively, when their masses are varied from the default values in POWHEG (left panel). We also plot their ratios (right panel). The cross section obtained from POWHEG is compared with FONLL (Fixed Order and Next to Leading Log) QCD calculations. The cross section for

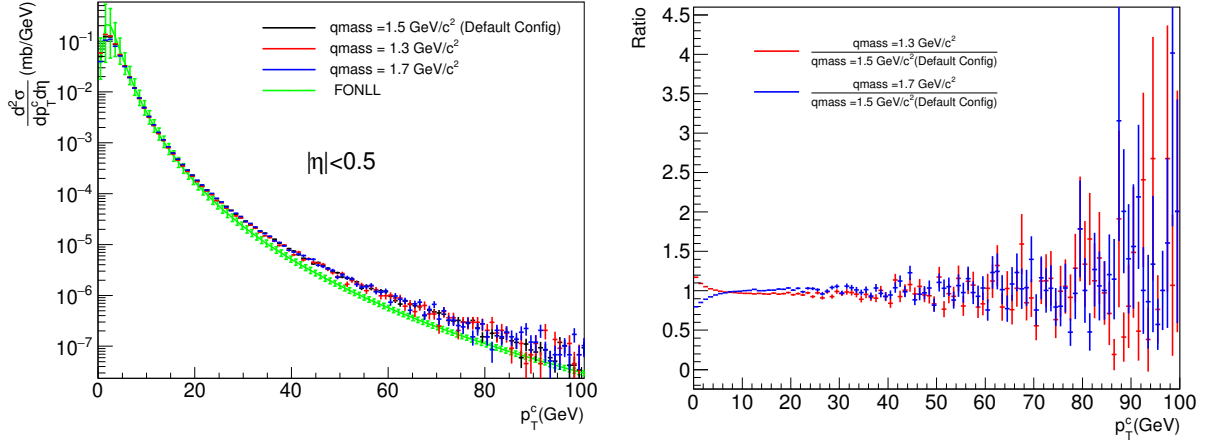


Figure A.1: Production cross section of c quark pair for mass variation of c quark, in mid rapidity as a function of transverse momentum, p_T (left) and their ratio as a function of p_T (right).

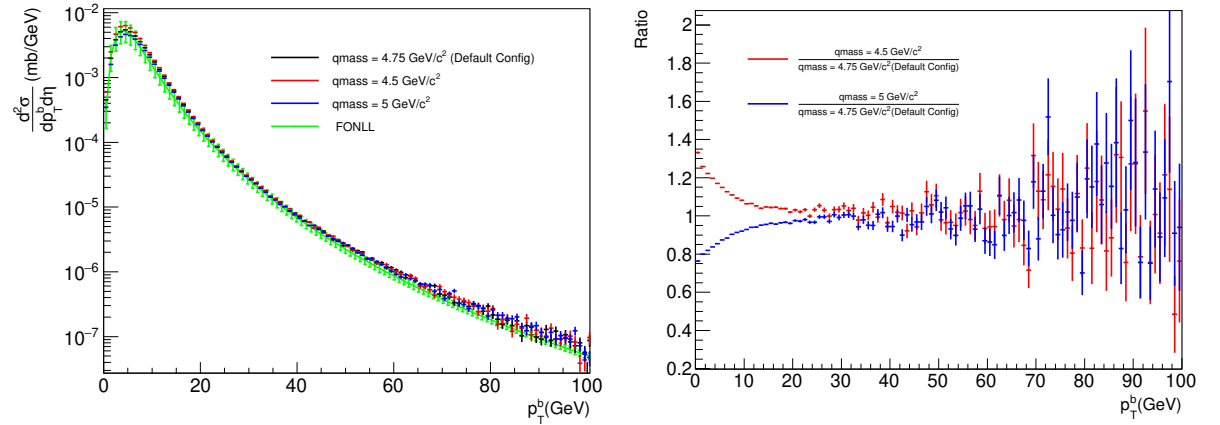


Figure A.2: Same as Fig. A.1, but for b quark pair.

default mass value of c and b quark agree well with FONLL calculation. The cross section for mass variation is close to the FONLL calculation.

Factorization Scale Variation

QCD factorization scale has been varied from 1 (default value) to 0.5 and 1 for two different renormalization scale values, 0.5 and 2.

Fig. A.3 displays c quark pair production cross section as a function of p_T for variation of factorization scale with two different values of renormalization scale, 0.5 and 2. The obtained cross

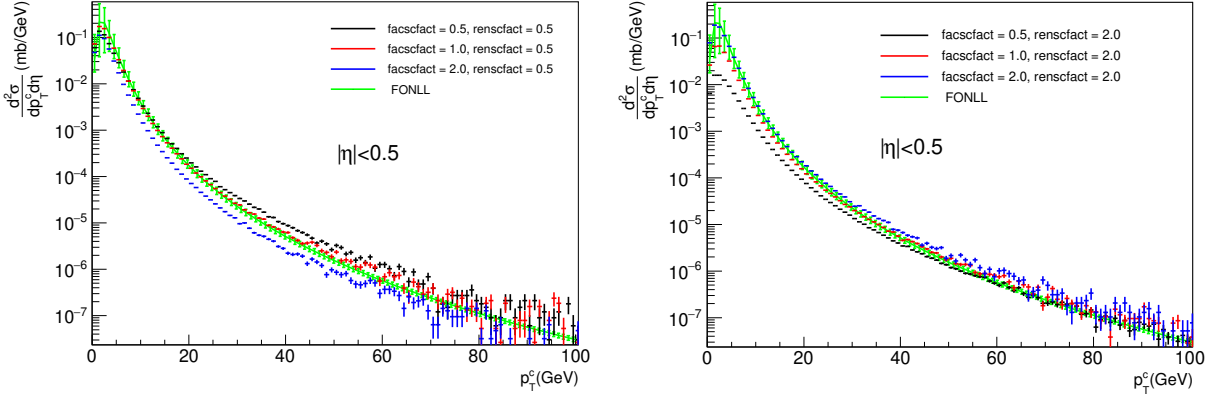


Figure A.3: c quark pair production cross section in mid rapidity as a function of p_T . The cross section is obtained for factorization scale variation with renormalization scale 0.5 (left) and 2 (right).

section is also compared with the FONLL calculation. They do not match FONLL calculation very much.

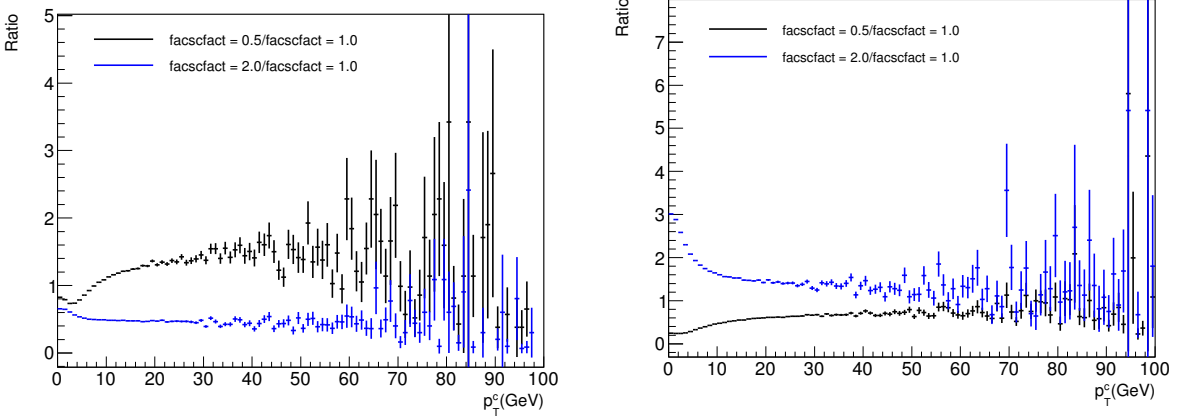
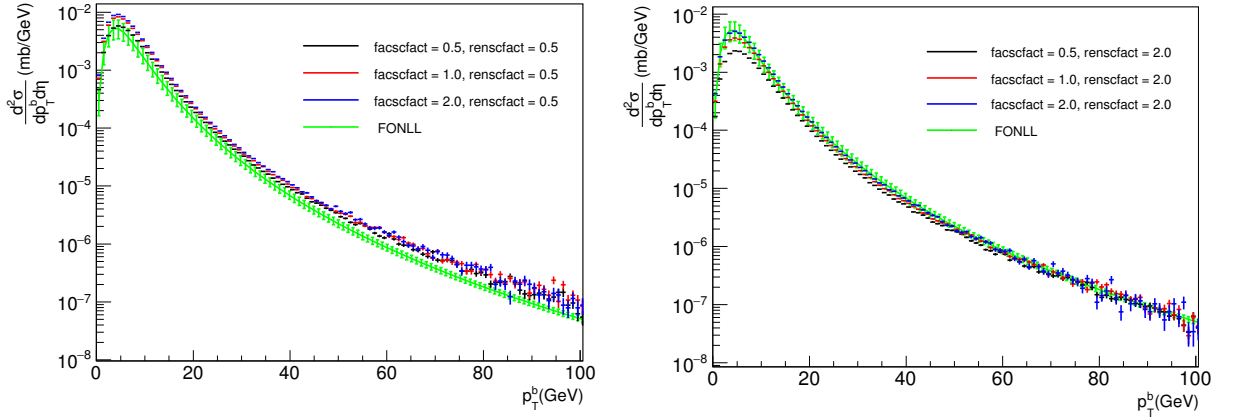


Figure A.4: Ratio of c quark pair production cross section. The ratio is between cross section from factorization scale 0.5 and 2 with the default value for renormalization scale value 0.5 (left) and 2 (right).

Fig. A.4 shows ratio of c quark pair production cross section obtained for factorization scale 0.5 and 2 with default value of factorization scale. The ratio is greater than 1 for factorization scale 0.5 and less than 1 for factorization scale 2.

b quark pair production cross section as a function of p_T for variation of factorization scale

Figure A.5: Same as Fig.A.3, but for b quark.

with two different values of renormalization scale, 0.5 and 2 has been displayed in Fig.A.5. The obtained cross section has also been compared with the FONLL calculation. They are close to the FONLL results.

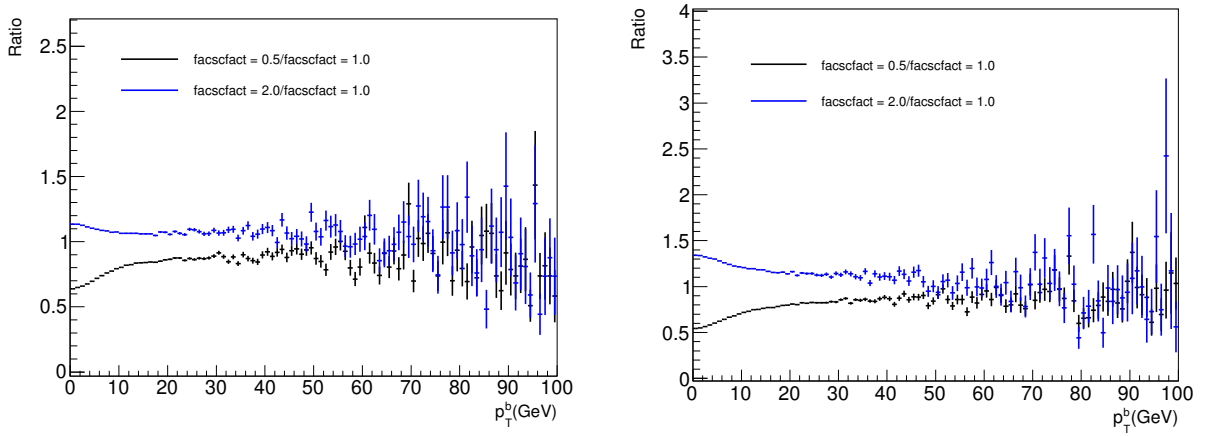
Figure A.6: Same as Fig.A.4, but for b quark. The left panel is for renormalization scale 0.5 and right panel is for renormalization scale 2.

Fig. A.6 shows ratio of b quark pair production cross section, obtained for factorization scale 0.5 and 2 with default value of factorization scale. The ratio is greater than 1 for factorization scale 0.5 and less than 1 for factorization scale 2.

Renormalization Scale Variation

We also vary QCD renormalization scale from 1 (default value) to 0.5 and 1 for two different factorization scale values, 0.5 and 2.

Fig. A.7 displays c quark pair production cross section as a function of p_T for variation of renormalization scale with two different values of factorization scale, 0.5 and 2. The obtained cross section is also compared with the FONLL calculation.

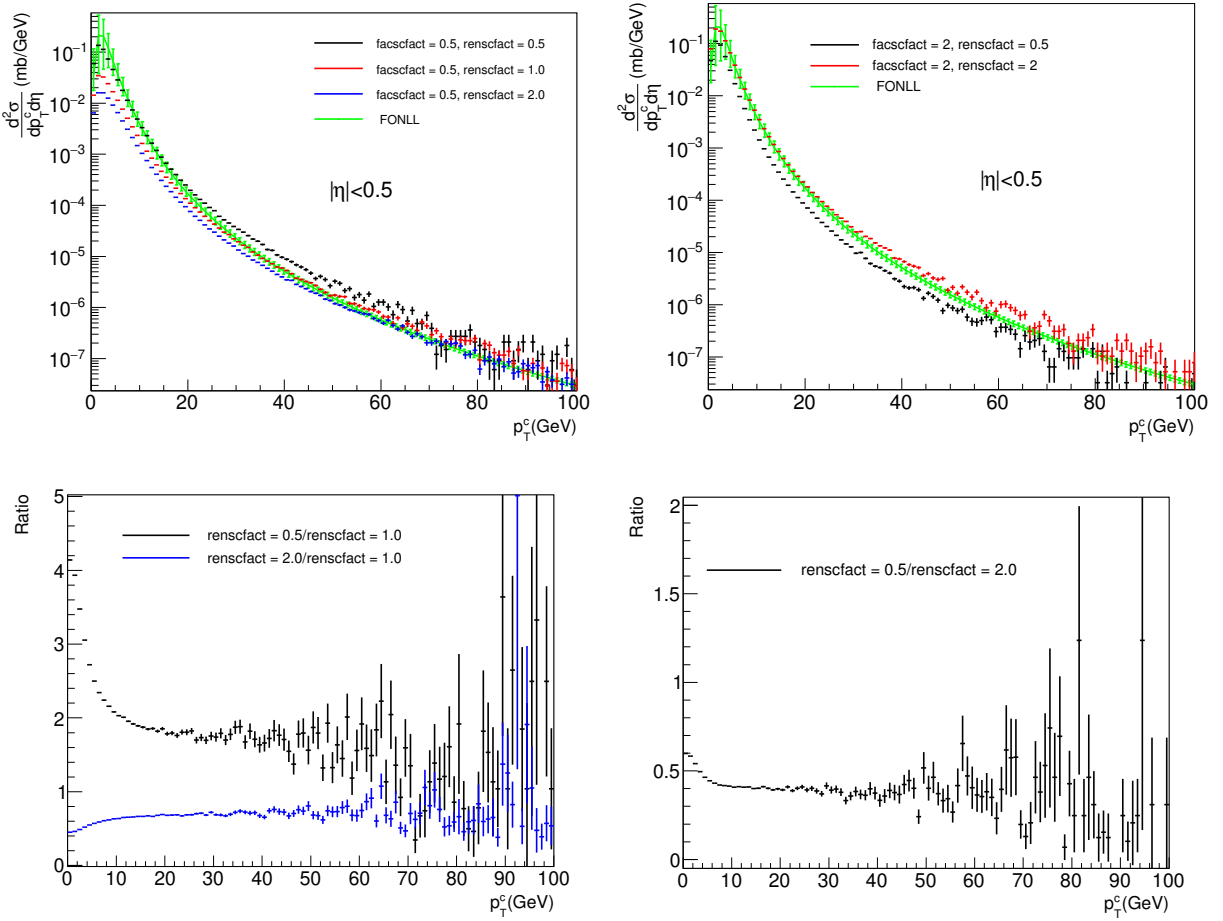


Figure A.7: c quark pair production cross section in mid rapidity as a function of p_T . The cross section is obtained for renormalization scale variation with factorization scale 0.5 (upper left) and 2 (upper right) and their ratio for factorization scale 0.5 (lower left) and 2 (lower right).

The ratios of c quark pair production cross section, obtained for renormalization scale 0.5 and 2 with default value of renormalization scale have been shown in the lower panel of Fig. A.7. The

ratio is greater than 1 for renormalization scale 0.5 and less than 1 for renormalization scale 2.

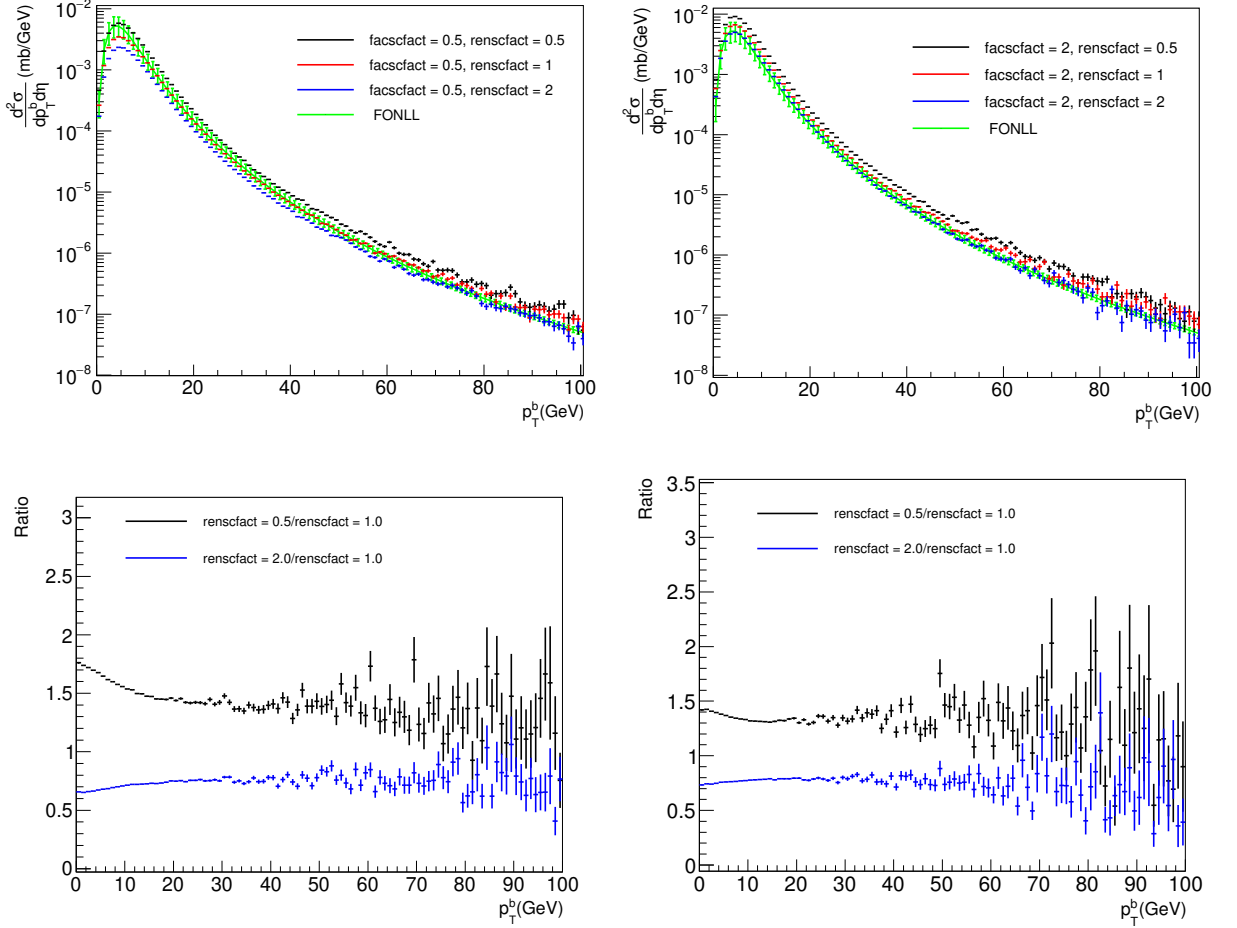


Figure A.8: Same as Fig. A.7, but for b quark.

Fig. A.8 shows b quark pair production cross section and their ratio as a function of p_T for variation of renormalization scale with two different values of factorization scale, 0.5 and 2. The obtained cross section is also compared with the FONLL calculation. The ratio is greater than 1 for renormalization scale 0.5 and less than 1 for renormalization scale 2. The observation is similar to c quark production.

A.3 Optimization of Tagging Cuts

Finding an efficient cut that reduces contamination from lighter flavor is essential in the analysis. Besides that we also want our method to be robust, to understand our efficiencies and sample purities. The tagging selection shouldn't be sensitive to peculiarities that may be biased in the Monte Carlo. Also we do not want to rely on any jet-shape-sensitive variables that might be influenced by nuclear modification, ie. we do not want to do a selection that depends our quantity to be measured. We want to exclude any bias on our evaluation variables, therefore we do not use the discrimination power provided by the secondary vertex mass, which is used in the data driven purity estimation.

The following variables are considered for discrimination of the b -jets:

- The (x, y) projection of the primary-secondary vertex, L_{xy} ;
- The normalized distance $SL_{xy} = L_{xy}/\sigma_{L_{xy}}$ (where $\sigma_{L_{xy}}$ is the width of the L_{xy} distribution);
- The vertex dispersion σ_{SV} .

This cut optimization concentrates on the following variables:

- Probability distributions of a given variable (eg. L_{xy} or σ_{SV}) in the beauty, charm and light jet samples;
- Cut efficiencies $\epsilon(x)$ of the given variable at given x points (eg. $SL_{xy} > x$ or $\sigma_{SV} < x$), for beauty, charm and light jet samples;
- The suppression factors of contaminating charm and light flavor in the beauty sample, $SF_{\text{charm}}(x) = \epsilon_{\text{charm}}(x)/\epsilon_{\text{beauty}}(x)$ and $SF_{\text{LF}}(x) = \epsilon_{\text{LF}}(x)/\epsilon_{\text{beauty}}(x)$.

More details can be found at [\[183\]](#).

A 2D Look at SL_{xy} Vs σ_{SV} :

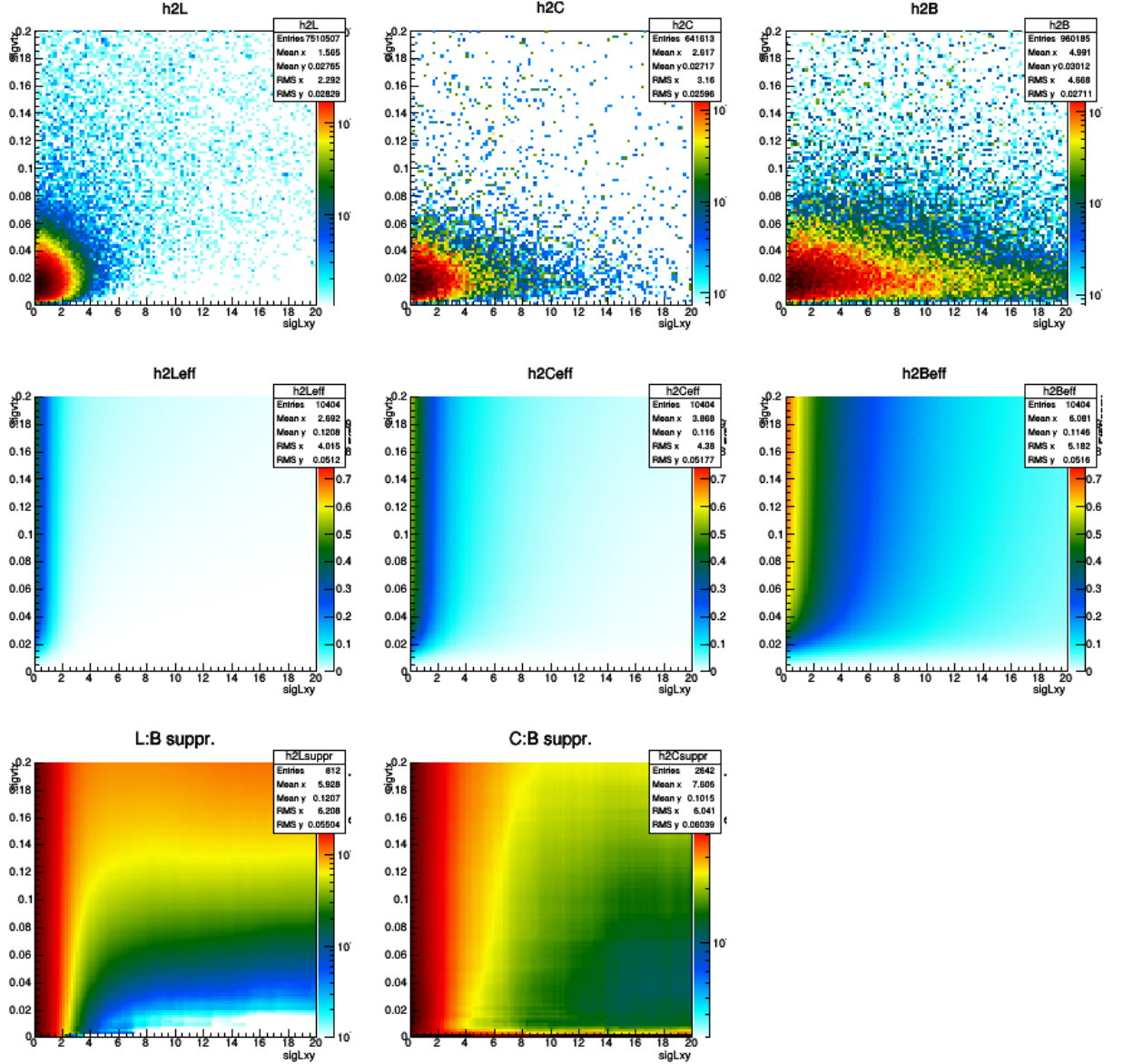


Figure A.9: $p_{T,jet}$ -integrated 2D distributions of SL_{xy} and σ_{SV} , as well as efficiencies and suppression factors of SL_{xy} & σ_{SV} cuts.

Fig. A.9 shows a ($p_{T,jet}$ -integrated) 2D distribution of SL_{xy} and σ_{SV} . Here the correlation between the two quantities is relatively weak, unless σ_{SV} is very small. If we apply some σ_{SV} cut at least, ≈ 0.02 , then the SL_{xy} cut can be chosen relatively independently for that. On the other hand, the suppression factors (especially light flavor suppression) of the σ_{SV} are mostly

independent of the SL_{xy} cut. These statements hold as long as we consider $p_{T,jet}$ -integrated efficiency. Whether the efficiencies are stable versus $p_{T,jet}$ is a crucial question for the robustness of our understanding of the corrections from simulations.

The SL_{xy} Cut Vs $p_{T,jet}$:

Fig. A.10 shows the SL_{xy} distributions and the effect of a cut on this quantity in several $p_{T,jet}$ bins.

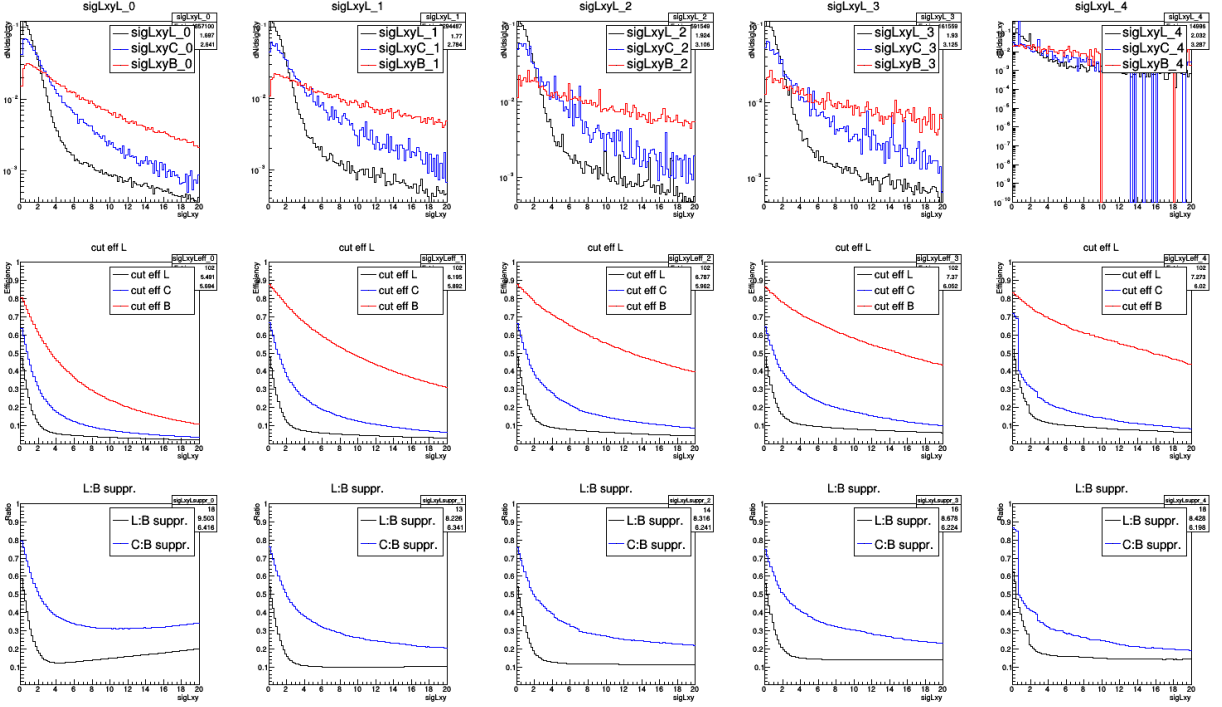


Figure A.10: Cut behavior on SL_{xy} distributions for b -jets (red), c -jets (blue) and light flavor jets (black), with different $p_{T,jet}$ selections (left to right, $p_{T,jet}$ -inclusive, $5 < p_{T,jet} < 20$ GeV/c, $20 < p_{T,jet} < 40$ GeV/c, $40 < p_{T,jet} < 60$ and $60 < p_{T,jet} < 100$ GeV/c. Top row is distributions, middle row is efficiency and bottom row is the suppression factor of a $SL_{xy} > x$ cut placed at a given x position.

There are two remarkable observations on this figure. The first is that the relative independence of the efficiencies of the SL_{xy} on the $p_{T,jet}$ window. This makes it an ideal quantity that ensures flat efficiency and purity curves (as long as other cuts are not very $p_{T,jet}$ -sensitive, of course). The other is that the suppression factors tend to saturate after a point (in the integrated case, there's

even a minimum, but that is coming from the low- $p_{T,jet}$ events less interesting in our analysis). Light flavor suppression saturates at around $SL_{xy} > 3$, meaning that sacrificing more b -jets will not help in achieving any better LF rejection. The charm suppression curve continues to fall slowly, so by placing SL_{xy} at higher values one can achieve higher purity, but it is obvious from the figure that we do not want to place this cut very high, perhaps nowhere beyond $SL_{xy} > 8$.

The σ_{SV} Cut Vs $p_{T,jet}$:

Here we have a look at the σ_{SV} cut. We consider the SL_{xy} as the first cut have already been done, so we examine some scenarios with the $SL_{xy} > x$ cut already applied. Figs. A.11–A.13 show the σ_{SV} distributions and the effect of a cut on this quantity in several $p_{T,jet}$ bins, after a preceding $SL_{xy} > 3, 5$ and 7 cut.

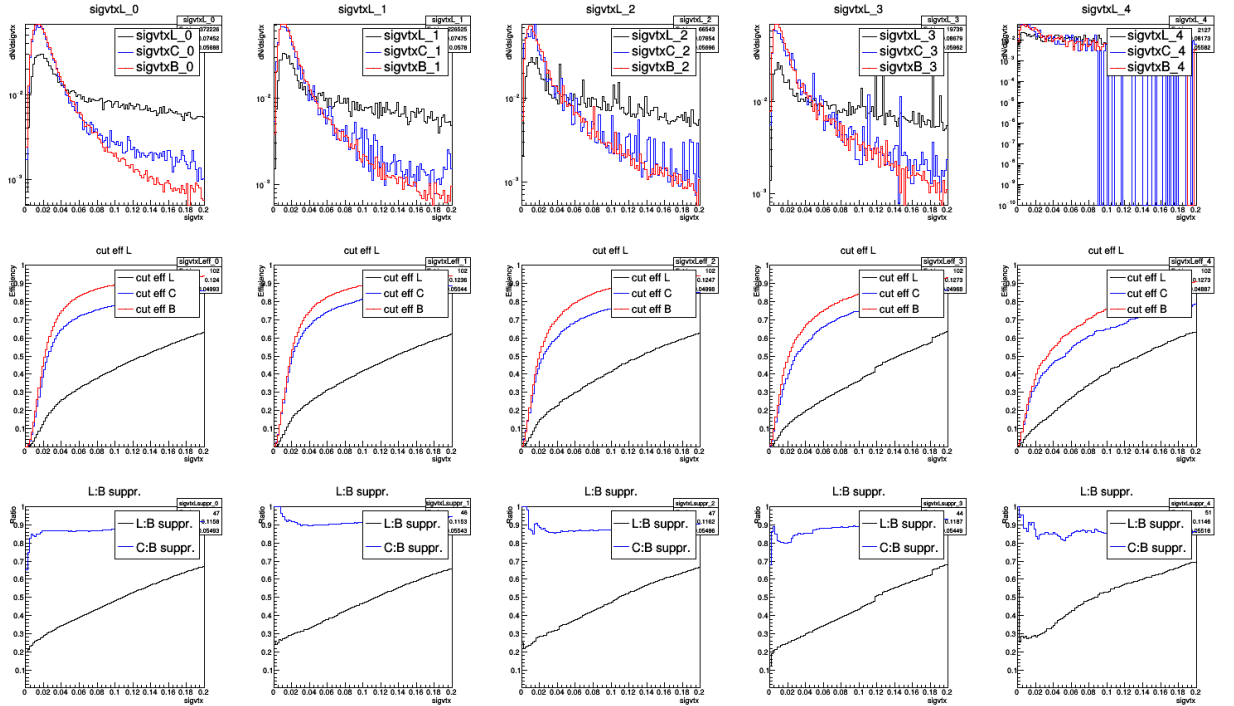


Figure A.11: Cut behavior on σ_{SV} distributions for b -jets (red), c -jets (blue) and light flavor jets (black), after an applied $SL_{xy} > 3$ cut, with different $p_{T,jet}$ selections (left to right, $p_{T,jet}$ -inclusive, $5 < p_{T,jet} < 20$ GeV/c, $20 < p_{T,jet} < 40$ GeV/c, $40 < p_{T,jet} < 60$ and $60 < p_{T,jet} < 100$ GeV/c. Top row is distributions, middle row is efficiency and bottom row is the suppression factor of a σ_{SV} cut placed at a given x position.

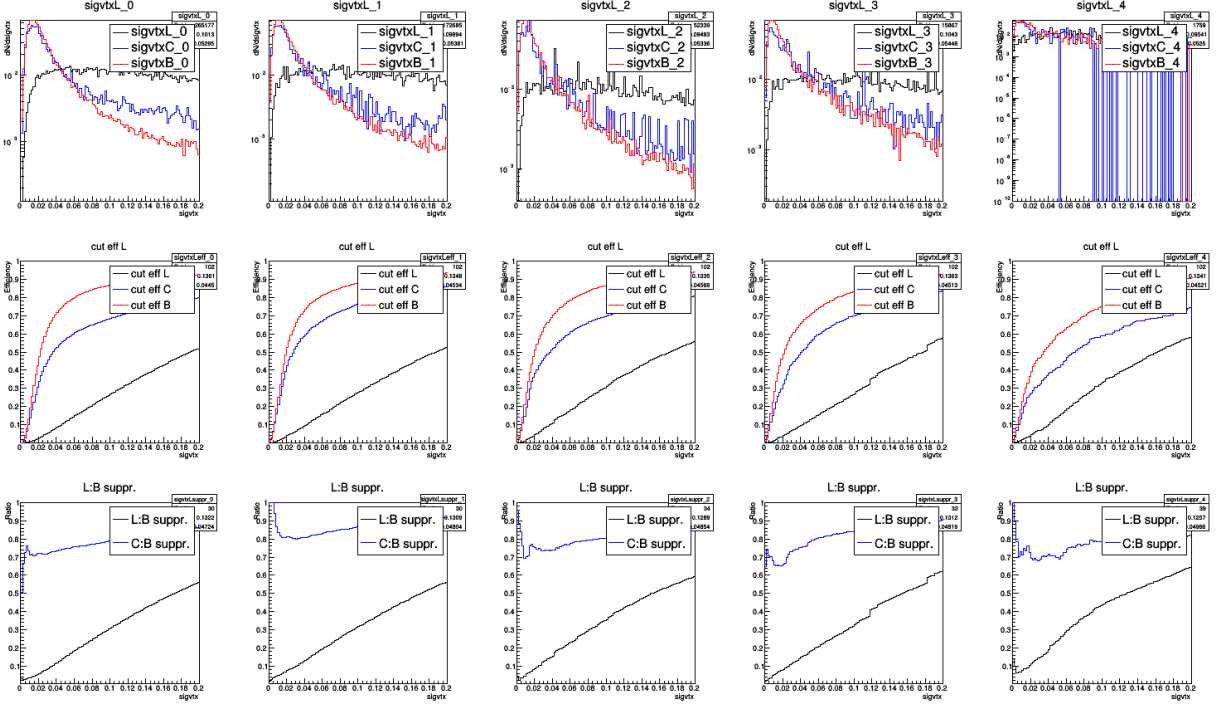


Figure A.12: Cut behavior on σ_{SV} distributions for b -jets (red), c -jets (blue) and light flavor jets (black), after an applied $SL_{xy} > 5$ cut, with different $p_{T,jet}$ selections (left to right, $p_{T,jet}$ -inclusive, $5 < p_{T,jet} < 20$ GeV/ c , $20 < p_{T,jet} < 40$ GeV/ c , $40 < p_{T,jet} < 60$ and $60 < p_{T,jet} < 100$ GeV/ c). Top row is distributions, middle row is efficiency and bottom row is the suppression factor of a σ_{SV} cut placed at a given x position.

A.3.1 Optimum Range for Tagging Cuts

Summarizing the above considerations on the suppression of contamination, the sweet region can be loosely defined as $\sigma_{SV} > 0.02$ cm to $\sigma_{SV} > 0.05$ cm and a $SL_{xy} > 3$ to $SL_{xy} > 8$. We may want to avoid strong losses from a harsh σ_{SV} cut, and also it seems better to avoid the very unstable low region, so the current choice is $\sigma_{SV} > 0.03$ cm & $SL_{xy} > 7$, while we vary the cuts in the above region for systematic checks.

A.4 Invariant Mass Templates

A.4.1 Data-Driven Purity Template Fits

Data-driven purity template fits for different tagging cuts are shown in Figs. A.14 to A.19:

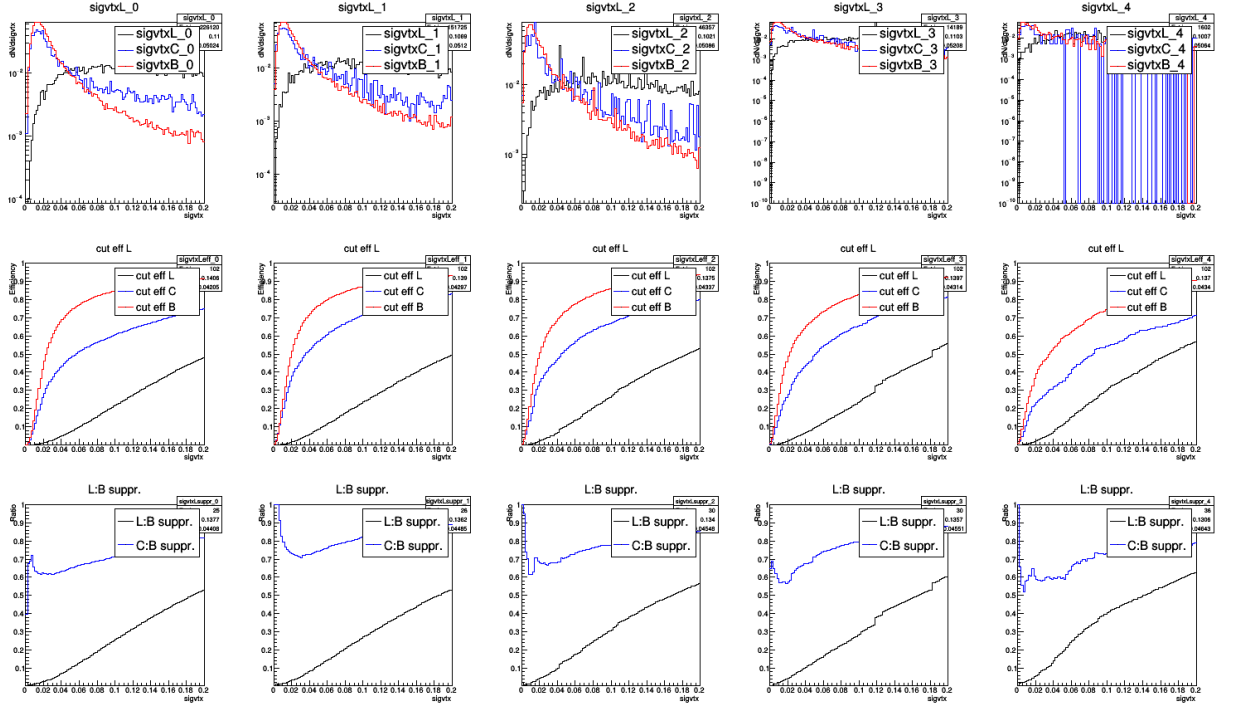


Figure A.13: Cut behavior on σ_{SV} distributions for b -jets (red), c -jets (blue) and light flavor jets (black), after an applied $SL_{xy} > 7$ cut, with different $p_{T,jet}$ selections (left to right, $p_{T,jet}$ -inclusive, $5 < p_{T,jet} < 20$ GeV/c, $20 < p_{T,jet} < 40$ GeV/c, $40 < p_{T,jet} < 60$ and $60 < p_{T,jet} < 100$ GeV/c. Top row is distributions, middle row is efficiency and bottom row is the suppression factor of a σ_{SV} cut placed at a given x position.

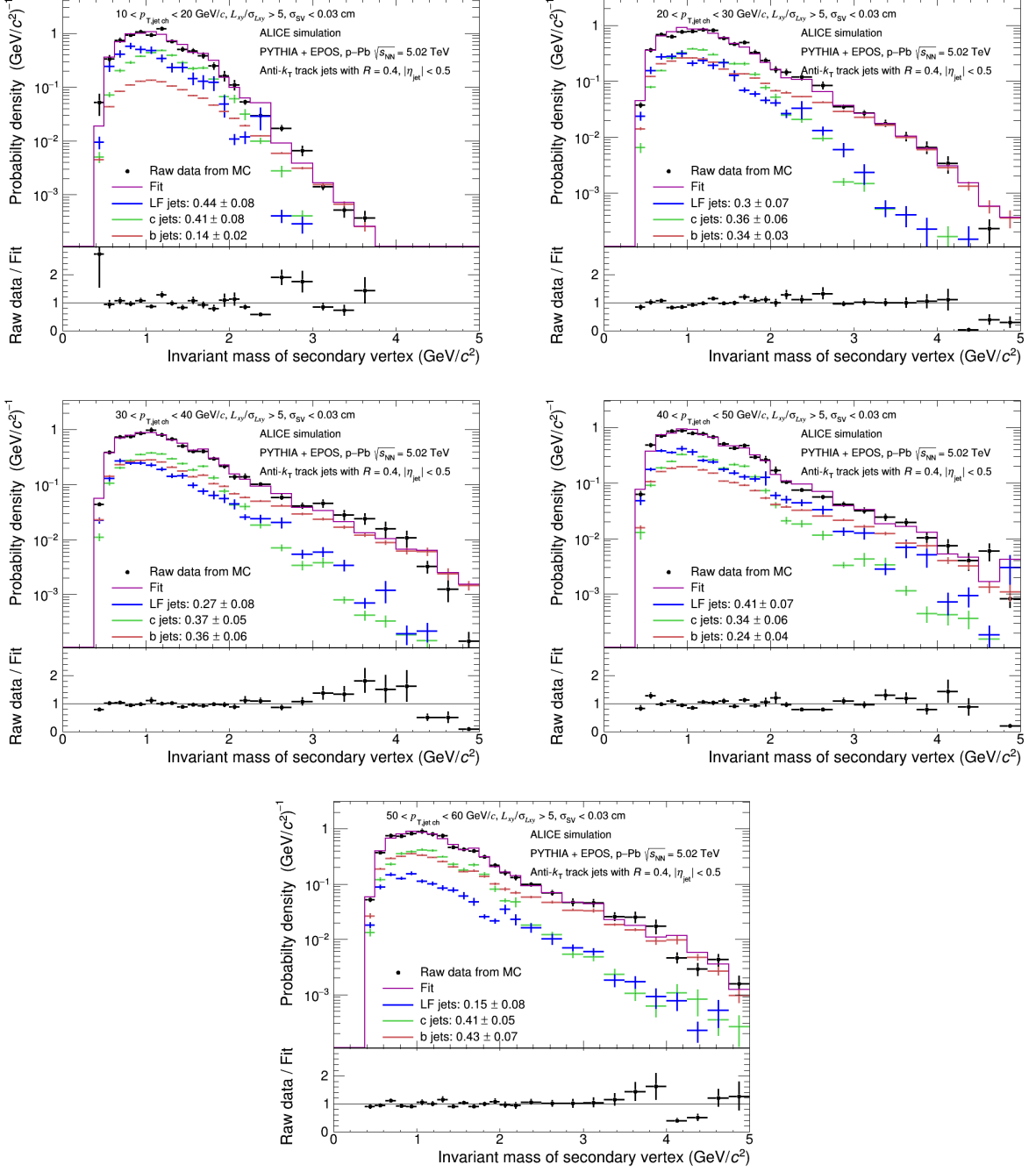


Figure A.14: Fit of the detector-level SV invariant mass distributions with smoothened MC templates. The cuts on SV were $\sigma_{SV} < 0.03 \text{ cm}$ and $L_{xy}/\sigma_{L_{xy}} > 5$. The bottom part of each panel shows the ratio of data to the fit.

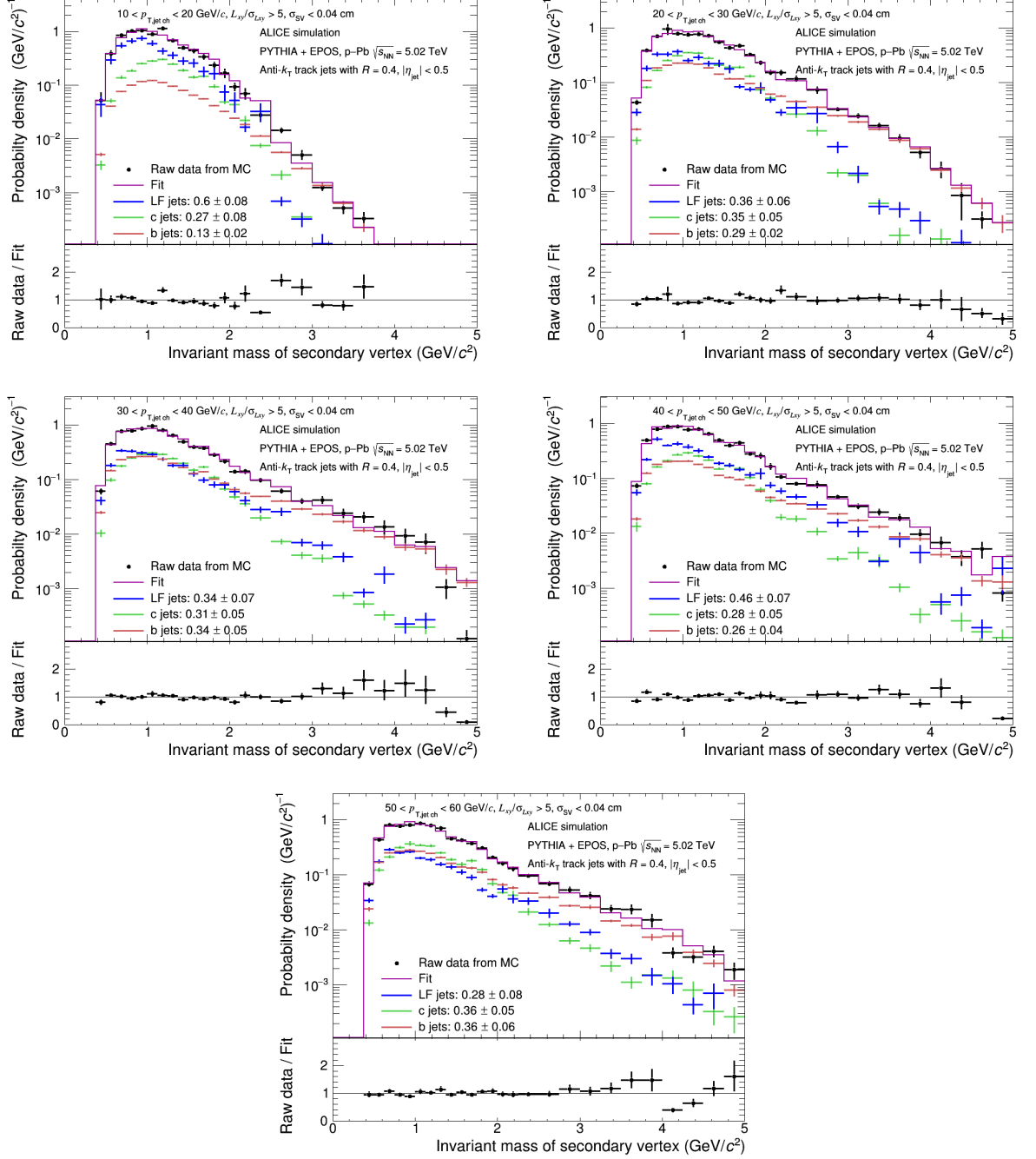


Figure A.15: Fit of the detector-level SV invariant mass distributions with smoothed MC templates. The cuts on SV were $\sigma_{\text{vertex}} < 0.04$ cm and $L_{xy}/\sigma_{L_{xy}} > 5$. The bottom part of each panel shows the ratio of data to the fit.

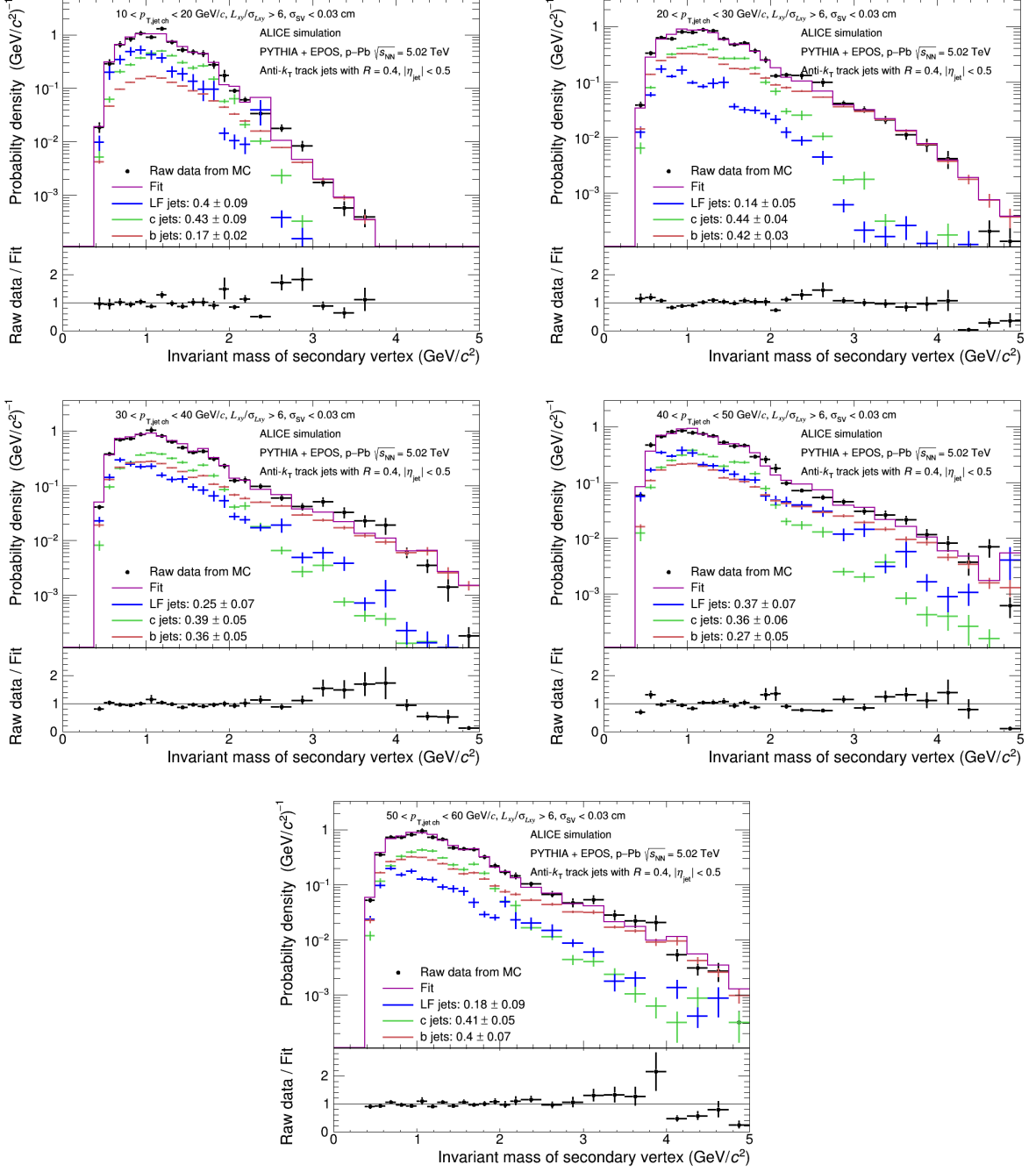


Figure A.16: Fit of the detector-level SV invariant mass distributions with smoothed MC templates. The cuts on SV were $\sigma_{SV} < 0.03 \text{ cm}$ and $L_{xy}/\sigma_{L_{xy}} > 6$. The bottom part of each panel shows the ratio of data to the fit.

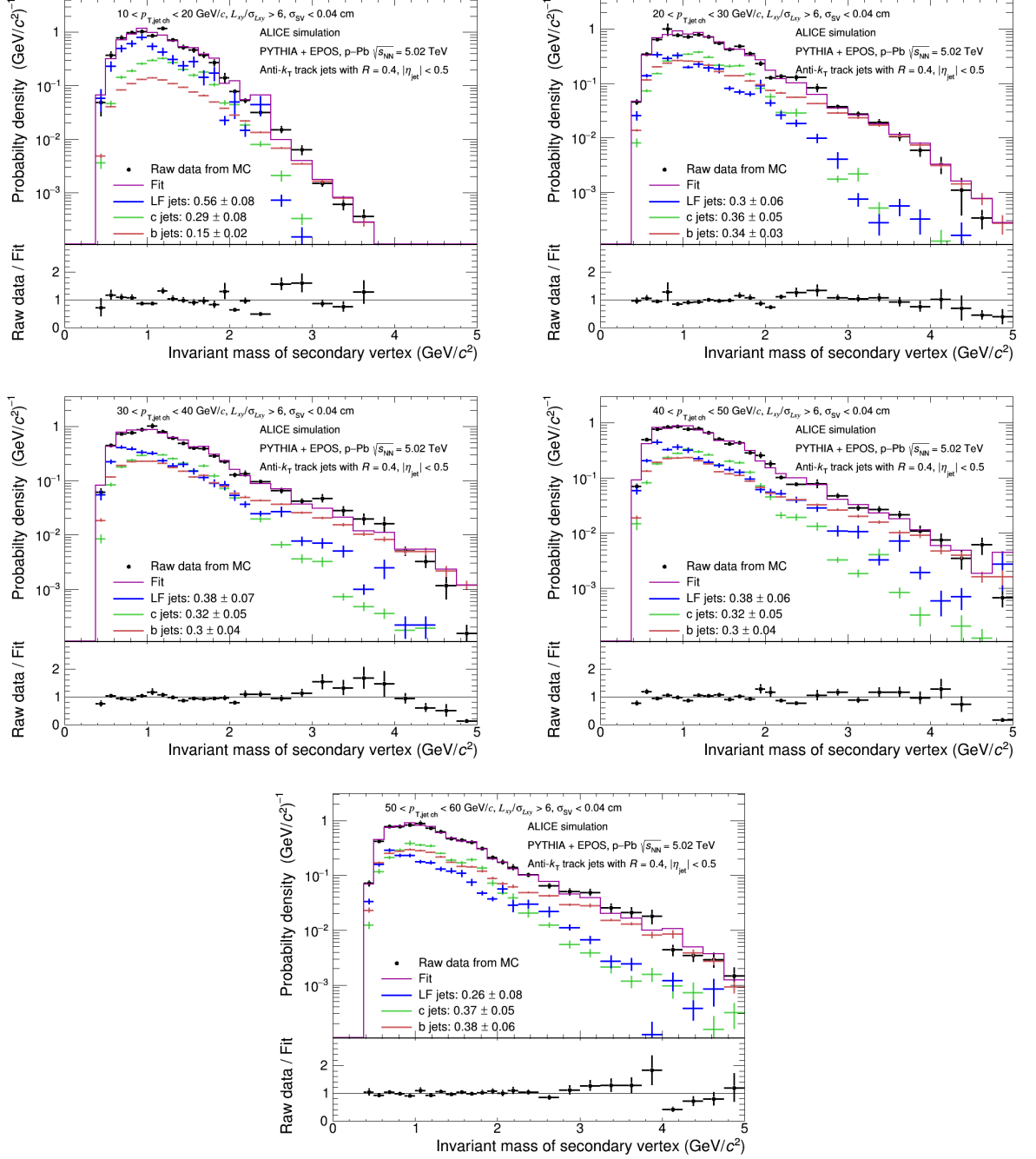


Figure A.17: Fit of the detector-level SV invariant mass distributions with smoothed MC templates. The cuts on SV were $\sigma_{SV} < 0.04 \text{ cm}$ and $L_{xy}/\sigma_{L_{xy}} > 6$. The bottom part of each panel shows the ratio of data to the fit.

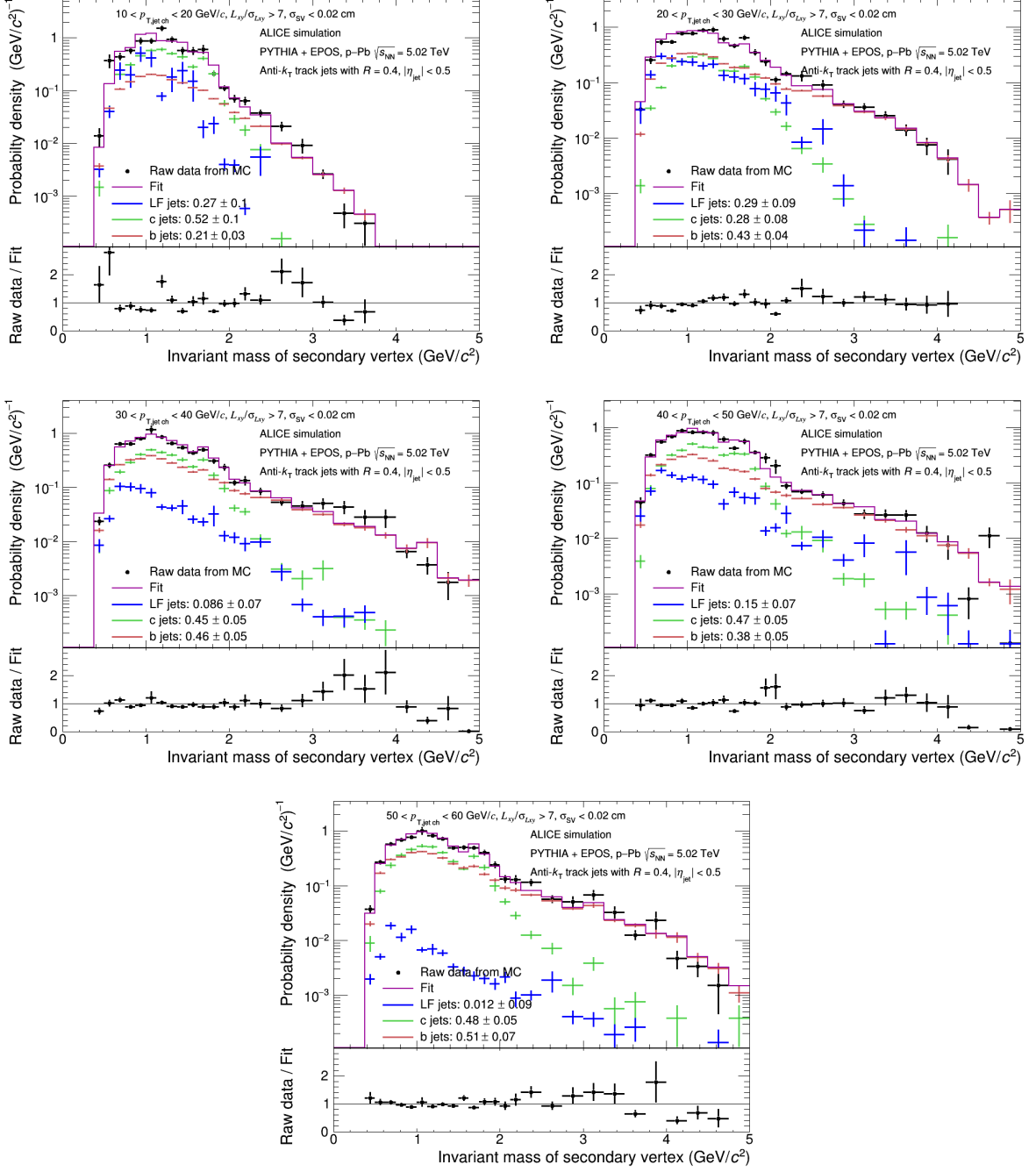


Figure A.18: Fit of the detector-level SV invariant mass distributions with smoothed MC templates. The cuts on SV were $\sigma_{SV} < 0.02 \text{ cm}$ and $L_{xy}/\sigma_{Lxy} > 7$. The bottom part of each panel shows the ratio of data to the fit.

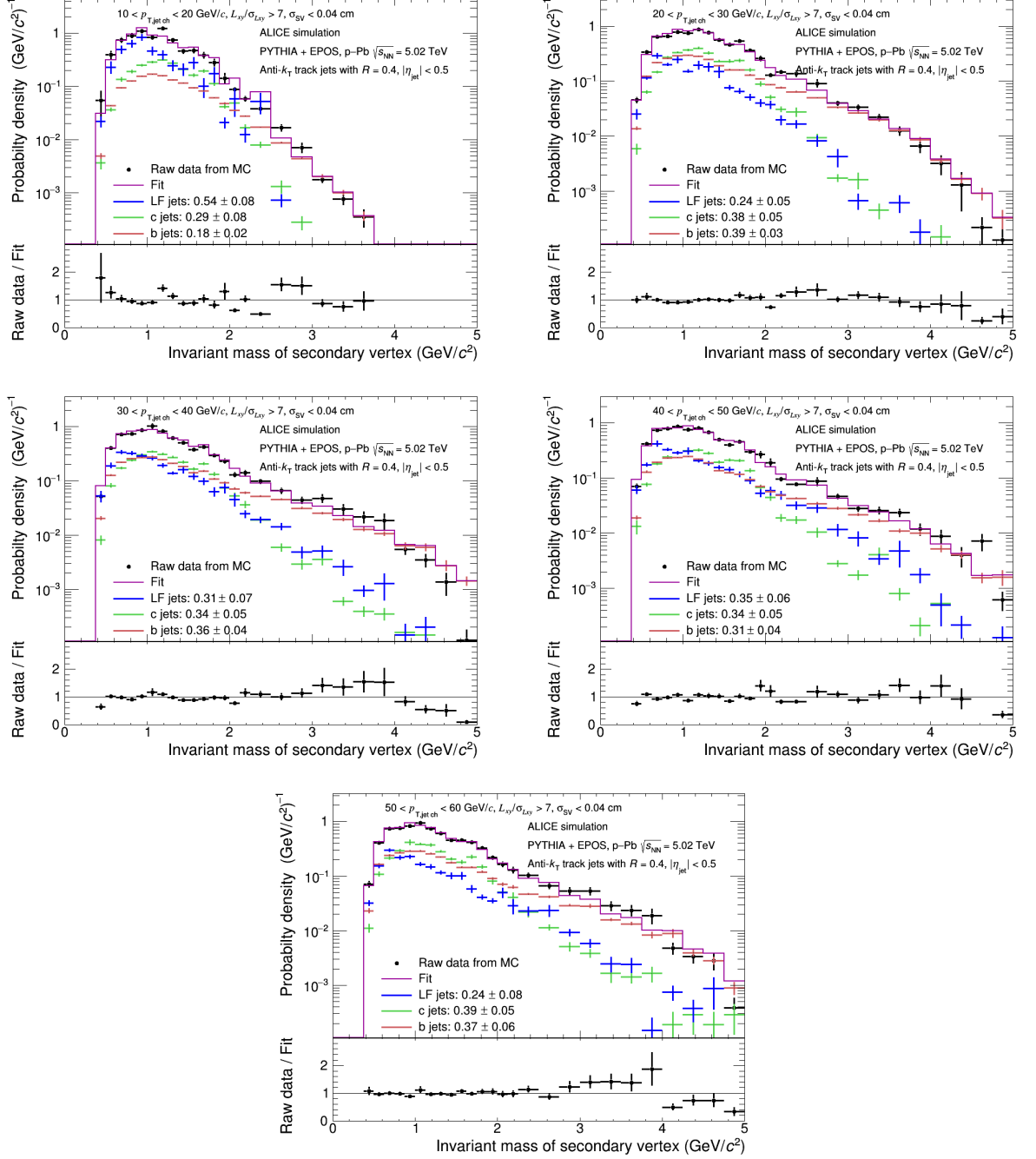


Figure A.19: Fit of the detector-level SV invariant mass distributions with smoothed MC templates. The cuts on SV were $\sigma_{SV} < 0.04 \text{ cm}$ and $L_{xy}/\sigma_{Lxy} > 7$. The bottom part of each panel shows the ratio of data to the fit.

Bibliography

- [1] P. W. Higgs, Phys. Rev. Lett. **13** (1964) 508.
- [2] ATLAS Collaboration, Phys. Lett. B **716** (2012) 1.
- [3] CMS Collaboration, Phys. Lett. B **716** (2012) 30.
- [4] Siegfried Bethke, Prog. Part. Nucl. Phys. **58** (2007) 351.
- [5] D. J. Gross and F. Wilczek, Phys. Rev. Lett **30** (1973) 1343; Phys. Rev. D, **8** (1973) 3633.
- [6] H. D. Politzer, Phys. Rev. Lett **30** (1973) 1346.
- [7] F. Karsch and E. Laermann, arXiv:hep-lat/0305025, (2003).
- [8] The DOE/NSF Nuclear Science Advisory Committee, arXiv:0809.3137 [nucl-ex], (2008).
- [9] IEBE-VISHNU, <https://u.osu.edu/vishnu/>
- [10] J. Rafelski and B. Muller, Phys. Rev. Lett. **48**, (1982) 1066 [Erratum Phys. Rev. Lett. **56** (1986) 2334].
- [11] P. Koch, B. Muller and J. Rafelski and, Phys. Rept. **142** (1986) 167.
- [12] WA97 Collaboration, Phys. Lett. B **449** (1999) 401.
- [13] STAR Collaboration, Phys. Rev. C **77** (2008) 044908.

- [14] ALICE Collaboration, Phys. Rev. Lett. **111** (2013) 222301; Phys. Lett. B **728** (2014) 216
[Erratum: Phys. Lett.B **734** (2014) 409].
- [15] E. Eichten, K. Gottfried, T. Kinoshita, K. D. Lane and T. M. Yan, Phys. Rev. D **17** (1978)
3090; Phys. Rev. D **21** (1980) 203.
- [16] NA50 Collaboration, Phys. Lett. B **477** (2000) 28.
- [17] PHENIX Collaboration, Phys. Rev. Lett. **98** (2007) 232301.
- [18] STAR Collaboration, Phys. Lett. B **722** (2013) 55.
- [19] ALICE Collaboration, Phys. Rev. Lett. **109** (2012) 072301.
- [20] CMS Collaboration, J. High Energy Phys. **05** (2012) 063.
- [21] J.D. Bjorken, FERMILAB-PUB-82-59-THY (1982).
- [22] STAR Collaboration, Nucl. Phys. A **757** (2005) 102.
- [23] PHENIX Collaboration, Nucl. Phys. A **757** (2005) 184.
- [24] ALICE Collaboration, Physics Letters B **783** (2018) 95.
- [25] CMS Collaboration, Phys. Rev. C **84** (2011) 024906.
- [26] ALICE Collaboration, arXiv:1311.2394v2 (2013).
- [27] STAR Collaboration, Nucl. Phys. A **757** (2005) 28.
- [28] S. Voloshin and Y. Zhang, Z. Phys. C **70** (1996) 665.
- [29] ALICE Collaboration, Phys. Lett. B **727** (2013) 371.
- [30] G. F. Sterman and S. Weinberg, Phys. Rev. Lett. **39** (1977) 1436.

-
- [31] T. Kaufmann, A. Mukherjee and W. Vogelsang, Phys. Rev. D **92** (2015) 054015.
- [32] Z.-B. Kang, F. Ringer and I. Vitev, J. High Energy Phys. **10** (2016) 125.
- [33] L. Dai, C. Kim and A. K. Leibovich, Phys. Rev. D **94** (2016) 114023.
- [34] L. Dai, C. Kim and A. K. Leibovich, J. High Energy Phys. **09** (2018) 10.
- [35] J. Huang, Z.-B. Kang and I. Vitev, Phys. Lett. B **726** (2013) 251.
- [36] Z.-B. Kang, J. Reiten, I. Vitev and B. Yoon, Phys. Rev. D. **99** (2019) 034006.
- [37] R. Rapp and H. van Hees, R.C. Hwa, and X.N. Wang (eds.), in Quark Gluon Plasma 4 (World Scientific, Singapore, 2010), p. 111.
- [38] G. D. Moore and D. Teaney, Phys. Rev. C **71** (2005) 064904.
- [39] S. Cao and S. A. Bass, Phys. Rev. C **84** (2011) 064902.
- [40] H. van Hees, V. Greco and R. Rapp, Phys. Rev. C **73** (2006) 034913.
- [41] A. Adronic et. al., Eur. Phys. J. C **76** (2016) 107.
- [42] F. Prino and R. Rapp, J. Phys. G **43** (2016) 093002.
- [43] R. Rapp et. al., Nucl. Phys. A **979** (2018) 21.
- [44] S. Cao *et al.*, arXiv:1809.07894.
- [45] X. Dong and V. Greco, Prog. Part. Nucl. Phys. **104** (2019) 97.
- [46] S.K. Das, F. Scardina, S. Plumari and V. Greco, Phys. Lett. B **747** (2015) 260.
- [47] S. Li, C. Wang, X. Yuan and S. Feng, Phys. Rev. C **98** (2018) 014909.
- [48] S. Li and C. Wang, Phys. Rev. C **98** (2018) 034914.

- [49] H. van Hees, M. Mannarelli, V. Greco and R. Rapp, *Phys. Rev. Lett.* **100** (2008) 192301.
- [50] P.B. Gossiaux et al., arXiv:1102.1114.
- [51] P.B. Gossiaux, J. Aichelin, M. Bluhm, T. Gousset, M. Nahrgang, S. Vogel and K. Werner, *PoS QNP* **2012** (2012) 160.
- [52] Y. Akamatsu, T. Hatsuda and T. Hirano, *Phys. Rev. C* **79** 054907 (2009); *Nucl. Phys. A* **830** (2009) 865.
- [53] W. M. Alberico et al., *Eur. Phys. J. C* **71** 1666 (2011); **73** (2013) 248.
- [54] C. Young, B. Schenke, S. Jeon and C. Gale, *Phys. Rev. C* **86** (2012) 034905.
- [55] M. He, R. J. Fries and R. Rapp, *Phys. Rev. C.* **86** (2012) 014903.
- [56] T. Lang, H. van Hees, J. Steinheimer and M. Bleicher, arXiv:1208.1643.
- [57] S. Cao, G.Y. Qin, S. A. Bass and B. Müller, *Nucl. Phys. A* **904** (2013) 653c.
- [58] S. Cao, G.Y. Qin and S. A. Bass, *J. Phys. G.* **40** (2013) 085103; *Phys. Rev. C.* **92** (2015) 024907.
- [59] H. Xu, X. Dong, L. Ruan, Q. Wang, Z. Xu and Y. Zhang, *Phys. Rev. C* **89** (2014) 024905.
- [60] M. He, R. J. Fries and R. Rapp, *Phys. Rev. Lett.* **110** (2013) 112301.
- [61] S.K. Das, F. Scardina, S. Plumari and V. Greco, *Phys. Rev. C* **90** (2014) 044901.
- [62] F. Scardina, S. K. Das, V. Minissale, S. Plumari and V. Greco, *Phys. Rev. C* **96** (2017) 044905.
- [63] Y. Xu, S. Cao, M. Nahrgang, J. E. Bernhard and S. A. Bass, *Phys. Rev. C* **97** (2018) 014907.

-
- [64] CMS Collaboration, JINST **8** (2013) P04013; Phys. Rev. Lett. **113** (2014) 132301; Phys. Lett. B **754** (2016) 59.
- [65] CMS Collaboration, Phys. Lett. B **772** (2017) 306.
- [66] ATLAS Collaboration, Eur. Phys. J. C **71** 1846 (2011); Phys. Lett. B **706** 295 (2012); ATLAS-CONF-2010-042.
- [67] B.L. Combridge, Nucl. Phys. B **151** (1979) 429.
- [68] K. Saraswat, P. Shukla and V. Singh, Nucl. Phys. A **961** (2017) 169.
- [69] W. Beenakker, H. Kuijf, W. L. van Neerven and J. Smith, Phys. Rev. D **40**, 54 (1989).
- [70] W. Beenakker, W. L. van Neerven, R. Meng, G. A. Schuler and J. Smith, Nucl. Phys. B **351**, 507 (1991).
- [71] H.L. Lai, M. Guzzi, J. Huston, Z Li., P.M. Nodolsky, J. Pumplin and C.P. Yuan, Phys. Rev. D **82** (2010) 074024.
- [72] K.J. Eskola, H. Paukkunen and C.A. Salgado, J. High Energy Phys. **0904** (2009) 065.
- [73] B. Muller, Phys. Rev. C **67** (2013) 061901.
- [74] V. Kumar, P. Shukla and R. Vogt, Phys. Rev. C **92** (2015) 024908.
- [75] I. Karpenko, P. Huovinen, M. Bleicher, Comput. Phys. Commun. **185** (2014) 3016.
- [76] R. Baier, A. H. Mueller, D. Schiff and D. T. Son, Phys. Lett. B **539** (2002) 46
- [77] G. D. Moore and D. Teaney, Phys. Rev. C **71** (2005) 064904
- [78] B. Svetitsky, Phys. Rev. D **37** (1988) 2484
- [79] P. Roy, J. Alam, S. Sarkar, B. Sinha and S Raha, Nucl. Phys. A **624** (1997) 687

- [80] P. Chakraborty, M.G. Mustafa and M.H. Thoma, Phys. Rev. C **75** 064908 (2007).
- [81] B. Svetitsky, Phys. Rev. D **37** (1988) 2484.
- [82] M. G. Mustafa, Phys. Rev. C **72** (2005) 014905.
- [83] S. K. Das, J. Alam and P. Mohanty, Phys. Rev. C **82** (2010) 014908.
- [84] M. Chojnacki, A. Kisiel, W. Florkowski and W. Broniowski, Comput. Phys. Commun. **183** (2012) 746.
- [85] M.H. Thoma and M. Gyulassy, Nucl. Phys. B **351** (1991) 491.
- [86] E. Brateen and M.H. Thoma, Phys. Rev. D **44** (1991) R2625.
- [87] A. Meistrenko, A. Pashier, J. Uphoff and C. Greiner, Nucl. Phys. A **901** (2013) 51.
- [88] S. Peigne and A. Peshier, Phys. Rev. D **77** (2008) 114017.
- [89] E. Brateen and M.H. Thoma, Phys. Rev. D **44** (1991) 1298.
- [90] M.G. Mustafa, D. Pal, D.K. Srivastava and M.H Thoma, Phys. Lett. B **428** (1998) 234;
Erratum: Phys. Lett. B **438** (1998) 450.
- [91] M. G. Mustafa, D. Pal, and D. K. Srivastava, Phys. Rev. C **57** (1998) 889.
- [92] Y. L. Dokshitzer and D. E. Kharzeev, Phys. Lett. B **519** (2001) 199.
- [93] Y. L. Dokshitzer, V. A. Khoze, and S. I. Troian, J. Phys. G **17** (1991) 1602.
- [94] R. Abir, C. Greiner, M. Martinez, M. G. Mustafa, and J. Uphoff, Phys. Rev. D **85** (2012) 054012.
- [95] O. Fochler, Z. Xu, C. Greiner, Phys. Rev. Lett. **102** (2009) 202301.

- [96] P. B. Gossiaux, J. Aichelin, T. Gousset and V. Guiho, J. Phys. G **37** (2010) 094019 .
- [97] W. A. Horowitz, [⟨arXiv:1011.4316\[nucl-th⟩](#) and references therein.
- [98] S. Wicks, W. Horowitz, M. Djordjevic, and M. Gyulassy, Nucl. Phys. A **784** (2007) 426;
Nucl. Phys. A 783 (2007) 493; M. Djordjevic and M. Gyulassy, Nucl. Phys. A **733** (2004)
265.
- [99] M. Gyulassy, P. Levai and I. Vitev, Phys. Rev. Lett. **85** (2000) 5535.
- [100] N. Armesto, M. Cacciari, A. Dainese, C. A. Salgado, and U. A. Wiedemann, Phys. Lett.
B673 (2006) 362.
- [101] B.Z. Kopeliovich, I.K. Potashnikova, I. Schmidt, Phys. Rev. C **82** (2010) 037901.
- [102] W.C. Xiang, H.T. Ding, D.C. Zhou and D. Rohrich, E. Phys. J. A **25** (2005) 75.
- [103] I. Vitev, J. Phys. G **35** (2008) 104011.
- [104] R. Abir, U. Jamil, M.G Mustafa and D.K Srivastava, Phys. Lett. B **715** (2012) 183.
- [105] K. Saraswat, P. Shukla and V. Singh, Nucl. Phys. A **934** (2015) 83.
- [106] C. Peterson, D. Schlatter, I. Schmitt and P. Zerwas, Phys. Rev. D **27** (1983) 105.
- [107] R. Sepahvand and S. Dadfar, Phys. Rev. D **95** (2017) 034012.
- [108] ALICE Collaboration, J. High Energy Phys. **1207** (2012) 191.
- [109] CMS Collaboration [CMS Collaboration], CMS-PAS-HIN-16-001.
- [110] CMS Collaboration, Phys. Rev. Lett. **119** (2017) 152301.
- [111] ALICE Collaboration, Phys. Lett. B **718** (2012) 295.

- [112] T. Sjostrand, S. Mrenna and P.Z Skands, J. High Energy Phys. **0605** (2006) 026.
- [113] R. J. Fries, B. Müller, C. Nonaka, and S. A. Bass, Phys. Rev. C **68** (2003) 044902.
- [114] C. B. Dover, U. W. Heinz, E. Schnedermann, and J. Zimanyi, Phys. Rev. C **44** (1991) 1636.
- [115] V. Greco, C. M. Ko, and P. Levai, Phys. Rev. C **68** (2003) 034904.
- [116] L.-W. Chen and C. M. Ko Phys. Rev. C **73** (2006) 044903.
- [117] Z. W. Lin and D. Molnar, Phys. Rev. C **68** (2003) 044901.
- [118] V. Greco, C. M. Ko, and R. Rapp, Phys. Lett. B **595** (2004) 202.
- [119] Y. Oh, C. M. Ko, S. H. Lee, and S. Yasui, Phys. Rev. C **79** (2009) 044905.
- [120] K. C. Han, R. J. Fries, and C. M. Ko, J. Phys. Conf. Ser. **420** (2013) 012044.
- [121] S. K. Das, J. M. Torres-Rincon, L. Tolos, V. Minissale, F. Scardina and V. Greco, Phys. Rev. D **94** (2016) 114039.
- [122] S. Gasirowicz, M. Neumann, and R. J. Riddell, Phys. Rev. **101** (1965) 922.
- [123] A.G. Sitenko, Electromagnetic Fluctuations in Plasma (Academic Press, New York, 1967).
- [124] A. I. Akhiezer et al., Plasma Electrodynamics (Pergamon Press, Oxford, 1975).
- [125] G. Kalman and A. Ron, Ann. Phys. **16** (1961) 118.
- [126] W. B. Thompson and J. Hubbard, Rev. Mod. Phys. **32** (1960) 714.
- [127] S. Ichimaru, Basic Principles of Plasma Physics (Benjamin, Reading, 1973).
- [128] A.I. Sheikh, Z. Ahammed, P. Shukla and M.G. Mustafa Phys. Rev. C **98** (2018) 034915.
- [129] ALICE Collaboration, J. High Energy Phys. **1603** (2016) 081.

- [130] CMS Collaboration [CMS Collaboration], CMS-PAS-HIN-15-005.
- [131] NA60 Collaboration, Phys. Rev. Lett **99** (2007) 132302 .
- [132] STAR Collaboration, Phys. Rev. C **90** (2014) 024906.
- [133] PHENIX Collaboration, Phys. Rev. Lett. **98** (2007) 232301.
- [134] PHENIX Collaboration, Phys. Rev. C **84** (2011) 054912.
- [135] ALICE Collaboration, J. High Energy Phys. **07** (2015) 051.
- [136] ALICE Collaboration, Phys. Rev. Lett. **109** (2012) 072301; Phys. Lett. B. **734** (2014) 314;
Phys. Lett. B. **766** (2017) 212.
- [137] CMS Collaboration, Eur. Phys. J. C **77** (2017) 252.
- [138] CMS Collaboration, Eur. Phys. J. C **78** (2018) 509.
- [139] L. Yan, P. Zhuang and N. Xu, Phys. Rev. Lett. **97** (2006) 232301.
- [140] A. Andronic, P. Braun-Munzinger, K. Redlich and J. Stachel, Phys. Lett. B **652** (2007) 259.
- [141] E. Ferreira et al., Phys. Lett. B **680** (2009) 50.
- [142] A.I. Sheikh and Z. Ahammed, arXiv:1903.10690 [hep-ph].
- [143] D. Banerjee, S. Datta, R. Gavai and P. Majumdar, Phys. Rev. D **85** (2012) 014510.
- [144] Y.Xu, S. Cao, M. Nahrgang, J.E. Bernhard, and S.A. Bass, Phys. Rev. C **97** (2018) 014907.
- [145] H. Barrebrah et al., Phys. Rev. C **90** (2014) 051901; F. Scardina, S.K. Das et al., Phys. Rev.
C **96** (2017) 044905.
- [146] A. Majumder, B. Muller and X. N. Wang, Phys. Rev. Lett. **99** (2007) 192301.

- [147] S. Mazumder, T. Bhattacharyya and J. Alam, Phys. Rev. D **89** (2014) 014002.
- [148] H. B. Meyer, Phys. Rev. D **76** (2007) 101701(R).
- [149] H. B. Meyer, Nucl. Phys. A **830** (2009) 641C.
- [150] S. Borsanyi, Z. Fodor, S. Mages, A. Schafer and K. K. Szabo, PoS (LATTICE2014) (2014) 232.
- [151] H. Haas, L. Fister and J. M. Pawłowski, Phys. Rev. D **90** (2014) 091501.
- [152] A.I. Sheikh and Z. Ahammed, Nucl. Phys. A **986** (2019) 48
- [153] LHC Machine, The CERN large hadron collider: accelerator and experiments, J. Instrum. **3** (2008) (S08001).
- [154] ALICE Collaboration, The ALICE experiment at the CERN LHC, J. Instrum. **3** (2008) S08002.
- [155] ATLAS Collaboration, The ATLAS Experiment at the CERN Large Hadron Collider, J. Instrum. **3** (2008) S08003.
- [156] CMS Collaboration, The CMS Experiment at the CERN LHC, J. Instrum. **3** (2008) S08004.
- [157] LHCb Collaboration, The LHCb Detector at the LHC, J. Instrum. **3** (2008) S08005.
- [158] C. Lefevre, The CERN accelerator complex. Complexe des accelerateurs du CERN. CERN-DI-0812015, Dec, 2008.
- [159] ALICE Collaboration, <https://alice-collaboration.web.cern.ch/>.
- [160] ALICE Collaboration, J. Instrum. **3** (2008), 8002; J. Instrum. **5** (2010), 3003.
- [161] ALICE Collaboration, <http://alicematters.web.cern.ch/?q=content/node/1080>.

- [162] Particle Data Group Collaboration, Phys. Rev. D **98** (2018) 3, 030001.
- [163] ALICE Collaboration, Phys. Rev. C **93** (2016) 2, 024917.
- [164] ALICE Collaboration, Eur. Phys. J. C **75** (2015) 5, 226.
- [165] ALICE Collaboration, J. Instrum. **8** (2013) 10016.
- [166] ALICE Collaboration, CERN-LHCC, 2004-025 (2004).
- [167] <https://alimonitor.cern.ch/production/raw.jsp>.
- [168] M. Cacciari, G. P. Salam and G. Soyez, Eur. Phys. J. C **72** (2012) 1896.
- [169] ALICE Collaboration, Phys. Lett. B **749** (2015) 68.
- [170] CMS Collaboration., J. High Energy Phys. **08** (2012) 130.
- [171] P. Nason, J. High Energy Phys., **0411** (2004) 040.
- [172] S. Frixione, P. Nason and C. Oleari, J. High Energy Phys. **11** (2007) 070.
- [173] S. Alioli, P. Nason, C. Oleari and E. Re, J. High Energy Phys. **06** (2010) 043.
- [174] T. Adye, arXiv:1105.1160 [physics.data-an]. <http://hepunix.rl.ac.uk/~adye/software/unfold/RooUnfold.html>.
- [175] G. D’Agostini, Nucl. Instrum. and Meth. A **362** (1995) 487.
- [176] A. Höcker and V. Kartvelishvili, Nucl. Instrum. and Meth. A **372** (1996) 469.
- [177] <https://twiki.cern.ch/twiki/bin/view/ALICE/BtagSecVtx#Tests>.
- [178] https://gitlab.cern.ch/ycorrale/repos_HFCJ_BJets-SV/tree/master/Unfolding/AliHeavyUnfold.

- [179] R. Haake, “Minimum bias charged jets in p-Pb collisions at $\sqrt{s_{NN}} = 5.02$ TeV”, ALICE-ANA-2013-933 (2014).
- [180] <https://aliceinfo.cern.ch/Notes/node/473>.
- [181] CMS Collaboration, Phys. Lett. B **759** (2016) 641.
- [182] S. Frixione and B. R. Webber, J. High Energy Phys. **0206** (2002) 029.
- [183] https://twiki.cern.ch/twiki/bin/view/ALICE/BtagSecVtx#Cut_optimization.